Study of Reaction Mechanisms and Short Range Correlations in Two Nucleon Emission off ^{4}He Using Polarized Photons

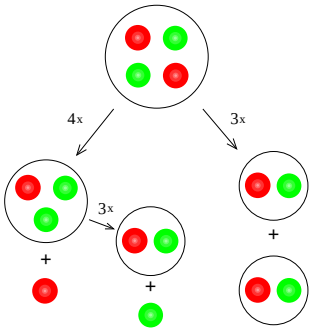

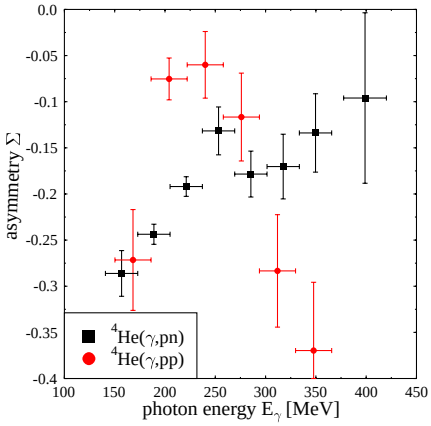

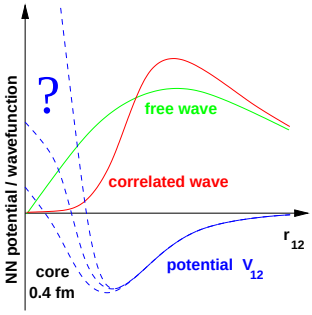

Dissertation

der Fakultät für Physik
der Eberhard-Karls-Universität zu Tübingen

zur Erlangung des Grades
eines Doktors der Naturwissenschaften

vorgelegt von
Frank Alexander Natter
aus Hohengehren

2002

Tag der mündlichen Prüfung :	14.06.2002
Dekan :	Prof. Dr. H. Müther
Erster Berichterstatter :	Prof. Dr. P. Grabmayr
Zweiter Berichterstatter :	Prof. Dr. H. Müther

Abstract

Diese Arbeit präsentiert die Ergebnisse des ^{4}He$(\vec{\gamma}, \mathrm{NN})$ Experiments, welches 1996 am MAMI (Mainz Microtron) im Rahmen der A2 Kollaboration durchgeführt wurde. Neben der präzisen Vermessung absoluter Wirkungsquerschnitte über einen großen Winkel- und Photon-Energiebereich ($E_\gamma = 110 \ldots 600$ MeV) stellen die gemessenen Asymmetrien unter Verwendung linear polarisierter Photonen ein Novum dar. Zum Einsatz für das 3-fach Koinzidenz-Experiments kamen die Detektoren PiP, ein mehrlagiges Plastikszinitillator-Hodoskop mit guter Orts- und Energieauflösung für Protonen, und ToF, eine großflächige Szintillatorwand zum Nachweis von Neutronen und Protonen mit Hilfe der Flugzeit-Methode, sowie der Glasgow-Tagger zur Energiemarkierung der Bremsstrahl-Photonen. Das Experiment hatte die Vermessung und Untersuchung nukleonischer Photoabsorptions-Mechanismen zum Ziel, um insbesondere durch die genuine 2N Absorption einen Zugang zum Studium der kurzreichweitigen Paarkorrelationen (short range correlations) zu finden. Diese Korrelationen basieren auf der hauptsächlich abstoßenden Nukleon-Nukleon Wechselwirkung bei kurzen Abständen, welche Ausdruck der Quark-Freiheitsgrade des Nukleons ist.

Neuerungen im Vergleich zum 1992er ^{12}C(γ, NN) Experiment sind das eigens für die Messung an ^{4}He entwickelte Kryotarget und der Einsatz eines Diamantkristalls als Bremsstrahl-Radiator. Die hohe Targetdichte und lange Standzeit des Kryotargets erlaubte eine vergleichsweise geringe Strahlzeit. Aufgrund des relativ großen Targetvolumens ergab sich leider eine kombinierte Energieauflösung aller Detektoren von ca. 5-10 MeV im Restenergie-Spektrum (E_{2m}). Durch die Verwendung des Diamant-Radiators am Eintritt des Taggers konnten linear polarisierte und energiemarkierte Photonen produziert werden. Eine verbesserte Beschreibung der Bremsstrahl-Erzeugung, unter Berücksichtigung der experimentellen Bedingungen, erlaubt die hinreichend präzise Bestimmung des Polarisations-Grades mit geringem systematischem Fehler.

Wie bei den Experimenten an Kohlenstoff, gelingt auch für Helium, durch Schnitte im Restenergie-Spektrum, die fast vollständige Abtrennung genuiner 2N Absorption von 3N Absorption, Pion-Produktion und FSI (final state interaction) Prozessen; besonders da letztere wesentlich schwächer ausgeprägt sind, als bei schweren Kernen. Obwohl diese Reaktionen, die bei mittleren und hohen Restenergien liegen, auch analysiert wurden und zum Verständnis der Photoabsorption beitragen, konzentriert sich diese Arbeit auf die Wirkungsquerschnitte und Asymmetrien der genuinen 2N Absorption. Von letzterer wird erwartet, daß sie besonders empfindlich auf Einflüsse der SRC (short range correlations) ist.

Hinweise auf SRC Effekte liefern vermutlich Abweichungen mancher Observabler von dem erwarteten Verhalten auf Grundlage des Schalenmodells, welche auch in der Auswertung des Experiments, z.B. in der Asymmetrie der Anregungsfunktion, gefunden wurden. Quantitative Aussagen können jedoch erst durch den Vergleich mit einem realistischen Modell gemacht werden. Besonders hilfreich für die Analyse von SRC Einflüssen ist die

Darstellung der Messung als Wirkungsquerschnitt und Asymmetrie für beide Isospinkanäle über eine Vielzahl von Observablen. Dadurch sind mehrere Randbedingungen an das Photoabsorptions-Modell und die korrelierte Wellenfunktion gestellt, welche entscheidend beitragen sollten, mögliche theoretische Beschreibungen von Korrelationen einzugrenzen.

Der Weg zur "Vermessung der SRC" ist von indirekter Natur: Der Vergleich von theoretischen Rechnungen mit verschiedenen SRC Modellen und 2N Photoabsorptions-Messungen sollte die adäquate SRC Beschreibung liefern, vorausgesetzt die theoretische Beschreibung der Photoabsorption ist vollständig und mathematisch exakt gelöst. Die Tatsache, daß sich die Helium-Wellenfunktion mittlerweile mikroskopisch aus der NN Wechselwirkung berechnen läßt, bedeutet, daß der Vergleich dieser Messung mit theoretischen Modellen ein Maß für die Qualität der theoretischen Beschreibung des (γ,NN) Prozesses sowie für den Nutzen bzw. Machbarkeit dieser Vorgehensweise liefert.

Nach einer Einführung (Kapitel 1) und der Beschreibung des experimentellen Aufbaus (Kapitel 2) wird die Theorie der Bremsstrahlung mit einer verbesserten Berücksichtigung experimenteller Randbedingungen in Kapitel 3 vorgestellt. Kapitel 4 beschreibt ein einfaches Modell zur Verdeutlichung des physikalischen Sachverhalts der 2N Photoabsorption, anhand welchem sich auch die kinematischen Bereiche bzw. der relevante Phasenraum und Observablen finden lassen, die besonders empfindlich auf SRC Effekte sind. Die notwendigen Schritte der Kalibrierung und Daten-Auswertung befinden sich in Kapitel 5. Untersucht wurden in dieser Arbeit Wirkungsquerschnitte und Asymmetrien in Abhängigkeit der Photonenergie sowie der Restenergie und des Restimpulses sowohl für den pn als auch den pp Endzustand (Kapitel 6). Desweiteren wurden diverse Winkelverteilungen mit Schnitten auf drei Photonenergie-Bereiche analysiert. Außerdem wurde die Ausbeute der 3N Emission, welche eine gute Abschätzung für den FSI Beitrag zu den inklusiven pn und pp Endzuständen liefert, studiert. Diese Analysen finden ihren Abschluss mit einem Versuch der physikalischen Interpretation und einer Zusammenfassung in Abschnitt 6.7 und 6.8.

Abstract

This work presents the results of the ^{4}He$(\vec{\gamma}, \mathrm{NN})$ experiment which was performed in 1996 at MAMI (Mainz Microtron) by the A2 collaboration. The measured asymmetries exploiting linear polarized photons are a novelty besides the precise measurement of absolute cross sections over a wide angular- and photon energy range ($E_\gamma = 110 \ldots 600$ MeV). The following detectors were employed for this 3-fold coincidence experiment: The multilayer plastic-scintillator PiP, a hodoscope with good position and energy resolution, and ToF, a large scintillator wall for detection of neutrons and protons via the time of flight method, and the Glasgow-Tagger for the energy-tagging of the bremsstrahl photons. The measurement and investigation of nucleonic photo-absorption mechanisms were the intention of this experiment. Particularly it aimed towards an understanding of the genuine 2N absorption to seek access to the study of short range correlations. These correlations are based on the short-range nucleon-nucleon interaction which is mainly repulsive and which is a result of the quark-degrees of freedom of the nucleon.

Innovations, compared to the ^{12}C(γ, NN) experiment in 1992, are the ^{4}He cryotarget, especially developed for the measurement on ^{4}He, and the application of a diamond crystal as bremsstrahl radiator. The beam time could be held relatively low due to the high target density and stand time of the cryotarget. The large target volume resulted unfortunately in a combined energy resolution of all detectors of about 5-10 MeV in missing energy (E_{2m}). The usage of a diamond radiator at the tagger entrance allowed the production of linearly polarized and energy-tagged photons. An improved description of the bremsstrahl production taking into account the experimental conditions results in a very precise determination of the polarization degree with small systematic error.

The nearly complete separation of genuine 2N absorption from 3N, pion production and FSI (final state interaction) processes succeeds via cuts in missing energy as it was established in the carbon experiments. This method works even more reliable for ^{4}He due to the smaller probability of FSI in lighter nuclei. These reactions which have higher missing energies also contribute to the understanding of photo-absorption and were thus analysed as well. Yet, this work concentrates on the cross section and asymmetry of genuine 2N absorption assumed to be particular sensitive on effects of short range correlations.

Differences of certain observables compared to the expected behaviour based on the shell model, which were found in this analysis (e.g. in the asymmetry of the excitation function), presumably hints towards SRC effects. However, quantitatively statements are only possible with a comparison to a realistic model. The results of this measurement, cross sections and asymmetries for both isospin channels and a wide spectrum of observables are particular helpful for the analysis of SRC influences. Therewith many boundary conditions are given for a photo-absorption model and the correlated wave function, which should contribute to reduce possible types of correlations. The method to determine SRC, which is exploited here, is an indirect one: The comparison of theoretical calculations with different SRC models and 2N photo-absorption measurements should discriminate all but the adequate

type of SRC, if the theoretical description of the photo-absorption process is complete and mathematical exactly solved. Meanwhile it is feasible to calculate the ^{4}He wave function based on the NN interaction solely. This means that the comparison of this measurement with theoretical calculations reveals the quality of the theoretical description of the (γ,NN) process. Moreover this comparison demonstrates the feasibility and benefit of this method to establish SRC effects.

The introduction (Chapter 1) and the description of the experimental set-up (Chapter 2) are followed by a presentation of the theory of bremsstrahlung and an improved consideration of experimental conditions (Chapter 3). Chapter 4 describes a simple model to clarify the physics of 2N photo-absorption. Therewith it may be searched for kinematical regions, relevant phase space and observables which are particular sensitive for SRC effects. The necessary steps of calibration and data-analysis are found in Chapter 5. In this work the cross section and asymmetries were studied in dependence of photon energy, missing energy and missing momentum for both, the pn and pp final states (Chapter 6). Additionally, various angular distributions with cuts on three photon energy regions were investigated. The yield of 3N emission was analysed as well, because it is a good estimate of the FSI contribution to inclusive pn and pp emission. The analysis of the data is concluded in section 6.7 and 6.8 by an attempt of a physical interpretation and a summary.

Contents

Chapter 1

Introduction

1.1 Overview

What are the fundamental constituents of matter, how do they interact and how do they form nuclear particles (hadrons, nucleons) and nuclei? Hadronic matter makes up almost the entire mass of the 'tangible' universe[1], ranging from the protons and neutrons in atomic nuclei and molecules to neutron stars. To unravel the rich and complex structure of the strongly interacting particles and their interactions is one of the remaining great challenges in physics. For nuclear physics, the primary aim is to understand the properties of nuclear particles on the basis of quarks and gluons and the characteristics of nuclei built by nucleons.

The strong interaction, which is responsible for hadronic structure and interactions, is widely believed to be described by a theory known as QCD[2]. The fundamental constituents of the QCD description of hadronic matter are referred to as quarks and gluons. Assuming that QCD is the correct theory for the strong interactions, it will be applied to understand the observed structure of hadrons and hadronic matter.

One of the most important questions in understanding the strong interaction is whether or not quarks and gluons play a significant role in nuclear systems. At high densities we need to explore the existence and nature of a deconfinement phase transition. At lower densities we wish to study the changes of hadron properties, such as mass and electroweak form factors, when immersed in nuclear matter. Finally, we may even ask whether the internal structure of the nucleon plays a role in the binding and properties of finite nuclei.

Therefore current investigations in subatomic physics aim to solve the nuclear many-body problem and to predict the properties of nuclei from the known interaction of protons and

[1] besides the speculative dark matter (WIMPs) which has been proposed to solve the puzzle of the missing mass in the universe

[2] Quantum Chromo Dynamics

neutrons. The formidable experimental and theoretical problems may become tractable using high-power computers [1–4] and exploiting new generations of electron and hadron beam facilities like MAMI (Mainz Microtron) [5], JLAB (Jefferson Laboratory) [6], ELFE (Electron Laboratory for Europe) [7] and GSI (Gesellschaft für Schwerionenforschung mbH) [8] and TRIUMF (Canada's National Laboratory for Particle and Nuclear Physics) [9]. The aim of our research group is to contribute to the study and understanding of nuclei, i.e. the nuclear force.

1.2 Shell model

One of the first and simplest nuclear models was the liquid drop model, which was the basis for the Weizsäcker parametrisation of nuclear masses and binding energies. Although single particle properties could not be described, it was very succesfully applied to quantify nuclear bulk properties. The experimental observation of the so-called magic numbers — neutron or proton occupation numbers of very stable nuclei — led to the SM[3], which was introduced in 1949 by Haxel, Jensen and Suess [10]. It comprised a phenomenological central potential (derived from measurements of charge density distributions) and a spin-orbit interaction, also implemented by Goeppert-Mayer [11].

In this model [12], the nucleons move as independent particles in a mean potential, which is solely generated by the interaction of the nucleons with each other. The Pauli principle keeps the nucleons mostly apart, so that their relative separation is of the order of their diameter, a prerequisite for the IPM[4]-model; thus the repulsion of the NN interaction at short distances has no large effect. Compared to the atom, the nuclear spin orbit interaction is much stronger but inverted. The splitting of the one-particle levels into LS doublets may in principle be derived from the spin-orbit and tensor interactions of the free NN force. For nucleons in the nuclear medium one depends on phenomenological models which typically use a Woods-Saxon central potential or, for the convenience of analytical calculations, an HO[5] potential and a spin orbit potential of Thomas type. The latter usually have a maximum near the nuclear surface.

Experimental confirmation of the SM was provided by measurements of proton and neutron binding energies, by the systematics of β and γ decay and magnetic dipole and quadrupole moments. Further investigations and tests of the SM exploited knock-out and pickup reactions like (p,2p), (d,^{3}He) and (d,t), which provided a spectroscopic tool to investigate nucleon probability distributions and thereby SM occupation numbers. With improved accelerators and beam quality (e,e'p) reactions with the following advantages became feasible: (i) The distortions of the incident projectile (ISI[6]) are entirely due to QED nature and so

[3] nuclear shell model
[4] independent particle model
[5] harmonic oscillator
[6] inital state interaction

are fully understood in contrast to the hadronic interactions. This allows the data to be analysed and the reaction to be described in the quasifree approximation. (ii) The energy and momentum transfer may be chosen independently, thus sampling a large kinematical regime. The drawback of electromagnetically induced reactions are the very small cross sections, which impose great demands on coincident experiments. All these experiments result from the attempt to find a consistent phenomenological nuclear potential which describes all single particle states similarly.

The SM provided the insight that nucleons really move in a way which is nearly independent of each other at low momenta, although that is scarcely conceivable, if one compares the size of a nucleon (≈ 0.8 fm) and their average distance (≈ 1.9 fm). Deviations from the SM, as show up for example in the occupation numbers, arising partly from the so-called SRC[7], were systematically studied at MAMI[8] by electromagentically induced one and two nucleon emission and are the subject of this thesis. Although nuclei are already rather well but not yet satisfactorily described by the SM, the holy grail in nuclear physics is the description of nuclei, their structure and nuclear reactions, in terms of a realistic NN interaction. Its parameters are constrained experimentally by free NN scattering, but in principle its derivation should also be possible from the fundamental QCD.

1.3 Short Range Correlations

There have been many attempts to describe the short-range part of the NN interaction based on the quark model and QCD [13, 14]. One would expect that the short-range repulsion originates from the Pauli-exclusion principle between the quarks by analogy to $\alpha\alpha$ scattering or the molecular potential. However, due to the spin, isospin (flavour) and colour degrees of freedom, the Pauli principle cannot account for the repulsion. The origin for this effect is found in the strong spin-spin interaction, also known as the colour magnetic interaction. In a simple constituent quark model [15] the mass of a hadron consisting of n s-wave quarks is written as the sum of the effective quark masses m_i and the spin interaction energy: $V_\sigma^{ij} \propto \alpha_s \vec{\sigma}_i \vec{\sigma}_j / m_i m_j$. Employing the phenomenological parameters of Tab. 1.1 below, the following mass formula describes the observed hadron masses astonishingly well:

$$M_H = \sum^n m_H + \sum_{i<j}^n V_\sigma^{ij} = \sum^n m_H + \big(2S(S+1) - 3n/2\big) E_\sigma$$

The constituent quark masses in the baryon system are larger than in the meson one. That is due to the dynamically generated masses of the constituent quarks, which is expected to be different in a 3-quark system than in a quark-antiquark one. In a 6-quark system one can expect that additional qq interaction graphs are possible increasing the effective quark

[7] short range correlations
[8] Mainz Microtron

[MeV]	Meson	Baryon	6-quark state
m_q	310	363	416
E_σ	160	50	50
$M_H(S)$	$\pi(0)$: 140	N($\frac{1}{2}$): 939	$S=0$: 2046
	$\rho(1)$: 780	$\Delta(\frac{3}{2})$: 1239	$S=1$: 2246

Table 1.1: Hadronic masses from a simple model. Note the parameters for the 6-quark state are just estimates.

mass. Therefore, the mass enhancement is assumed to be of the same amount as that for the baryon quark mass compared to the meson one, hence $m_6 = m_B + (m_B - m_M)$. The mass formula yields $M_6 \approx 2050$ MeV for the 6-quark system, if it is also supposed further that the same spin-spin interaction constant E_σ as in the baryon sector can be applied. Thereby the NN repulsion at short distances can be explained: If two nucleons are separated by a distance R, the total energy relative to the mass of two free nucleons is identified as the NN potential. This derivation of the potential is referred to as an adiabatic treatment (compare Section 4.3). In this simple model the repulsive core would have the strength: $V_r(R=0) = M_6 - 2M_N \approx 170$ MeV. The authors of more sophisticated constituent quark models [16, 17] conclude that the strength of the resultant NN repulsion is about 200-500 MeV, reaching its maximum at about 0.4 fm. These calculations are of a phenomenological nature, because a nuclear state dependence is not fully considered and the qq-potential is described by a simple (linear or quadratical) confinement and only a OGEP[9] is included. However, these studies indicate the principal source of the short-range NN repulsion.

The short-range force is not included in the mean-field model of the SM. For an improved description, the nucleon wave function has to be calculated using a realistic NN potential which includes the short-range part. This potential is obtained, for example, from a fit of a general ansatz, which is based on fundamental interaction operators and invariance principles, to NN scattering data. However, due to the extreme complexity in solving a coupled system of A Schrödinger equations, the microscopic description of the atomic nucleus using realistic NN potentials is still an unsolved problem. The apparent success of independent particle models (like the SM) with respect to single particle properties is surprising considering the strong repulsion at NN distances below 0.4 fm compared with the average separation of nucleons in nuclei. It is well known that Hartree-Fock calculations succeed to produce correct binding energies only with effective potentials; realistic potentials with mean-field wave functions generally lead to unbound nuclei [18]. Great theoretical and experimental efforts have been made in recent years to solve that problem. It is necessary to go beyond the IPM model with its wave functions given by Slater-determinants. The use of correlated wave functions, which account for the short range repulsion, is mandatory. In contrast to mean-field wave functions, correlated wave functions allow for short range central repulsion and state-dependent tensor forces beyond the trivial effects (due to Pauli blocking, translational invariance etc.). Fig. 1.1 below illustrates the suppression of the correlated wave function at short distances in a very schematic way.

[9] one gluon exchange potential

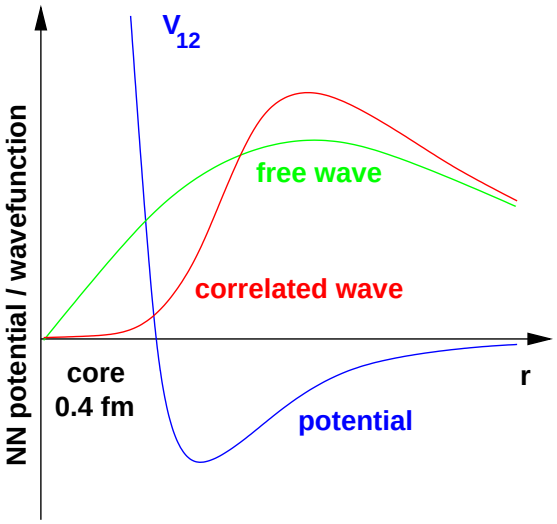

Figure 1.1: Schematic plot of the NN potential and the corresponding difference between an uncorrelated and correlated wave function of the nucleon; r is the relative NN separation. The trend of the repulsive part of the potential and how it saturates is still unknown.

Because correlations are not directly observable, various attempts have been made in the past to find evidence for their existence. Indirect evidence can be found of their influence on the momentum distribution of nucleons in nuclei: correlations lead to population of states beyond the Fermi edge k_f and to depletion of otherwise filled states, as indicated in Fig. 1.3(a) on page 7. In Fig. 1.3(b) the occupation numbers have been extracted using the CERES sum rule [19] from spectroscopic factors measured in exclusive (e,e′,p) reactions. Up to now, one of the most precise (e,e'p) measurements was performed at NIKHEF with an energy resolution of about 100 keV at electron energies of 500 MeV, using large magnetic spectrometers. In one-nucleon knock-out experiments the effect of correlations is only important for excitation energies of the residual nucleus far above the 2N emission threshold [20]. Therefore electromagnetically induced two-nucleon emission is expected to give a more direct access to short range correlations.

As early as the 1950s Gottfried [21] showed that (with some approximations) the cross section of 2N photo-absorption should factorize as

$$\sigma \sim S_{fi}\big(\langle\phi(k)\rangle\big) \cdot F(K)$$

with K and k being the initial pair momentum and their relative momentum, respectively. The kinematical features of the cross section are determined by the pair momentum distribution $F(K)$, whereas S_{fi} describes the reaction dynamics. The latter depends on the relative momentum distribution, which is strongly affected by correlations. The study of the simultaneous ejection of two hadrons after absorption of real photons aims to provide a detailed understanding of photo-absorption reaction mechanisms which is a prerequisite for addressing short-range effects.

Due to their purely transverse character, real photons will not only be absorbed by correlated nucleon pairs (1BC), but also by meson exchange (MEC) and Δ isobar currents (IC). Fig. 1.2 below shows the respective diagrams; MEC absorption being dominant in the

(γ,pn) channel. The calculation of all contributions, based on a realistic NN potential and including final state interaction, is the goal of recent theoretical calculations.

1.4 Previous experiments and results

The recent (γ,NN) experiments on lithium [22] and carbon [23–30] provided a great deal of progress on the experimental side and on methods of analysing the data. All the detailed corrections needed to obtain the accurate physical observables were extensively studied. For example the implementation of the so-called range method (Section 5.1.4) allowed the correction for hadronic losses in the detectors. Furthermore the detailed investigation of systematic errors gave confidence in the stated absolute cross sections. Direct NN absorption could be identified over a wide photon energy range and missing mass spectra showed that it contributes most at low missing energy (small excitation energy of the residual nucleus), the so-called nuclear shell model region. The excitation function for photo-absorption on the deuteron cluster in Lithium can be described by the absorption on a free deuteron moving with the Fermi motion of the cluster. Comparison to calculations involving a correlated cluster wave function from the Moscow group [31] supports this picture. These experiments provided a good understanding of the (γ,NN) reaction which is especially demonstrated in the good agreement of the measured (γ,pn) cross section and the Valencia model [32–34]. Those comparisons are reliable and meaningful due to the inclusion of the experimental thresholds and acceptance in the model calculation. In the (γ,pp) case the shapes agree well, but the model overestimates the cross section by a factor of about 3.5. Information about the MEC contribution and the influence of FSI were gained from a comparison of the (γ,pn) and (γ,pp) reactions, in particular for small missing energies. In these experiments an energy resolution of about 6 MeV was obtained, which allowed determination of the shells from which the nucleons were ejected. In the shell model region the results are well explained by the quasi-deuteron model [21,22,35], whereas for higher missing energies quasifree pion production and FSI dominate the cross section. In the analysis an enhancement of high relative momenta were found for ^{6}Li and ^{12}C compared to deuteron. This

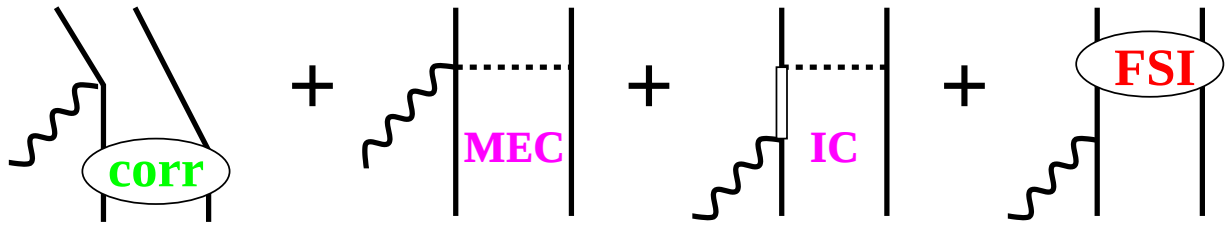

Figure 1.2: Processes contributing to two nucleon emission: absorption on a correlated pair (1BC), on meson exchange currents (MEC), on Δ isobar currents (IC) and via final state interactions (FSI). Additional diagrams arise from the exchange of both nucleons and from the time ordering.

might be an effect driven by medium dependent SRC. In [36], however, it was argued that it could be explained by acceptance effects alone. There is an additional argument against a SRC effect: Even though SRC should enhance high relative momenta in the initial state (see Chapter 4), there is only a very marginal kinematical correlation between the latter and the final relative momentum. Hence, it is not possible to draw conclusions from the final relative momentum distribution about the initial state.

1.5 Why ^{4}He and why polarization?

Due to the low mass number and high central density of the ^{4}He nucleus, there is great interest in ^{4}He as a target for experiments in intermediate energy nuclear physics. On one side, ^{4}He can be treated as a few body system permitting almost exact calculations of its ground state properties [37] and response functions. On the other side, in many respects, the ^{4}He nucleus behaves like other medium or heavy nuclei (e.g. consider the total photo-absorption cross section per nucleon). For some of the p-shell nuclei the α particle is one of the building blocks described in a cluster model. Investigating partial reaction channels, the four nucleons in ^{4}He have the advantage of reduced pertubations due to final state

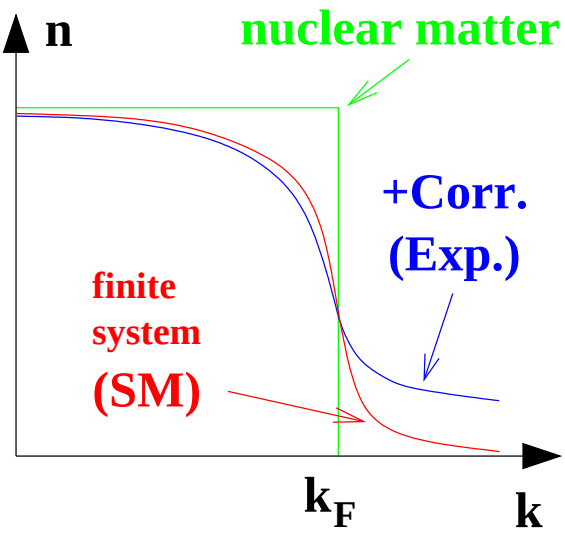

(a) Correlations deplete the occupancy below the Fermi edge, the strength is shifted to larger momenta. (Green line) without correlations, (red line) with correlations in nuclear matter.

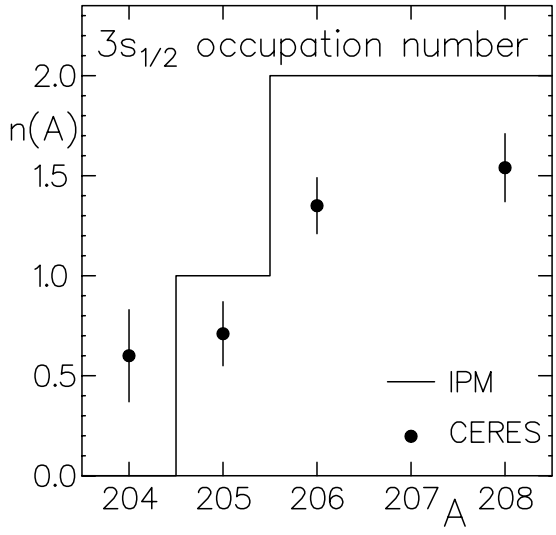

(b) Occupation numbers as extracted via the CERES sum rule (dots), compared to IPM predictions (line). Measured on Lead ($Z = 82$) for different neutron numbers $N = A - Z$.

Figure 1.3: Schematic and measured nuclear shell occupancies, which demonstrate the softening of the Fermi edge due to correlations.

interactions, compared to heavier nuclei.

The ^{4}He nucleus was selected for a detailed study of the (γ,NN) reaction for several reasons: (i) In contrast to other targets (like ^{6}Li and ^{12}C) ^{4}He has only 1s nucleons in an uncorrelated SM. (ii) It is expected that the impact of short range correlations should be large due to the high central density (which is twice the average density of heavier nuclei). (iii) As a result of the small number of nucleons, FSI should have only a small influence and therefore the observables will be less distorted. (iv) Recently, the four-nucleon system becomes accessible to few-nucleon models [2, 37, 38], making ^{4}He a meeting ground with many-body theories or phenomenological models [39]. The latter still need many approximations even for light nuclei. Furthermore, the availability of linearly polarized photons produced with coherent bremsstrahlung (see Chapter 3) yields a new degree of freedom in (γ,NN) experiments. In particular, the photon asymmetry is predicted to be sensitive to central and tensor correlations [40–42].

There have been previous studies of the ^{4}He(γ,NN) reaction, which were performed at MAMI-A by Doran *et al.* [43] for $E_\gamma = 80 \ldots 131$ MeV and at TagX [44, 45]. Adamian *et al.* [46] carried out a measurement of the photon asymmetry of the ^{4}He(γ,pn) cross section in the photon energy range $450 \ldots 550$ MeV and the one of ^{6}Li ($E_\gamma = 300 \ldots 900$ MeV). The MAMI-A experiment had a limited photon energy range (80-130 MeV) and a rather small neutron acceptance. However, amongst other things it was ascertained that the two body absorption (γ,pn) dominates the four body breakup. At TagX, the excitation functions for two and three nucleon emission, (γ,np)d and (γ,npp)n, were investigated at photon energies from just above MAMI-A energy up to 455 MeV. Hints of a three body absorption mechanism were found in this measurement. Adamian *et al.* performed a comparative study of photon asymmetry on D, ^{6}Li, ^{4}He in the region $E_\gamma = 300 \ldots 900$ MeV. They found the energy dependence of the photon asymmetry was similar in all these nuclei but small deviations could not be ruled out owing to experimental limitations such as the use of untagged bremsstrahlung and small angular acceptance. These results are compared in Chapter 6 with the current measurements reported in this thesis.

Chapter 2

Experiment

2.1 Experimental setup

The data analysed in this thesis are based on the ^{4}He(γ,X) experiment carried out in 1996 in collaboration with Edinburgh and Glasgow Universities using the electron accelerator MAMI at the Institut für Kernphysik at Mainz. With an electron beam energy of 855 MeV bremsstrahlung photons were tagged in an energy region from 110 to 800 MeV. Their energies are determined by measuring the energies of the associated residual electrons employing the Glasgow Tagger[1]. The collimated photon beam induces in the target, a specially designed ^{4}He cryotarget, hadron knock-out interactions. For a sufficient target density a liquid helium target had to be used. It had a reasonable refill period of about 12 hours due to an appropriate heat shielding. Geometrical constraints and the purpose of minimizing the particle energy loss demanded a rather compact and low density cell. A segmented double ring array of thin ΔE scintillators (SVD[2]) surrounds the targed to define the timing for ToF[3] [47, 48] and to provide triggering information. The inner ring provides a start signal for the whole readout system and the outer one serves to derive a veto signal for discrimination of charged and uncharged reaction products. Two major detector systems were employed to identify the resulting products of the photonuclear reaction: PiP[4], a segmented plastic scintillator hodoscope, for the detection of pions and protons and ToF, a large versatile scintillator array for protons, deuterons and neutrons. PiP is made up of 19 thick horizontal plastic scintillator blocks and four thin vertical ΔE sheets, see Fig. 2.6(a) on page 18. The particle energy is obtained from the amplitudes, whereas the good angular resolution follows from the segmentation and the readout of the bars by a PMT[5] at both ends. ToF consists of 107 plastic scintillator bars, $300 \times 20 \times 5$ cm^3

[1] photon-tagging magnetic spectrometer
[2] start and veto detector
[3] time-of-flight detector
[4] pion-proton hodoscope
[5] photo multiplier tube

each [47], which are mounted vertically in groups of eight, see Fig. 2.6(b) on page 18. In this experiment, ToF covered nearly half of the reaction plane and was arranged in double layers, which results in an average neutron detection efficiency of 10 %. The high polar angular resolution comes from the segmentation whereupon the azimuthal angle is reconstructed from the hit position along the bar, which again are read out at both ends adducing a resolution of 2°. The complete experimental setup located in the A2-hall of MAMI is shown in Fig. 2.1 below.

2.2 The Mictrotron MAMI at Mainz

The relative high electron beam energy of MAMI accompanied by a very high quality and stability is reached by three succesively larger RTM[6] stages. The accelerator achieves thereby a duty factor of 1 at beam currents in the range of ∼1 pA up to 0.1 A. If the beam is directed in the Tagger-hall (A2-hall), then the count rate restriction of the Tagger PMTs demand a beam current of 1-50 nA. A typical RTM stage is shown schematical in Fig. 2.2 on page 12, consisting of a linear accelerator (linac) and two bending magnets, which recirculate electrons back into the linac for another acceleration through an array of return pipes. For each pass the electron orbit radius is increased accordingly by the same ΔE to ensure that the electrons are in phase with the acceleration field in the radio frequency cavities. Although this method allows to operate the klystrons in continuous wave (c. w.) mode, their radio frequency of 2.45 GHy generates a microstructure in the beam. However this is not yet resolved by the detectors having time resolutions in the same order of magnitude, which means the beam can be considered essentially continuous for practical purposes.

Fig. 2.3 on page 13 shows the schematic floor plan of the MAMI facility with its three RTMs and experimental halls A1 ... A4. The electrons which are emitted by the source with 100 keV are accelerated by three linacs to 3.5 MeV and fed into the first 18 turn microtron (RTM1). There the beam energy is increased to 14 MeV and in RTM2 (51 turns) to 180 MeV before it is injected into the 90 turn RTM3, boosting the beam with a RF power of 70 kW to a final energy of 854.6 MeV with an energy spread of 30 keV FWHM[7] and emittance of about $13 \cdot 1.7$ (π mm mrad)^2. A series of dipoles and quadrupoles guide the electrons along the beam line as shown in Fig. 2.3 on page 13 and allow to steer the beam in any of the experimental halls.

[6] race track microtron
[7] full width at half maximum

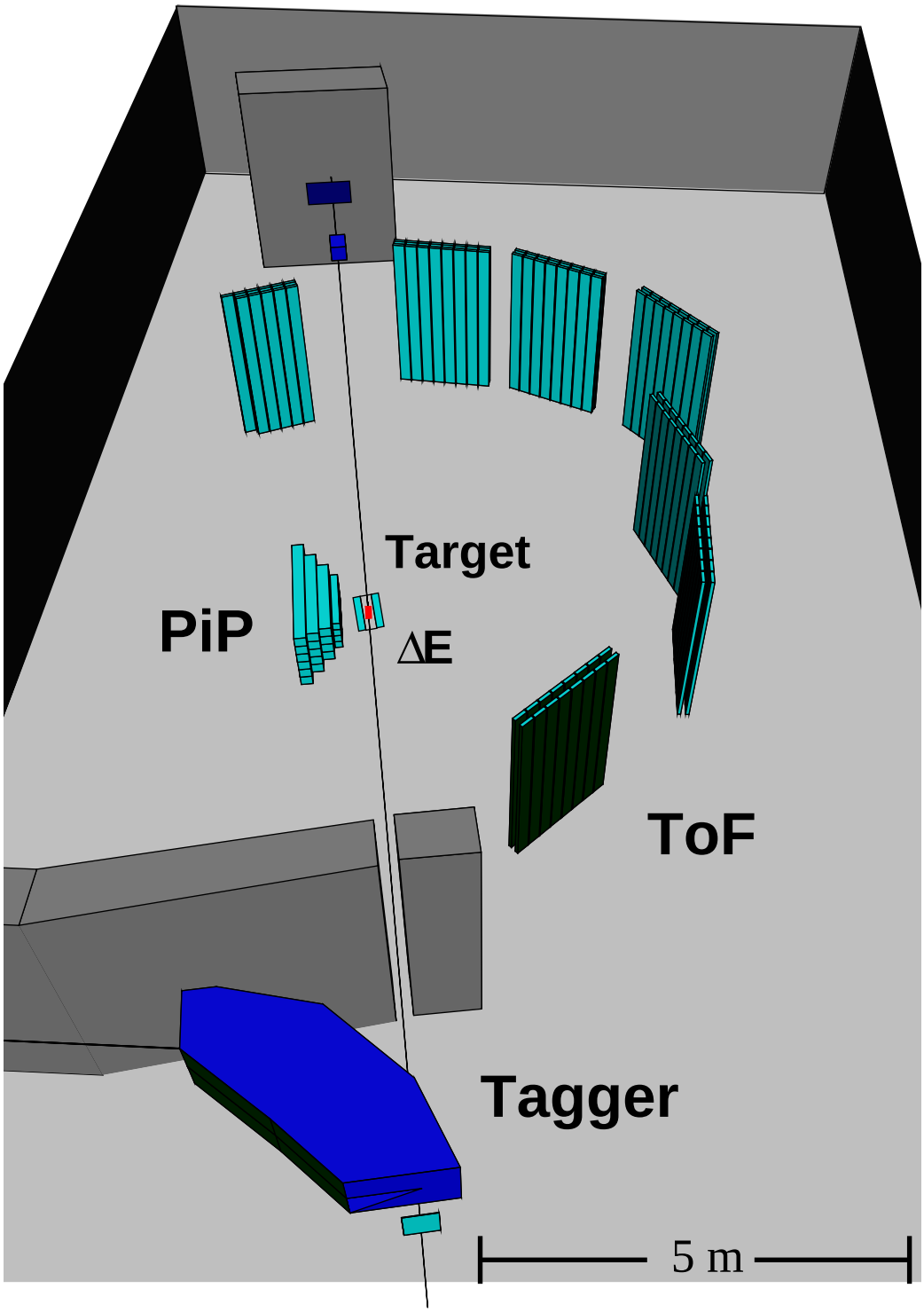

Figure 2.1: MAMI A2 hall and detector setup of the ^{4}He(γ,NN) experiment.

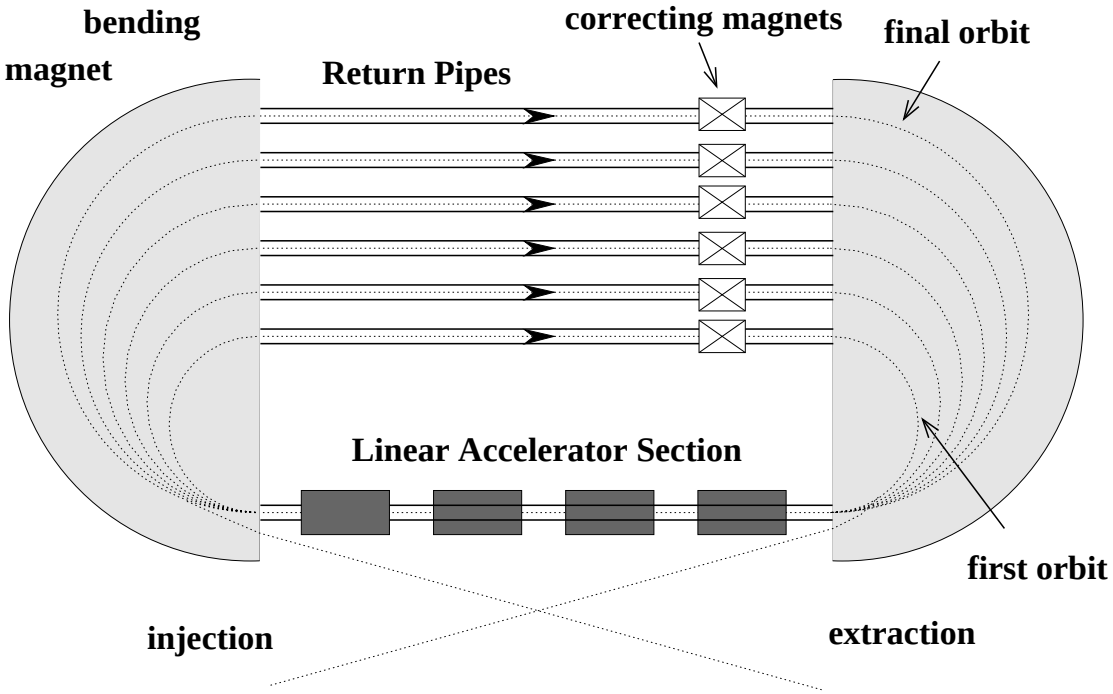

Figure 2.2: Schematic diagram of one typical RTM.

2.3 Photon tagging

The photons used for the experiment are produced via bremsstrahlung of the electrons from MAMI inside the A2 hall, where they are focused on a radiator. Employing a 4 μm Ni foil yields an incoherent photon beam, whereas the use of a crystal radiator (100 μm diamond) produces an additional coherent component resulting in a partially polarized photon beam (see Chapter 3). The photons have an energy spectrum which decreases approximately with $1/E_\gamma$ and they emerge the radiator in a forward directed cone with an opening angle of about $\langle \vartheta_\gamma \rangle \approx 1/E_e$. In order to reject of the photon beam halo and to reach a defined photon flux the Bremsstrahlung photons are collimated, forming a small spot (smaller than the target cell) on the target downstream. The Tagger is a dipole magnet which provides typically a field of ≈ 1 Tesla and which measures the momentua of the scattered electrons. The photon energy is deduced from the energy of incident (E_0) and scattered electron (E_e) [49, 50]:

$$E_\gamma = E_0 - E_e \tag{2.1}$$

Two magnets, in front of and afterwards the radiator, allow to steer the beam onto the radiator and to focus the electrons vertically at the focal plane, if necessary. which is shown schematically in Fig. 2.4 on page 14. The shape of the large dipole magnet creating a homogenious field is such that it focuses mono-energetic electrons on a defined point of the focal plane, which is shown schematically in Fig. 2.4 on page 14. Electrons which have not interacted with the radiator are bent away into the Faraday cup outside the

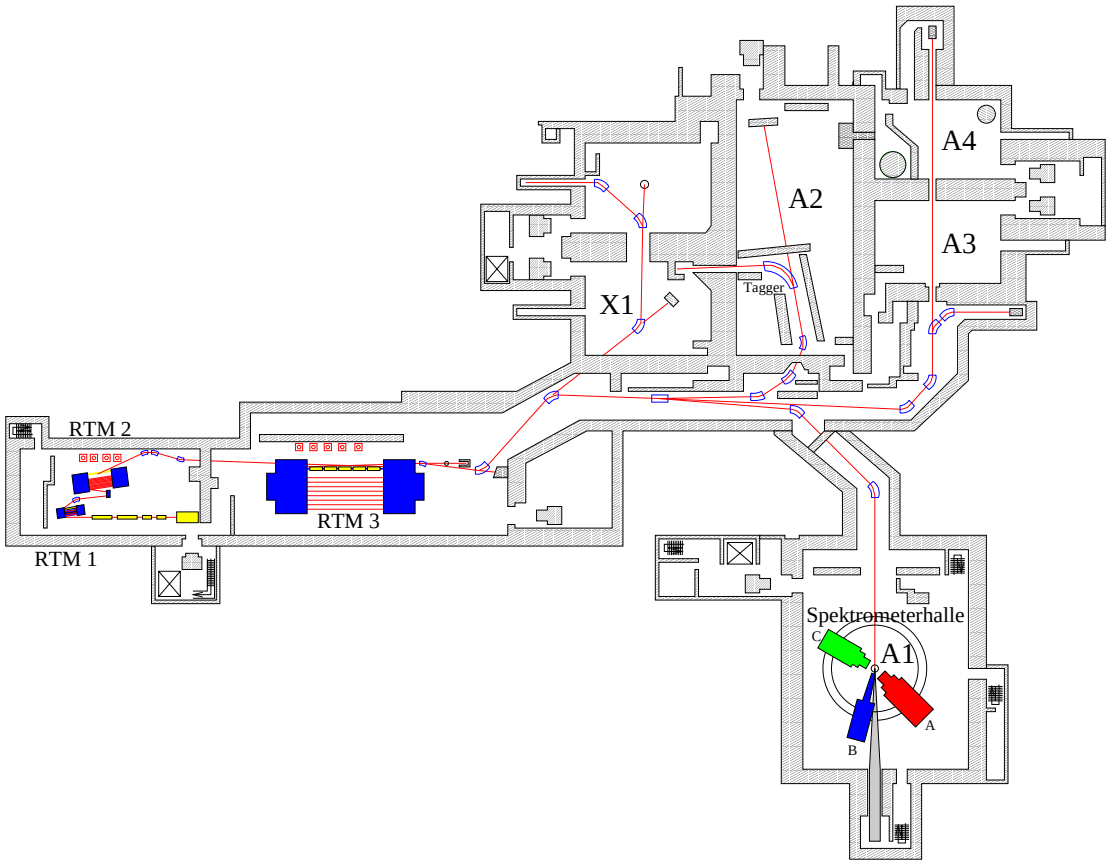

Figure 2.3: Schematic diagram of the floor plan of the MAMI facility with its three RTM and five experimental halls A1 ... A4 and X1.

experimental hall causing only a very low background in the hall. The focal plane houses a series of 352 overlapping scintillators placed at an angle perpendicular to the electron trajectory, which ensures that a real electron event will fire two elements (see Fig. 2.4 below). Demanding neighbouring coincidences reduces the contribution from background electrons or noise from the PMT. The dimension of the tagger dipole magnet with its high homogeneity ($\lesssim 0.5\%$) results in a large energy acceptance: 40.9 ... 792.4 MeV and a high intrinsic energy resolution of about 110 keV [49]. However the electron energy resolution of $\lesssim$1 MeV is given by the width of the scintillators of the FPD[8] which amounts to 2.14 MeV in average. Each scintillator is equipped with a PMT followed by a threshold discriminator and TDC[9] with a timing resolution of 200 ps. The main detector trigger-system gates these TDCs to limit the number of random events. The electron hits for each element are counted by FASTBUS scalers, which together with the tagging efficiency determine the photon flux through the target. The scalers are enabled and disabled by a PiP/ToF trigger during the readout of an event by the data acquisition system, thus avoiding the need for any deadtime

[8] focal plane detector
[9] time to digital converter

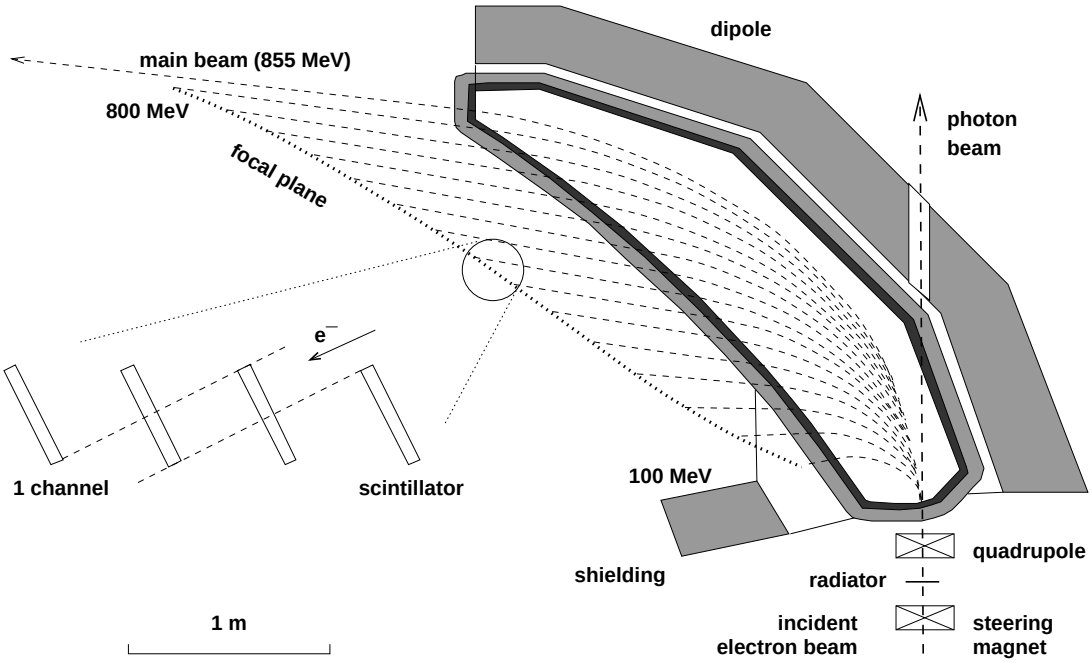

Figure 2.4: Schematic diagram of the Tagger with a zoomed part of the focal plane detectors.

correction.

In order to obtain a well defined beam spot which is central to and smaller than the target cell, the photon beam has to be collimated. In addition, if a crystal radiator is used (see Chapter 3) collimation is necessary to counterbalance the depletion of the polarization due to experimental deficiencies. Collimators of radii of 2.5 and 1.5 mm were employed, which led to a beam spot of ≤ 1.5 cm in diameter on the target. Hence the number of photons incident on the target is smaller than the number of electrons counted on the focal plane and accordingly in the scalers. Their ratio, the so-called tagging efficiency, accounts for that effect and is obtained in seperate measurements, which are carried out several times during the experiment. The tagging efficiency measurement is performed by placing a Pb glass detector with 30 radiation lengths thickness, which correspond to an efficiency of 1, downstream of the collimator. The use of a sufficiently low electron beam current of about 0.5 pA avoids random hits in the focal plane and deadtime problems in this detector. The tagging efficiency is derived from coincidence measurements between the Pb glass detector and the tagger.

To guarantee its stability the photon beam could be monitored during the experiment with the help of a video camera viewing a plastic scintillator in the beam. In addition, an ionisation chamber is mounted in front the photon beam dump to indicate a rough on-line measure of the tagging efficiency via the ratio of the count rate in the tagger and the ionisation current. The intensity of the photon beam depends on the radiator properties (charge Z, thickness, structure) and the electron beam current, which is limited

by the count rate of the Tagger PMTs at the lowest photon energy of about 800 kHz. For some runs the lowest Tagger section was switched off which reduced the tagging range to 114.2 . . . 792.4 MeV but allowed to increase the electron current from $\approx$ 5 nA to $\approx$ 20 nA, thereby enhancing the photon flux.

2.4 ^{4}He cryotarget

Having ^{4}He chosen as target, the low density of gaseous targets had to be overcome because the total cross section is proportional to the target density. In order to reach sufficient statistics within reasonable beam time the density had to be increased by either compression or liquefaction. Not only would the density of a high pressure gas-target amount to about a tenth of the density of a liquid target, but also the necessary thick walled pressure container would lead to high energy losses of the particles. Therefore liquid helium was used as target material, for which a cryotank [51] had to be constructed. Because the MAMI ^{4}He retrieval system was not yet finished by that time, the dewar needed to be refilled periodically.

The mechanical construction was demanding since geometrical constraints had to be complied: the target jar had to fit into the narrow (13 cm diameter) inner ring of the ΔE detector (see Fig. 2.6(c) on page 18) and yet should be easily adjustable. Shifts, rotations and tilts were made possible by hanging the target beneath a table mounted on top of PiP. There were two other objectives: a long lifetime between refills and the minimization of energy loss and straggling by the use of thin, low density and small Z cell and surrounding material. Therefore the target cell, which is cylindrical along the photon beam axis (8 cm length and 3 cm diameter), is made of 200 μm Kapton with entrance and exit windows for the photons of 60 μm. A carbon fibre cylinder (2 mm thickness and 12 cm diameter) with Kapton windows for the photon beam was used as a vacuum vessel around the target cell. This permitted the reliable detection of low energy charged particle; nevertheless the energy loss of protons while traversing the cryotarget reached up to about 30 MeV.

Due to the high temperature gradient and pressure differences safety standards had to be followed by affixing overpressure safety valves at critical locations. To minimize the heat intake, the helium tank was heat-shielded by a dewar filled with liquid nitrogen. The connecting pipe between the cell and the helium reservoir of volume 3.2 l and its heat shield are made of copper. The rest of the cryostat is made of stainless steel. In addition superisolation foil used at various critical places improved the evaporation rate even further. This measure resulted in a rather long lifetime of 12 h between refills which took about 30 min. The target was operated successfully for about 3 months during the (γ,NN) and (γ,Nπ) experiments [52] and proved its reliability.

2.5 The start and veto detector

The target cell is surrounded by an array of thin plastic scintillators [53], the so-called SVD, which are read out on both ends positioned on two rings with radii of 11 cm and 30 cm, respectively. A coincidence of the elements A0...A6 of the inner ring (see Fig. 2.5) with a hit in PiP identifies charged particles from the target and serves as a trigger. The

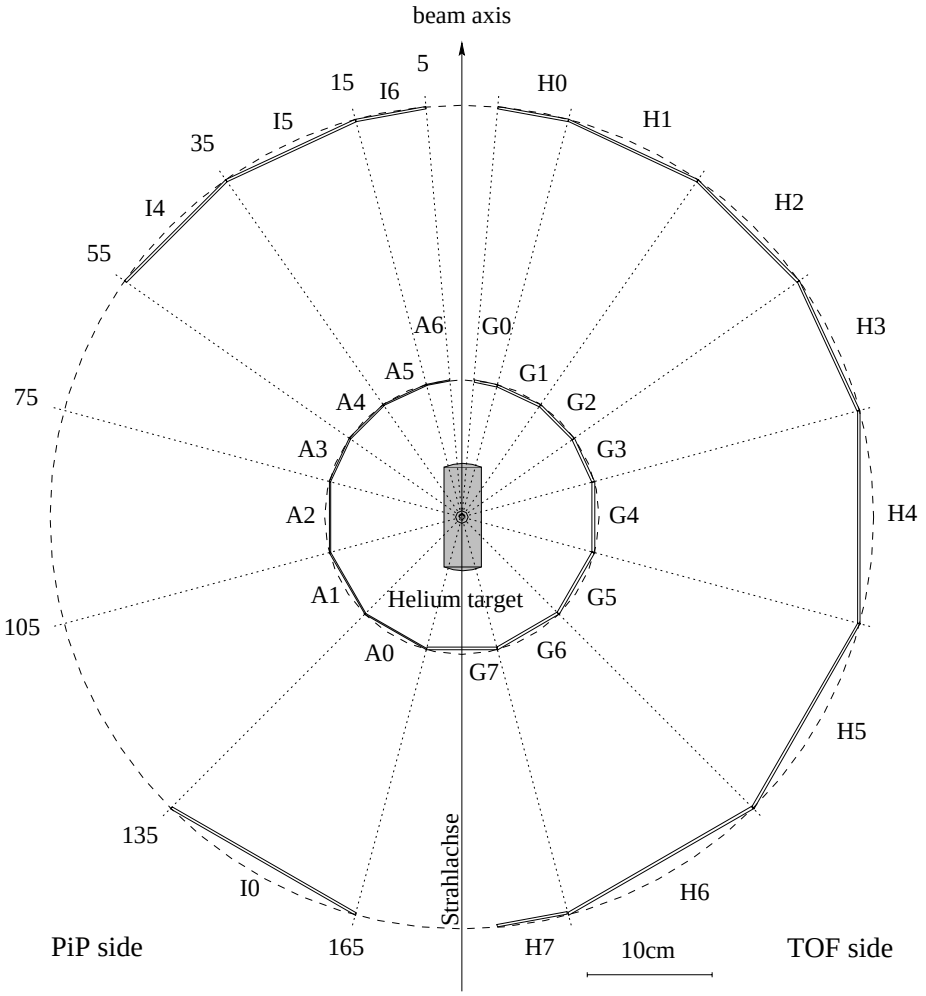

Figure 2.5: Top view of the Start and veto detector

scintillators of the first ring tightly encompass the target, thus their timing information reflects approximately the time of photo-absorption. It is therefore used as reference start time for the TDCs of all detectors The outer ring is an enlarged copy of the inner one scaled by about a factor of 3. However, there is no backward scintillator and those in front of PiP have been omitted, because PiP has its own thin ΔE_{pip}[10] detectors. In the off-line analysis with the additional information from the outer ring, the particle charge and type can be determined. The segmentation was made such that the scintillators and PMTs are

[10] start and ΔE detector of PiP

able to cope with the multiplicity of ejected particles and the atomic background which is rather forward directed. Therefore the scintillator widths decrease towards smaller angles to distribute the count rates more evenly, which was suggested by simulations based on data taken with a prototype detector [54]. For charge identification and polar coverage the inner ring suffices; however, the rates of charged particles in the inner ring are too high to permit a first level trigger. Therefore, a coincidence with a second ΔE detector and a thick scintillator of either PiP or ToF is necessary to reduce the rates to a manageable level. Thresholds on the analog sum of two detector layers give a rough, but very fast particle identification, which is used on-line to reduce unwanted electron background on page 21.

2.6 The Pion Proton detector PiP

The groups from Edinburgh and Glasgow developed and built a large solid angle ΔE-E hodoscope [55, 56] for detection of pions up to 180 MeV and protons up to 350 MeV. PiP houses a thin ΔE layer consisting of four vertical sheets which defines the acceptance of PiP and four horizontally segmented layers (E_{pip}[11]) comprising altogether 19 thick plastic scintillator blocks with successively increasing dimensions. All elements are made from NE110 organic scintillator and are wrapped into aluminium foil which diffusively reflects the light from a hit to the light guides attached on both ends with subsequent PMT. A supplementary black foil encloses the elements to avoid that day light enters the scintillators. PiP was designed to cover a large solid angle and energy range with a high angle and energy resolution and to allow the identification of different charged particles. This can be accomplished via the ΔE-E method, whereas the particle energy is reconstructed from the pulse height or by use of the superior range method, which is implemented in the present data analysis, see Section 5.4.3. The horizontal hit position is deduced from the time difference of both ends of an element and the vertical one from the segmentation, which results in a polar and azimuthal angular resolution of about 3° and 6°, respectively. A track finding algorithm was coded [57] and implemented in the off-line analysis, summarizing the hit positions of each element per event. If the particle type is known, its energy is determined by the corrected pulse amplitude of the respective PMTs. Kinematical overdetermination was used to calibrate proton energies via the D(γ,pn) reaction and pion energies via H($\gamma, n\pi^+$); in addition the Landau distribution of the energy loss of cosmic rays was used to calibrate the response. To distinguish π^+ the after pulse originating from decay into a positron ($\approx 2\ \mu$s) is used [30, 58]. PiP was placed at a distance of 50 cm to the target and rectangular to the photon beam, thus covering a polar angular range of 44 to 133 degrees. Compared to a magnetic spectrometer, PiP has the advantage of a large angle acceptance, but its penalty lies in a worse energy resolution.

[11] energy layer of PiP

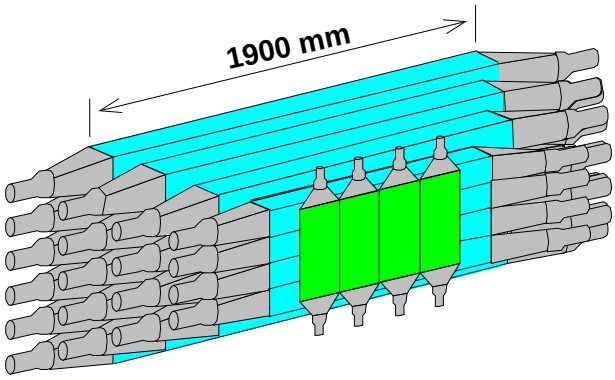

(a) The Pion and Proton hodoscope PiP with its own ΔE detectors

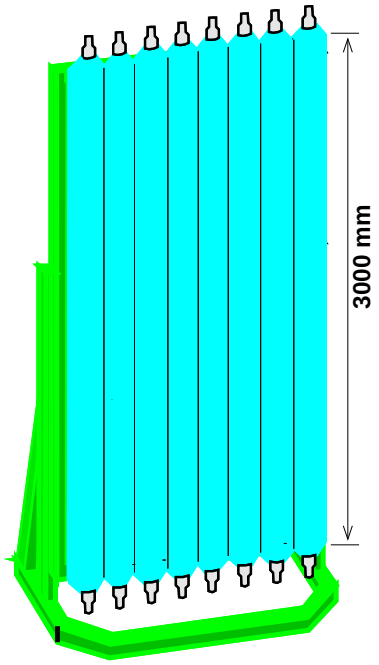

(b) ToF stand with 8 scintillator bars mounted on a frame

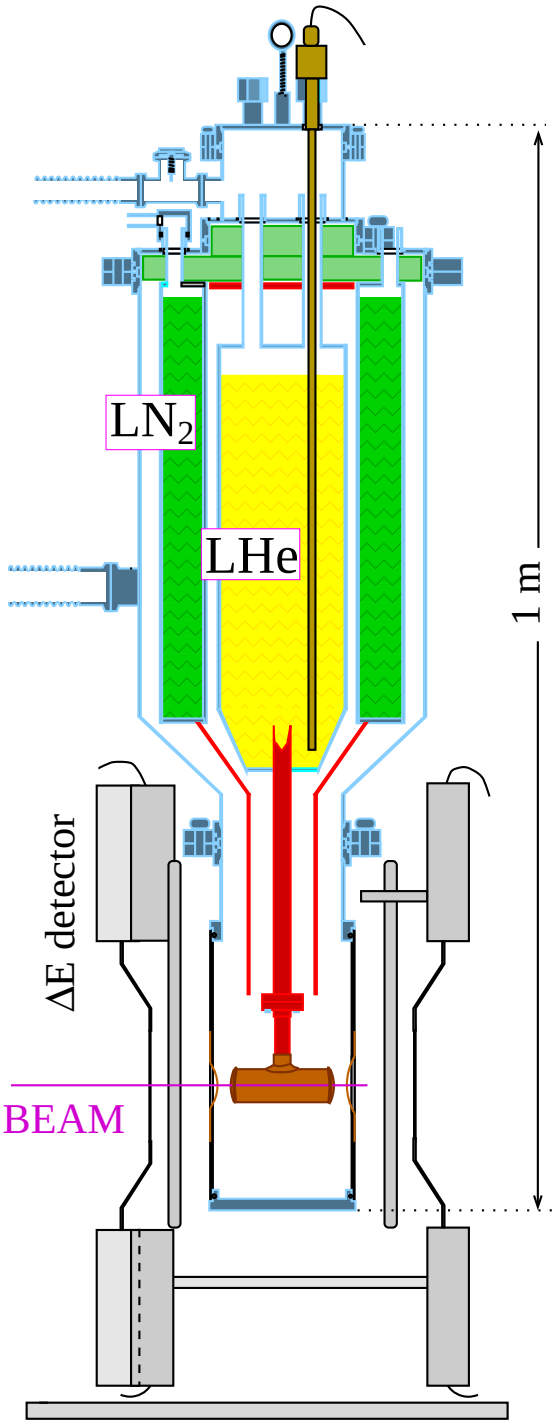

(c) Cryostat and target cell with vacuum vessel surrounded by the SVD

Figure 2.6: Main detector components (PiP, ToF) and the ^{4}He target

2.7 The time of flight array ToF

The time of flight array ToF, developed and built from the group of Tübingen [47], provides the second arm of the experiment and is optimized to detect neutrons, but is able also to identify charged particles. As it is shown in Fig. 2.6(b) above eight of the scinitillator bars, made from NE110 with dimensions $300 \times 20 \times 5$ cm^3, make up one layer, which is mounted on a frame to a ToF stand. Up to four layers fit on one stand, thus increasing the probability to detect a neutron, the so-called neutron detection efficiency. The ToF system is a very flexible and versatile detector system due to its large number of ToF bars (108) which are variable and relatively fast and easy assembled allowing the geometry to be tailored to the experiment. Each bar is viewed by two PMTs. Their timing information provides time of arrival of a particle from the mean time and the hit position along the bar, which is derived from the time difference using an effective speed of light. In the ^{4}He experiment, ToF covered a wide polar angle range form 7 to 157 degrees (note, there was a stand at about 14–23 degrees on the side of PiP) and the mean distance entailed an azimuthal resolution of about 3° and a polar one of 2 degrees; for more details see Tab. 5.3 on page 97. The energy resolution depends quadratically on the ToF time resolution and the thickness of a bar with respect to its target distance [57]. Hence, the thickness of a bar of 5 cm is a compromise between energy resolution and neutron efficiency, which is about 5%. In this experiment the ToF stands were fitted with two layers resulting in an effective neutron efficiency of approximately

$$\epsilon_n^{[2]} = \epsilon_n^{[1]} \left(2 - \epsilon_n^{[1]}\right) \approx 0.1 \tag{2.2}$$

The covered area of 33.6 m^2 corresponds approximately to a solid angle of about 1.1 sr, see Section 5.6 for details. To monitor the stability of the PMT amplifications, which would influence the energy determination from time of flight and the detector thresholds and with it the neutron efficiency, a control system (ToF pulser [48]) was developed and installed. Thereby it was possible to correct for fluctuations. Fortunately it turned out that the amplifications were rather stable during each run period [59].

2.8 Electronics and data acquisition

Many steps have to be performed in order to gain physical observables like energy, momenta and angles from the raw detector response. First the light output from the scinitillator bars are transformed to an electrical signal by PMTs, then this signal is converted into a digital value via a QDC[12]. The timing information is obtained by TDCs, which are started by the trigger (see below) and stopped when the respective PMT signals exceed a preset threshold, accomplished by a LED[13] used in common start mode [60]). The analog signal

[12] charge to digital converter
[13] leading edge discriminator

of the PMT is splitted via passive splitter to serve two lines. One enters a QDC, the other feeds the LED, see Fig. 2.8. Phillips FASTBUS QDCs as well as scalers were used in the electronic setup, which were chosen because of their high resolution, fast timing and fast clear capabilities with 32 channels per module. Compared to CFD[14], these LED have the disadvantage of a pulse height dependent timing. To cope with the large number of channels in the experiment their use was an economical decision. If an event is accepted, i.e. the trigger condition is satisfied, the QDCs and TDCs are read out via various bus systems and control modules and written to tape. For this purpose three linked bus systems [61] were installed: CAMAC to provide flexible programmable logic and control modules and allows to set LED thresholds and trigger condition remotely, FASTBUS as gates and latches and VME for master control and readout. The latter comprises an Eltec E7 computer based on the Motorola 68040 CPU. The software was developed at the Kelvin Lab [62] and runs on an OS9 operation system.

[14] constant fraction discriminator

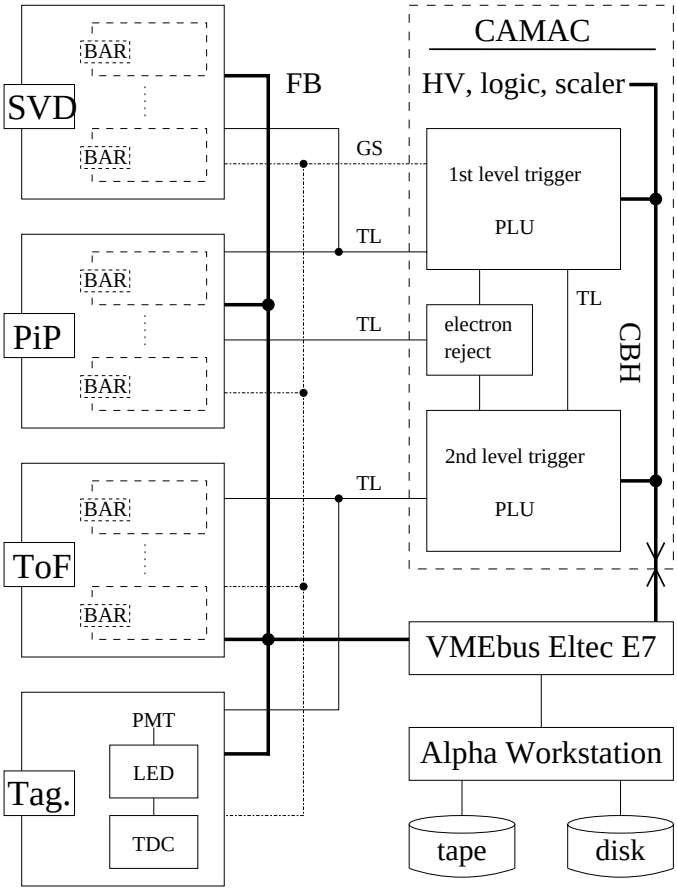

(a) acquisition and trigger electronics

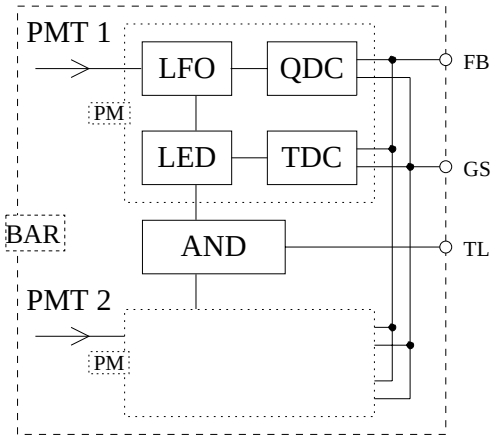

(b) electronics per bar

Figure 2.7: Schematic diagram of electronics. Abbrevations: LFO (linear fan out, passive splitter for ToF), CBH (CAMAC branch highway), HV (high voltage unit), FB (FASTBUS ECL-bus), GS (QDC-gate, TDC-start) and TL (trigger logic)

The trigger has to fulfill various requirements and take over tasks. Its decisions have to be fast in quickly rejecting background events, such as electrons from compton scattering and pair production, and in identifying charged particles in PiP in order to minimize the dead time. To obtain a fast trigger, its decisions are reached within two levels (see Fig. 2.8 above): a simple first trigger, which comprises a PiP particle and a cosmic ray event trigger and a subsequent trigger, which is able to make a more complex decision involving ToF and Tagger. A cosmic ray event is identified by insisting that both, the top and bottom scintillator of a PiP layer have fired. Those PiP events are recorded throughout the experiment for monitoring and calibrating purposes, see Section 5.4.1. The PiP particle trigger demands a coincidence between the start and veto detector and the analog sum of ΔE_{pip} and sets a latch to disable further events until the present event is completely processed. From that coincidence the detection of an electron, pion or proton is derived which selects (γ,X) events.

The 2nd level trigger condition for a (γ,NN) event requires a coincidence with the PiP particle trigger and at least a hit in ToF and Tagger in between a time window of 400 ns and 80 ns respectively. Additionaly 2nd trigger rejects electrons in PiP. This is implemented using cuts on 2d spectra of the pulseheight analog sum of two sequential PiP layers. In this spectrum electrons occupy the area near the origin, because they leave small pulse heights on both layers. This hardware on-line cut employs the weighted (set by attenuators) analog sum from two layers, which must exceed a given threshold for a non-electron particle hence a pion or proton. These logic evaluations, i.e. the 1st and 2nd level triggers, are handled by two PLU[15]s, which map 8 input to 8 output signals with arbitrarily programmable logical operations. If the event passes the conditions of both triggers, the acquisition computer is interrupted, the event is read out and stored and finally the TDCs and QDCs are then cleared ready for the next event.

[15]programmable lookup unit

Chapter 3

Bremsstrahlung

3.1 Introduction

Tagged and polarized photons play an increasingly important role in medium energy physics as they have provided a large amount of recent progress. In particular high intensity tagged photons have been employed for investigations of nuclear structure at small distances, for studies of hadrons in media and, for example, test of chiral perturbation theory.

In order to minimize systematic errors stemming from the photon polarization it is of vital importance to pin down its degree very accurately. By use of a crystal radiator a polarized photon beam at medium energies with a high flux (typically $\lesssim 10^8\gamma/s$) and high degree of polarization is achieved through coherent bremsstrahlung in a very efficient way. This is due to the additional coherent contribution (coh) from the crystal radiator – here diamond (di) was used – which is polarized in contrast to the incoherent bremsstrahlung (inc) off nickel (ni), an amorphous radiator. The degree of polarization was not monitored during the experiment (via Compton scattering for example), therefore it has to be deduced from the bremsstrahlung spectrum. This can be done in an indirect way only: the bremsstrahlung cross section $\sigma^{\mathrm{cry}} = \sigma_\perp + \sigma_\parallel + \sigma^{\mathrm{inc}}$ and the polarization $P = (\sigma_\perp - \sigma_\parallel)/\sigma^{\mathrm{cry}}$ have to be calculated with the same model and parameters. Here, σ denotes an abbreviation of the cross section $d\sigma/dk$ differential in photon energy k and $\perp, \parallel$ the orientation of the photon polarization vector relative to a reference plane. If the calculation of the cross section fits the experimental yield, it is assumed the polarization is determined, see Fig. 3.1 below. Therefore it is quite important to reach the possibly best description of the bremsstrahlung spectrum. This is not an easy task if different radiators, electron beam divergence, a finite beam spot size, multiple scattering in the target and the effect of a collimator need to be modelled.

Original work has been published by M. May [63] and had been continued by H. Überall [64,65], G. Diambrini [66] and U. Timm [67]. More recently this work found its application at MAMI by D. Lohman [68,69] and F. Rambo [70,71], which is further referred to as LR.

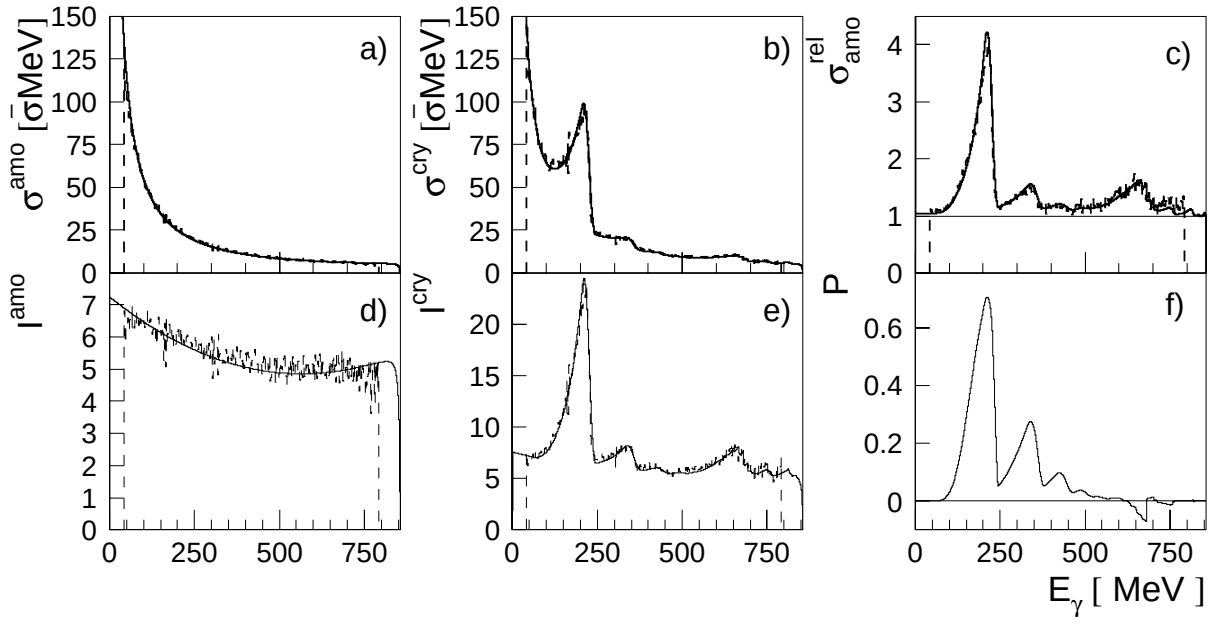

Figure 3.1: Predictions obtained with the analytical code are compared to measured bremsstrahlung spectra for a) σ^{amo} on 4 μm nickel, b) σ^{cry} on 100 μm diamond, c) σ^{rel}_{amo} and f) polarization. In d) and e) the corresponding intensities are plotted. The electron beam energy is 855 MeV.

Therefore the most important variables are briefly introduced and improvements are then focussed with respect to the incoherent cross section and the methods used. To refine the description of the collimation effect and Z-dependence of the incoherent contribution, the Hubbell cross section [72] with energy dependent photon angular distribution was used instead of the asymptotic angular dependence of the Bethe-Heitler cross section, as used by LR. This has an influence of up to $\sim 10\%$ on the relative spectra $\sigma^{rel}_{cry} = \sigma^{cry}/\sigma^{inc}$ and the polarization. Although the contribution of electronic bremsstrahlung compared to the nucleonic one is only about 4% for the nickel and around 20% for the diamond radiator, the adoption of a more sophisticated formula from [73] further improved the description. Compared to LR the angular- and Z-dependence is now treated more exactly for both contributions and thus meets the requirements of the experiment, where measured relative yields $y_{rel} = y_{di}/y_{ni}$, with $y_{di} \propto \sigma^{coh}_{di} + \sigma^{inc}_{di}$ and $y_{ni} \propto \sigma^{inc}_{ni} \doteq \sigma^{amo}$, come from different radiators (amorphous and crystal) and collimators and thus has to be compared with $\sigma^{rel}_{amo} = \sigma^{cry}/\sigma^{amo}$.

For investigation of the experimental effects on collimated spectra an analytical collimation function was deduced for the simple case of a circular collimator. Furthermore the two-dimensional integral of the coherent intensity over electron divergence is replaced by an analytical approximation. Both permit rapid calculations for quick surveys. To be able to take into account all experimental influences with full extend, like an off-axis, tilted collimator with a certain length or non spherical beam profiles, a Monte Carlo code was

also developed

3.2 Kinematics and cross sections

Bremsstrahlung is created when fast electrons interact with a charge. The incoming electron, described by $(E_0, \vec{p}_0)$, is deflected into $(E, \vec{p})$. It thus creates a photon $(k, \vec{k})$ by transferring a small amount of momentum $\vec{q}$ to a third partner (in general an atomic nucleus of charge Z). Processes considered here are treated in the extreme relativistic limit and the recoil energy is neglected, thus E and p conservation yield $(E_0, \vec{p}_0) = (E + k, \vec{p} + \vec{k} + \vec{q})$. Natural units ($m_0 = c = \hbar = 1$) are used in this chapter and in appropriate cases the mass m_0 of the electron is omitted. The decomposition of the momentum transfer $\vec{q}$ with respect to $\vec{p}_0$ in longitudinal q_l and transversal q_t components permits the formulation of kinematical limits in dependence of the relative photon energy $x = k/E_0$:

$$\frac{\delta_x}{x} \geq q_l \geq q_l^{\min} = \frac{q_t^2}{2E_0} + \delta_x \tag{3.1a}$$

$$1 \gtrsim q_t \geq 0 \qquad \text{with} \quad \delta_x = \frac{x}{2E_0(1-x)} \tag{3.1b}$$

This momentum transfer range is referred to as the 'pancake' due to its large lateral extension. Often the upper limit in (3.1a) is simplified to $q_l \lesssim 2\delta_x$. This is justified by the strong decrease of the cross section by more than one order of magnitude.

When the bremsstrahlung cross section is calculated without the summing over the photon polarization ϵ [74, 75], then the following asymptotic term is obtained in the soft photon (low energy) limit: $\frac{d\sigma}{d\Omega} \propto \frac{1}{k}\cos^2\phi$ with ϕ being the polar angle of the polarization vector $\vec{\epsilon}$ with respect to the scattering plane $(\vec{p}_0, \vec{q})$. This exhibits that the cross section drops in first order with $1/k$ and that the maximum linear polarization is found within the scattering plane ($\phi = 0$) defined by the momentum transfer. When an electron scatters off a single atom, i.e. incoherent bremsstrahlung, the momentum transfer $\vec{q}$ may lie anywhere inside the pancake, leading to an isotropic distribution of $\vec{\epsilon}$, hence to a non-polarized photon beam. However the regular structure of a crystal, which is described by the reciprocal lattice basis-vectors $\vec{b}_k$, restricts the possible momentum transfer. On the other hand, whenever the momentum transfer $\vec{q}$ coincides with a reciprocal lattice vector $\vec{q} = \vec{g} = \sum_{k=1}^{3} h_k \vec{b}_k$ for given Miller indices $h_k = [h, k, l]$, the recoil is absorbed by the whole lattice and the contributions of all atoms add coherently to the bremsstrahlung process, thus enhancing the yield. As $\vec{g}$ fixes $\vec{q}$, the overall photon polarization lies dominantly in a single plane only, therefore producing a polarized beam.

When the relative photon energy x is increased q_l increases monotonically until $\vec{q}$ is outside the allowed range, the pancake (3.1), which leads to a discontinuity at $x_d = x(q_l^{\min})$. As the incoherent contribution remains almost constant while the coherent strength increases

(see Fig. 3.1 on page 24 and Fig. 3.7 on page 37), the photon energy range up to the discontinuity is the interesting one for the production of polarized photons.

$$x_d = \left(1 + 1/(2E_0 g_l - g_t^2)\right)^{-1} \tag{3.2a}$$

$$\text{with} \quad g_l = g_1 \cos\Theta + (g_2 \cos\alpha + g_3 \sin\alpha)\sin\Theta \tag{3.2b}$$

$$g_t^2 = g_1^2 + g_2^2 + g_3^2 - g_l^2 \tag{3.2c}$$

where g_l and g_t are defined by the orientation of the crystal $\Omega = (\Theta, \alpha)$, see Fig. 3.4 on page 33. To maximize the enhancement of the cross section due to the coherent contribution, the crystal must be oriented such that one of its lowest order lattice vectors falls within the pancake, possibliy near its border. This means orienting the lattice such that the desired vector is nearly perpendicular to the electron beam, with an inclination on the order of a few mrad. By varying the orientation, the peaks of the coherent cross section can be shifted in the energy spectrum to provide the greatest photon flux at the energy of interest.

The five-fold differential cross section for bremsstrahlung production on a crystal [63, 67] is composed of a coherent (coh) and incoherent (inc) contribution and a term accounting for bremsstrahlung which originates from the interaction with the atomic electrons (e):

$$\begin{aligned}\sigma^{\text{cry}} &= \left[\frac{f_{\text{Deb}}}{N_{\text{cell}}}\left(\frac{2\pi}{a}\right)^3 \sum_{\vec{g}} |S(\vec{g})|^2 \delta(\vec{q} - \vec{g}) + (1 - f_{\text{Deb}})\right](1 - F)^2\, \sigma^{\text{amo}} + \sigma^{\text{e}} \\ &= \sigma^{\text{coh}} + \sigma^{\text{inc}} + \sigma^{\text{e}}\end{aligned} \tag{3.3}$$

The factor $S(\vec{g})$ describes the interference of the coherent cross section from the N_{cell} atoms of the fundamental cell with spacing a, whereas the form-factor $F(q^2)$ models the atomic structure, i.e. the charge distribution. $f_{\text{Deb}}(q^2) \in [0, 1]$, the so-called Debye-Waller factor, which depends on temperature and crystal properties, describes the influence of thermal motion and thus governs the fractioning of the total cross section into coherent and incoherent contributions. In other words, this factor indicates the probability for a given photon to be absorbed or emitted by the crystal without absorbing or emitting additional phonons. They would introduce extra momenta to the problem and change the kinematics. This bremsstrahlung contribution would not interfere constructively with the phonon-free process, thus reducing effectively the coherent cross section. The choice of crystal is influenced through the Debye temperature; see [76] for a detailed overview of possible crystals. Diamond is preferred, because it has a very high Debye temperature and almost perfect crystals can be found with a sufficiently small mosaic spread. The mosaic distribution describes small non-planarities of the crystal which also contribute to the smearing of the edge x_d, such as the BD[1] which is discussed in detail in Section 3.3. Up to now there has been no experimental test of beryllium carbide in our field of interest and moreover defect free crystals with small mosaic spread are difficult to manufacture.

[1] beam divergence

The cross section is renormalized by $\bar{\sigma}/x$ with $\bar{\sigma} = \alpha^2 Z^2 = 0.57947 \cdot Z^2\text{mb}$ to obtain a photon intensity per atom. The latter and the polarization P can be expressed in terms of the functions $\Psi^j_{1,2,3}$ with j = coh,inc,amo,e :

$$I^j = \frac{x}{\bar{\sigma}}\frac{d\sigma^j}{dx} = \left(1 + (1-x)^2\right)\Psi_1^j - \frac{2}{3}(1-x)\Psi_2^j \tag{3.4a}$$

$$P = 2(1-x)\Psi_3 \,/I^{\text{cry}} = 2(1-x)\Psi_3 \,/\left(I^{\text{coh}} + I^{\text{inc}} + I^{\text{e}}\right) \tag{3.4b}$$

In the LR treatment the electron contribution is added to the incoherent one via the correction $\Psi^{\text{e}}_{1,2} = 4.05, 3.94$ taken from a calculation of Wheeler and Lamb based on the Thomas-Fermi-Model [77]. The incoherent part described by the Bethe Heitler cross section [78] (eq. 3BSb) is very accurately approximated by $\Psi^{\text{inc}}_{1,2} = 13.79, 13.12$ except from the endpoint region. When the angular dependence on the photon polar angle $u = U^2 = (E_0\vartheta_k)^2$ is approximated as $d\sigma/du \propto (1+u)^{-2}$, a restriction in maximum photon angle u_c, hence a collimation of the beam, leads to a reduction by a factor $f_c = u_c/(1+u_c)$. LR use the form factor from Cromer in the whole q range which results in an overestimation of the cross section, because the applied parametrisation is valid only up to $q = 0.1$ and does not tend to zero for higher q but remains constant. The formulation above describes the shape of the angle integrated cross section very well, however the angular distributions depend on Z and x (see Fig. 3.2 on page 30). In the factorized approach of LR, this dependence is not taken into account.

In contrast, the coherent intensity exhibits a more complicated angular dependence than the incoherent one. Due to kinematical constraints the angle u depends on the lattice vector and also on the azimuthal photon angle (ψ_k) and relative energy:

$$U(\psi_k, x) = \Gamma(\psi_k) + \sqrt{\Gamma^2(\psi_k) + \frac{g_l}{\delta_x} - \frac{g_t^2}{x} - 1} \tag{3.5a}$$

$$\text{with} \quad \Gamma(\psi_k) = -g_2\cos(\psi_k - \alpha) + g_3\sin(\psi_k - \alpha) \tag{3.5b}$$

This photon energy dependence of the polar angle has to be accounted for in the triple differential cross section, which is formulated by use of Dirac's delta distribution δ_D:

$$I^{\text{coh}}_\Omega = \frac{d^2 I^{\text{coh}}}{du\, d\psi_k} = \left[\left(1 + (1-x)^2\right)\Phi_1 - \frac{2}{3}(1-x)\Phi_2\right]\delta_D(u - u(\psi_k, x)) \tag{3.6a}$$

$$P_\Omega\, d^2 I^{\text{cry}} = 2(1-x)\Phi_4(\psi_k)\,\delta_D(u - u(\psi_k, x))\, du\, d\psi_k\, dx \tag{3.6b}$$

The Φ functions are related to the Ψ functions via an integration over ψ_k as may be found in [67]. It is more intricate to calculate the intensity after collimation as the integral has to run over ψ_k and u. Both are mutually dependent angles. Therefore the analytical integration of (3.6) is performed with the justified approximation of averaging (3.5) over all (U, ψ_k) values which correspond to the same energy x. Due to the δ_D distribution a condition in terms of the collimator angle u_c is obtained for the energy dependent photon

angle: the coherent cross section vanishes for $u(x) > u_c$.

$$x_c = \left(1 + \frac{u_c + 1 - g_t^2}{2E_0 g_l - g_t^2}\right)^{-1} \overset{(3.2a)}{=} \frac{x_d}{1 + (u_c - g_t^2)(1 - x_d)} \tag{3.7}$$

Omitting the q_t terms in (3.2a) and (3.7), as done by LR, causes a shift of x_c and x_d by about 1%. Because many lattice vectors contribute to the total spectrum (see Fig. 3.7 on page 37), individual variations of these discontinuities cause a distortion of the total spectrum.

Collimation makes use of the differences of angular distributions ($\bar{U}^{\mathrm{coh}} \approx \frac{2}{\pi}\sqrt{x_d} < \bar{U}^{\mathrm{inc}} \approx \frac{1}{E_0}$) [75] and can be used to enhance the ratio of coherent to incoherent bremsstrahlung, thus increasing the degree of polarization. While the incoherent cross section is reduced approximately by f_c, the coherent one stays unaffected in the energy range $x(\vec{g}\,) \in [x_c, x_d]$. However, it vanishes elsewhere:

$$I_c = \int_0^{2\pi}\int_0^{u_c} du\, d\psi_k\, I_\Omega^{\mathrm{coh}} = \int du\, I^{\mathrm{coh}} \delta_D(u - u(x)) \overset{(3.7)}{=} I^{\mathrm{coh}}(x)\Theta(x - x_c) \tag{3.8}$$

Therefore collimation leads to an enhancement of both the relative cross section and the polarization. Based on (3.3)–(3.8) the coherent intensity of an ideal electron beam without any experimental deficiencies can be expressed by means of the functions ψ_i^{coh} as derived in [63]. There is a very good summary in [78] about formulas to calculate the incoherent contribution in different energy regimes and materials. Both intensities applied subsequently are stated also in Section A.1.

3.3 Experimental deficiencies and improvements

The coherent contribution is more affected by the experimental conditions than the incoherent one and it is therefore emphasized in the following discussion. Up to now an ideal electron beam and thin radiator was assumed, which can not be realized in experiments, but deficiencies of the electron beam affect the photon spectra [79], especially the collimated ones. A finite electron beam spot size on the radiator has the same effect as a collimator with a fuzzy edge: it smears out the collimator cut-off in the photon spectra at x_c (3.7). The divergence of the electron beam (BD) has a similar effect on x_c, but in addition it causes a variation of the crystal orientation with respect to the electron beam, changing the intensity due to the dependence of the momentum transfer on the crystal angles Ω. The deviation of the electron from the ideal beam direction is not given by the beam divergence alone, but it is changed in addition because the electron undergoes many small-angle scattering-processes. The latter is also termed multiple scattering, mainly due to Coulomb interaction with atoms while traversing the radiator (thickness z_R). This distribution is well represented by Molières theory [80] using a Gaussian approximation. Another effect on the photon spectra stems from the energy spread (ES[2]) of the electron beam, which

[2] beam energy spreading

causes a broadening of the structures. The experimental photon intensity is a convolution of the ideal intensity with all these effects weighted by the appropriate distributions. Usually a collimator with radius r_c is situated at distance z_c to define the photon flux on the experimental target. Due to the complicated dependence of r_γ on all integration variables the collimation condition $r_\gamma < r_c$ leads to topological non-trivial integration limits. Thus an evaluation of this integral calls for a MC-treatment:

$$I_c^{\mathrm{exp}} = \frac{1}{z_R}\int_R dz \int_{\mathsf{MS}} d^2m \int_{\mathsf{ES}} dE_0 \int_{\mathsf{BD}} d^2p \int_{\mathsf{BS}} d^2s \times w_{\mathsf{MS}}(\underline{m}, z)\, w_{\mathsf{ES}}(E_0)\, w_{\mathsf{BD}}(\underline{p})\, w_{\mathsf{BS}}(\underline{s})\, I^{\mathrm{coh}}\big(\Omega_0, \underline{e}(\underline{p}, \underline{m})\big)\Big|_{r_\gamma < r_c} \tag{3.9}$$

Underlined vectors denote the transversal component, i.e. perpendicular to the incident beam axis z (Fig. 3.4 on page 33), of the respective unit vectors.

Among other things, the LR approach lacks the small but not negligible influence of the Z and energy dependence of the photon polar angle distribution, which becomes important in case of collimation, and necessitates a refined description of the bremsstrahl process:

(i) A non-trivial energy and Z dependent electron bremsstrahlung contribution [73].

(ii) An accurate treatment of collimation and Z dependence of incoherent intensity by means of an unfactorized (in photon energy and polar angle) formulation [78] (eq. 3BSe) and [72].

(iii) Inclusion of electron beam energy spread.

(iv) Approximative analytical formula of coherent and incoherent intensity under full considerations of all experimental deficiencies as a complement method to the time-consuming MC-treatment.

(i): To improve on the electron-electron bremsstrahlung by distinguishing different materials and energies, it is also possible to introduce a photon energy and Z dependence in the incoherent electron shell contribution [78]. This is necessary since we compare incoherent yield from nickel and coherent and incoherent from diamond. The discrepancy of (A.2), (3.11) and (3.10) to the LR treatment shows clearly when compared with the (nearly) constant values for $\Psi_{1,2}$:

$$\Psi_1^e = \Psi_2^e - \frac{2}{3Z} = \frac{1}{Z}\left[\psi(\epsilon) - 4 - \frac{8}{3}\ln Z\right] \tag{3.10a}$$

$$\psi(\epsilon) = \begin{cases} 19.19 - 4\ln\epsilon & \text{for } \epsilon \geq 0.88 \\ \sum_{n=0}^{5} e_n (0.88-\epsilon)^n & \text{for } \epsilon < 0.88 \end{cases} \tag{3.10b}$$

$$\text{with} \quad \epsilon = \frac{100}{E_0 Z^{2/3}} \frac{x}{1-x}$$

$$e_n = 19.7, 4.177, 3.806, 31.84, 58.63, 40.77$$

The photon energy and Z dependent function $\Psi^e(\epsilon)$ taken from [73] is given as polynomial for different ϵ regions. It was corrected for binding effects.

(ii): The shell-electron distribution used in the two fold differential Schiff cross section for incoherent bremsstrahlung off an amorphous radiator, which is stated in Section A.1, eq. (A.2) in terms of $v = (1+u)^{-1}$, is of Yukawa type $(Ze/r)\exp(-rZ^{\frac{1}{3}}/C)$. This screening of the nuclear charge by the atomic one leads to a dipole form factor (A.6) to account for atoms with different charges [72]. The analytical integration of (A.2) over the photon angle u from zero up to the collimator angle u_c, respectively v_c, is feasible and was performed by J.H. Hubbell. This integrated intensity, denoted by I^{amo}, will be used further on:

$$\Psi_1^{\text{amo}} = 2\big[1 + M(1) - \big(1 + M(v_c)\big)v_c - c\big] \tag{3.11a}$$

$$\Psi_2^{\text{amo}} = -\frac{40}{3}v_c^3 + 18v_c^2 - \big(8\delta_z^2 + 6\big)\,v_c + 8\delta_z^2 + 2M(1) + \frac{4}{3} \tag{3.11b}$$
$$+ \big(4v_c^3 - 6v_c^2\big)\,M(v_c) - 6\delta_z^2\left(M(v_c) - M(1) + \frac{2}{3}c\right)$$

$$\text{with}\quad c = 2\delta_z \arctan\left(\frac{1 - v_c}{\delta_z + v_c/\delta_z}\right) \qquad \text{and}\quad \delta_z = \frac{C\delta_x}{Z^{1/3}} \tag{3.11c}$$

The energy dependence of the Schiff angular distribution is shown in Fig. 3.2 and compared to the asymptotic distribution f_c (see above). For sake of comparison the latter is

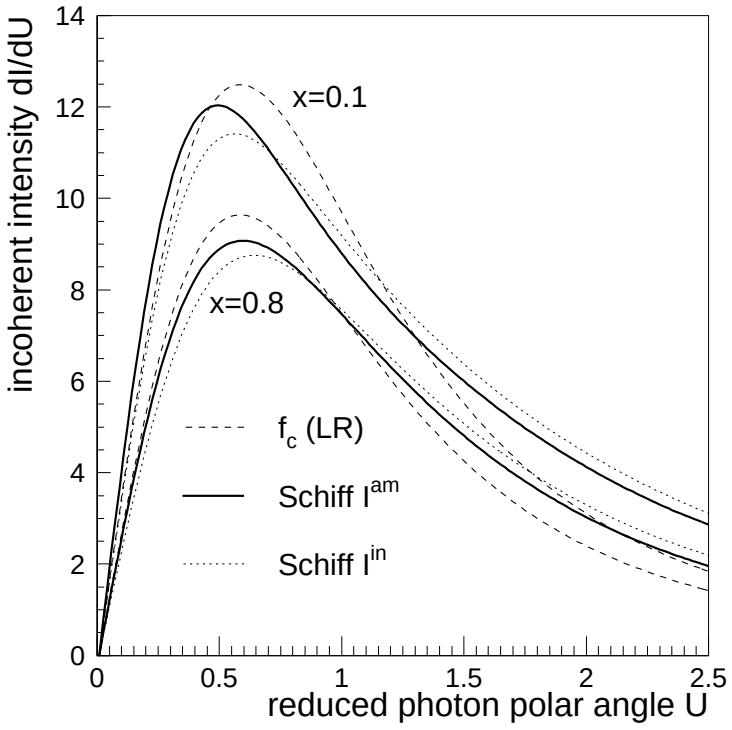

Figure 3.2: Approximative Bethe Heitler $f(\vartheta_\gamma)$ (dashed) and amorphous Schiff (solid) intensities for incoherent bremsstrahlung according to LR and (A.2) in dependence on the photon angle $U = \vartheta E_0$ for two photon energies (x=0.1 and 0.8). Both the angular distribution $f(\vartheta_\gamma)$ and the incoherent Schiff intensity are normalized to the amorphous Schiff for comparison.

normalized to the Schiff distribution (same integral) and reveals a narrower peak which does not show a shift for different photon energies. In Fig. 3.3 below the Hubbell intensities

for different collimation angles u_c are displayed; they are normalized to the same integral for better comparison of the shapes. The slope of the intensity does not monotonically increase with the collimation angle proving the non-trivial dependence of the intensity on the collimation angle which may not be described by a constant reduction factor f_c. The use of the latter would lead to a collimated incoherent intensity which is inaccurate and thus predict a wrong polarization. The influence of Moller scattering, which contributes

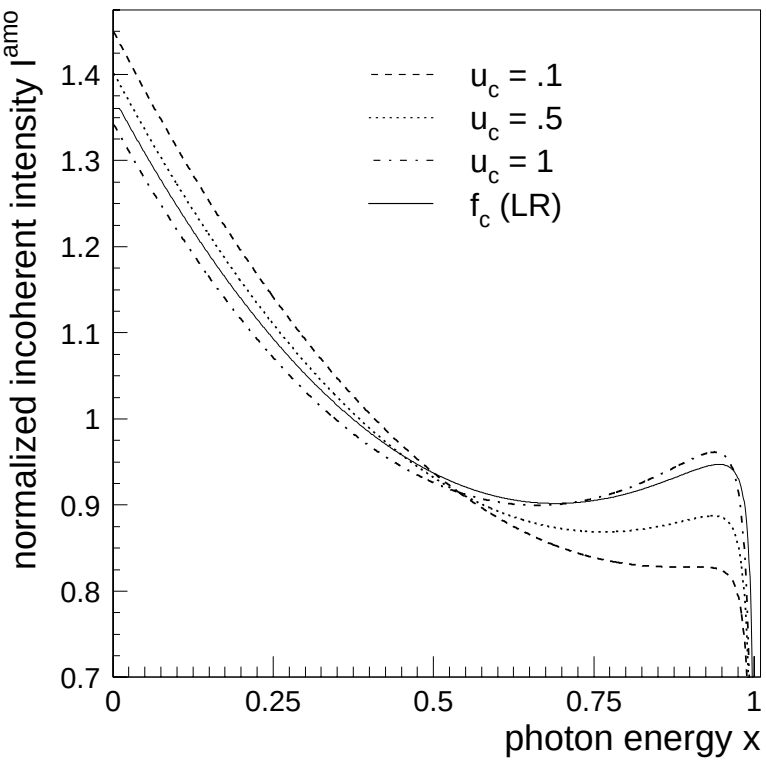

Figure 3.3: Comparison of amorphous Hubbell intensities from (3.11) for different collimation angles $U_c = \vartheta_c E_0$ with the factorized LR treatment: $\sigma(x, \vartheta_\gamma) = \sigma_{BH}(x) f(\vartheta_\gamma)$. The intensities are normalized on the same integral for comparison.

mostly at the endpoints to the measured bremsstrahlung yield, was also studied but was found to be at the $\lesssim 1\%$ level and therefore negligible, as we are interested in the medium energy range.

To calculate the incoherent contribution I^{inc} of a crystal radiator in comparison to an amorphous one, the Debye-Waller factor f_{Deb} has to be taken into account (3.3). Its impact can be considered as the use of an effective form factor: $\sqrt{1 - f_{\text{Deb}}}(1 - F_r)$. Here F_r represents the realistic carbon form factor from a relativistic Hartree-Fock calculation, see Section A.2. The analytical integration of the Schiff cross section seems no longer feasible in cases where the realistic or the modified form-factor is applied. Therefore two approximative treatments were investigated in Section A.2: (i) The utilization of a reduction factor $I^{\text{inc}} = r_D I^{\text{amo}}$ and (ii) a modification of the screening constant C_{inc} used for the Hubbell cross section. Both methods were studied and compared, whereby a clear agreement of the intensities obtained was found, which proves the validity of these approaches. Furthermore the temperature dependence of the effective screening constant could be ascertained.

3.4 Methods

The calculation of the photon energy dependence of the polarization in full consideration of all experimental deficiencies via (3.9) is very expendable in terms of computer time. This procedure can be accelerated by applying some approximations to obtain an analytical expression for this 8-fold integral. This approach is described here (ANB[3]) in contrast to a Monte Carlo method for full precision calculations (MCB[4]), which permits a precise study of collimation effects on the photon beam and its polarization in full dependence of all parameters describing electron beam, radiator and collimator properties.

3.4.1 Description of ANB

The following approximations were used to derive an analytical function for the complicated expression (3.9):

(a1) All two-dimensional transversal distributions, i.e. $w_i(\underline{t})$, are assumed to be Gaussians with the variances σ_t^x, σ_t^y and approximated by single azimuthal symmetrical Gaussian $w_i(t)$ with $\sigma_t^2 = \sigma_t^x \sigma_t^y$.

(a2) A mean multiple scattering (MS) variance $\bar{\sigma}_m^2$, averaged over the crystal depth, is used.

(a3) A combined total electron divergence distribution $w_{\mathsf{ED}}(\sigma_e)$ is obtained by folding the MS and BD(σ_p) distributions: $\sigma_e^2 = \sigma_p^x \sigma_p^y + \bar{\sigma}_m^2$, which implicates an effective electron divergence viewed by the collimator: $\sigma_c^2 = \sigma_s^x \sigma_s^y / z_c^2 + \sigma_e^2$.

(a4) The variation of the transverse momentum transfer g_t, being in second order of $\Delta\Omega$ and therefore much smaller than the variation in g_l, is neglected in the intensity.

Within an appropriate volume $V_{\vec{g}}$ in reciprocal lattice space, defined by the range of miller indices $\prod_{k=1}^{3}(2h_k^{\max}+1)$, a set of lattice vectors $\vec{g}_i$ is selected. Then for each of these vectors the maximum coherent intensity taken at the discontinuity $x = x_d(\vec{g})$ is calculated via (note the vanishing of Ψ_2^{coh} at x_d):

$$I_{\max}(\vec{g}\,) = \left(1 + (1 - x_d)^2\right) \Psi_1^{\mathrm{coh}}(\vec{g}, x_d) \tag{3.12}$$

Consequently the above lattice vectors are sorted by their intensity $I_{\max}$ and the strongest only are considered further on. The relative importance depends on crystal orientation. In general, however, it suffices to consider the 30 strongest lattice vectors only as the respective incremental contribution by the next to the intensity has reached the 10^{-4} level.

When considering approximation (a3) the effect of beam divergence and multiple scattering is accounted for by an effective electron divergence (ED) and translated into a distribution of the longitudinal momentum transfer $w_l(q_l)$. With $\underline{b}_e(\Omega_e) = \underline{b}_1 - \underline{e}$ being the transverse

[3] analytical bremsstrahlung-calculation

[4] Monte-Carlo bremsstrahlung-calculation

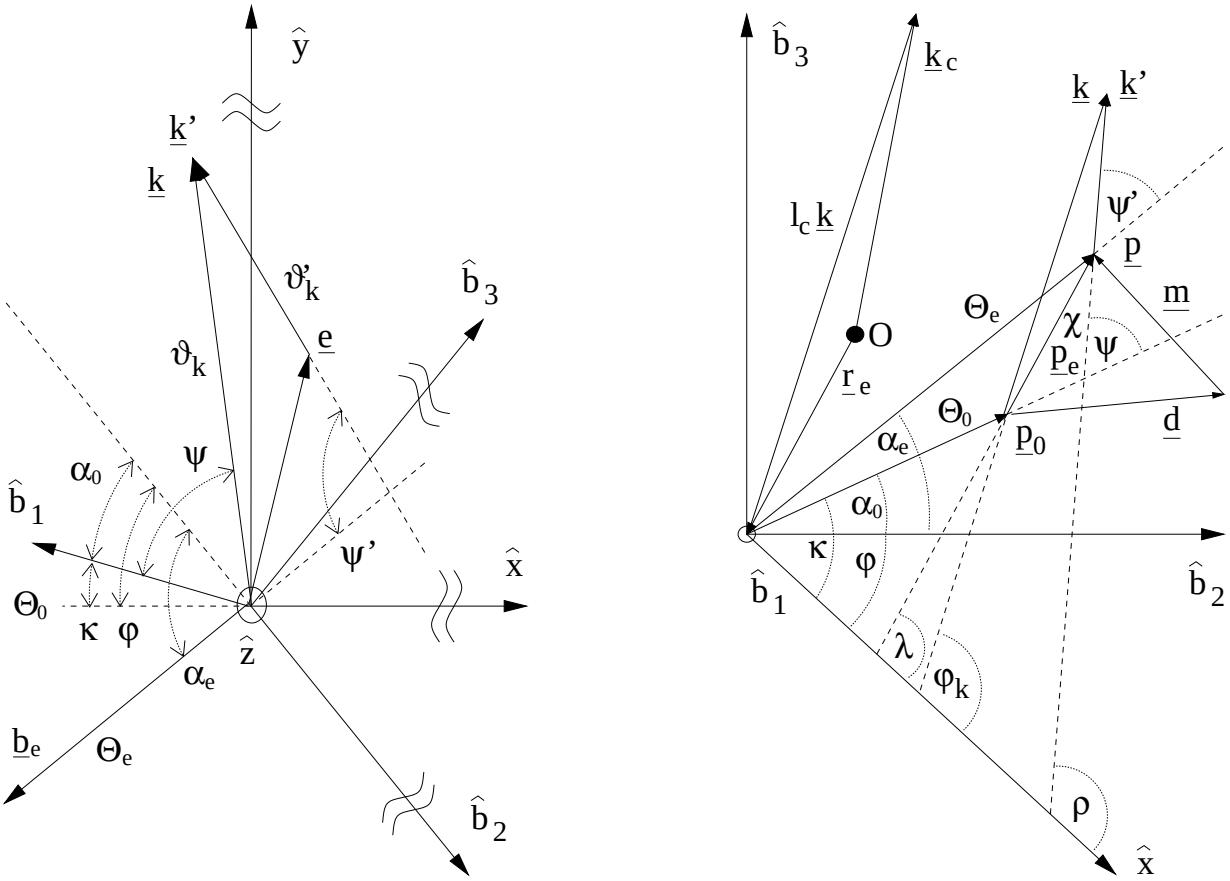

(a) Angles and vectors, i.e. reciprocal basis vectors $\underline{b}_i$, in reference to the laboratory system $\hat{e}_i$

(b) Vectors (electron $\underline{p}_0, \underline{k}$, photon $\underline{k}$) and angles with respect to the crystal axes $\hat{b}_i$

Figure 3.4: Angles and vectors in the laboratory and lattice basis vector system

component of the lattice vector $\underline{b}_1(\Omega_0) = \theta_0 \binom{\cos\alpha_0}{\sin\alpha_0}$ in the electron coordinate system (see Fig. 3.4(a)), which is defined by $\underline{e}$, the transverse direction of the electron divergence with respect to the laboratory system, the coherent intensity of a divergent electron beam (3.9) is approximated (a4) by:

$$I_{\mathsf{ED}} = \int d^2\underline{e}\; I(\underline{b}_e) w_{\mathsf{ED}}(\underline{e}) \approx \int d^2\underline{e}\; I\big(g_l(\underline{b}_1), g_l(\underline{b}_e)\big) w_{\mathsf{ED}}(\underline{e}) \tag{3.13}$$

Based on (3.2) the longitudinal momentum transfer, which enters the coherent intensity, for a divergent electron is expressed as follows (note that $|\underline{e}| \ll |\vec{e}|$ and $|\underline{b}_1| \ll |\hat{b}_1|$):

$$g_l(\underline{b}_e) \overset{(3.2b)}{=} \vec{g}\,\hat{b}_e = \vec{g}\,\hat{b}_1 - \underline{g}\,\underline{e} = l_0 + l \tag{3.14a}$$

$$\text{with} \quad l_0 = g_l(\underline{b}_1) = g_1 + \theta_0(g_2\cos\alpha_0 + g_3\sin\alpha_0) \tag{3.14b}$$

With the approximation in (3.13) the two-dimensional integral over ED may be converted to a one-dimensional integral over l via an integral transformation [81]. The kinematical constraint of the pancake is accounted for by the lower limit of the l integration:

$$I_{\mathsf{ED}} = \int_{g_l > \delta_x} dl\ w_l(l) I(g_t, l_0 + l) \tag{3.15a}$$

$$\text{with} \quad w_l(l) = \frac{d}{dl} \int_{l > l(\underline{e})} d^2\underline{e}\ w_{\mathsf{ED}}(\underline{e}) \tag{3.15b}$$

In general (3.15) has to be calculated numerically, but if w_{ED} is a Gaussian then $w_l(l)$ is Gaussian with variance $\sigma_e^2/4 = (g_2\sigma_x^e)^2 + (g_3\sigma_y^e)^2$, as well. For that reason, a second order expansion of the distribution function $w_l(l)$ is sufficient in case of small beam divergences ($\sigma_e \ll l_0$) and results in:

$$w_l(l) \approx w_2(l) = \begin{cases} \frac{3}{4\sigma_e}\left(1 - \frac{l^2}{\sigma_e^2}\right) & l \in [-\sigma_e, +\sigma_e] \\ 0 & \text{else} \end{cases} \tag{3.16}$$

The integration of (3.15a) with $w_2(l)$ yields for the coherent intensity:

$$\psi_1^{\mathsf{ED}} = \sum_{\vec{g}} \frac{3G\delta_x g_t^2}{\sigma_e^3 l_1}\left[l_1^2 - 2l_1(l_0 \ln\tfrac{l_1}{l_2} - \sigma_e) + \sigma_e^2 - l_0^2\right] \tag{3.17a}$$

$$\begin{aligned}\psi_2^{\mathsf{ED}} = \sum_{\vec{g}} \frac{3G\delta_x^2 g_t^2}{\sigma_e^3 l_1^3 l_2^3}\Big[&6l_1^3 l_2^3 \ln\tfrac{l_1}{l_2} - 6(\delta_x + 2l_0)(l_1 - l_2)l_1^2 l_2^2 \\ &+ 3(2l_0\delta_x - \sigma_e^2 + l_0^2)(l_1^2 - l_2^2)l_1 l_2 + 2\delta_x(\sigma_e^2 - l_0^2)(l_1^3 - l_2^3)\Big]\end{aligned} \tag{3.17b}$$

$$\begin{aligned}\psi_3^{\mathsf{ED}} = -\sum_{\vec{g}} \frac{G\delta_x^3}{\sigma_e^3 l_1^3 l_2^3}&\Big[\left(g_2^2 - g_3^2\right)\cos 2\phi + 2g_2 g_3 \sin 2\phi\Big] \\ &\times \Big[l_1^3(3l_2^2 + l_0 - 3l_0 l_2 - \sigma_e^2) - l_2^3(3l_1^2 + l_0 - 3l_0 l_1 - \sigma_e^2)\Big]\end{aligned} \tag{3.17c}$$

Here the following abbreviations were used: $l_1 = \max(\delta_x, l_0 - \sigma_e)$ and $l_1 < l_2 = l_0 + \sigma_e$. The definition of l_1 reflects the pancake condition.

So far the effects of ED,BS and MS on the intensity are described by (3.17) for the uncollimated case only. To include collimation of the photon beam with regard to these deficiencies a collimation function is derived in the following paragraph. The beam spot effect translates into a 'fuzzy' collimator: instead of 'moving around' the beam, the same effect is achieved by 'moving around' the collimator by a lateral displacement $\delta r, \phi$ in polar coordinates. Due to a finite beam spot size the collimator is no longer spherical symmetric with respect to the incident electron (see Fig. 3.5 below) and the dependence of the collimator angle U_c on the collimator displacement has to be considered by a convolution of the intensity with the beam profile (compare with (3.6) and (3.8)). By use of approximation (a3) the transversal displacement $\vec{r}_t$ of the collimator origin at distance z_c complies

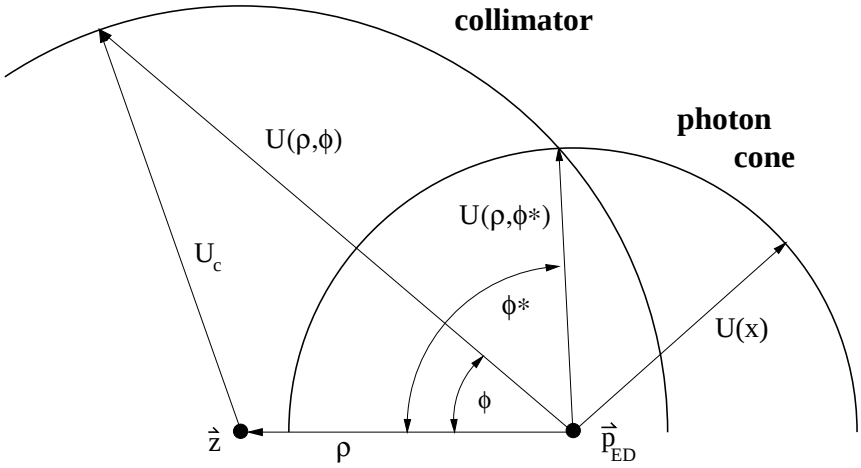

Figure 3.5: The collimator at distance z_c viewed in the electron system (origin $\vec{p}_{ED}$) is displaced by $\delta r = z_c\rho$ which implicates that the collimator is no more symmetric but its radius $z_cU(\rho,\phi)$ depends on the azimuthal angle of the photon. ϕ^* denotes the limit of the ϕ integration in (3.18a)

with a Gaussian distribution (width $\sigma_c z_c$), when viewed in the electron system. In terms of angles, the intensity has to be folded with the CD[6] distribution $w_{\mathsf{CD}}(\rho)$ which describes the variation of the polar angular displacement $\rho = |\vec{r}_t|E_0/L$:

$$I_C^{\mathrm{coh}} = \int \rho d\rho\, d\phi\, w_{\mathsf{CD}}(\rho) \int_0^{u(\rho,\phi)} du\, I_{\mathsf{ED}}^{\mathrm{coh}}(x)\delta(u-u(x)) \tag{3.18a}$$

$$\text{with} \quad U_c^2 = U^2(\rho,\phi) + \rho^2 - 2U(\rho,\phi)\rho\cos\phi \tag{3.18b}$$

The dependence of the polar angle $u(x)$ of the photon on its energy x is given from (3.7) and (3.2a) by $u(x) = (x_d/x - 1)/(1 - x_d)$. Due to the Heaviside function the ϕ integration is trivial and separates the collimated intensity into the uncollimated intensity in terms of the Ψ_i^{coh} functions (A.1) and a collimation function: $I_c^{\mathrm{coh}} = \sum_{\vec{g}} I_{\mathrm{ED}}^{\mathrm{coh}}(x, x_d)\, C\big(U(x, x_d)\big)$.

$$C(U) = \int_{|U_c-U|}^{U_c+U} \rho\, d\rho\, w_{\mathsf{CD}}(\rho) \frac{1}{\pi} \arccos \frac{\rho^2 + U^2 - u_c}{2\rho U} + \Theta(U_c - U) \int_0^{U_c-U} \rho\, d\rho\, w_{\mathsf{CD}}(\rho) \tag{3.19}$$

The ρ integration of the first term in (3.19) is left as a numerical task while the second term gives: $\Theta(U_c - U)[1 - \exp(-(U_c - U)^2/2\sigma^2)]$. The collimation function $C(U)$ is plotted in Fig. 3.6 on page 37 together with the combined effect of beam spot size, beam divergence and multiple scattering from (3.19) on the lower energy part of a lattice vector peak, hence the part influenced by a collimator.

[6] collimator displacement

The treatment of collimation in the incoherent case works analogous (up to (3.18)), but the different angular dependence leads to a remaining integral (note: $v = 1/(1+U_c^2)$):

$$I_c^{\text{inc}} = \int dv\; c(v) I^{\text{inc}}(v) \qquad \text{with} \quad c(v) = -\frac{1}{2v\sqrt{v-v^2}} \frac{dC(U)}{dU} \tag{3.20}$$

Therefore, a single collimation function accounts for experimental deficiencies in both cases of coherent and incoherent bremsstrahlung production. Consequently to these derivations, $C(U)$ and $c(v)$ have to be calculated numerically only once. The remaining evaluation of the intensities is a closed analytical calculation (apart the ES folding), providing very fast results at only a tiny loss of accuracy.

The total cross section is written as a sum over the contributions of the respective crystal lattice vectors, which are plotted individually and appropriately summed in Fig. 3.7 below for the ideal uncollimated case and the three most strongly contributing vectors. For the collimated case the discrete impact of the total electron divergence on the discontinuities x_d and x_c as well as the combined effect is shown in the insert. The calculation of these intensities made use of the coherent intensity formula (3.17) respecting the total electron divergence and the collimation function (3.19) and thereby demonstrates the effect of a divergent electron beam on the intensity spectrum.

3.4.2 Description of MCB

Monte Carlo method is well established for simulation of complicated processes in nuclear physics. (3.9) with its interrelated boundary condition is an excellent example. Due to this method the approximations (a1)–(a4) used for ANB can be omitted and the intricate mutual angular dependence in (3.5) can be treated in full consideration. Measured electron beam parameters and their standard deviation as well as radiator and collimator properties are the basic input. For a preset number of electrons N_e a certain set of physical values are chosen randomly in parameter space. First the direction (transverse components only) $\underline{d} = (d_x, d_y)$ and energy E_p of an incident electron impinging at $\vec{s}_t = (x, y)$ on the radiator is determined by the beam energy w_{ES} and divergence w_{BD} distributions. Both distributions are assumed to be of Gaussian shape with parameters σ_E, $\sigma_d^{x,y}$ and $\sigma_s^{x,y}$ respectively:

$$w_{\text{BD}}(d_{x,y}) = \frac{1}{\sqrt{2\pi}\sigma_d^{x,y}} \exp -\frac{d_{x,y}^2}{2\sigma_{d_{x,y}}^2} \tag{3.21a}$$

$$w_{\text{BS}}(x,y) = \frac{1}{2\pi\sigma_s^x\sigma_s^y} \exp\left(-\frac{x^2}{2\sigma_{s_x}^2} - \frac{y^2}{2\sigma_{s_y}^2}\right) \tag{3.21b}$$

$$w_{\text{ES}}(p) = \frac{1-1/2p}{\sqrt{2\pi}\sigma_E} \exp -\frac{(p-E_0)^2 - E_0}{2\sigma_E^2} \tag{3.21c}$$

The mean polar angle deviation $\underline{m}(\sigma^m_{\text{plane}}(z))$ from the incident direction depends in accordance with Molières theory on the depth z of the bremsstrahlung process in the radiator,

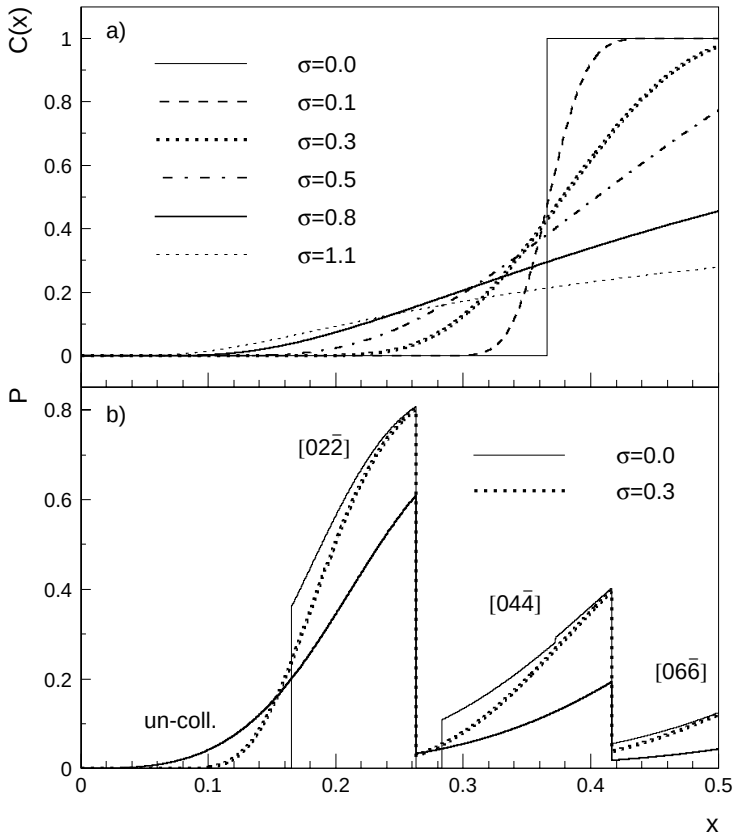

Figure 3.6: a) Collimation function $C(U)$ versus $x(U)$ for $U_c = 0.94$, $x_d = 0.5$ and various displacement variances σ_c. The polarization is shown in b) for the collimated case with variance $\sigma_c = 0.3$ (dotted thick line) and is compared to the ideal (thin solid) and uncollimated case (thick solid). The kink at $x = 0.37$ in the $\vec{g}[04\bar{4}]$ contribution originates from lattice vector $[06\bar{6}]$

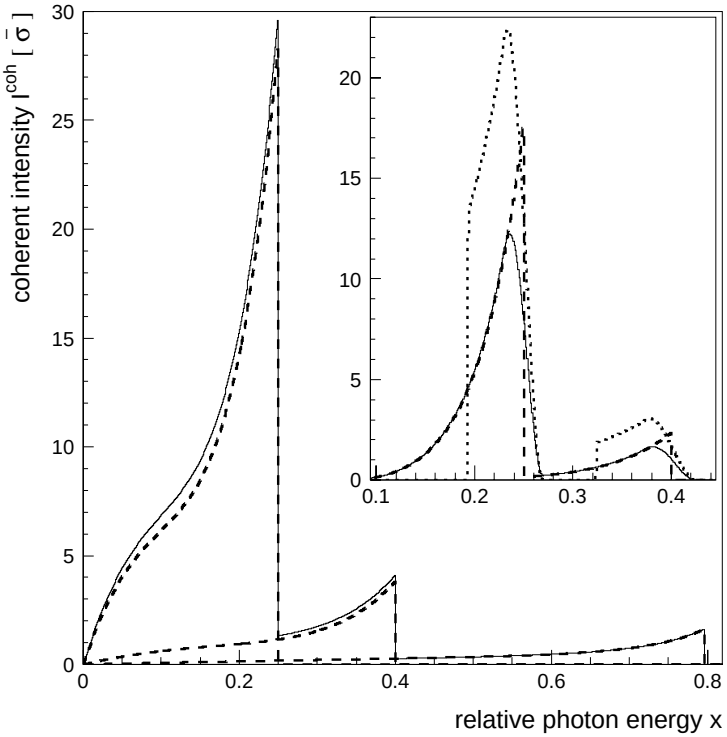

Figure 3.7: Individual (dashed lines) and total (solid line) uncollimated contribution of the two strongest lattice vectors. For the collimated case, the insert shows the discrete effect of ED on the discontinuity x_d (dotted line) and x_c (dashed) as well as the combined effect (solid line).

which is chosen randomly from a homogeneous distribution within the radiator thickness z_R. To calculate the coherent bremsstrahlung for this particular electron the lattice has to be rotated into the coordinate system of this electron, involving a transformation of the crystal angles Ω_0. For small polar angles the total transversal electron deflection $\underline{e}$ off $\vec{p}_0 \parallel \hat{z}$ due to multiple scattering and beam divergence and the transformation of the crystal (Θ, α) in the electron system is given by:

$$\underline{e} = \underline{d} + D_z(\phi_d)\underline{m} \qquad \underline{k} = \underline{e} + \underline{k}^e \tag{3.22a}$$

$$\underline{b}_e = D_z(\kappa)\underline{b}_1 - \underline{e} \qquad \underline{b}_1 = -\Theta_0(\cos\alpha_0, \sin\alpha_0) \tag{3.22b}$$

Here $D_z(\phi_i)$ denotes the rotation around $\hat{z}$ by the azimuthal angle of the transverse vector $\underline{i}$. **MCB?** [7] does not treat the distributions as azimuthal symmetric (like **ANB?** [8]) and hence more care has to be taken of the azimuthal dependence. To clarify the complicated relations between the involved angles and vectors, they are sketched in Fig. 3.4 on page 33 viewed within two coordinate systems. Subsequent to the transformation a lattice vector is chosen uniformly in reciprocal space $V_{\vec{g}}$ (see Section 3.4.1) and then the coherent cross section $\sigma^{\mathrm{coh}}(\vec{\Sigma})$ is calculated with these parameters $\vec{\Sigma} = (h, k, l, \underline{b}, \underline{m}, \underline{s}, z, \underline{k}^e, \vec{p}, x)$. The cross sections are differential in energy and the azimuthal ψ_k and polar angle ϑ_k of the photon. If the event is accepted, which is determined via the rejection method (see [NumRec]) with the parameter $\sigma^{\max}$, the maximum value of the cross section σ^{coh} in the available parameter space $V_{\vec{\Sigma}} = \prod_i \left(\Sigma_i^{\max} - \Sigma_i^{\min}\right)$, $\vec{\Sigma}$ is stored in list-mode for further investigation. In addition a logic variable is also stored indicating whether the emitted bremsstrahlung photon has passed the collimator:

$$r_k(z_c) < r_c \ \cup \ r_k(z_c + l_c) < r_c \qquad \text{with} \quad \vec{r}_t^{\,k}(z) = \vec{s}_t + z\underline{k} - \vec{s}_t^{\,c} \tag{3.23a}$$

$$r_k^{x,y}(z_c) < r_c^{x,y} \ \cup \ r_k^{x,y}(z_c + l_c) < r_c^{x,y} \qquad \text{and} \quad r_k = |\vec{r}_t^{\,k}| = |(r_k^x, r_k^y)| \tag{3.23b}$$

Here r_c, z_c and l_c denote the radius, distance to the radiator and length of the collimator, respectively. In case of a rectangular collimator, r^x, r^y label its width and height. If the collimator axis does not coincide with the $\hat{z}$ axis, it can be accounted for by a non zero transversal collimator dislocation $\underline{s}_c(z)$, which in case of a tilted collimator becomes z dependent.

The desired distributions are obtained from the MCB output by reading the PAW *hbook* files into *ntuples* and projecting into histograms with appropriate cuts, i.e. on 'collimator passed'. Absolute values are calculated from those distributions via a normalization on the incident electrons N_e and the random volume $V_\Delta = \prod_i \left(\Delta_i^{\max} - \Delta_i^{\min}\right)$ made up from $\vec{\Delta}^{\mathrm{coh}} = (\sigma^{\max}, k, \psi_k)$ or $\vec{\Delta}^{\mathrm{inc}} = (\sigma^{\max}, k, \vartheta_k)$ and taking the histogram binning into account:

$$f(\Sigma_i) = \frac{V_{\Delta_i}}{N_e \cdot \mathrm{binwidth}(\Sigma_i)} h(\Sigma_i) \tag{3.24}$$

Here $h(\Sigma_i)$ denotes a histogram containing the total number of photon events N_γ, which belongs to the distribution $f(\Sigma_i)$ of a certain observable or parameter, i.e. $\sigma^{\mathrm{coh}}, \vartheta_k, k$, etc.

[7] **MCB?**
[8] **ANB?**

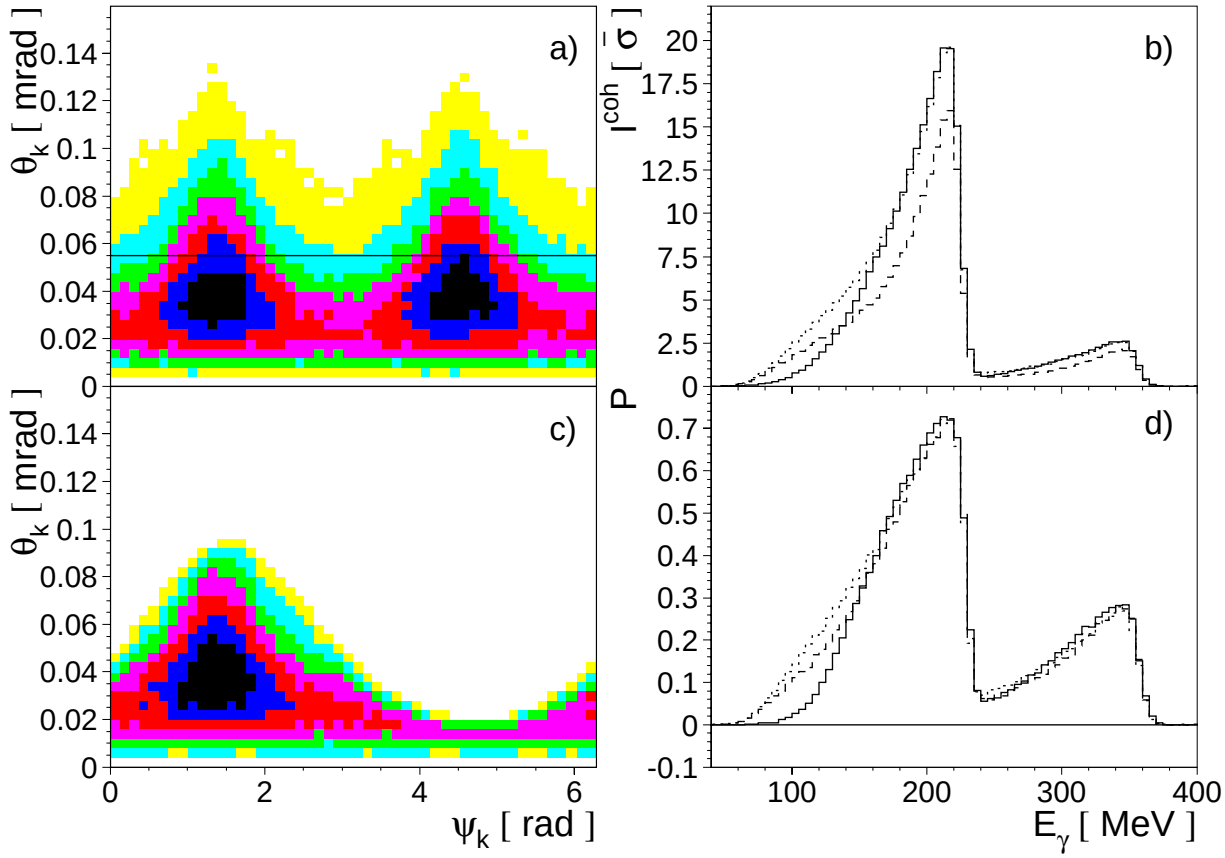

Figure 3.8: a) Predicted intensity distribution (polar versus azimuthal photon angle [rad]) for coherent bremsstrahlung production off a diamond crystal for the uncollimated case and c) for an off-axis (1 mm) circular collimator ($r_c = 1.5$ mm, $z_c = 2.5$ m). The lines in a) indicate the circular and rectangular collimator. The off-axis collimator results in coherent intensities b) and polarizations c), indicated by dashed lines and the aligned by solid lines. The results for the rectangular collimator (2 mm×4.5 mm) are plotted with dotted lines.

The power of the Monte Carlo treatment is demonstrated by a typical application which is described subsequently. In contrast to the azimuthal dependence of the incoherent contribution, the coherent one is not isotropic which is substantiated by (3.5). Fig. 3.8 professes for a rectangular collimator to comply approximately with the azimuthal distribution of coherent bremsstrahlung and therewith the one of high polarized photons as well. The collimator boundaries follow the iso-parametric lines with constant polarization much better than a circular one. In making use of the condition (3.23b) respecting the boundaries of a rectangular collimator, a simulation was performed. The outcome ascertained that the polarization can be better preserved for lower photon energies compared to a circular collimator. Note that the geometric dimensions of the rectangular collimator are such that the same photon flux, respectively the same tagging efficiency, is achieved.

3.5 Results

The calculation via ANB and MCB to reproduce the measured spectra employed the parameters of Tab. A.4 on page A13. The comparison of experimental yield and ANB calculation for three crystal settings is shown in Fig. 3.9, where the experimental yield was normalized on the calculation. This normalization factor was fitted and is the only free parameter apart some small adjustments (in the uncertainty range) of the MAMI beam parameters. The agreement is very good even over the whole energy range and is not achieved to that level by the LR treatment, i.e. the use of [78] (eq. 3BSb), the application of the collimation reduction factor f_c and the from factor from Cromer. From this figure it is noted that the beam quality at MAMI is excellent compared to TagX [82], which obviously has a much larger electron beam emittance. Additionally, the absolute cross sections from the calculation and the measured Tagger yield normalized to the incident electron flux were compared, see Section A.6. They show a resonable accordance but differ about 15%, which might be partly due to the inaccurate measurement of the radiator thickness and the electron beam current at MAMI.

The comparison between the two methods (ANB and MCB) in Fig. 3.10 below shows that

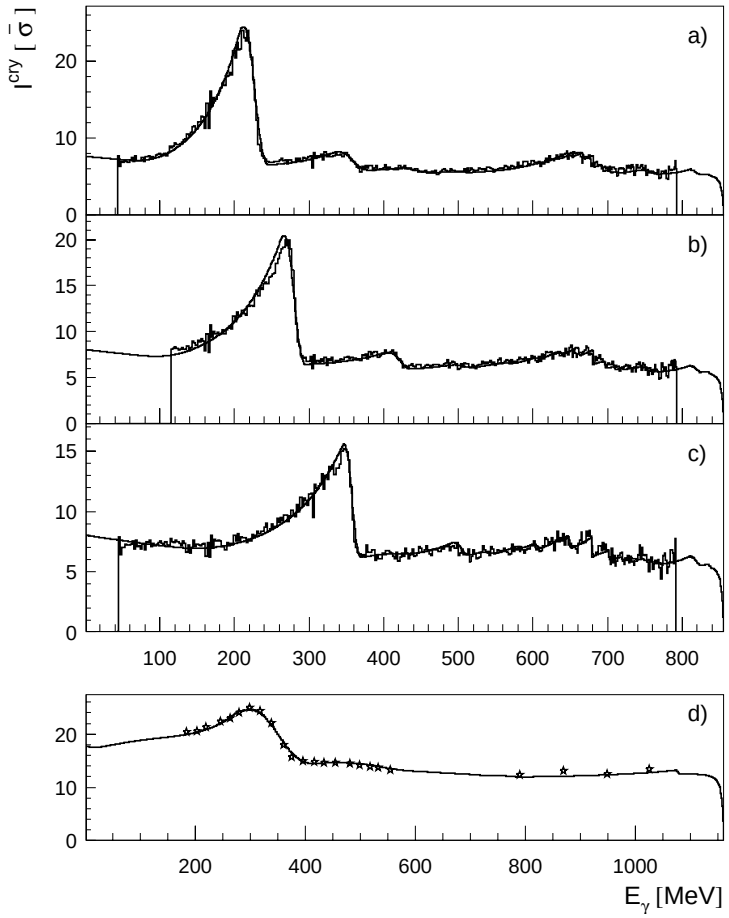

Figure 3.9: Comparison of total crystal intensities from ANB and experimental spectra, taken from measurements at MAMI during the ^{4}He(γ,X) experiment and a TagX measurement. They show more sensitivity to the parameters used in the calculation than the relative spectra. Note that for each panel different diamond settings were applied, whereas for the first three nearly the same beam parameters were used.

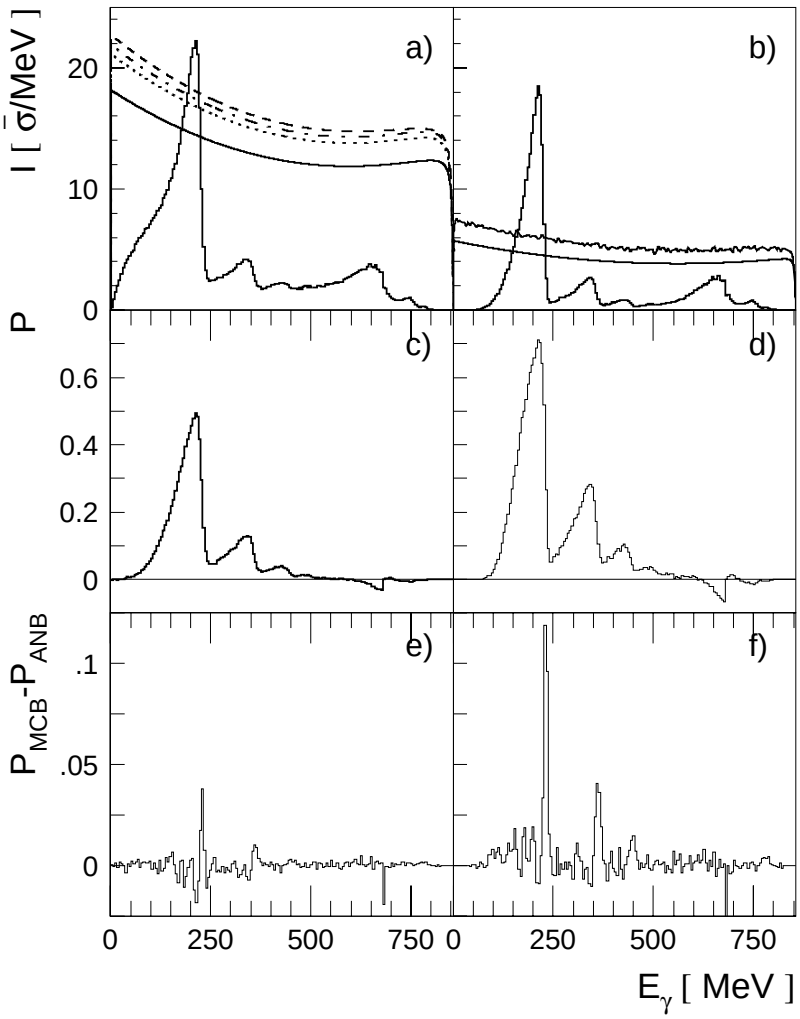

Figure 3.10: Uncollimated (left) and collimated (right) intensity distributions (a,b) and polarization (c,d) calculated by MCB. a) amorphous (Z_{amo}=28) and incoherent (Z_{inc}=6) intensities from ANB without electron contribution (dotted and solid) and with (dot-dashed and dashed). b) The incoherent intensity with electron contribution stems from MCB and without from ANB. The differences in polarization are displayed in (e,f)

the main differences arise near the discontinuity. However, otherwise they are of statistical nature only due to the Monte Carlo method exploited by MCB and thus indicate that the approximations used for ANB prove to be valid. Nevertheless, for an off-axis collimator or highly non-spherical symmetric electron beam MCB is essential. Furthermore this figure indicates, that the variation of incoherent and electronic intensities amounts up to $\approx 25\%$. Therefore the improved (compared to LR) description of these contributions is of significant relevance.

In 1996 a measurement of the π^0 photoproduction off ^{4}He was performed at MAMI by the TAPS[9] collaboration [70] The cross section and beam asymmetry was obtained mainly in the energy range of the Δ excitation energy using two photons for identifying the π^0. The beam asymmetries are used to determine the degre of linear polarization of collimated coherent bremsstrahlung. Both the nucleus and the π^0 meson are spin zero particles, therefore the mesons are exclusively emitted as p waves through *M1* excitation of the Δ resonance.

[9] originally 'two arm', then 'three arm' and now 'travel around photon spectrometer'

Consequently the degree of linear polarization of the bremsstrahlungs photons is completely transferred to the azimuthal asymmetry of the π^0 mesons. On that account this process can be used to measure the degree of linear polarization on an absolute scale. The measured asymmetry for two collimators is compared with calculations [83] from ANB and MCB in Fig. 3.11. In principle a very good agreement is found, apart from the dip right past the discontinuity which cannot be explained up to now.

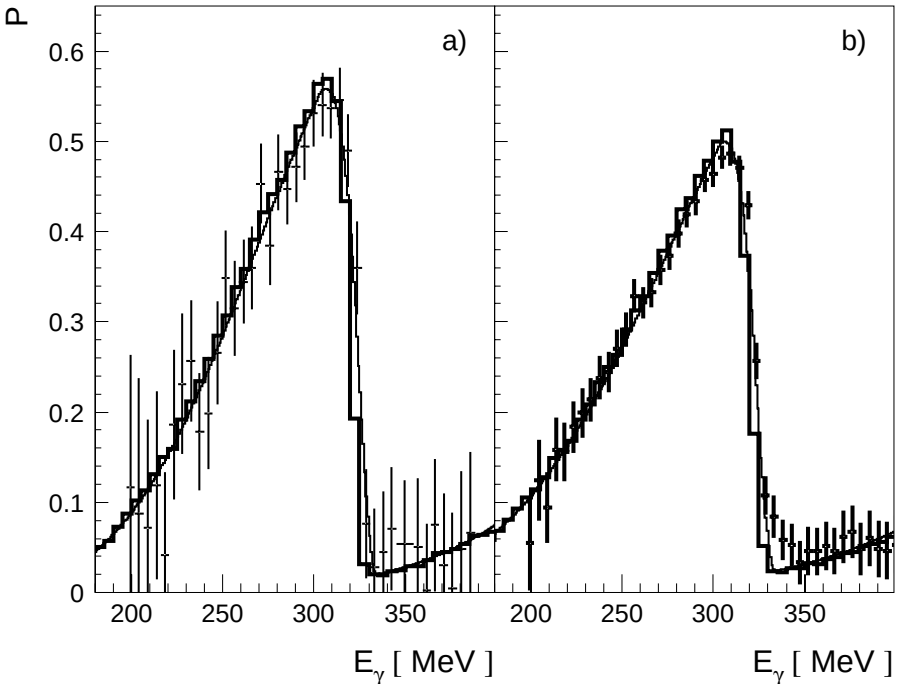

Figure 3.11: Degree of linear polarization from a calculation using the parameter of Tab. A.4 on page A13 in comparison with a measurement of the asymmetry of coherent π^0 photoproduction [70]. Two collimators were applied with $\vartheta_c = 0.7$ (upper) and 0.7 mrad (lower). The tighter collimator leads to a smaller photon flux, which is revealed by the larger statistical errors. The thick and thin lines mark a calculation from MCB and ANB respectively.

For possible future applications of coherent bremsstrahlung [84–86], there are some predictions shown Fig. 3.11. These studies demonstrate that the polarisation and enhanced photon flux from the coherent contribution increase with beam energy making it more valuable at high energy. A contingent implementation at DALINAC[10], hence at low beam energies around 120 MeV, seems also feasible with dedicated beam and crystal properties. An exploratory study was already performed [87]. The polarization prediction used for the analysis of the ($\vec{\gamma}$,NN) data is plotted in Fig. 3.12 below.

[10]Darmstadt linear accelerator, 120 MeV beam energy

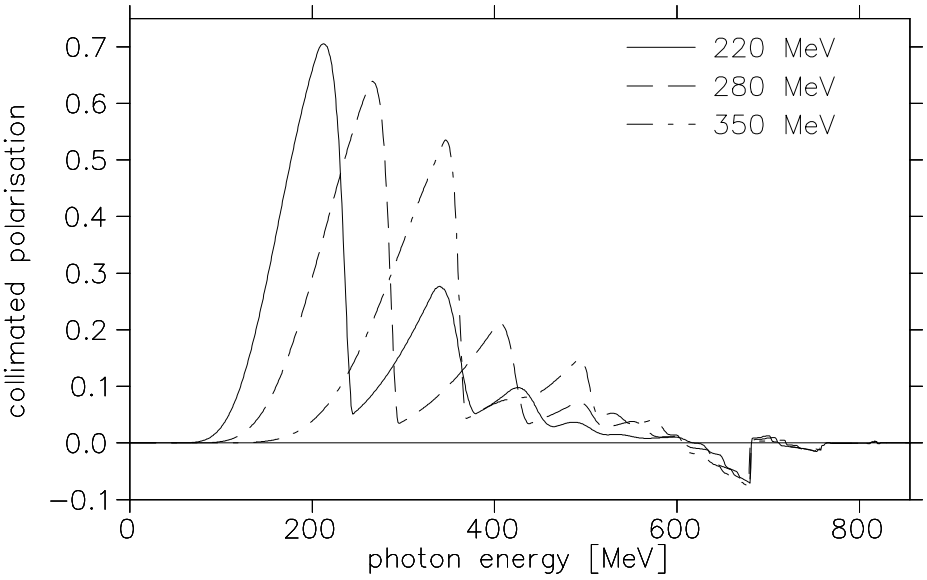

Figure 3.12: Plotted are the collimated polarizations for the three crystal angle settings, see Tab. A.5 on page A13, for comparison.

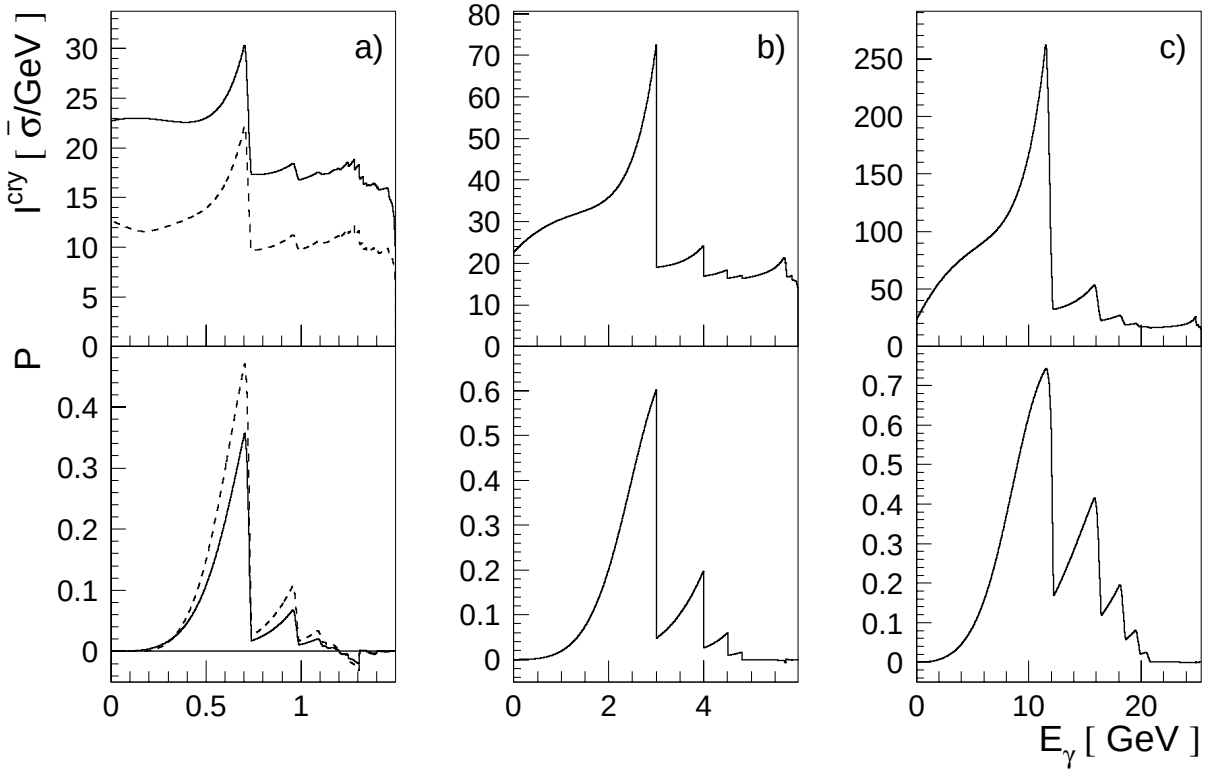

Figure 3.13: Prediction of the crystal intensities at the accelerators a) MAMI-C (uncollimated and collimated with $u_c = 0.9$), b) JLAB (uncollimated, ideal) and proposed c) ELFE maschine (expected beam properties, see [85, 86]).

Chapter 4

Theory

4.1 Overview

Although the basic processes of photo-absorption on a nucleus vary substantially with photon energy, they are principally understood over a large E_γ range. At around 10-30 MeV the photon wavelength is about the size of a nucleus explaining the collective excitation of the whole nucleus. The photon is dominantly absorbed by an electric dipole transition which leads to an oscillation of the neutrons and protons relative to each other: the giant dipole resonance. At about 300 MeV the photon wavelength is smaller than a nucleon; thus it mainly couples to one or two quarks resulting in an excitation of the respective nucleon. The lowest nucleon excitation is termed Δ resonance (with $m_\Delta = 1232$ MeV) generated by a M1 transition giving rise to a peak in the cross section. In the energy region between the giant- and the Δ resonance, the so-called dip region (~ 100 MeV), the photon couples mainly to one or two nucleons. Early experiments in that energy domain observed that most of the absorption strength originates from 2N being emitted back to back. Levinger [35] explained this observation by the coupling of the photon to the electric dipole of a pn pair which must have been in close proximity to each other. Thus the photon momentum is transferred to both nucleons, whereby the residual nucleons act as spectators with respect to the escaping two nucleons. This phenomenological model, termed QD[1], was put on a better theoretical footing with a more sophisticated description by Gottfried including a correlation function. In this model the 2N-emission cross section is written as a product of a pair momentum distribution $F(K)$, which depends only on long range properties of the 2N wave function, and a transition amplitude S_{fi}. The latter describes the dynamics of the reaction beyond the IPM by including short range aspects via the use of a correlation function proposed by Jastrow [88]. Gottfried started all the theortical work in this field by his publication [21] and suggested the 2N knock-out to be used as a promising tool to study SRC.

[1] quasi-deutron (model)

For a long period the quality and statistics of the data remained rather poor due to experimental limitations. Improved electron accelerators and technology allowed the production of high quality, tagged photon beams with a high duty factor. Experiments in the last decade resulting in accurate 2N-emission cross sections triggered again theoretical interest in that field. Next progress was provided by Boato and Giannini [89], who calculated the pn transition matrix S_{fi} in a microscopic approach including one- and two body currents (seagull only). In a subsequent publication [90] effects of FSI were studied employing an optical potential. In recent years there are essentially three groups and models which deal with real and virtual photo-induced two nucleon emission, namely the Valencia, Gent and Pavia groups. Intermediate Δ configuration were first introduced in that field in a (γ,pp) calculation by Guisti et al. [91]. These results together with similar pn calculations show that absorption on a np pair in relative $^3S_1$ and isotriplet state dominates whereas the absorption probability on an isosinglet pair with $L = 1$ is about 4-5 times smaller. The Pavia group used different SRC dependences and optical potential in their calculation, but considered pion exchange only (no heavier mesons). They concentrated on a detailed and realistic description of the nuclear structure, but all relevant diagrams are not yet included in the calculation.

Both the Pavia and Gent groups follow Gottfrieds description and calculate the transition amplitude exploiting a small set of Feynman graphs derived from minimal substitution of lowest order Meson-NN interaction. The Valencia model [34] is based on a different approach: If a photon passes through nuclear matter, various reactions like particle-hole (ph) and Delta-hole (Δh) excitations take place. These are established on basic interaction [32, 33] between γ, π and the nucleon and Δ. The photon-nucleon reactions are described by an altered photon propagator comprising the photon self-energy in the nuclear medium in dependence of the nuclear density ρ. The imaginary part of this self energy $\Pi(q, \rho(r))$ describes the loss of photon flux which is directly related to the absorption cross section (Cutkosky rules). In this model the self energy is calculated very precisely because all important contributing diagrams are considered. A weak point is the treatment of the nuclear structure due to the use of a nuclear density $\rho(r)$ from a Fermi-gas model, which cannot be applied in few body systems. Furthermore, FSI is treated semi-classically and the nuclear density is only taken into account via an approximation, the so-called LDA[2], which is based on folding the cross section calculated for a given density with the nuclear density $\rho(r)$. The advantage is its implementation as a Monte Carlo method allowing the study of various reaction mechanisms, their contributions and the ease of comparison with experimental data.

One major study of the Gent group [92] dealt with the validity of the factorized approach. They found by comparison to an unfactorized plane wave model, that the discrepancy between both, which is about a factor of 1.7 at low energies (around 100 MeV), diminishes with increasing photon energy. FSI and the one body contribution were not included in the models, but both MEC, the seagull and pion-in-flight term for pion and rho exchange

[2] local density approximation

were considered. The IC was calculated for both mesons as well. A destructive interference between the MEC-π and MEC-ρ as well as between the IC-π and IC-ρ was observed. It was shown that the ρ-π interference is particular severe in the isobar channel reducing the IC-π current by about half of the strength. In the MEC contribution the interference has considerably less impact on the total strength, but it alters significantly the angular distribution. In a realistic model [93], FSI was included in an unfactorized treatment by use of a DWIA[3], where the outgoing nucleons may interact with the residual nucleus. An interaction between the outgoing nucleons itself is not considered yet, as for example in [94][4]. The inclusion of FSI resulted in a reduction of the cross section, as already observed by the Pavia group. It turned out that the reduction is stronger in the pn case compared to the pp channel. These studies proved, as was also shown by Vanderhaeghen [92,95], that the inclusion of heavier mesons like ρ, σ and ω improve the reliability of these predictions for higher photon energies, say $E_\gamma > 300$ MeV. The σ and ω mesons contribute, due to their uncharged nature, only via particle-antiparticle diagrams. Experimental indications of the importance of heavier mesons were also found in an ^{12}C(γ,2N) measurement at MAMI. Effects beyond the π exchange have been observed in the angular distribution [96]. Special care was taken in this model, which is presented in detail in [97], concerning the orthogonality of the initial and final wave functions thus avoiding spurious contributions. However, in this model FSI is not sufficiently treated yet. Lot of work from this group was dedicated on calculations of the asymmetry in 2N knock-out reactions off ^{12}C, ^{16}O, see [41, 42, 98].

In all these studies, the one body contribution was found to depend strongly on the correlation function. Its contribution increases with stronger (harder) correlation function whereas the MEC contribution decreases. Furthermore, FSI proved to affect mainly the magnitude of the cross section, however, the shape of the excitation function and the angular dependences are not much altered. It has to be noted though, that these statements stem from factorized models and might change quantitatively in an unfactorized one. The Gent and Pavia groups adopted a similar approach which differs only in the diagrams taken into account and the approximations applied for the calculation of the cross section. A very detailed overview of the publications about this subject is given in [23].

4.2 Kinematics and phase space

The kinematics of the quasi-free (SPA[5]) two nucleon knock-out reaction $A(\gamma, N_a N_b)A-2$ is shown in Fig. 4.1 below in a simplified picture. Initially the two nucleons have momenta $\vec{k}_a$ and $\vec{k}_b$ which can also be described in terms of the relative and CM[6] motion: $\vec{k}, \vec{K}$. In the spectator model the photon momentum and energy $q = (|\vec{q}|, \vec{q})$ is completely transferred

[3] distorted wave impulse approximation

[4] In this publication, a final state correlation, unfortunately termed as FSI, is included in the calculation.

[5] spectator approximation

[6] center of momentum system

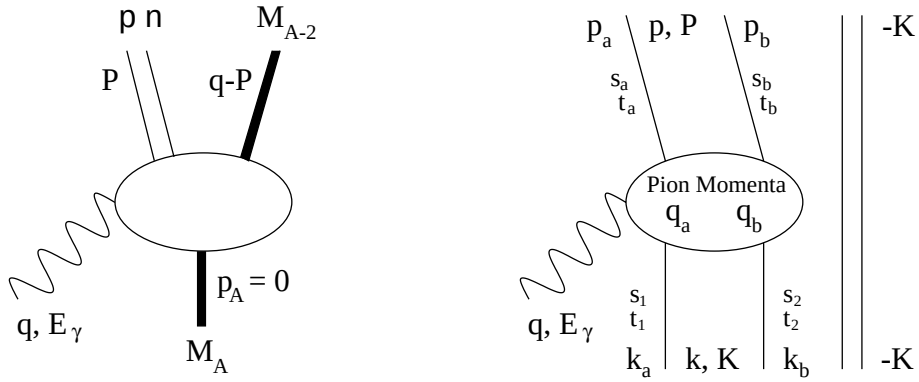

Figure 4.1: General kinematics of two nucleon knock-out (left) and in the scope of the spectator model (right). Initial momenta are denoted by $\vec{k}_a, \vec{k}_b$, final by $\vec{p}_a, \vec{p}_b$ and the photon and pion momenta by $\vec{q}$, respectively $\vec{q}_a$, $\vec{q}_b$, see (4.1).

to the pair, and omitting FSI the nucleons leave the nucleus with momenta $\vec{p}_a, \vec{p}_b$ resulting from the knock-out reaction:

$$\vec{K} = \vec{k}_a + \vec{k}_b \qquad \vec{R} = (\vec{r}_a + \vec{r}_b)/2 \tag{4.1a}$$

$$\vec{k} = (\vec{k}_a - \vec{k}_b)/2 \qquad \vec{r} = \vec{r}_a - \vec{r}_b \tag{4.1b}$$

$$\vec{P} = \vec{p}_a + \vec{p}_b = \vec{K} + \vec{q} \qquad \vec{p} = (\vec{p}_a - \vec{p}_b)/2 \tag{4.1c}$$

The (relative) momentum exchanged by the pair mediated via meson interaction reads:

$$\vec{q}_{a,b} = \vec{p}_{a,b} - \vec{k}_{a,b} = \vec{p}_\pm \mp \vec{k} \qquad \vec{p}_\pm = \vec{q}/2 \pm \vec{p} \tag{4.2}$$

It has to be emphasized though, that in case of the MEC in flight $\vec{q}_{a,b}$ cannot be defined via $\vec{p}_\pm$ due to the two pion propagators involved, see (4.35b).

There are two extreme cases: the photon couples to particle a and no momentum is transferred to nucleon b, hence $\vec{q}_b = 0$ and vice versa. Assuming that one of these cases has occurred, the initial relative momentum is determined by:

$$\text{particle a}: \quad \vec{q}_b = 0 \;\rightsquigarrow\; \vec{k} = -\vec{p}_- \tag{4.3a}$$

$$\text{particle b}: \quad \vec{q}_a = 0 \;\rightsquigarrow\; \vec{k} = \vec{p}_+ \tag{4.3b}$$

However, given the same values of the final-state observables $\vec{p}_a$,$\vec{p}_b$ and $\vec{q}$ both cases are possible corresponding with both values of $\vec{k}$. Generally, an arbitrary initial state, characterized by the value of $\vec{k}$, can lead to the same final state. While $\vec{K}$ is clearly given by $\vec{P}$ and $\vec{q}$, the relative momentum $\vec{k}$ of the initial state is undefined. In fact all values of $\vec{k}$ contribute, just weighted by the transition amplitude, compare with the integral over relative momentum in (4.30). Hence, $\vec{k}$ is *not* an observable, which means one cannot distinguish how the photon coupled to the two-nucleon system.

In (4.1) the momentum conservation was exploited. Applying these relations, the energy in the initial E_i and final E_f state can be expressed as follows, if the mean nucleon mass $M = (M_p + M_n)/2$ is introduced:

$$E_i = E_\gamma + M_A \tag{4.4a}$$

$$E_f = E_a + E_b + E_{A-2} = \frac{p^2}{M} + \frac{P^2}{4M} + 2M + \frac{K^2}{2M_{A-2}} + M_{A-2} \tag{4.4b}$$

$$\Rightarrow \quad p^2 = M\left(E_\gamma - Q - \frac{(\vec{P}-\vec{q})^2}{2M_{A-2}}\right) - \frac{P^2}{4} \tag{4.4c}$$

Thereby use was made of the definition of the Q-value, the threshold energy of this process, which reads: $Q = 2M + M_{A-2} - M_A$. The derivation of E_f was limited to the case of a non-excited residual system; otherwise the term E_x has to be added to the right hand side of (4.4b). Non-relativistic expressions are used for the kinetic energy in terms of the CM and relative momenta. More details about the relation of photon energy and final relative momentum and a complete relativistic treatment of the missing respectively excitation energy can be found in the appendix, see Section B.1. The experimental kinematical observables, which are related to the energy- and momentum conservation, are derived from the measured proton and neutron momentum and are defined as follows, whereby the index r denotes the recoiling system:

$$E_{2m} = E_\gamma - T_p - T_n - T_r \tag{4.5a}$$

$$\vec{p}_{2m} = \vec{q} - \vec{p}_p - \vec{p}_n \stackrel{!}{=} -\vec{K} \tag{4.5b}$$

$$T_r = \begin{cases} p_{2m}^2/2M_D & (\gamma,\mathrm{pn})\mathrm{D} \\ p_{2m}^2/4M + p_{34}^2/M & (\gamma,\mathrm{pn})\mathrm{pn} \end{cases} \tag{4.5c}$$

It has to be remarked, that in a multi nucleon reaction the quantity p_{2m} is not identical to the momentum of the recoiling system, as is the case in a PWIA[7] description. For the analysis of the experimental missing energy E_{2m}, the recoil formula of the deuteron final state (4.5c) was used, because the relative momentum of the residual two nucleons p_{34} or the momentum of a possibly produced pion was not measured. Therefore, if no pion was produced, the excitation energy of the residual system $E_x = E_{2m} - Q$ reflects the relative energy $T_{34} = p_{34}^2/M$ of the two unobserved nucleons.

A simple model to calculate the cross sections and asymmetries of photo-induced 2N emission from ^{4}He is presented in the subsequent paragraphs. Short range correlations in the wave function and the relevant photo-absorption processes, like 1BC, MEC and IC are implemented. It is not the purpose of this section to develop a realistic model being able to produce quantitatively results, but to provide an understanding of the basic principles and processes entering theoretical calculations. Furthermore the effects of short range correlations on the cross section and asymmetry of various observables are studied with several choices of correlation functions of the Jastrow type.

[7] plane wave impulse approximation

With the momenta and kinematical relations introduced above, the differential cross section of the photo-induced 2N knock-out process is described in the lab frame as:

$$d^6\sigma = d\Gamma \cdot \mathcal{M} = \frac{1}{(2\pi)^5 E_\gamma} d^3p_a d^3p_b\, \delta(E_f - E_i)\, \mathcal{M} \tag{4.6a}$$

$$= \frac{1}{(2\pi)^5 E_\gamma} d\Omega_a d\Omega_b dE_a dE_b\, p_a E_a p_b E_b\, \delta(E_f - E_i)\, \mathcal{M}(p_a, p_b, q) \tag{4.6b}$$

with (using (4.1) and (4.4a))

$$E_f = M_{A-2} + \frac{1}{2M_{A-2}} \left(\hat{p}_a \sqrt{E_a^2 - M^2} + \hat{p}_b \sqrt{E_b^2 - M^2} - \vec{q} \right)^2 + E_a + E_b \tag{4.6c}$$

Natural units with $\hbar = c = 1$ are used in this section. To express the cross section in the unit mb it has to be multiplied by $100(\hbar c)^2$. The integration of (4.6) would be rather complicated due to the non trivial δ function, so for the sake of a straight-forward analytical description, the actual pair momentum K in (4.6c) is approximated by its mean value[8] $\bar{K} = \langle F(K) \rangle \approx 130$ MeV with the appropriate pair momentum distribution F(K). Then the total cross section from (4.6), or the reduced cross section with the limits $\mathcal{D}$ due to detector acceptances (see Section 5.6), reads using $dE = pdp/E$:

$$\sigma = \frac{1}{(2\pi)^4 E_\gamma} \int_{\mathcal{D}} d\Omega_a d\Omega_b dE_a\, p_a p_b E_a E_b\, \mathcal{M} \tag{4.7a}$$

$$\text{with} \quad E_b \overset{(4.4a)}{=} E_\gamma + M_D - Q - \frac{\bar{K}^2}{2M_D} - E_a \doteq E'_\gamma - E_a \tag{4.7b}$$

$$\mathcal{D} = (\phi_a, \vartheta_a, T_a, \phi_b, \vartheta_b, T_b)\, \epsilon \left[(\phi, \theta, T)(\mathrm{PiP}, \mathrm{TOF}) \right]_{\text{lower}}^{\text{upper}}$$

The set $\left[(\phi, \theta, T)(\text{detector})\right]$ denotes the detector acceptance and quantifies the ranges of the angles ϕ, θ and kinetic energy T measured by the respective detector.

To achieve an estimate of the yield and shape of the excitation function, which one can be expect to measure in this experiment, a simple phase space calculation is performed in the subsequent paragraph. In (4.6a) it is stated, that the cross section $d\sigma$ is proportional to the phase space factor $d\Gamma$ and the transition matrix element $\mathcal{M}$. The physics resides in the latter, whereas the phase space governs the kinematical distributions of the final state. Given a constant matrix element, $d\Gamma$ reflects the cross section. The integral over the phase space is thus a rough measure of σ and the ratio of it with respect to the measured cross section determines the matrix element. From (4.7) the integrated phase space Γ, hence the cross section if $\mathcal{M} = 1$, is given in a relativistic treatment by

$$\Gamma(E_\gamma) \propto \frac{1}{E_\gamma} \int_M^{E'_\gamma - M} dE_a \sqrt{E_a^2 - M^2} \sqrt{(E'_\gamma - E_a)^2 - M^2}\, (E'_\gamma - E_a) E_a \tag{4.8}$$

[8] A similar procedure was already employed by Gottfried, see definition of $\bar{\epsilon}$ in [21].

and rises roughly quadratically with photon energy. This unphysical behaviour indicates that the use of a constant matrix element ($\mathcal{M} = 1$) is a totally unsufficient ansatz. In a factorized approach, as derived by Gottfried [21], the transition probability $\mathcal{M}$ is determined by the product $F(K)S_{fi}$. A less severe approximation would mean to assume $S_{fi} = 1$, thus employing $F(K)$ instead of $\mathcal{M}$ for the phase space integral. By use of a non relativistic ansatz this integral, marked by Γ_F, over the pair momentum distribution reads in CM variables:

$$\Gamma_F(E_\gamma) \propto \frac{1}{E_\gamma} \int \sin\vartheta_P d\vartheta_P P^2 dP\, \bar{p} F(\vec{P} - \vec{q}) \tag{4.9a}$$

$$\text{with} \quad \bar{p}^2 = M\left(E_\gamma - Q - \frac{\bar{K}^2}{2M_D}\right) - \frac{P^2}{4} \tag{4.9b}$$

For the pair momentum distribution an uncorrelated wave function, namely an HO wave function with oscillator constant $a_0 = 0.534$ fm^{-1} according to (4.14), is applied. Γ_F is plotted in Fig. 4.2 and reveals that most of the strength should reside around 100 MeV. However, in the experiment a peak-like structure about 260 MeV is observed (see Fig. 6.7

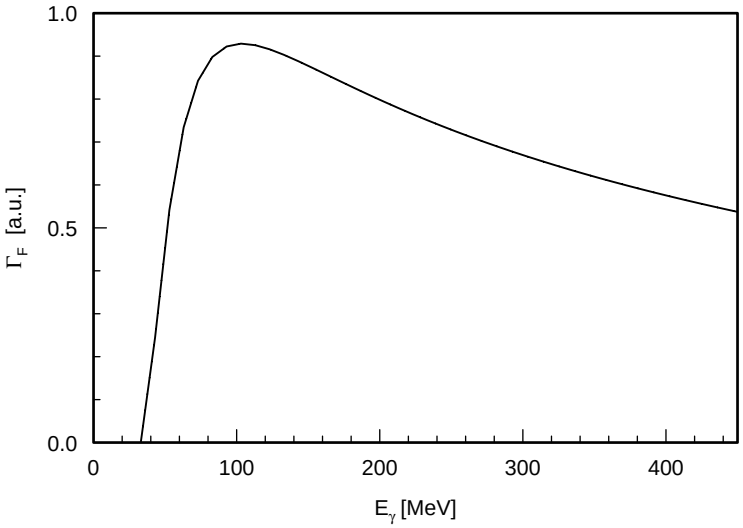

Figure 4.2: Integrated (total) phase space Γ_F according to (4.9) *using an HO pair momentum distribution $F(K)$ for ^{4}He. An oscillator constant $a_0 = 0.534$ fm^{-1}, see* (4.14c)*, is applied.*

on page 111), which indicates a resonance behaviour obviously due to the IC contribution. Asides that resonance, Γ_F resembles rather well the cross section and indicates therewith the dominant influence of the phase space and $F(K)$ on the yield.

4.3 Correlated wave functions

For the initial, uncorrelated ^{4}He ground state a product wave function is utilized consisting of a purely symmetric space wave function and an antisymmetric spin-isospin wave function. This completely antisymmetric wave function is thus written as:

$$\left|{}^4\mathrm{He}\right\rangle = (\phi_{1s})^4 \left[|0000\rangle\,|1100) + |1100\rangle\,|0000)\right] / \sqrt{2} \tag{4.10}$$

The four indices in the spin $|S_{12}S_{34}SS_z\rangle$ and isospin $|T_{12}T_{34}TT_z)$ functions denote the (iso)spin of the coupled pairs of particles 1 and 2, 3 and 4, and the total (iso)spin and projection of the four particle system. By use of the Clebsch-Gordon coefficients one obtains the following expression, whereby the isospin wave functions have the appropriate analogous terms:

$$|0000\rangle = |(\uparrow\downarrow - \downarrow\uparrow)_{12}(\uparrow\downarrow - \downarrow\uparrow)_{34}\rangle\,/2 \tag{4.11}$$

$$|1100\rangle = \left[|\uparrow\uparrow\downarrow\downarrow\rangle + |\downarrow\downarrow\uparrow\uparrow\rangle + |(\uparrow\downarrow + \downarrow\uparrow)_{12}(\uparrow\downarrow + \downarrow\uparrow)_{34}\rangle\,/2\right]/\sqrt{3} \tag{4.12}$$

Due to the isospin structure of the final states and the 2N knock-out operator, which acts only on two particles, one can omit certain terms in the initial wave function. These are proportional to $|\mathsf{pp})$ and $|\mathsf{nn})$ in case of the $(\mathsf{pn}|$ final state and $|\mathsf{pn})$, $|\mathsf{np})$ and $|\mathsf{nn})$ in case of the pp knock-out operator respectively Hence the relevant terms of the two particle initial wave function read:

$$\Phi_{2N}\,|i_{\mathsf{pn}}\rangle = \frac{\left(\phi_{1s}\right)^2}{\sqrt{6}}\Big[\left(|\uparrow\uparrow + \downarrow\downarrow\rangle + |\uparrow\downarrow + \downarrow\uparrow\rangle\,/\sqrt{2}\right)|\mathsf{pn} - \mathsf{np})\,/\sqrt{2} \tag{4.13a}$$

$$+\,|\uparrow\downarrow - \downarrow\uparrow\rangle\,|\mathsf{pn} + \mathsf{np})\,/2\Big] \doteq \Phi_{2N}(s_0 i_0 + s_1 i_1) \tag{4.13b}$$

$$\Phi_{2N}\,|i_{\mathsf{pp}}\rangle = \frac{\left(\phi_{1s}\right)^2}{\sqrt{6}}\Big(|\uparrow\downarrow - \downarrow\uparrow\rangle\,/\sqrt{2}\Big)\,|\mathsf{pp}) \doteq \Phi_{2N}\,s_1 i_2 \tag{4.13c}$$

Within the SM the multi-particle basis-wave functions are defined by Slater determinants of single particle wave functions. In this calculation, for simplicity, the wave function basis shall be restricted to $l = 0$ states only, which is a good approximation for ^{4}He and sufficient for this toy model. Thus the 2N wave function Φ is given as a product of two single particle HO wave functions ϕ. They can be expressed in terms of the single particle or the CM variables and read in momentum and configuration space:

$$\phi(r_{a,b}) = \left(\tfrac{a}{\pi}\right)^{\frac{3}{4}} e^{-a r_{a,b}^2/2} \qquad \phi(k_{a,b}) = (\pi a)^{-\frac{3}{4}}\, e^{-k_{a,b}^2/2a} \tag{4.14a}$$

$$\Phi(R,r) = \phi(r_a)\phi(r_b) \quad = \quad \phi(R)\phi(r) = \left(\tfrac{2a}{\pi}\right)^{\frac{3}{4}} e^{-aR^2}\left(\tfrac{a}{2\pi}\right)^{\frac{3}{4}} e^{-ar^2/4} \tag{4.14b}$$

$$\Phi(K,k) = \phi(k_a)\phi(k_b) \quad = \quad \phi(K)\phi(k) = (2\pi a)^{-\frac{3}{4}}\, e^{-K^2/4a}\left(\tfrac{2}{\pi a}\right)^{\frac{3}{4}} e^{-k^2/a} \tag{4.14c}$$

The oscillator constant a is defined by the well known rms[9] charge radius of ^{4}He which is given (to first order) by: $\langle r^2\rangle = \int d^3 r_a\, w(r_a) = 3/2a$. The experimental value of $\langle r^2\rangle^{1/2} = 1.676$ fm results in $a_0 = 0.534$ fm^{-2}. The form of the HO wave functions in (4.14) is chosen such that they automatically satisfy the Heisenberg uncertainty relation: $\Delta r \cdot \Delta k = \sqrt{a/4}\cdot\sqrt{1/a} = 1/2$.

To go beyond the IPM and to include SRC, one has to replace the Slater determinant Φ by correlated wave functions Ψ which account for the short range force. They can be

[9] root mean square

found via various approaches like the variational Monte Carlo [1, 2] or Greens function method [99,100]. Assuming correlations depend on the relative coordinate only, the helium wave function can be written as a product of correlated relative wave functions depicted in Fig. 4.4 below *(left)* :

$$\Psi_{He} \propto \psi(r_{12})\psi(r_{13})\psi(r_{14})\psi(r_{23})\psi(r_{24})\psi(r_{34}) \quad \text{with} \quad r_{ij} = |\vec{r}_i - \vec{r}_j| \tag{4.15}$$

The correlated relative wave function is usually written as a product of a mean field wave function and a correlation function or as a sum of the former with a so-called defect function:

$$\psi(r) = f(r)\phi(r) \quad \text{or} \quad \psi(r) = \phi(r) + \chi_{\text{def}}(r)$$

Several correlation functions are found in the literature, the most prominent ones are the RSC (f_1) and the OMY (f_2):

$$f_1(r) = \left(1 - e^{-a_1^2 r^2}\right)^{a_2} + a_3 r^{a_4} e^{-a_5^2 r^2} \tag{4.16a}$$

$$f_2(r) = \begin{cases} \left(1 - e^{-b_1(r-b_2)^2}\right)\left(1 + b_3 e^{-b_1(r-b_2)^2}\right) & r > b_2 \\ 0 & r < b_2 \end{cases} \tag{4.16b}$$

$$a_i = 2.05\ \text{fm}^{-1}, 1.479, .901, 5.501, 1.661\ \text{fm}^{-1}$$

$$b_i = 1.12\ \text{fm}^{-1}, .6\ \text{fm}, 2.08$$

$$f_3(r) = 1 - c_1 e^{-c_2 r^2} + c_3 r^3 e^{-c_4 r^2}$$

$$f(r) = 1 - c e^{-b r^2/4} \tag{4.16c}$$

However, the simplest (modified) Jastrow type function $f(r)$ in (4.16c) was used further on. The comparison with the other correlation functions, see Fig. 4.3 below, yields a useful range for $b : 0.9 \ldots 4.5$, which corresponds with the findings in [89] (compare to parameter β, pg. 1615) and [101,102]. On account of the missing bump, which is present in the realistic correlation functions around $1 \ldots 1.5$ fm (the c_3 term of f_3 for example), the parameter c should not exceed ~ 0.5.

The implementation of correlated wave functions in nuclear processes, like the photo-induced 2N emission, is based on a technique called perturbation expansion method. Rather than presenting this approach which is derived in detail in [97], its outcome shall be illustrated and applied subsequently.

For the 2N emission reaction, correlations between nucleons not involved directly in the knock-out process, are of minor relevance and can be neglected. Moreover, in the (γ,2N) calculation presented in the following paragraphs only two particles are affected by the operator, so this process can be expressed as a sum of two-body operators. Here, just the dominant terms of the perturbation expansion in lowest order is taken further on:

$$\left\langle f \middle| \hat{J} \middle| \Phi_0 \right\rangle \xrightarrow{\text{SRC}} \left\langle f \middle| \hat{J}(1,2)\hat{O}^c_{2N} \middle| \Phi_0 \right\rangle = \left\langle f \middle| \hat{J}(1,2) \middle| \Psi_{2N}(1,2)\Phi_0^{A-2} \right\rangle \tag{4.17}$$

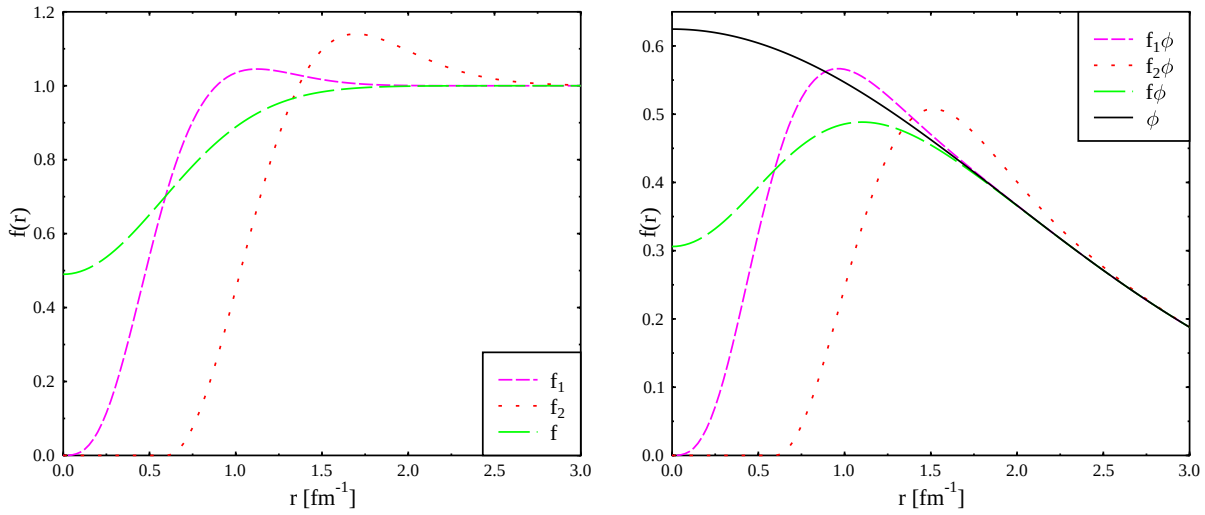

Figure 4.3: (left) Plots of different types of correlation functions and (right) the respective correlated wave functions according (4.16). *$f = 0.51\exp(1.52\,fm^{-2}\,r^2)$ denotes the correlation function suggested in [103] and used in this chapter for various combinations of b, c.*

That means, only correlations in the initial state of the active nucleon pair are considered. Φ_0 denotes the ground state and $\hat{O}^c_{2N}$ a correlation operator comprising spin and isospin dependent two body correlations. The following calculation is restricted to the so-called central correlation, i.e. the spin and isospin dependence are omitted. Further, as mentioned above, the dependence of $\hat{O}^c$ on the CM coordinate R, assumed to be small, is not considered. This leads to an approximate expression of a 2N wave function suitable to account for correlations in a $(\gamma, 2N)$ calculation and is depicted in Fig. 4.4 *(middle)* :

$$\Psi_{He} = \Psi_{2N}(1,2)\Psi_{2N}(3,4) \qquad \text{with} \quad \Psi_{2N}(1,2) \approx \psi(r_1)\psi(r_2)\psi(r_{12}) \tag{4.18}$$

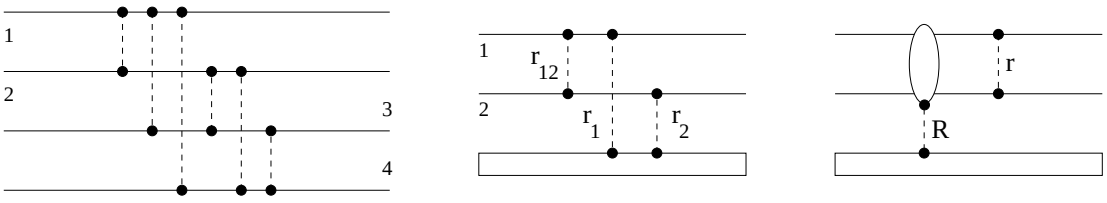

Figure 4.4: Graphical representation of correlation expansion and approximations as given in (4.15), (4.18) *and* (4.19). *(left) Full correlated state of ^{4}He. (middle) Correlations between two (active) particles and the rest nucleus only. (right) Factorized treatment still retaining the major correlation effects.*

A calculation based on a wave function similar to this type is referred to in the literature

as unfactorized model. Although providing a rather realistic description, it would need enormous amounts of computing power. Factorizing the 2N wave function into a CM and relative wave function as in the HO case, see (4.14), reduces the needs of computing power considerably. Therefore the 2N wave function is further approximated by:

$$\psi_{2N} \approx \psi_c(R)\psi(r_{12}) \tag{4.19a}$$

$$F_c(R) = |\psi_c(R)|^2 = \int d^3r_{12}|\psi(r_1)\psi(r_2)\psi(r_{12})|^2 \tag{4.19b}$$

which is illustrated in Fig. 4.4 above *(right)* . This means that terms containing the product of the CM and relative coordinates are omitted.

Therewith the correlated, relative wave functions in configuration space $\psi(r)$ with $r = r_{12}$ and after Fourier-transformation into momentum space $\psi(k)$ read:

$$\psi(r) = N_r^{-\frac{1}{2}}\left[\exp\left(-\frac{a}{4}r^2\right) - c\exp\left(-\frac{b+a}{4}r^2\right)\right] \tag{4.20a}$$

$$N_r = (2\pi)^{\frac{3}{2}}\left[a^{-\frac{3}{2}} + c^2(a+b)^{-\frac{3}{2}} - 2c(a+b/2)^{-\frac{3}{2}}\right]$$

$$\psi(k) = N_k^{-\frac{1}{2}}\left[\exp\left(-\frac{k^2}{a}\right) - c\exp\left(-\frac{k^2}{b+a}\right)\right] \tag{4.20b}$$

$$N_k = \left(\frac{\pi}{2}\right)^{\frac{3}{2}}\left[a^{\frac{3}{2}} + c^2(a+b)^{\frac{3}{2}} - 2c\left(\frac{a^2+ab}{a+b/2}\right)^{\frac{3}{2}}\right]$$

The correlation function $f(r)$ and the correlated wave functions $\psi(r), \psi(k)$ are plotted in Fig. 4.5 on page 57 along with their respective densities defined as $w(r) = r^2|\psi|^2$ and $w(k)$ analogous. Panel *b)* and *c)* demonstrate that the parameter c controls the strength of the repulsion at short distances and thus its impact on the relative wave function, whereas the range of the altered region of the wave function is determined by parameter b. The larger c and b the stronger is the suppression of the wave function at small distances and the more pronounced is the kink in the relative-momentum wave function, see panel *d)*. The density in momentum space is shown in *e)* indicating that the location of the node shifts towards lower momenta with larger b and c. Also, the probability of high momenta increases.

The calculation of the CM wave density $|\psi_c(R)|^2$, see (4.19) is presented in the following paragraph. Using a relative wave function of the form $f(r)\phi(r)$ with $f(r)$ from (4.16c) would lead to 27 terms in the integral of (4.19b). The calculation of $F_c(R)$ is rather lengthy but straight-forward because it can be shown that the CM wave function can be written as a sum of Gaussians. Retaining the most dominant two terms yields a wave function, which has two maxima and therefore a larger width than an HO distribution, as it is observed in the relative wave function, shown in Fig. 4.5 on page 57 *d)* ; yet the effect is much smaller (compare with Fig. 6.9 on page 114):

$$|\psi_c(R)|^2 \sim \exp\left[-2aR^2\right] - 4c(1+b/4a)^{-\frac{3}{2}}\exp\left[-2a\left(\frac{1+b/2a}{1+b/4a}\right)R^2\right] \tag{4.21a}$$

To keep the successive calculation simple, a single Gaussian is used instead. However, an oscillator constant denoted by d, which differs from $a_0 = 0.534$ depending on the correlation parameters, is applied to account at least for the main effect of the correlations on the CM wave function. This oscillator constant is determined in (4.21b) by demanding that this altered HO wave function has the same width as the one calculated from (4.21a):

$$d(a,b,c) = \frac{1 - 4c(1+b/2a)^{-3/2}}{1 - 4c(1+b/4a)(1+b/2a)^{-5/2}}\, a \tag{4.21b}$$

For vanishing correlations, i.e. $b = c = 0$, the standard HO constant is resumed: $d(a,0,0) = a$ implicating the uncorrelated description given in (4.14). The factorized treatment of the correlations according (4.19) leads to a correlated wave function which differs quantitatively to a realistic one; but the qualitative effect of correlations compared to an HO description is retained.

From the two body correlated wave function $\Psi(k_a, k_b) = \psi_c(K)\psi(k)$ based on (4.19) and (4.20) the single particle momentum or space density is obtained by integrating the two body momentum density $w(x_a) = x_a^2 \int d^3x_b\, |\psi(x_a, x_b)|^2$ with $\vec{x}_i = \vec{r}_i, \vec{k}_i$ over the second particle $\vec{x}_b$. All integrals which appear along the calculation are of the following type:

$$\begin{aligned}\int d^3x_b \exp\left[-A^2(\vec{x}_a^{\,2} + \vec{x}_b^{\,2}) - 2AB\vec{x}_a\vec{x}_b\right] \\ = 2\pi \int_0^\infty x_b^2 dx_b \int_{-1}^1 dy\, \exp\left[-A^2(x_a^2 + x_b^2) - 2ABx_a x_b y\right] \\ = \left(\frac{\pi}{A^2}\right)^{\frac{3}{2}} \exp\left[-(A^2 - B^2)x_a^2\right]\end{aligned}$$

So the single particle densities in momentum and configuration space are finally given in dependence of the correlation parameters and the CM oscillator constant d by:

$$w(r_a) = \frac{r_a^2}{N_r}\left(\frac{2d}{\pi}\right)^{\frac{3}{2}} \left\{h(d,a) + c^2 h(d,a+b) - 2ch(d,a+b/2)\right\} \tag{4.22a}$$

$$w(k_a) = \frac{k_a^2}{N_k}\left(\frac{\pi}{d}\right)^{\frac{3}{2}} \left\{h(d,a,1) + c^2 h(d,a+b,1) - 2ch(d,a+b,a+b/2)\right\} \tag{4.22b}$$

with
$$h(\alpha,\beta) = \left(\frac{2\pi}{\alpha+\beta}\right)^{\frac{3}{2}} \exp\left(-\frac{2\alpha\beta}{\alpha+\beta} r_a^2\right)$$
$$h(\alpha,\beta,\gamma) = \left(\frac{2\pi\alpha\beta}{\alpha\gamma+\beta}\right)^{\frac{3}{2}} \exp\left(-\frac{2\gamma}{\alpha\gamma+\beta} k_a^2\right)$$

The influence of the correlation on the single particle density is shown in Fig. 4.5 below, panel *f)*. Compared to an HO distribution, the occurrence of high momenta, i.e. in the region $k_N = 300 \ldots 500$ MeV depending on the correlation parameter b and c, is more probable. Again, as seen already in the relative wave function, the larger the correlation parameters

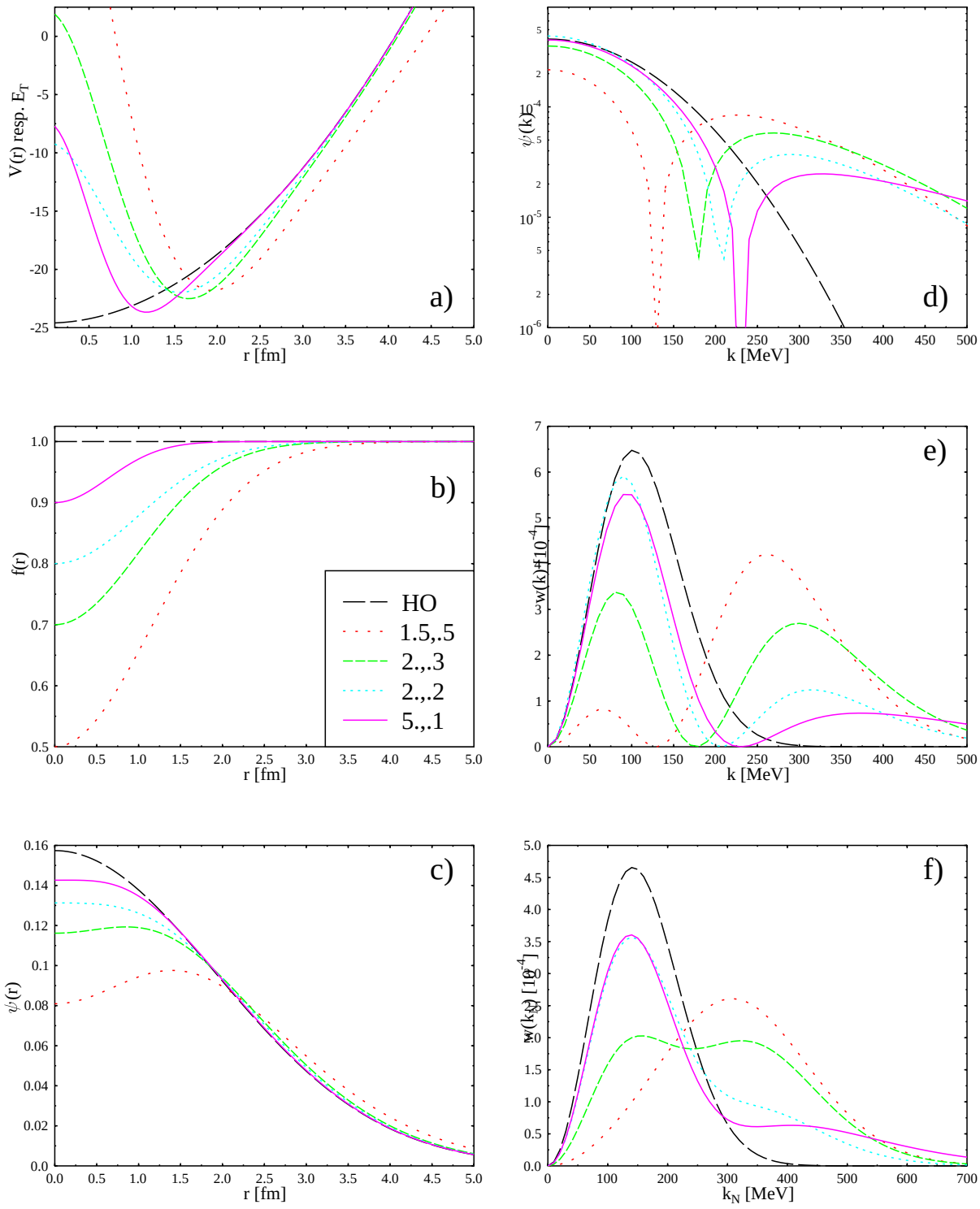

Figure 4.5: a) potential $V(r)$, b) correlation function $f(r)$ and c) relative wave function $\psi(r)$ in dependence of four parameter sets for b and c which are recorded in Tab. 4.1 on page 59. d) Relative wave function in momentum space $\psi(k)$ and e) its density $w(k)$. f) single particle density $w(k_N)$ as given in (4.22a).

the more likely are these high momentum components. In Fig. 6.18 on page 123 this single-particle momentum-density is compared with the three-body missing momentum, which approximately corresponds to the neutron momentum distribution in ^{4}He to test the SRC description outlined here.

All four parameters are constrained by the rms charge radius, as mentioned above. In the correlated case, the rms of ^{4}He leads to the following equation:

$$\left\langle r_{\mathrm{ch}}^2 \right\rangle = \int d^3 r_a w(r_a) = \left(\frac{2d}{\pi}\right)^{\frac{3}{2}} \frac{3\pi^3}{4N_r} \left\{ \frac{d+a}{[da]^{\frac{5}{2}}} + c^2 \frac{d+a+b}{[d(a+b)]^{\frac{5}{2}}} - 2c \frac{d+a+b/2}{[d(a+b/2)]^{\frac{5}{2}}} \right\} \tag{4.23}$$

This expression includes the HO description, which is characterized by vanishing correlation parameters $b, c = 0$, because it yields in this limit the relation: $d = \left(\frac{4}{3}\left\langle r_{\mathrm{ch}}^2 \right\rangle - \frac{1}{a}\right)^{-1}$. Using $a_0 = 0.534$ from the HO case presented on page 52, $d = a_0$ is achieved as expected from (4.14). However, for non-trivial correlation parameters, this equation is solved numerically; its outcome is recorded in Tab. 4.1 below. This equation describes a constraint for all four parameters and defines, together with (4.21b), the HO constants a, d by b and c.

The following paragraph demonstrates that the correlation function can be generated by an appropriate repulsive potential and motivates therewith the choice of the correlation function applied in this toy model. The Schrödinger equation of an IPM, i.e. for a nucleon pair in an harmonic oscillator potential with $l = 0$ and without correlations, reads in radial coordinates (note, $\Delta_r = \partial_r^2 + \frac{2}{r}\partial_r$):

$$\left[\sum_{i=a,b} \left(-\frac{\Delta_i}{2M} + \frac{a^2 r_i^2}{4M} + U_N \right)\right] \Phi_{2N} = \sum_{i=a,b} E_i \Phi_{2N} \tag{4.24}$$

E_i and U_N denote the total energy and the binding constant of the attractive HO potential for a single particle state. This form of the Schrödinger equation allows to use uncorrelated product wave functions $\Phi_{2N} = \phi(r_a)\phi(r_b)$ given by Slater determinants; here, these are HO-states which are symmetric in position space. The potential is constrained due to the single particle energies which are given by the binding energy, respectively the Q value:

$$E_{a,b} = \frac{3a}{2M} + U_N \stackrel{!}{=} -E_B = -Q/4 \tag{4.25}$$

This expression defines the binding constant to $U_N = -40.3$ MeV for the standard value of the HO constant $a_0 = 0.534$ fm.

In the correlated case, a repulsive potential has to be introduced: V_c denotes the repulsive core of the total potential giving rise to particle-particle correlations. Since it is assumed here that the repulsion is determined by the inter-nucleonic distance only, SRC affect mainly the relative wave function and thus it is advisable to use CM coordinates:

$$\left[-\frac{1}{M}\left(\Delta_r + \frac{1}{4}\Delta_R\right) + \frac{a^2 R^2}{M} + \frac{a^2 r^2}{4M} + 2U_N + V_c(r) \right] \Psi_{2N} = E_{2N} \Psi_{2N} \tag{4.26a}$$

$$\text{with} \qquad V_c(r) = \frac{b}{4M} \frac{6 - (b+2a)r^2}{\exp(br^2/4)/c - 1} \tag{4.26b}$$

V_c describes a repulsive harmonic oscillator potential at short distances which is damped exponentially with larger nucleon-nucleon distances. This form allows the factorization of the wave function $\Psi_{2N} = \phi_R\psi_r = \phi_R f\phi_r$, as described above. It is readily derived that the potential in (4.26b) generates a correlated wave function, respectively the correlation function $f(r)$ of the Jastrow type (4.20a), i.e. the one utilized here. If ϕ_R and ϕ_r have different HO constants d and a instead of the standard a_0, the energy is given by (4.27) instead of (4.25). That implies that the binding constant U_N is altered by SRC as well, see Tab. 4.1. Hence, the total, relative potential $V(r)$ in dependence of the correlation parameters reads:

$$E_{2N} = \frac{3}{2M}(d+a) + 2U_N \tag{4.27}$$

$$V = V_a + V_c = \frac{a^2r^2}{4M} + U_N + V_c(r) \tag{4.28}$$

An approximate measure for the strength and range of the repulsive core can be deduced from the parameters of the correlated wave function a, b, c. The strength of the repulsion s_c may be defined as the value of the total potential at zero distance compared to the pure attractive one (adiabatic treatment, see on page 4): $s_c = V(0) - V_{c=0}(0)$. The range of the repulsive potential may be characterized by two parameters: r_c, the relative distance where the repulsive potential reaches zero and r_f, where the correlation function has dropped to half the value, which means that $\psi(r_c) = \left(1 - \frac{c}{2}\right)\phi(r_c)$:

$$s_c = \frac{3bc}{4M(1-c)} \qquad r_c = \sqrt{\frac{3}{a+b/2}} \qquad r_f = \sqrt{\frac{4}{b}\ln 2} \tag{4.29}$$

From the correlation parameters achieved by fits to the measured p_{3m} momentum distribution (see Fig. 6.17 on page 123), the values and limits obtained in this simple picture are given in Tab. 6.3, whereas the respective potentials and densities for 5 sets of parameters used in this chapter are plotted in figure Fig. 4.5 on page 57 and recored in Tab. 4.1.

Table 4.1: Parameters of the correlation function used in the calculations. Note, that d is determined by (4.21b) and that each parameter set satisfies (4.23).

param.	HO	1,.28	1.5,.2	2,.15	1,.3	2,.13	3,.08
a	.534	.53	.534	.536	.524	.536	.534
b	0	1	1.5	2	1	2	3
c	0	.28	.2	.15	.3	.13	.08
d	.534	.81	.64	.59	.85	.58	.55
s_c	-	12.1	11.7	11	13.3	9.3	8.1
r_c	-	1.7	1.5	1.4	1.7	1.4	1.2
r_f	-	1.6	1.36	1.2	1.67	1.2	.96
U_N	-40.29	-47.85	-44.4	-42.9	-48.62	-42.58	-41.46

4.4 Transition amplitude and currents

The nuclear-dynamics of the photo-induced 2N knock-out process is described by the nuclear current operator $\hat{J}$ evaluated in the initial and final states. The latter is given by the (iso)spin $\langle S_f, T_f|$ and momentum state $\langle p_a, p_b|$ of the two knocked-out nucleons and the spectating ones $\langle f_{34}|$. The initial states are defined in Section 4.3 and the involved kinematical and (iso)spin variables are given in Fig. 4.1 on page 48. The interaction of the photon with the nuclear current is described in minimal substitution by $\epsilon\hat{J}$, whereby $\vec{\epsilon}_\lambda$ marks the photon polarization, and thus the matrix element entering the cross section is given by:

$$\mathcal{M}_\lambda = \frac{1}{4}\sum_{S_f}\left|\left\langle S_f, T_f, p_a, p_b; f_{34}\right| \epsilon_\lambda \hat{J} \left|i_{2N}, \vec{K}/2+\vec{k}, \vec{K}/2-\vec{k}; i_{34}\right\rangle\right|^2 \tag{4.30}$$

It goes without saying that computing the above expression (4.30) will be very involving when accounting for the full complexity of nuclear structure and FSI. Therefore several assumptions have to be made to simplify the calculation. Here, it is assumed that the two nucleons involved in the photon absorption mechanism will escape without being subject to inelastic collisions with the residual nucleons; consequently they are described by plane waves. This is the basic assumption of the so-called SPA (spectator approximation). The nuclear current operator acts on two nucleons only and allows thus to pull out the factor $f_\sigma = \langle f_{34}|\, i_{34}\rangle$, which is constant within the scope of the SPA. In case of pp or pn knock-out the isospin wave function of the final state is given by $(pp|$, $(pn|$ and the initial two nucleon wave function as derived on page 51 by $|i_{pp}\rangle$, $|i_{pn}\rangle$ respectively. In ^{4}He the nucleons have essentially no angular momentum and thus two nucleons are in a symmetric state. For a pn pair both triplet and singlet isospin states are allowed, whereas a pp pair occupies only iso-triplet states. The wave function and current operators are defined and calculated in a single particle basis. However, the sum of many body wave functions is defined in a coupled basis only. Therefore an operator projecting onto a two particle coupled basis (B.7) denoted by Λ has to be inserted in (4.30). The isospin dependence is removed by introducing the spin-current $\vec{J} = (T_f|\, \Lambda\hat{J}\, |i_{2N}\rangle$. The last step to calculate $\mathcal{M}_\lambda$ is the integration over the initial relative momentum, where the resulting amplitude is denoted by J_λ, and reads:

$$\mathcal{M}_\lambda = \frac{1}{4}\sum_{S_f}\left|\psi_c(K)\,\langle S_f|\, J_\lambda\right|^2 = F(K)\,|J_\lambda|^2 \tag{4.31}$$

$$\text{with}\quad J_\lambda = \vec{\epsilon}\langle p|\,(T_f|\,\Lambda\hat{J}\,|i_{2N}\rangle\,|k\rangle = \vec{\epsilon}\int\frac{d^3k}{(2\pi)^3}\,\vec{J}\psi(k) \tag{4.32}$$

In the last expression the completeness relation $\frac{1}{4}\sum_{SM}\langle SM|\, SM\rangle = 1$ was exploited and the CM momentum density $F(K) = |\psi_c(K)|^2$ was introduced. The cross section and asymmetry Σ are thus given as follows (see also [40]), whereby the phase space factor is

denoted by $d\Gamma$ (compare expressions on page 50):

$$d^5\sigma = d\Gamma\,(\mathcal{M}_x + \mathcal{M}_y) \tag{4.33a}$$

$$\Sigma\, d^5\sigma = d\Gamma\,(\mathcal{M}_x - \mathcal{M}_y) \tag{4.33b}$$

The most direct source of 2N knock-out strength is the coupling of the photon to the hadronic two body currents, which are mediated by mesons if the NN interaction is described in an one boson exchange picture. Treating the two body currents in pseudo-vector coupling and in the non relativistic limit results in the well-known π-exchange operators presented in (4.35b). The first term refers to the seagull graph (see Fig. 4.4) and the last term, involving two π propagators, is the pion-in-flight current. Both MEC together satisfy the continuity equation of the OPEP, the one pion exchange potential. In the impulse ap-

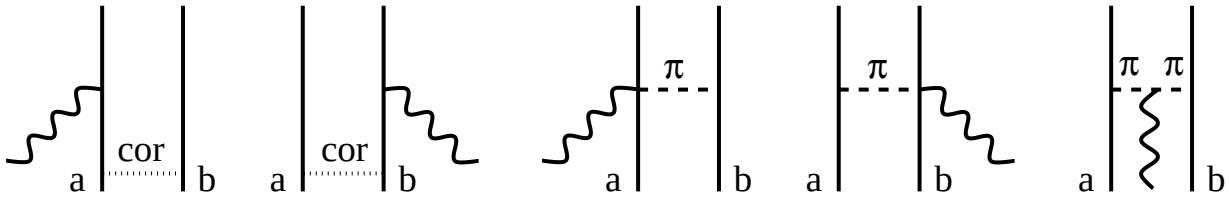

Figure 4.6: One Body (1BC) currents and both MEC (seagull and pion-in-flight). Note, there is also a pion-in-flight with particle exchange ($a \leftrightarrow b$).

proximation, the contribution from the 1BC is based on a convection and magnetization part of a single nucleon: J_N. Due to the correlation operator $\hat{O}^c_{2\mathrm{N}}$ the 1BC which leads to two emitted nucleons can be formally treated as a two body operator:

$$\hat{J}_{1\mathsf{BC}}(r_a, r_b) = \left\{ \hat{J}_N(r_a) + \hat{J}_N(r_b) \right\} f(|r_a - r_b|) \tag{4.34}$$

It is thus evident that in the absence of correlations corresponding to $f = 1$, there is no contribution to the 2N emission from the 1BC.

In addition to the MEC and 1BC contribution, there are processes associated with the excitation of a nucleon to a Delta with subsequent pion exchange. These so-called isobar currents (IC) have an intrinsically larger model dependence, as the transverse current cannot be constrained by the continuity equation. Utilizing the standard $\pi\mathrm{N}\Delta$ and $\gamma\mathrm{N}\Delta$ coupling Lagrangian [97, 104] one arrives at the expression for the IC with pion exchange stated in (4.35c). G^r and G^n denote the Delta propagator for the resonant and the non-resonant diagrams (Fig. 4.7 below), respectively. In the literature there is still no agreement on the expression of this propagator, see for example [105–108]. More details on this subject are given in the appendix, see Section B.4. From the structure of the IC-ρ current, it is noticed that the expression contains a subset of the IC-π terms but with opposite sign. Due to the larger ρNN coupling compared to πNN, a strong destructive interference is expected. In [109] this interference is observed and illustrated by Fig. 11 in this publication, which leads to a reduction of the IC strength of about 2/3, as was already stated

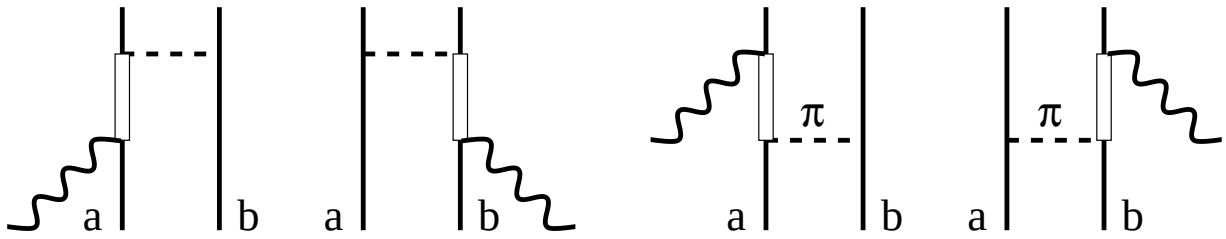

Figure 4.7: Resonant and non-resonant Delta currents (IC).

by Riska [110, 111]. It has to be noted, however, that the resulting IC strength depends strongly on the ρNΔ coupling constant, which are not well known up to now. In the model presented here, this effect is simulated in a poor man's way, by multiplying the Δ current with a reduction factor of $f_\rho \approx 0.5$. Mass and width of the Delta resonance in nuclei seems to increase almost linearly with the nuclear density [112]. Therefore the Δ mass shift $V_\Delta = -30 - 40i$ as given in [97] was not used, but a larger value of $V_\Delta = -80 - 55i$ due to the higher density of ^{4}He. Calculations with this model (Section 6.7) have shown that these values are best able to reproduce the data. It was shown [92, 95], that the inclusion of ρ exchange is essential for a realistic model, whereas the σ and ω contributions are small and may be taken into account by an effective pion cutoff parameter Λ_c in (4.36b).

These currents shall not be derived here, as they can be found in most of the theoretical publications cited in this chapter:

$$\hat{J}_{\mathsf{1BC}} = \frac{e}{2M}\Big[\tau_a^p\ \delta(q_a - q)\big(2p_a - q + i\mu_p\sigma_a \times q\big) + \tau_a^n\ \delta(q_a - q)\, i\mu_n\sigma_a \times q\ + (a \leftrightarrow b)\Big] \tag{4.35a}$$

$$\hat{J}_{\mathsf{MEC}} = -i\frac{e f_{\pi NN}^2}{m^2}\Big[T_{ab}\sigma_a Q_b\ + (a \leftrightarrow b)\ - T_{ab}Q_aQ_b\big(q_a - q_b\big)\Big] \tag{4.35b}$$

$$\hat{J}_{\mathsf{IC}} = \frac{f_\Delta^3}{9m^3}\Big\{Q_b\Big[G_a^r\big(2i\tau_b^z + T_{ab}\big)\big(2q_b - iq_b \times \sigma_a\big) + G_a^n\big(2i\tau_b^z - T_{ab}\big)\big(2q_b + iq_b \times \sigma_a\big)\Big]\ + (a \leftrightarrow b)\Big\} \times q \tag{4.35c}$$

The coupling constants are defined as: $f_\Delta^3 = f_{\gamma N\Delta} f_{\pi NN} f_{\pi N\Delta}$ and $f_{\pi NN} = 0.996$, $f_{\pi N\Delta} = 2.156$, $f_{\gamma N\Delta} = 0.12$ and are taken from [113]. In the above expressions the pion propagator with two pion-nucleon vertices including a pion nucleon form factor (monopol form factor was adopted) for each vertex was abbreviated by:

$$Q_{a,b} = (\vec{\sigma}_{a,b}\vec{P}_{a,b})F_{a,b} \qquad \vec{P}_{a,b} = \frac{\vec{q}_{a,b}}{q_{a,b}^2 + m^2} \tag{4.36a}$$

$$F_{a,b} = \left(\frac{\Lambda_c^2 - m^2}{\Lambda_c^2 + q_{a,b}^2}\right)^n \qquad n = \begin{cases} 1 & \text{pion-in-flight current} \\ 2 & \text{seagull, Delta current} \end{cases} \tag{4.36b}$$

Λ_c denotes the pion cutoff parameter and m the pion mass.

The isospin operator structure of the currents is such that only terms with τ^z,the projection operator on proton and neutron states $\tau^{p/n} = (1 \pm \tau^z)/2$, and the charge exchange operator $T_{ab} = (\vec{\tau}_a \times \vec{\tau}_b)^z$ with the following properties occur:

$$(pn|\, T\, |pp, nn, pn) = 0 \qquad (pn|\, T_{ab}\, |np) = -\,(pn|\, T_{ba}\, |np) = 2i \tag{4.37}$$

Therewith the isospin decomposition of the hadronic current in a term which leads to charge exchange and an isosinglet one, gives the following current matrix elements (the respective isospin matrix elements are shown in Section B.1). Note, that the units of the currents are omitted for convenience. The amplitudes J_λ are rewritten such that the spin operators are pulled out of the integral over the inital relative momentum and read:

$$J^{pn,\lambda}_{\mathsf{1BC}} = \frac{1}{\sqrt{2}}\Big[\vec{\epsilon}(2\vec{p}_a - \vec{q})\, H^B_a + i\vec{\epsilon}_q \left(\mu_p \vec{\sigma}_a H^B_a + \mu_n \vec{\sigma}_b H^B_b\right)\Big]\,(s_1 + s_0) \tag{4.38a}$$

$$J^{pn,\lambda}_{\mathsf{MEC}} = \sqrt{2} i\vec{\epsilon}\left[\vec{\sigma}_a(\vec{\sigma}_b H^S_b) - (\vec{\sigma}_a H^S_a)\vec{\sigma}_b - \vec{\sigma}_a \underline{\vec{H}}^F \vec{\sigma}_b\right]\,(s_1 - s_0) \tag{4.38b}$$

$$J^{pn,\lambda}_{\mathsf{IC}} = \sqrt{2} i\big(J^{-+}(s_1 - s_0) - J^{+-} s_0\big) \tag{4.38c}$$

$$J^{pq} = 2\vec{\sigma}_b \underline{H}^p_a \vec{\epsilon}_q + i\vec{\sigma}_b\big(\underline{H}^q_a \times \vec{\epsilon}_q\big)\vec{\sigma}_a \;-\; (a \leftrightarrow b)$$

The underline marks 2nd rank tensors and $\vec{\epsilon}_q$ abbrevates $\vec{q} \times \vec{\epsilon}$. The photon polarization λ enters the expressions via the respective polarization vector $\vec{\epsilon}_\lambda$.

The respective currents for pp emission are based on $\vec{J} = (\mathsf{pp}|\, \Lambda \hat{J}\, |i_{\mathsf{pp}}\rangle$ with $|i_{pp}\rangle = s_1 i_2$, which leads to an altered expression for the IC current and in a vanishing MEC contribution:

$$J^{pp,\lambda}_{\mathsf{1BC}} = \Big\{\big[\vec{\epsilon}(2\vec{p}_a - \vec{q}) + i\vec{\epsilon}_q \mu_p \vec{\sigma}_a\big] H^B_a \;+\; (a \leftrightarrow b)\Big\}\, s_1 \tag{4.39a}$$

$$J^{pp,\lambda}_{\mathsf{IC}} = 2i\Big\{2\vec{\sigma}_b \underline{H}^+_a \vec{\epsilon}_q + i\vec{\sigma}_b\big(\underline{H}^-_a \times \vec{\epsilon}_q\big)\vec{\sigma}_a \;+\; (a \leftrightarrow b)\Big\} s_1 \tag{4.39b}$$

The variables H subsumise the integrals over the initial relative momentum and are defined subsequently. They are presented in more details in Section B.2.

$$H^B_{a,b} = \int \frac{d^3k}{(2\pi)^3}\, \psi\big(k^2\big)\, \delta(q_{a,b} - q) = \psi\big(p^2_\mp\big) \tag{4.40a}$$

$$\vec{H}^S_{a,b} = \int \frac{d^3k}{(2\pi)^3}\, \psi\big(k^2\big)\, \vec{P}_{a,b} F_{a,b} \tag{4.40b}$$

$$(\underline{\vec{H}}^F)^{ij} = \int \frac{d^3k}{(2\pi)^3}\, \psi\big(k^2\big)\, P^i_a P^j_b (\vec{q}_a - \vec{q}_b) F_a F_b \tag{4.40c}$$

$$(\underline{H}^p_{a,b})^{ij} = \int \frac{d^3k}{(2\pi)^3}\, \psi\big(k^2\big)\, P^i_{b,a} q^j_{b,a} F_{b,a} G^p_{a,b} \tag{4.40d}$$

4.5 Model predictions

The integration over the final phase space is performed with standard numerical methods [114] and it is limited to 'in plane' kinematics, hence $\phi_p^0 = 0°$ and $\phi_n^0 = 180°$. The integration over the proton E_p or neutron E_n energy uses $E_\gamma/5$ MeV sampling points and over PiPs polar angle range 15 sampling points, weighted by $\Delta\phi_p = 45°$ (compare Tab. 5.3 on page 97). For the neutron polar angle, the sampling points are chosen such that they coincide with the mean polar angles of the ToF frames or bars depending on the desired resolution. Furthermore the differential cross section is weighted by the individual solid-angle acceptance of the respective frame or bar, see Tab. 5.4 on page 97:

$$\int d\Omega_p d\Omega_n \mathcal{K} \longrightarrow \sum_{x_p \in \mathsf{PiP}} \Delta x_p \Delta\phi_p \sum_{\theta_n \in \mathsf{ToF}} \Omega_{\mathsf{ToF}}(\vartheta_n) \mathcal{K}(\theta_p, \theta_n, \phi_p^0, \phi_n^0) \tag{4.41}$$

Here, x is defined as $\cos(\theta)$ and $\mathcal{K}$ abbrevates the matrix element $\mathcal{M}$ and part of the phase space $d\Gamma$, that is $dE_p dE_n p_n p_p/(2\pi)^4 E_\gamma$. The detector thresholds according Section 5.6 are taken into account by appropriate integration limits. Apart from the correlation parameters b and c there are two additional parameters which enter the model: The mesonic cutoff parameter $\Lambda_c = 1200$ MeV and the Delta mass shift $V_\Delta = -80 - 55i$ which accounts for the influence of the nuclear medium on the Delta. The appropriate final phase space integrals respecting the treatment of PiPs and ToFs angular acceptance according (4.41) thus read:

$$\sigma(E_\gamma) = \int dE_p d\Omega_p d\Omega_n \; \mathcal{K}\big(E_n(E_\gamma, E_p)\big) \tag{4.42a}$$

$$\sigma(K) = \int dE_p dE_n d\Omega_p d\Omega_n \; \mathcal{K}\big(E_\gamma(E_n, E_p, P)\big) \tag{4.42b}$$

$$\sigma(\theta_{pn}) = \int dE_p dE_n d\Omega_p \Omega_{\mathsf{ToF}}(\theta_n) \; \mathcal{K}\big(\theta_n, E_\gamma(\vec{p}_p, \vec{p}_n)\big)\Big|_{\theta_n(\theta_{pn}, \theta_p)} \tag{4.42c}$$

$$\sigma(\phi_d) = \int dE_p dE_n d\phi_p \sum \Omega_{\mathsf{ToF}}(\theta_n) \; \mathcal{K}\big(\phi_n(\phi_d, \phi_p)\big)\Big|_{\theta_p^{\mathsf{PiP}}} \tag{4.42d}$$

Based on the model presented here the contributions to the excitation function of the 1BC, IC, seagull and pion-in-flight current are calculated in total and individually for 5 sets of the correlation parameters (one characterizes the HO case) and plotted in Fig. 4.8 below. The PiP-ToF solid angle acceptance is used but no limitations originating from detector thresholds are included, which is denoted by FEA. Additionally, their asymmetries are presented in the lower panels. The parameter sets used here are recorded in Tab. 4.1 on page 59. The upper right panel reveals that the 1BC current, a direct result of SRC being present, has its largest contribution at low photon energies and that it depends rather strong on the correlation parameters. Larger values of b and c produce in general a 'harder' correlation function and enhance the 1BC contribution. Yet, the strength of the other currents is influenced by the presence of SRC, as well. Generally, they reduce the

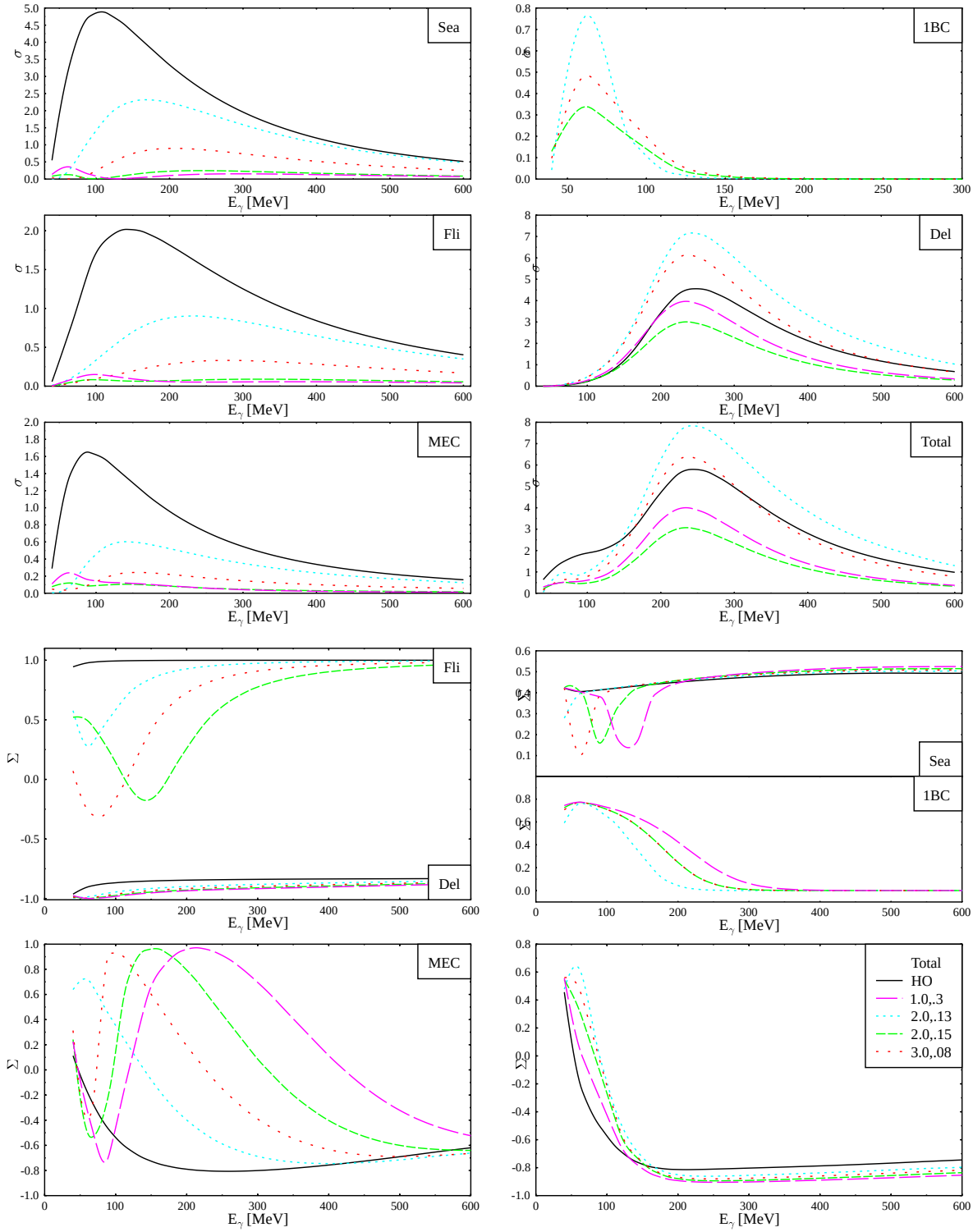

Figure 4.8: Cross sections and asymmetries of the excitation function for 4 different correlation functions and an HO wave function. The experimental acceptances are taken care of but no thresholds are applied.

contributions of the MEC currents, in particular at low energies: The harder the correlation the stronger the reduction. The destructive interference between the seagull and pion-in-flight current is marginally altered by the correlations. The correlation parameters have different influences on the MEC and IC current which leads asides an altered total strength to different shapes of the excitation function. The IC contribution is enhanced or reduced by the correlations depending on the parameters b, c. This originates from the different MEC and IC propagators which sample distinct regions of the wave function. Generally the IC strength is shifted by the influence of SRC to lower photon energies. Due to the interference of all three currents the strength and shape of the total excitation function is subject to the correlation parameters. Depending on the strength of the repulsive correlations, the reduction of the MEC at low energies is rather severe. Therefore the 1BC is comparable in magnitude to the MEC or may even be dominant around $E_\gamma = 60 \ldots 70$ MeV (note, the IC current has a vanishing strength at these energies).

The asymmetry of the IC contribution is close to -1 as has been expected from the structure of the current, i.e. from the cross product of the photon momentum $\vec{q}$ with its polarization $\vec{\epsilon}$. The seagull asymmetry is less affected by the choice of the correlated wave function than the pion-in-flight term, which originates from the different propagators involved. The major influence of SRC on the seagull and pion-in-flight is at low energies, i.e. $E_\gamma \lesssim 200$ MeV. Due to the interference of both currents, the total MEC asymmetry is extremely sensitive on the type of correlation (see lowest left panel). The convection current of the 1BC, which is insensitive to the photon polarization, causes the asymmetry to reach about 0.8 instead of +1 as expected from the spin current only. The dominant effect of SRC on the total asymmetry is seen at low energies, where the asymmetry tends to positive values due to the MEC and 1BC contributions. The harder the correlations the steeper the slope of the asymmetry because the positive asymmetry of the 1BC contributes relatively stronger. Asides this observation the influence of different types of SRC seems rather small. However, it has to be noted that this simple model does not take into account tensor correlation which are supposed to alter the asymmetry behaviour predicted here.

Fig. 4.9 below presents the cross sections and asymmetries of the neutron polar-angle distribution for various correlation parameters broken down into the individual contributions of all currents. The photon energy range was set to $E_\gamma = 140 \ldots 237$ MeV corresponding to the P220 period. The interference between the seagull and the pion-in-flight shifts the distribution a bit to forward angles. The reduction of the MEC strength and the change in magnitude of the IC contribution, induced by the influence of the correlations, exhibits no neutron angular dependence. However, the total angular distribution shifts to backward angles for the correlated wave functions compared to the HO calculation. Most of the 1BC strength resides at forward angles. At extreme neutron angles its contribution is comparable with the other currents, see also Fig. 4.12 on page 72, which could be used for the planning of an experimental setup to maximize the 1BC strength. At backward angles, i.e. $\vartheta_n \gtrsim 160$ degrees, it is even dominant. The acceptance studied with these calculations corresponds to the so-called super parallel kinematic, which was exploited in (e,e'NN) experiments performed at MAMI [115, 116]. The situation in the asymmetry is quite similar:

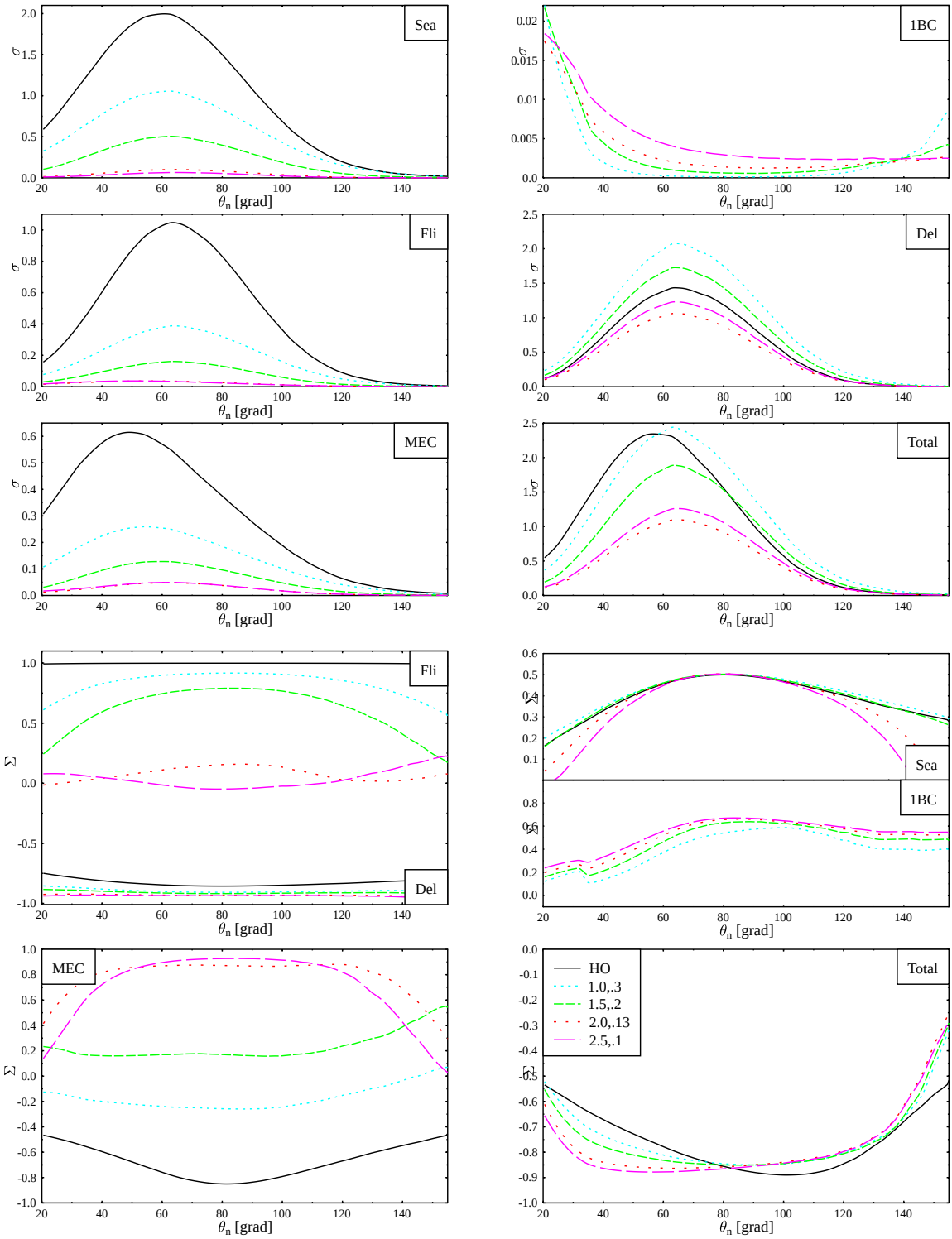

Figure 4.9: Cross sections and asymmetries of neutron angular distribution for 4 different correlation parameters and an HO wave function. The photon energy was limited to the region $E_\gamma = 140 \ldots 237$ MeV corresponding to the P220 period.

The asymmetries of the IC, seagull and 1BC are hardly affected by correlations, as was also found in their energy dependence. The pion-in-flight term and thus the total MEC via interference with the seagull current exhibit a strong dependence on the choice of SRC: The harder the correlation function, the more positive is the MEC asymmetry. This even leads to a change of the sign of the asymmetry, as also predicted in [40] (see Fig. 6 therein). The regions of the total angular asymmetry which are found to have the highest sensitivity on SRC effects are around 40° and at far backward angles ($\gtrsim$ 160°).

The influence of thresholds and acceptances in the measurement is an important point in the discussion about SRC effects and has be clarified in order to avoid misinterpretations. Therefore the excitation function and missing-momentum distribution is plotted in Fig. 4.10 to demonstrate the effects which are to be expected by the limitations due to experimental conditions. Calculations with this model showed that the thresholds and acceptances have virtually no influence on the asymmetry, in contrast to the visible cross section. The FEA calculation of the excitation function demonstrates through the compar-

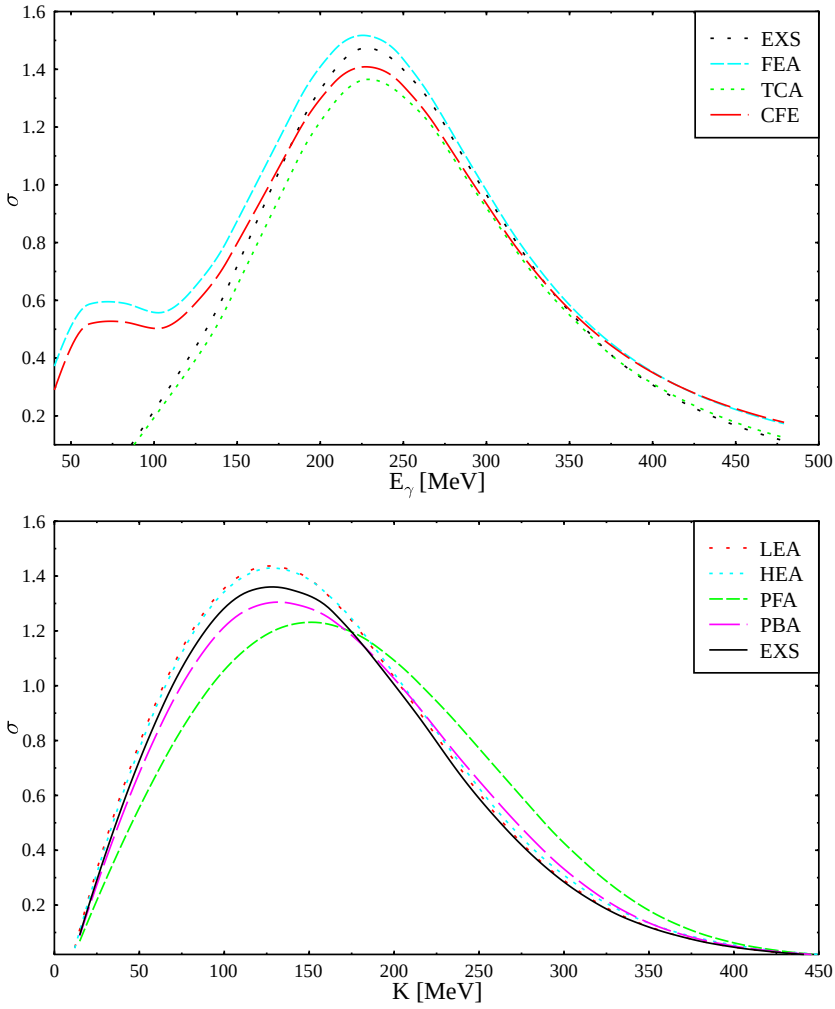

Figure 4.10: Calculation of excitation function and p_{2m} distribution for the detector thresholds and acceptances as given in this experiment (see Section 5.6). Additionally the cross sections for enlarged angular acceptance and without limitations due to detector threshold are plotted. The PiP-ToF experimental setup is denoted by EXS and the other labels are defined in the text, respectively in Tab. 4.2 below.

*Table 4.2: Definition of thresholds and acceptances used in the model calculation. All labels denote the deviation from **EXS**, which marks the acceptances and thresholds of the PiP-ToF detector setup, as described in Section 5.6.*

LEA,HEA,FEA: Low/high/full energy acceptance.
The respective calculations were performed without lower/upper/any detection limitation(s) in the final energy spectrum.

PFA,PBA: PiP forward/backward acceptance.
These studies simulate PiP at forward ($\vartheta_p = 10° \ldots 120°$) and backward ($\vartheta_p = 60° \ldots 170°$) positions with an enlarged angular acceptance.

TCA: ToF continuous acceptance.
ToF is considered in this scenario, as if it would have a constant solid angle acceptance over its full polar angle range. The total solid angle is the same than the one of the experimental setup.

CFE: TCA und FEA.

TFR: Calculation of the cross section where the sampling points of the neutron angle coincide with the center of the ToF frames.

TIA: A continuous neutron angular acceptance is simulated via an interpolation of the ToF acceptance, i.e. there are no gaps in the detector.

ison to the EXS curve that below $E_\gamma < 150$ MeV the detector thresholds cut rather severe into the measured cross section. Tab. 4.2 records the various acceptances and thresholds entering these calculations. The excitation function would start rising again for low energies due to the MEC and 1BC which are dominant there. Also, the cross section measured by the PiP-ToF setup underestimates the strength at high photon energies due to the upper limit of detecting protons in PiP. Yet, the effect on the total cross section, the one integrated over all observables and photon energy, is small. The gaps in ToF have only a small effect on the excitation function: Below $E_\gamma < 200$ MeV in photon energy the visible cross section would be a bit larger, see TCA calculation. That is supported by a plot of the pair momentum for different acceptances, see lower panel in Fig. 4.10 above. An experimental setup with no limitations on the energy acceptance would measure a larger strength which is uniformly distributed in the missing momentum spectrum. The effect is strongest in the peak, yet absolutely not relatively. The result of a continuous ToF angular acceptance (TCA) on the excitation function was only small. Additionally, the influence of an enlarged proton angular acceptance (PFA/PBA) on the measured pair momentum was investigated. In the PFA case, the missing momentum distribution shifts about 20 MeV

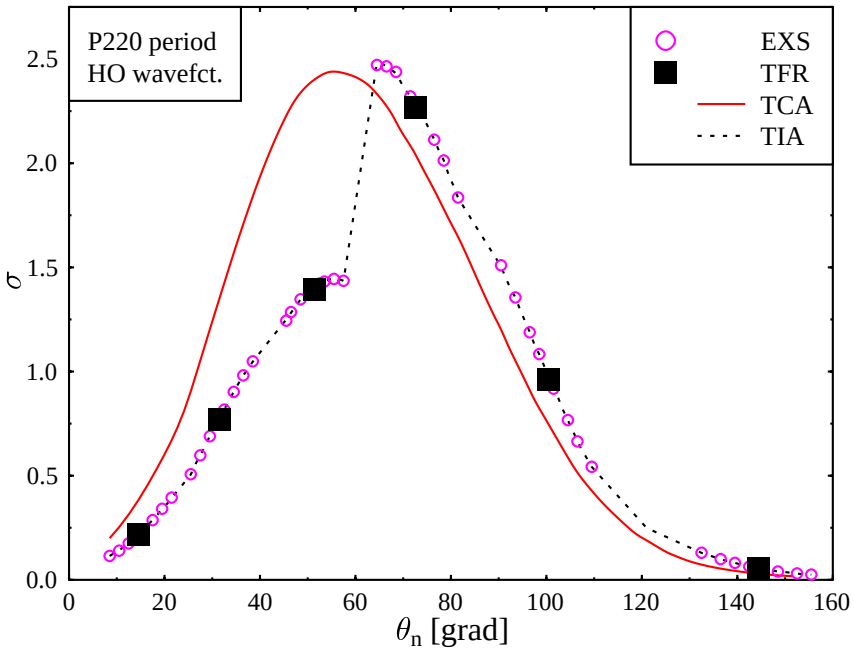

Figure 4.11: Calculation of neutron angular distribution for various ToF acceptances. The experimental setup is denoted by EXS and the other labels are defined in the text and are also recorded in Tab. 4.2 above. Note, the result of the TFR calculation is scaled by 1/8.

toward higher momenta. For PBA the same tendency of this effect is found; however, it is much smaller. Obviously the influence of limitations in the acceptance is very small for high momenta, i.e. above 300 MeV. This statement is important for the interpretation of the comparison of the measured missing momentum with distributions of pair wave functions as shown in Fig. 6.9 on page 114. To summarize, the detector thresholds have a negligible consequence on the shape of the missing-momentum spectrum and the limitations due to angular acceptance of the detectors lead to a small underestimation at medium momenta, i.e. around 200 . . . 300 MeV only.

The largest deviation between the distributions of the cross section and the ones of the measured visible cross section is found in the neutron polar-angle which is due to the variations in the solid angle acceptance of ToF. The effect of the ToF detector acceptance on the measured strength is demonstrated in Fig. 4.11, where the distribution of the neutron angle for an HO wave function is plotted for various neutron acceptances. The actual acceptance is shown by a calculation denoted by EXS, where each bar is represented by a cirlce. A similar result (TFR) is achieved by considering whole frames only, whereby the strength is divided by 8, the number of bars per frame. The TIA curve presents an interpolated ToF acceptance, which means that there are no gaps in the detector. The distribution of the cross section, as would be measured by a constant solid angle acceptance (same as total ToF), is plotted in this figure as well and marked by TCA. The difference of the EXS and TCA calculation reflects the distinct distances of the ToF frames with respect to the target. The first 3 frames (A,C and E) at forward angles are farther positioned than the other resulting in a lower yield. This was done to reduce the forward peaked background. These surveys show that it is essential to include the acceptances and thresholds of the experimental setup for comparative calculations.

The investigations with this model revealed, that the 1BC, the most direct access to SRC, is particular strong at photon energies around 70 MeV and at extreme neutron angles, compare Fig. 4.8 on page 65 and Fig. 4.9. Therefore a calculation was performed at far forward and backward angles. The resulting asymmetries and cross sections of each contributing current and in total are displayed in Fig. 4.12 below. The strength of the 1BC with respect to the other contributions depends strongly on the correlation parameters; yet only a typical parameter set is shown. For this set, the 1BC gets dominant above 160° and below 10° (the wiggles around 150° are of numerical nature). That has a dramatic effect on the respective asymmetry which changes even its sign.

According to the factorized model, the cross section can be written as the product of a pair-momentum (missing momentum) distribution $F(K)$ and a matrix-element. This ansatz induces that the shape of the missing-momentum strength should not depend on any other observable. However, the calculations (Fig. 4.13 below) demonstrate that there is an energy dependence of the cross section plotted versus the missing momentum, which is also observed in the measured data, see on page 148. The distributions are scaled to the same integral for comparison. The model suggest a slight shift of the peak and the centroid of the pair momentum distribution toward higher momenta with increasing photon energies. Additionally the width of the pair-momentum strength increases a bit. These observations comply with the experimental data: The ratio of the missing momentum distribution subject to a cut on photon energy with respect to this distribution for the whole E_γ range is shown in Fig. 6.43 on page 150. For low photon energies this ratio has a negative gradient, whereas at high E_γ the gradient is positve. To summarize, the photon energy dependence is not strong, at least for $E_\gamma \gtrsim 200$ MeV. Therefore the factorized approach is a valid approximation for sufficient high photon energies; but it should not be used for comparative calculations or quantitative predictions.

The model calculations of the pp channel reveal a similar dependence of the cross section on photon energy than in the pn final state. The 1BC strength is somewhat smaller than in the pn case due to the missing contribution of the spin current, but, as in the pn knock-out, most of the yield is located around $100 \ldots 150$ MeV. Concerning this statement, it has to be noted that these calculation were performed having regard to the experimental thresholds, which cut strongly in the yield below ~ 80 MeV and which are stated in Section 5.6. Likewise ToF's solid angle acceptance is implemented. Therefore the energy range of $E_\gamma = 110 \ldots 120$ MeV was chosen for the calculation of the cross section versus the polar angle of the (PiP-side) proton shown in Fig. 4.14 on page 74. The angular distribution of the 1BC strength depends strongly on the impact of the correlation function. However, for all sets of the correlation parameters there is one commen feature: Most of the 1BC contribution is located at extreme angles, especially at forward ones. In contrast, the Delta current shows its strength predominantly perpendicular to the photon direction, which originates from the cross product with the photon momentum stated in (4.35c), and in the kinematical domain of the QD[10], that is opposite to the ToF-side proton (in the CM

[10] quasi-deutron (model)

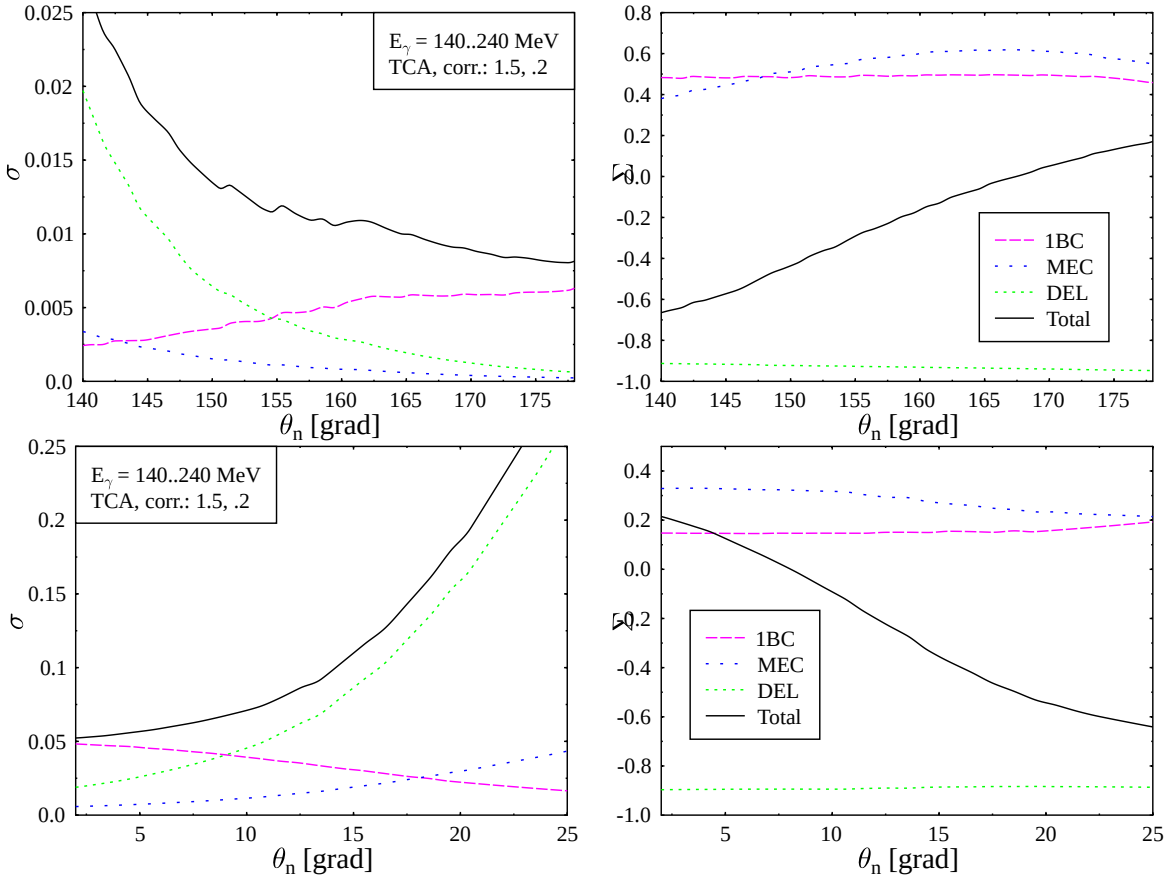

Figure 4.12: Cross sections and asymmetries of neutron angular distribution at extreme forward and backward angles.

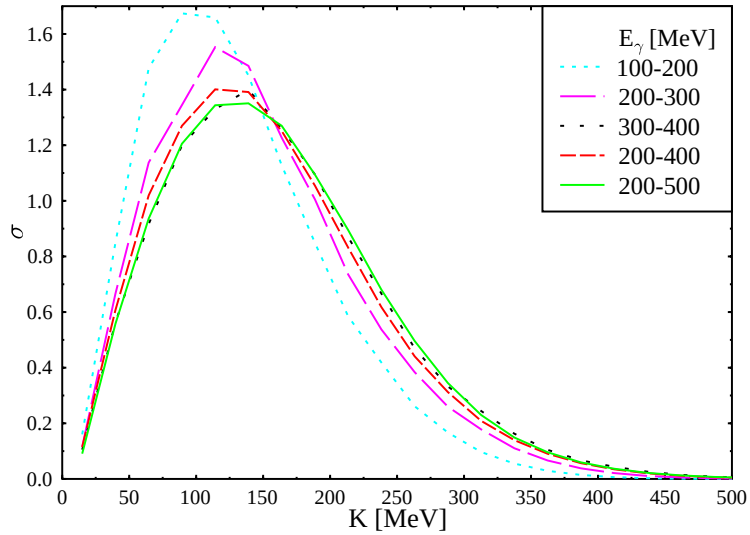

Figure 4.13: Distribution of the initial pair momentum K for the HO case at different photon energy ranges. The curves are scaled to the same integral for comparison.

frame). The slope at forward angles of the total angular distribution for the correlated wave functions is not as steep as in the HO case. That means, the ratio of the yield at the peak to the one at forward angles, say around 30°, should provide an indication of the magnitude of the 1BC contribution and hints therewith at the impact of the correlation function. The largest asymmetry of the 1BC contribution is observed around $40° \ldots 70°$ depending on the correlation parameters and at backward but not at far forward angles. Nevertheless at these extreme angles the correlation function has a particular strong impact on the knock-out process. Thus both the cross section and the asymmetry of the pp channel at forward angles — and the asymmetry in addition at backward angles — have the potential to provide information obout SRC.

This model has several deficiencies, as there are: (i) Instead of a DWIA ansatz it employs plane waves to describe the ejected nucleons. To eliminate spurious contributions to the amplitude $\mathcal{M}$ originating from the non-orthogonality of the initial and final wave functions, a Gramm-Schmidt orthogonalization procedure should be adopted. Such a procudure was not performed for the sake of computer power needs. (ii) Moreover FSI effects are not accounted for, as for example outlined in [117], because a pure SPA ansatz is adopted. This means that in the scope of this model there is no E_{2m} distribution, but the missing energy is always identical to the Q value. Hence the two spectator nucleons have no influence on the asymmetry or cross section whatsoever, which results in an overestimation of strength and asymmetry. If a significant amount of photon energy is transferred to one of the spectator nucleons, part of the photon polarization is transferred in average as well. The net effect is an reduction of strength and asymmetry. (iii) To cut down computer power needs and to keep the model simple, the initial wave function was factorized in a CM motion and a relative one. (iv) This model, as many others presented in the respective literature, lacks a proper treatment of the Delta propagator, which is still uncertain (Section B.4). (v) For quantitative comparisons of model predictions and experimental spectra it is mandatory to include the experimental resolution of the detectors, which is not done here. Yet, besides all these drawbacks, the model avoids the Gottfried approximation by integrating all currents over the initial relative momentum still providing fast results.

To partially make up for these deficiencies a phenomenological treatment, namely the application of two fit factors for the cross section and asymmetry, is utilized for the comparison of these calculations with the measurement:

$$\sigma_p = f_\sigma \left(\sigma_0 \pm f_\Sigma \Sigma_0\right) \qquad f_i \lesssim 1 \tag{4.43}$$

However, this ansatz is justified only, if these reduction factors are close to one. σ_0, Σ_0 denote the cross section and asymmetry as calculated by this model, and σ_p the polarized cross section respectively asymmetry which is compared with the measured spectra. For the calculations presented in this section $f_i = 1$ was used, whereas for the comparative spectra in Section 6.7 the factors were fitted to the data and are presented in Tab. 6.5 on page 152.

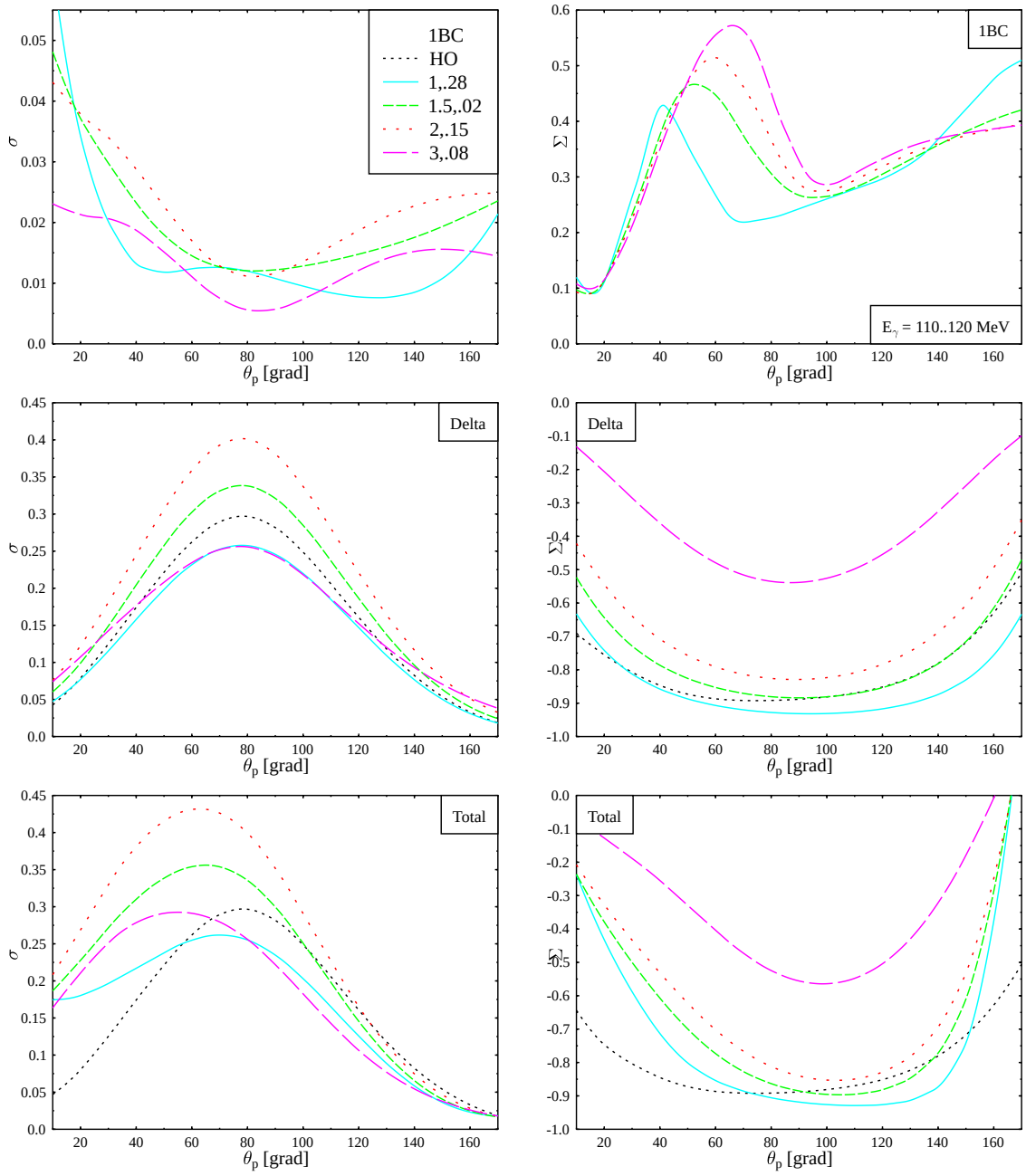

Figure 4.14: Cross section of pp knock-out versus the polar angle of the (PiP-side) proton for photon energies of $E_\gamma = 110 \ldots 120$ MeV. The experimental thresholds of the detectors, see Section 5.6, are implemented as well as ToF's solid angle acceptance.

Chapter 5

Detector calibration

5.1 Basic detector properties

If a charged particle traverses a scintillator, it excites the molecules along its path by electromagnetic interaction with the atomic electrons. They reach their ground state again by the emission of radiation, which is reflected onto a PMT and converted into an electric pulse. There is a linear dependence of the number of photons produced on the deposed energy E_{ee} of an electron passing the scintillator. But for slow and heavier particles, such as pions and protons, the energy loss might exceed the maximal possible excitation and ionisation energy in the scintillator along their path. To correct for that effect, known as quenching, conversion formulas are used [118, 119], which calculate proton or pion energies from the given electron equivalent energy E_{ee} or vice versa. Neutrons cannot induce scintillation light directly, but there is a certain probability (Section 5.5.4) to produce charged secondary particles through their strong interaction with the scintillator material. Consequently the secondary particle produces light, however not proportional to the neutron energy.

The QDC integrates the charge of an analog signal from the PMT during a gating pulse, which is longer than the signal. Even if there is no signal present, the integration of the constant current in the QDC results in a constant offset, the so-called pedestal. The pedestals have to be obtained for each QDC and subtracted from their values before further processing. These corrected QDC values are denoted in the following by q and referred to as pulse height.

It was necessary to subdivide the data into nine periods (see Tab. 5.1 below), because different collimators and crystal angles of the diamond radiator, which influenced the tagging efficiency, were used. There were also experimental shutdowns between some of those data taking periods, which affect the amplification of the PMT and electronics and consequently the calibration parameters. Therefore for each period a separate set of calibration parameters was obtained, which in addition gave the possibility to investigate fluctuations and

Table 5.1: The data had to be subdivided into 9 periods and a separate set of calibration parameters had to be obtained for each period.

label	period	run data-files		
1	^{4}He un-pol	gpn_apr96_126.dat	...	gpn_apr96_201.dat
2	^{4}He un-pol	gpn_apr96_226.dat	...	gpn_may96_571.dat
3	^{4}He pol220	gpn_may96_368.dat	...	gpn_may96_384.dat
4	^{4}He pol220	gpn_may96_387.dat	...	gpn_may96_416.dat
5	^{4}He pol220	gpn_may96_426.dat	...	gpn_may96_468.dat
6	^{4}He pol280	gpn_jul96_916.dat	...	gpn_jul96_995.dat
7	^{4}He pol350	gpn_may96_13.dat	...	gpn_may96_40.dat
8	^{4}He pol350	gpn_may96_47.dat	...	gpn_may96_57.dat
9	^{4}He pol350	gpn_may96_326.dat	...	gpn_may96_518.dat

systematic deviations in the appropriate sets of parameters. All parameters were checked for consistency between those periods and the respective observables indicated no significant deviation, which is exemplified through the PiP position parameter po_1 shown in Fig. 5.2 on page 78.

5.1.1 Pulse height stability

Compared to previous experiments on that subject performed at MAMI, all PiP and ToF PMTs were constantly monitored during the whole experiment by a so-called flasher system [48]. This technique uses a LeD[1] which periodically illuminates directly the PMT through a fibre glass cable coupling into the light guide of the bar and which itself is controlled by means of a semi permeable mirror and a PIN[2] diode feeding a QDC. With the latter, reference values are provided which enables one to obtain a time dependent correction factor [120] for each PMT. Apart from some rare but significant drifts, which were found in the data, the average fluctuation of the amplifications was about 5%. With this method these effects could be reliably corrected [59], providing a consistent calibration of PiP and ToF pulse heights.

5.1.2 Pulse height and position

The propagation of light produced at the hit position is quite complicated due to different possible paths towards the PMTs. Therefore a code was developed [121,122] which is able to

[1] light emitting diode
[2] positive intrinsic negative doted diode

deal with arbitrary detector geometries. For long scintillator bars it is a good approximation to assume that the attenuation of the light obeys an exponential law (attenuation constant λ) and that it travels with an effective speed c_{ef} along the bar:

$$\begin{aligned} n_1 &= n_0 e^{-x/\lambda} & n_2 &= n_0 e^{(x-L)/\lambda} \\ t_1 &= t + x/c_{\text{ef}} & t_2 &= t + (L-x)/c_{\text{ef}} \end{aligned} \tag{5.1}$$

The indices refer to the PMTs with respective QDCs and TDCs on each ends of the bar. L denotes the bar length, n the number of photons and t and x are the time and position of the hit, respectively. From these equations the following important observables can be deduced: The mean of both TDC values, $t_m = (t_1 + t_2)/2$, is the hit time t independent of the position x, whereupon the time difference $t_d = t_1 - t_2$ yields the position x (note, that t_1, t_2 denotes the walk corrected times, see Section 5.1.3). From the pulse heights q_1, q_2, which depend linear on the number of photons n_1, n_2, a position independent pulse height is given by $q_m = \sqrt{q_1 q_2}$ reflecting the electron equivalent energy E_{ee}. In addition the hit position may be calculated from q_1 and q_2 as well:

$$x_q = \frac{1}{2}\left(L - \lambda \ln \frac{q_1}{q_2}\right) = \text{ph}_0 + \text{ph}_1 \cdot \ln \frac{q_1}{q_2} \tag{5.2}$$

$$x_t = \text{po}_0 + \text{po}_1 \cdot t_d$$

$$E_{ee} = \text{pe}_0 + \text{pe}_1 \cdot q_m \tag{5.3}$$

From these connections all necessary calibration parameters ph_i, po_i can be gained from the values q_i, t_i. There are some events, which produce a lot of light near the end of a block. These PMT signals are greater than the range of the QDCs and so an 'overflow' is recorded. If the above calibration parameters are known, this missing QDC value can be estimated from the opposite one via (5.2).

ToF position

For a small ratio of cross section and length, as it is realized with the ToF bars, the arrival times of scintillation light at each end of a detector bar depend linear on the hit position of a particle. So the walk corrected (see below) time difference t_d between both TDCs gives the hit position x_t along the bar, as it is stated in (5.2). Comparing the extremes of the t_d spectra with the known scintillator dimensions, a linear calibration via the constants $\text{po}_{0,1}$ is obtained. The selection of events with one overflow in the corresponding ADCs, hence high energetic hits right in front of a PMT, leads to much steeper slopes of the edges in the t_d spectra, see Fig. 5.1 below. This results in a reduced systematic error in deriving the calibration parameters. The position resolution along the bar, thus in azimuthal direction, was found to be 6 cm in the middle of ToF increasing up to 8 cm at the ends of the bar [47, 59].

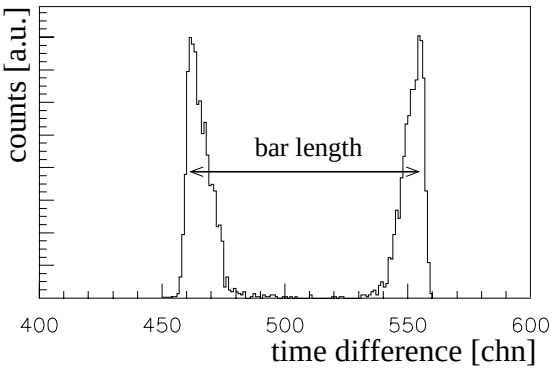

Figure 5.1: Walk corrected time difference t_d with one ADC overflow required. This is a typical spectrum of one ToF bar.

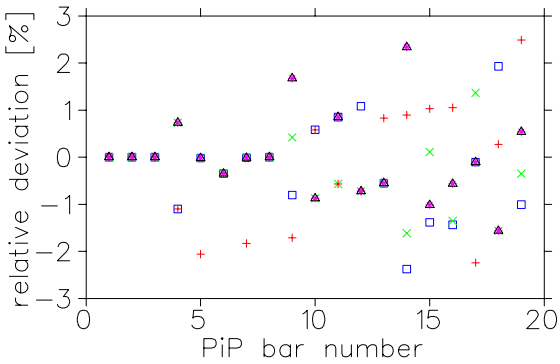

Figure 5.2: Relative deviation of PiP position calibration parameter po_1 for five periods of Tab. 5.1 on page 76. Different symbols reflect the periods.

PiP position

For PiP an improved method can be used by exploiting the segmented design of the detector. For each bar a t_d spectra is produced whilst insisting on a hit in each of the four ΔE_{pip} layers. Having normalized these four spectra per bar to the same number of events, which is necessary to eliminate the broadening due to different counts, the intersection points correspond to the position of the joins between the ΔE_{pip} elements, see Fig. 5.3 below. A fit of those intersections gives the parameter for (5.2). The reverse process, gating on the E_{pip} elements, is used to position calibrate the ΔE_{pip} scintillators. As an example for the stability and consistency of the calibration, the relative variation of po_1 is shown in Fig. 5.2 for different periods per bar compared to the mean values. The deviation was found to be less than 2%, which translates to a systematic uncertainty of the polar angle to less than $\sigma^{\vartheta}_{\text{PiP}} = 1°$. Utilizing the D($\gamma$,np) reaction, where the PiP angle is given by the well-defined neutron angle, allows to determine the approximate uncertainty in the proton angle, which was found to be about 5° FWHM.

5.1.3 Walk correction

The TDCs are started and stopped by the LED (see Fig. 2.8 on page 20) if the respective PMT signal exceeds a preset threshold. Although the time t_x (from $t = 0$) the signal takes to reach its maximum a_x is independent from the latter, the time t_0 to reach the threshold a_0 is not. This means that the TDC value has an offset dependent on the pulsheight which is termed 'walk'. Approximating the rising edge of the PMT signal by a parabola:

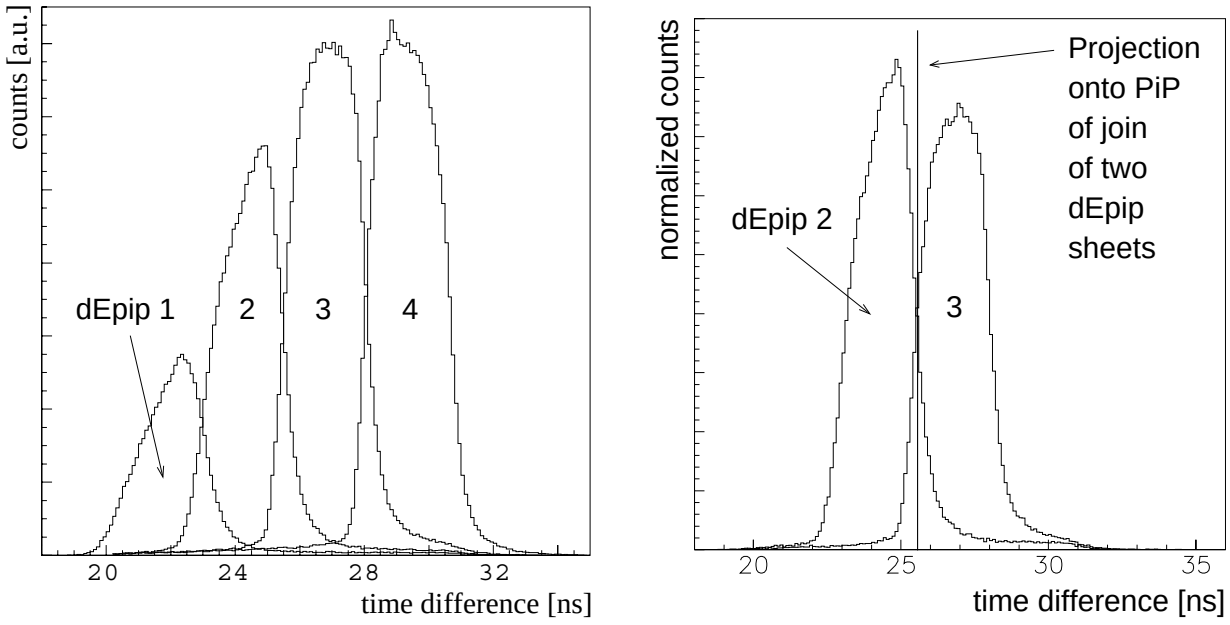

Figure 5.3: (left) t_s spectra (arbitrary offset) with conditions on a hit in each ΔE_{pip} for the same layer. (right) Intersection of two of those spectra after normalization.

$a(t) = -mt^2$, which implicates that the curvature m scales with a_x/t_x^2, yields for the offset:

$$t_0 = \sqrt{a_0/m} \propto \sqrt{a_0 t_x^2/q} \overset{\text{def}}{\propto} r\sqrt{a_0/q} \tag{5.4a}$$

$$t_w = t + r\left(1 - \sqrt{a_0/q}\right) \tag{5.4b}$$

For the second step use was made of the proportionality of the QDC value q to the signal amplitude a_1. The threshold a_0 and the rise time r comprising t_x, the proportional constants in (5.4a), can be derived from the data. Therefore these two parameters allow the correction of this effect via (5.4b), whereby t denotes the raw TDC value and t_w the walk corrected one. The threshold values are set such they are well above electronic noise and are obtained in the offline analysis from the QDC spectra on condition that the corresponding TDCs have fired. The rise time r is determined by the requirement that the walk corrected time t_w is independent of the pulse height q.

5.1.4 Energy loss

Only part of the energy of a charged particle is converted in the scintillators into light and is recorded. Therefore the measured value must be corrected for the energy loss in the air, wrappings and dead layers along its path from the reaction location in the target until the particle stops in a scintillator layer. This energy loss can be calculated using the

Bethe-Bloch equation [123, 124]:

$$-\frac{dE}{dx} = 2\kappa \left(\ln \frac{T_{\max}}{I} - \beta^2 - \ln \gamma \right) \tag{5.5a}$$

$$\kappa = 2\pi N_A r_e^2 m_e c^2 \frac{z^2 Z}{A\beta^2} \tag{5.5b}$$

where $I \approx 16Z^{0.9}$ eV denotes a material dependent ionisation constant, $T_{\max} = 2m_e c^2 \beta^2 \gamma^2$ the maximal transferred energy to an electron and some other constants are gathered in κ. From this an easy and fast-to-use technique based on the so-called stopping power theory [23, 125, 126] for handling energy losses of charged particles is derived and presented subsequently: For a given material, R_E denotes the stopping length (range) of a charged particle with initial energy E which can be calculated based on (5.5). A particle with energy $E_1 > E_2$ penetrates deeper into the material by $x = R_1 - R_2$, so that its energy loss amounts to $\Delta E/\Delta x = E_1 - E_2$. From the Bethe-Bloch equation very precise parametrizations between initial energy, stopping power and range can be deduced for low and high (above 1 MeV) energies [127]:

$$\text{low:} \quad E = -\int_0^R \left(\frac{dE}{dx} \right) dx = \left(\frac{R}{a} \right)^{1/b} \quad \rightsquigarrow \quad R = aE^b \tag{5.6a}$$

$$\text{high:} \quad -\frac{dE}{dx} = a_1 \kappa \left[\ln a_2 \beta^2 \gamma - \beta^2 - \sum_{n=0}^{4} b_n (\ln E)^n \right] \tag{5.6b}$$

whereby a and b depend on the material properties and the particle type, see Tab. 5.2. The parameters a_i, b_i are fitted to data and presented together with this theory in [125] and references therein. The range table used in this analysis are based on (5.6). From this parametrization the energy loss, especially the calculation backward, can be performed conveniently.

	CD_2	air	NE110
$a \cdot 10^3$	2.0265	2.3503	1.8917
b	1.8023	1.7844	1.8054

Table 5.2: Parameters of stopping power from [127] for low energy protons and three materials

To clarify its application the following example using the low energy parametrization is considered: a particle with initial energy E_1 traverses air until it reaches the scintillator at distance x, where its remaining energy is measured as E_2. With the energy E_1 the particle would have reached $R_1 = aE_1^b$ in air, therefore its energy E_2 just before entering the scintillator is determined by the fact that it could have travelled additional $R_1 - x$ with it, hence:

$$E_2 = \left(\frac{R_1 - x}{a} \right)^{1/b} = \left(E_1^b - \frac{x}{a} \right)^{1/b} \tag{5.7}$$

With this method the energy losses, ranges and the initial energy can be easily and very quickly interpolated from the same range table. This table has to be specific to a given material and particle type. In addition the quenching effect (see on page 75) has to be considered for a well-defined comparison with the scintillator light-output over the whole energy range. More detailed information, especially regarding the material properties of the cryotarget, particle ranges and energy loss in it, is gathered in [128].

5.2 Tagger

5.2.1 Energy calibration

The magnetic field of the tagger, which was accurately mapped [49], is constantly monitored by an NMR probe set up inside the spectrometer. These two determine the actual spectrometer field profile, which allows to calculate the trajectories of the scattered electrons. Together with the positions of the focal plane scintillators, the FPD, a relationship between the hit position (Tagger channel c_T) and the energy of the scattered electrons respectively the energy of the photons was deduced. Calibration tests with mono-energetic electrons agreed in an energy resolution of about 500 keV [50], which has to be compared with the average tagger channel width of ≈ 2 MeV.

5.2.2 TDC alignment

In Fig. 5.4 below a typical Tagger TDC spectrum is shown. Each of the 352 PMTs of the focal plane detector has different cable length and amplifications, which means that the signals reach the discriminator threshold at different times. Hence, all TDC spectra have to be aligned by a time offset, which allows to treat all channels in common. In plot *a)*, there is a peak of electrons which are correlated in time with the respective photons having caused a hadronic reaction in the target. These electrons are marked as prompt, whereas electrons at other times are uncorrelated with the experiment trigger and therefore homogeniously distributed (randoms). This figure also serves as an example of a drift of the PMT amplifications during the experiments, which results in a momentous misalignment. Plot *b)* reveals that only the lower tagger channels drifted. This complies with the fact that the power unit of the lowest tagger section failed and had to be replaced during the measurement. Plot *c)* demonstrates how these channels gets more and more misaligned over the period whereas the others stay put. By subdividing the respective runs into several subperiods (see Tab. 5.1 on page 76), each with its own calibration, the drift could be overcome. The Tagger, respectively its TDCs, has an intrinsic time resolution of 200 ps per channel. From the resulting aligned time spectrum the overall time resolution is obtained from the width of the prompt peak to $\sigma = 1.2$ ns. The influence of the position and width of the prompt peak and the random regions on the cross section was investigated by

comparison of the cross sections obtained for these regions separately, see label '1,2,3 and P' in Fig. 5.4. The cross section ratio from the random regions among each other as well as the ratio from two different width of the time window of the prompt region, i.e. 1 and 2 ns, was found to be constant and showed no photon energy dependence.

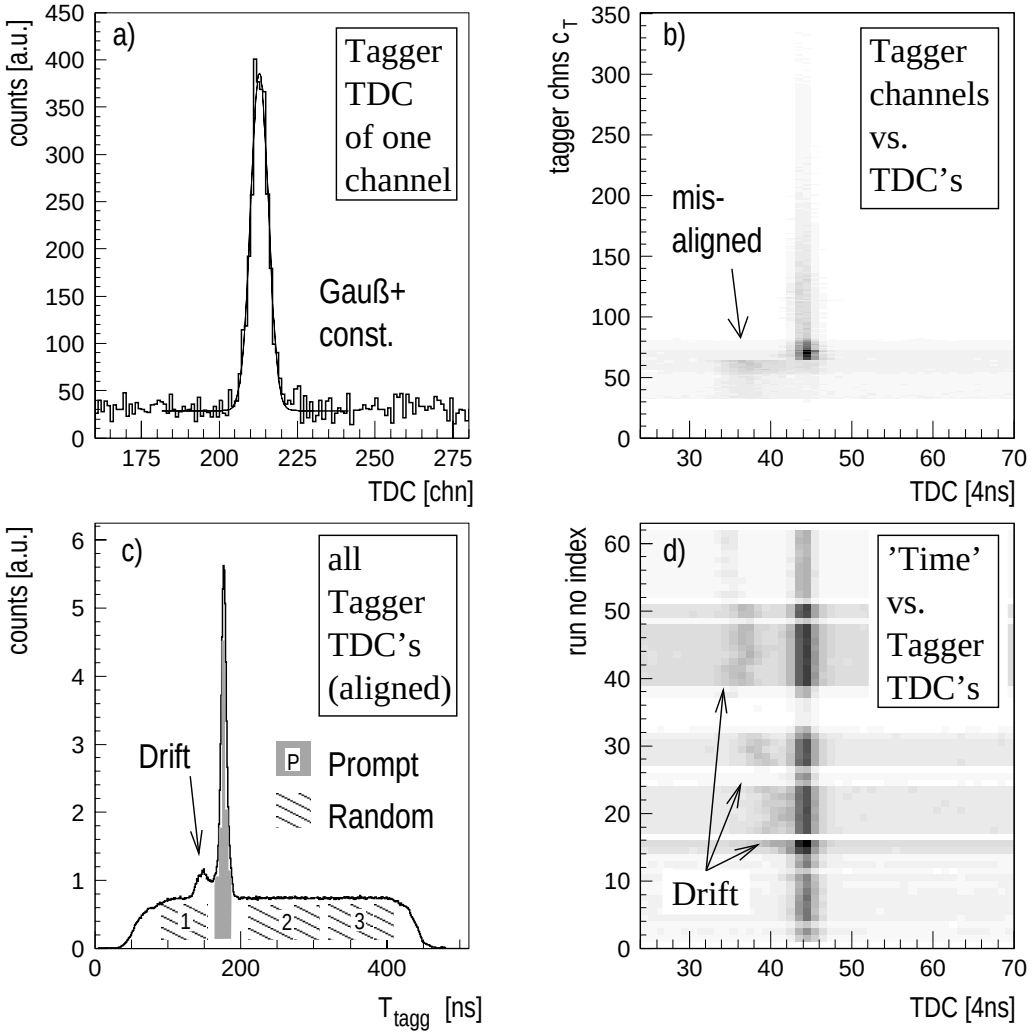

Figure 5.4: a) Time spectrum of one Tagger TDC channel with clipping on prompt peak. b) Time spectrum of all channels for several runs showing a drift of the alignment for the lower channels. c) Prompt and random regions of all channels. d) Alignment drift of some channels during the measurements

5.2.3 Tagging efficiency

Tagging efficiency is simply defined as the ratio of tagged photons reaching the target to tagged electrons. This fraction is always less than one since the necessary collimator removes some tagged photons. During the ^{4}He experiment, there were several tagging efficiency runs made for the various settings. For the unpolarized measurements, a nickel radiator was used and for the polarized ones a diamond radiator positioned at three different angles. In so doing, polarized photons are produced in three energy regions (see Chapter 3), which are denoted conveniently by 220, 280 and 350 MeV referring to the energy of maximum polarization. Most of the data has been taken with a 3 mm collimator in diameter, but a 5mm collimator was exploited also. The angular distribution of bremsstrahlung off a crystal radiator depends strongly on the photon energy, which is presented in more detail in Section 3.2 eq. (3.5). Therefore the use of a diamond radiator implicates a highly varying tagging efficiency in contrast to nickel where it is relatively smooth. For

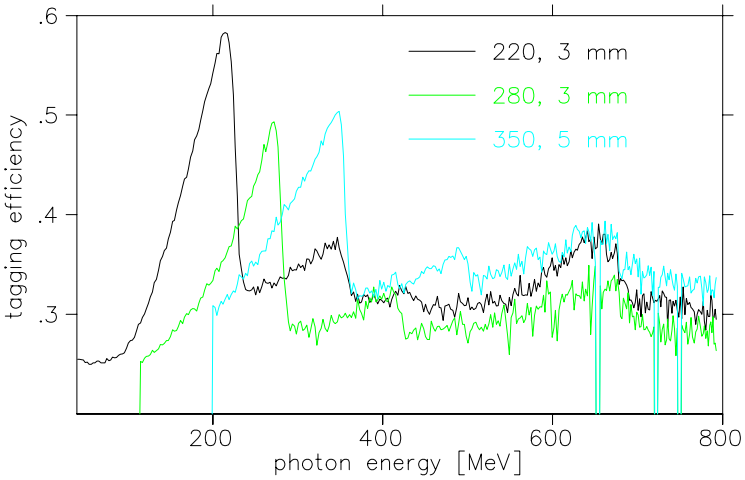

Figure 5.5: Tagging efficiencies for three different diamond settings and with 3 and 5 mm collimator radius. The use of an amorphous radiator such as nickel results in a relatively smooth efficiency of about 0.3 [57]

demonstration, some tagging efficiencies obtained from the respective measurements are shown in Fig. 5.5. Unfortunately, no efficiency for the 350 MeV setup with 3 mm collimator could be ascertained because the dedicated run gave unusually high scaler counts resulting in improbable values for the efficiency, this is yet to be understood. From an ANB calculation, for details see Section 3.4.1, for this diamond setting and 3 as well as 5 mm collimator an efficiency ratio was deduced and applied to the measured tagging efficiency of a 5 mm collimator. The resulting 3 mm efficiency was then taken for this data period. For the polarized runs some of the lower Tagger sections were disabled, because the polarization tends to zero at low photon energies. If this almost unpolarized photon flux would have contributed to the nuclear reaction, no additional information would have been obtained from the measurement, but the beam time would have gone up unnecessary. The (remaining) scaler distribution over the runs and Tagger channels is quantified in Fig. 5.7 on page 86. Some gaps in the scalers induced by bad channels can be seen in this figure but they are interpolated for Fig. 5.5.

Due to the sizeable background in the tagger the mean electron multiplicity is rather large, namely 5 but up to 15 electrons can be found. This results sometimes accidentally in multiple neighbouring hits in the FPD, which occur in the same manner from electrons having scattered from one scintillator to the next. Successive hits in a time window of 6 ns [129] are considered as a cluster and treated in the analysis as a single electron. Motivated by the Tagger geometry, the electron with the lowest energy is taken. This procedure omits events, independently whether they are in the prompt or random region (see Fig. 5.4 on page 82 and Section 5.7). Therefore, this has to be corrected channelwise by individual factors [57]. This multi-hit correction factor is given as follows, whereby the number of clusters with length i is denoted by N_i and the total number of electrons per Tagger channel c_T by $N_e(c_T)$.

$$f_{\mathrm{mhc}}(c_T) = \frac{N_e(c_T)}{N_e(c_T) - \sum_{i=2} N_i(c_T + 1 - i)} \tag{5.8}$$

5.2.4 Incident flux

To evaluate the yield, which is proportional to the cross section from measured detector hits, an eventwise method adding weights per event was used. A charged particle in PiP was required to cause a PiP trigger, which opens the gate for the other detectors. This might lead to multiple hits in the PiP - ToF - Tagger detector system, which are analysed as subevents in all possible combinations in the same way as a single hit event. The total number of subevents is given by the product of the multiplicities in each detector. In order to extract a cross section from the measured yield, the latter has to be normalized on the incident photon flux (for more details see Section 6.1). The photon flux per tagger channel c_T is determined by the electron flux counted by the Tagger scaler modules and the tagging efficiency $\epsilon_t(c_T)$. The latter specifies the ratio of photons at the target to the number of electrons at the FPD (see also Chapter 3). The total number of incident electrons $N_e(c_T)$ is given by the sum over the appropriate events E and enters the normalization together with the tagging efficiency: $Y(c_T) \propto N_t^{-1}(c_T) \sum_E \epsilon_t^{-1}(c_T)$. In addition, the effect of the bremsstrahlung distribution of the photon energies is unfolded by this procedure.

For all runs of the 1996 ^{4}He experiment scaler dumps from the raw data containing the tagger scaler were produced, see Fig. 5.7 on page 86. The projection of the scaler onto the run number provides a measure of the number of events per run and the projection onto the hit channel reveals the bremsstrahlung yield. The two-dimensional plot shows in addition that for some runs the lower Tagger channels were switched off. That provided a higher photon flux in the energy regions of interest. These scalers were obtained by counting the scaler with condition on the state of photon polarization, i.e. parallel (para), perpendicular (perp) polarization and unpolarized (upol), hence disregarding the polarization state. In order to check the consistency of the scaler dumps for these conditions, a relative difference further denoted as deviation is defined as:

$$d_S = (S_{\mathrm{upol}} - S_{\mathrm{para}} - S_{\mathrm{perp}})/S_{\mathrm{upol}} \tag{5.9}$$

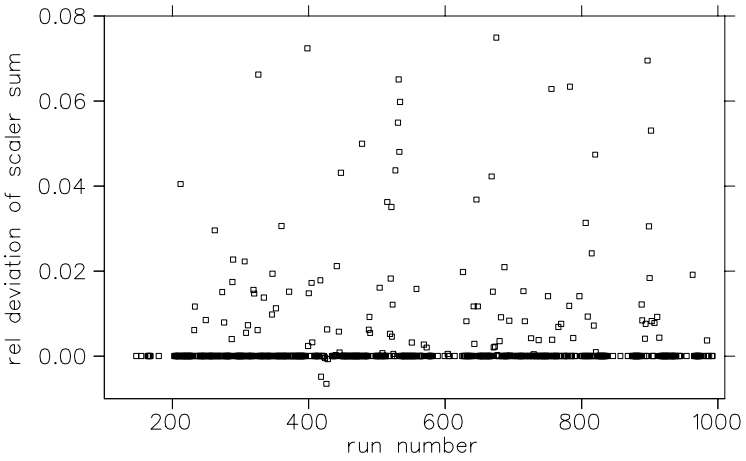

Figure 5.6: Deviation d_S (5.9) of polarized to unpolarized tagger scaler plotted over the run number.

The deviation was calculated (see Fig. 5.6) for each run with S being the integral of the tagger spectrum and for a single channel as well to check its consistency. As can be seen in the figure, there are only a few negligible deviations above 2%. Nevertheless, in the analysis, the effect was corrected for by scaling the polarized scaler appropriately to match the unpolarized ones.

5.3 Start and veto detector

The signals of the PiP-side SVD, i.e. the analog sum, enter the trigger. The latter is responsible for the start time t_s from which the t_r, the time of the nuclear reaction, is derived. It is the aim to fix the time when the reaction takes place in the target. The ToF-side operates mainly as a veto detector to tag charged particles in ToF. Having aligned the start times (t_{zero}) of the SVD elements among each other, there are still corrections to be made in order to deduce the nuclear reaction time [60] from t_s, such as the flight time from the target t^{tof} and the walk:

$$t_r = t_s + t_{\mathrm{zero}} - t_{\mathrm{walk}} - t_{\mathrm{tof}} \tag{5.10}$$

Note, that for events with large pulse heights, the time difference between the SVD and a stop detector is larger compared to those with lower ones. Therefore the walk correction for the start detector has to have the opposite sign than the one for stop detectors. If PiP is calibrated, the the kinetic energy and hit position in PiP is known and therewith the flight time t^{tof} between the target and the SVD can be deduced. Only then the SVD walk can be corrected. This is achieved from a plot of the pulse height from one SVD element versus the fixed time of a Tagger TDC. The maxima of the pulse height distribution for discrete time slots are determined from a two dimensional plot of pulse height versus Tagger TDC (the crosses in Fig. 5.8 on page 87). From this one dimensional distribution the walk parameters are deduced via a fit of the walk function. The time reflects the combined flight time of the

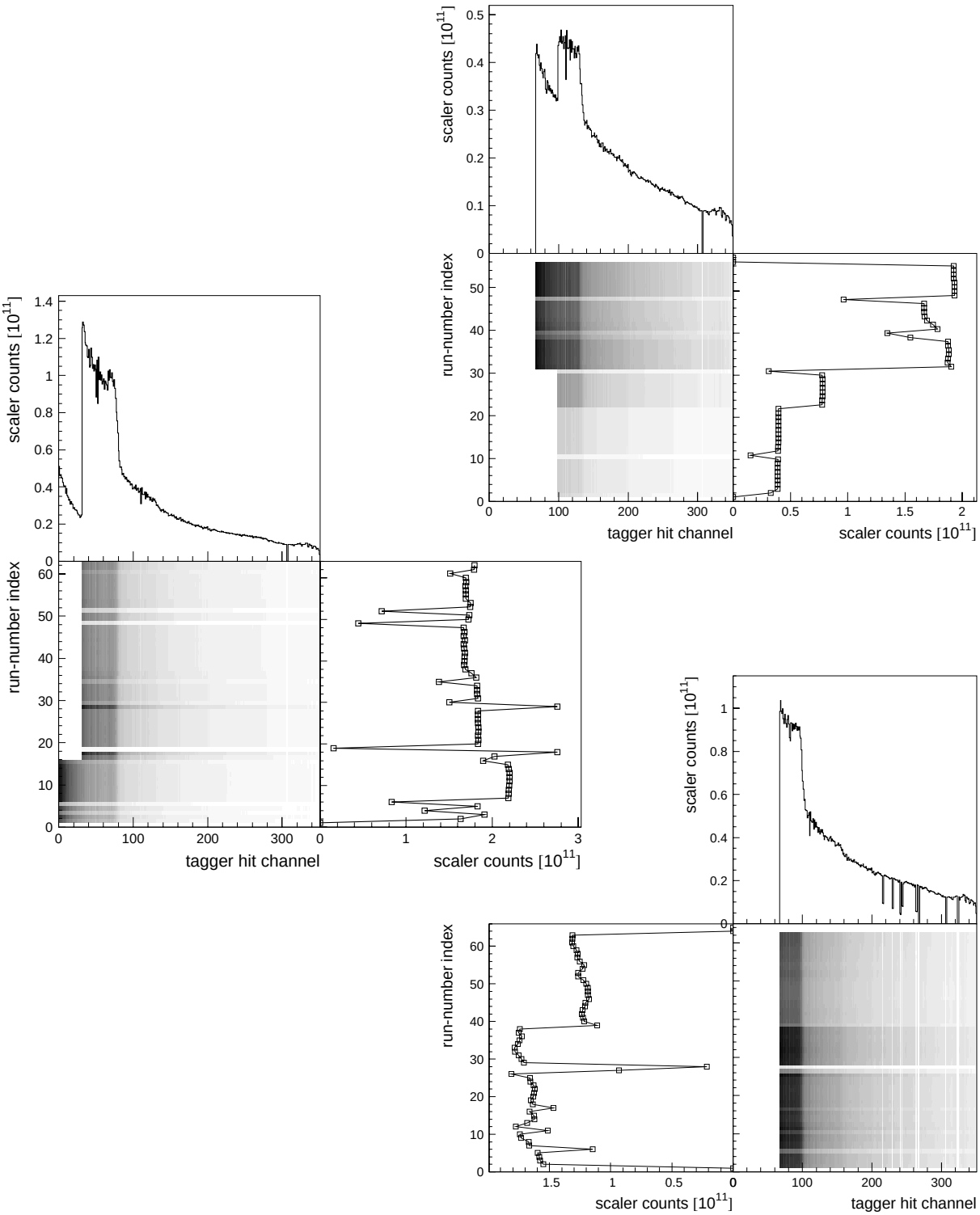

Figure 5.7: Total Tagger scaler distribution plotted versus run number and photon energy for (left) 220, (lower) 280 and (upper) 350 MeV crystal setting. The respective projections are given also.

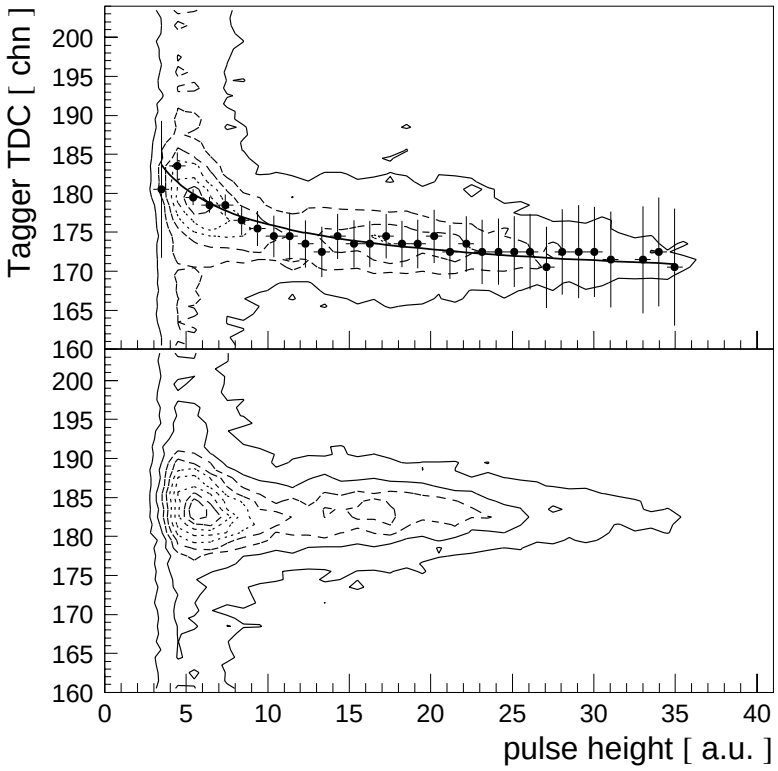

Figure 5.8: Walk correction of SVD detector. (upper) The Tagger TDCs are plotted versus the pulse height of one SVD scintillator. The pulse height maxima are marked by the dots and fittey by the walk function (5.4b). *(lower) Same diagram after the application of the walk correction.*

electron from the radiator to the focal plane detector and of the photon from the radiator to the target. Both are relativistic particles moving with the speed of light and for this reason the walk corrected spectrum shows a ridge which is constant in time.

5.4 PiP detector

5.4.1 Energy calibration

Cosmic radiation comprises various high energetic particles, however the most numerous charged particles at ground level are muons. After they have lost about 2 GeV to ionization in the atmosphere, their mean energy on the ground is about 4 GeV [123]. Muons are detected in PiP but scarcely in ToF because of their geometry and the low muon intensity, which amounts to about 1 cm^{-2} min^{-1}. At these energies, the muons are minimizing particles and lose about 27 MeV in average for 10 cm NE110 plastic scintillator, due to ionization. For thin absorbers the energy loss fluctuates strongly, which is described either by a Landay distribution [124], or by the more precise Vavilov distribution [130]. Both

formulas are too lengthy to present them here, but they can be approximated as follows:

$$V(\lambda) = (1 + p_1\lambda + p_2\lambda^2 + p_3\lambda^3) \cdot L(\lambda) \tag{5.11}$$
$$L(\lambda) = (2\pi)^{-1/2} \exp\left[-\left(\lambda + e^{-\lambda}\right)/2\right] \quad \text{with} \quad \lambda = \frac{\Delta E - \Delta E_{\mathrm{mp}}}{\kappa\rho x}$$

λ denotes the deviation from the most probable energy loss ΔE_{mp} normalized on the target density ρx and κ is given in (5.5b). ΔE_{mp} is calculated from the Bethe-Bloch equation (5.5) and amounts in this case to 21.9 MeV. The parameters p_i of the approximation of the Vavilov distribution are given in [130, 131]. The energy in electron equivalent units depositioned in a PiP scintillator bar depends linear on the pulse height, as already stated in (5.3). Having corrected the pulse height response of a scintillator for the muon pathlength caused by variation of angle of incidence, the pulse height could be compared with the muon Vavilov distribution, see Fig. 5.9 below). The comparison allows to extract the parameters of (5.3) per bar completing the PiP energy calibration.

A second method was used to check and refine the cosmic calibration by exploiting the kinematical overdetermination of the D(γ,np) and H(γ,nπ^+) reaction. In the first case the proton energy of each event is given by the neutron polar angle alone, which is very precisely measured and well-defined due to the segmentation of ToF. With it the energy deposited in PiP by the proton can be calculated having regard of the energy loss in the target, the air in between and dead layers like the wrapping of the scinitllators [57]. Comparing this result with the pulse heights yields again the parameters in (5.3). By use of the proton energy determined from neutron angle and from pulse height, a resolution of 4.5 MeV FWHM could be ascertained. If the calibration has to be optimized for pions, then the same method can be applied by use of the pion production off hydrogen.

5.4.2 Droop correction

The light attenuation along a straight line inside the scintillator is described by an exponential law, as stated above ((5.1) on on page 77), but if there are reflections at the scintillator boundary along its way a residual dependence of the intensity on the hit position occurs. The dependence on the hit position is complicated due to the additional influence of the ratio of direct light to reflected light. For larger cross section of the scintillator with respect to its length, this effect, which is named 'droop', is more pronounced. Therefore for ToF the effect is negligible and even for PiP it is small and successfully described by a polynomial of second order. This correction is rather important for PiP because it measures the energy of a particle based on the pulse height, in contrast to ToF where the energy is deduced by the flight time alone. So the linear dependence of the energy (5.3) has to be replaced by:

$$E_{ee} = \frac{\mathrm{pe}_0 + \mathrm{pe}_1 \cdot q_m}{c_0 + c_2(x_t - c_1)^2} \tag{5.12}$$

The parameters c_i were determined by plotting the pulse height from cosmic events versus the position and by obtaining the centroid of the Landau distribution for 64 discrete position regions, which are marked by the crosses in Fig. 5.9. A polynomial fit of second order

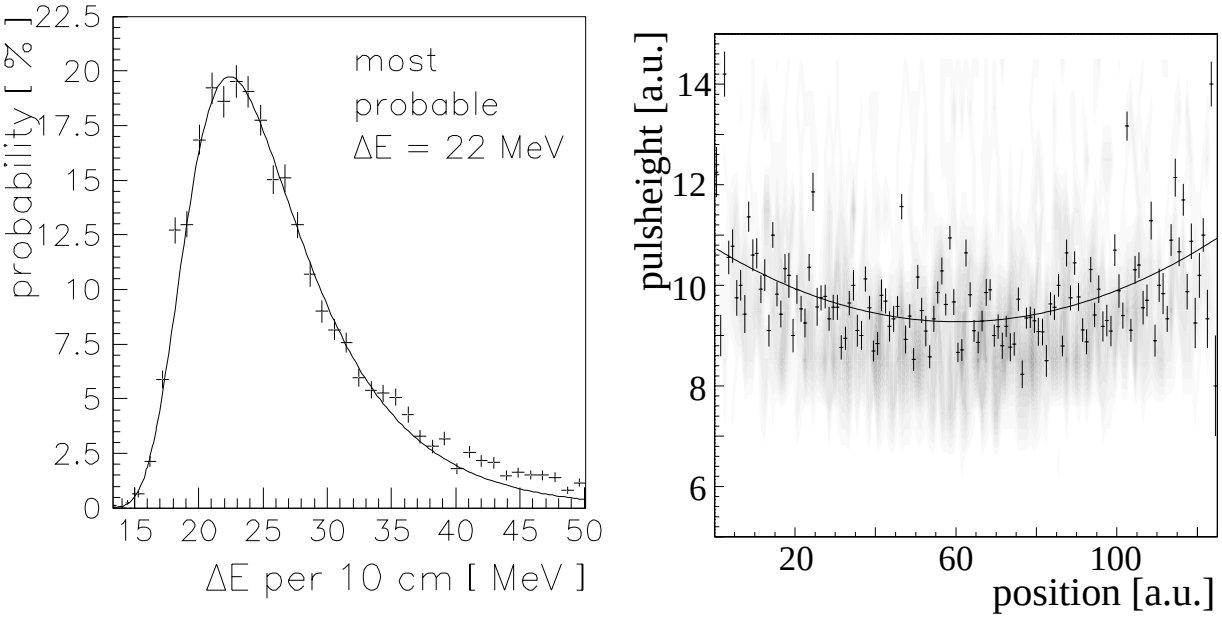

Figure 5.9: (left) Energy loss of muons in PiP after calibration and theoretical Vavilov distribution. (right) Fit of droop in PiP by use of the Vavilov maxima in pulseheight for 64 positions along the bar (denoted by the crosses).

of this one dimensional distribution of the centroids then yields the c_i. With this method, the energy calibration (pe_i) and droop correction can be performed in one step.

5.4.3 Particle identification

Protons or pions can be selected in a ΔE-E plot (Fig. 5.10 below), where they occupy two different ridges as a result of their distinct mass to charge ratio. However, it is difficult to separate exactly those particles because these regions are contaminated with particles which have suffered inelastic hadronic reactions, thus producing less scintillation light. This energy loss is energy dependent, making the identification and corrections for that effect complicated. Therefore, another technique is necessary, namely the range method which is described in the following and applied for protons and pions only. The particle energy is obtained from two approches: (i) The initial energy E_c is deduced from the energy deposited in the stopping layer by considering the energy losses along its path to the target (including all scintillators and dead layers like air and wrappings) as it were applying the reversed range method (Bethe-Bloch equation, see Section 5.1.4). (ii) The measured energy E_m is calculated from the sum of all energy depositions in the bars derived from their pulse

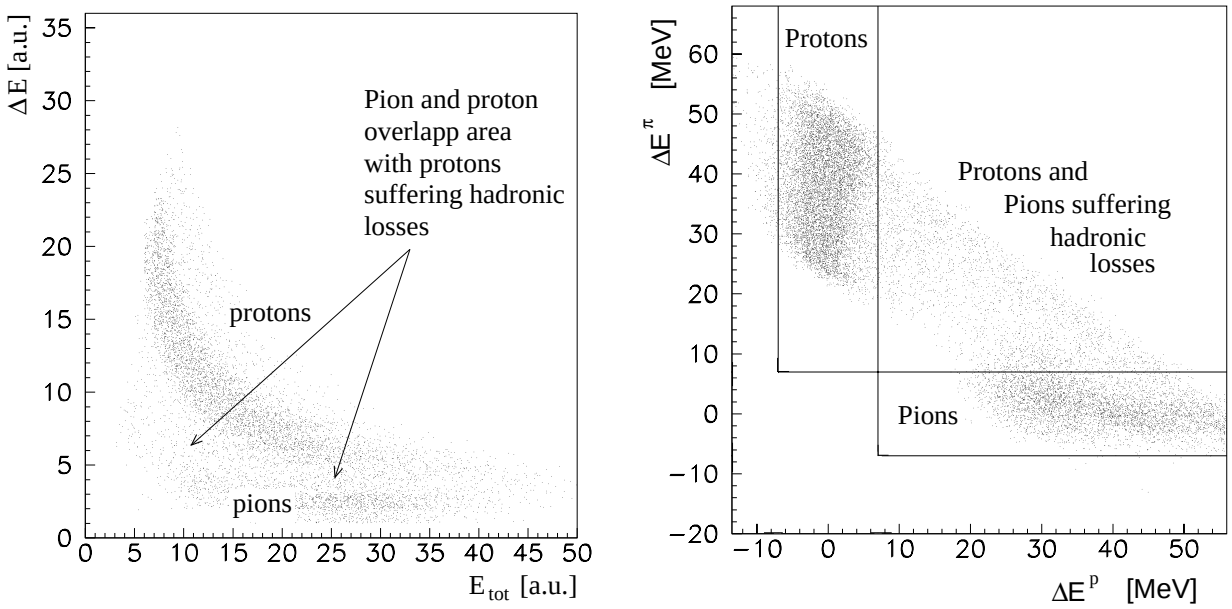

Figure 5.10: (left) Conventional method via ΔE-E cuts. (right) Range method.

height via (5.3) and the calculated energy losses in the dead layers. For both methods the particle type has to be known, which it is not at that stage. So the energy difference

$$\Delta E^{\text{part}} = E_c^{\text{part}} - E_m^{\text{part}} \qquad \text{part} = p, \pi \tag{5.13}$$

is calculated twice, viz. for the assumptions of particle type pion *and* proton. If the particle was a proton then $\Delta E^p \approx 0$ and ΔE^π is large and vice versa in case of a pion. If inelastic hadronic processes have taken place, both variables are large, hence these events are situated between the proton and pion ridge, see Fig. 5.10.

5.4.4 Detection efficiency

Protons are selected via the range method [57] being superior to the ΔE-E method. With it, the events which have undergone inelastic reactions in PiP, may be identified, which is necessary because the remaining yield must be scaled to account for the lost events. In order to quantify the reaction losses of protons λ_p and therewith the misinterpretation of the measured energy in PiP, a simulation using the package GEANT [131] was performed. The simulation matches very well the experimental two-dimensional spectra of the range method for the appropriate region of incident proton energy [23]. The events subject to the cut $|\Delta E^p| < 7$ MeV (see (5.13)) have to be rescaled by an energy dependent proton efficiency defined as: $\epsilon_{\text{PiP}} = 1 - \lambda_p$. This cut corresponds to the energy resolution of PiP and is not at random like a cut in the conventional ΔE-E spectrum would be.

5.5 ToF detector

5.5.1 Pulse height calibration

The energy determination from pulse height can be calibrated by two methods. Before the experiment some runs were recorded, where each ToF bar was exposed to an AmBe source with a well-defined energy deposition in the scintillators. A fit of the obtained pulse height spectra by a Gaussian with a smooth background contribution [132] yields the calibration parameters ph_i in (5.3). The second method is based on a plot of pulse height versus time of flight, the so-called sail spectrum. From the ToF scintillator properties it is possible to deduce that protons up to ≈ 78 MeV kinetic energy are stopped in the bar, whereas higher energetic protons punch through. Protons with this energy are situated at the sail top, where the ridge of the sail spectrum has a turning point, see Fig. 5.11 below. Due to different pathlengths in the scintillator both variables show variations and therefore only the very bottom of the sail top can be identified with the punch through energy of 78 MeV. After smoothing the sail spectra by a 100 point spline of 6th order in both variables to reduce the influence of statistical fluctuations, the lines of the inner edges are obtained from the points at half height of the maxima, see Fig. 5.11 below. With these lines a clear definition of the relative pulse height of a ToF bar is obtained and used to match all sail spectra by rescaling the pulse height via ph_i. The parameters from the AmBe and the punch through calibration agreed satisfactory [132], but the latter method has the advantage, that it could be used all along the experiment to correct for drifts or the like. A reliable pulse height calibration is needed for the neutron efficiency which depends strongly on it (Section 5.5.4), but is also used to check the time of flight energy calibration by comparing proton energies derived from flight time and pulse height.

5.5.2 Energy calibration

The proton energy can be deduced from its pulse height in ToF as described in the last section, but in case of neutrons this method fails. The neutron energy has to be identified by their velocity from flight time and path, see Fig. 5.12 on page 93. In order to obtained a well-defined time of flight it is crucial to precisely determine the offset between reaction time and the time of the hit in ToF (t_m, see Section 5.1.2) due to delays in cables and electronics. The introduction of a new variable, namely t_{path} (timeter), which is defined as flight time t_{tof} over flight path s_{path}, ceases to apply the variation due to different flight paths. In these spectra the so-called gamma peak, relativistic events like photons from π^0 production for example, should be situated at a well-defined position viz at $t^c_{\mathrm{path}} = 1/c$ with c being the speed of light. Having shifted this peak for all bars to t^c_{zero} allows to calculate the neutron energy from the flight time t_{tof}:

$$E_n = M_n \Big/ \sqrt{1 - (ct_{\mathrm{path}})^{-2}} \tag{5.14}$$

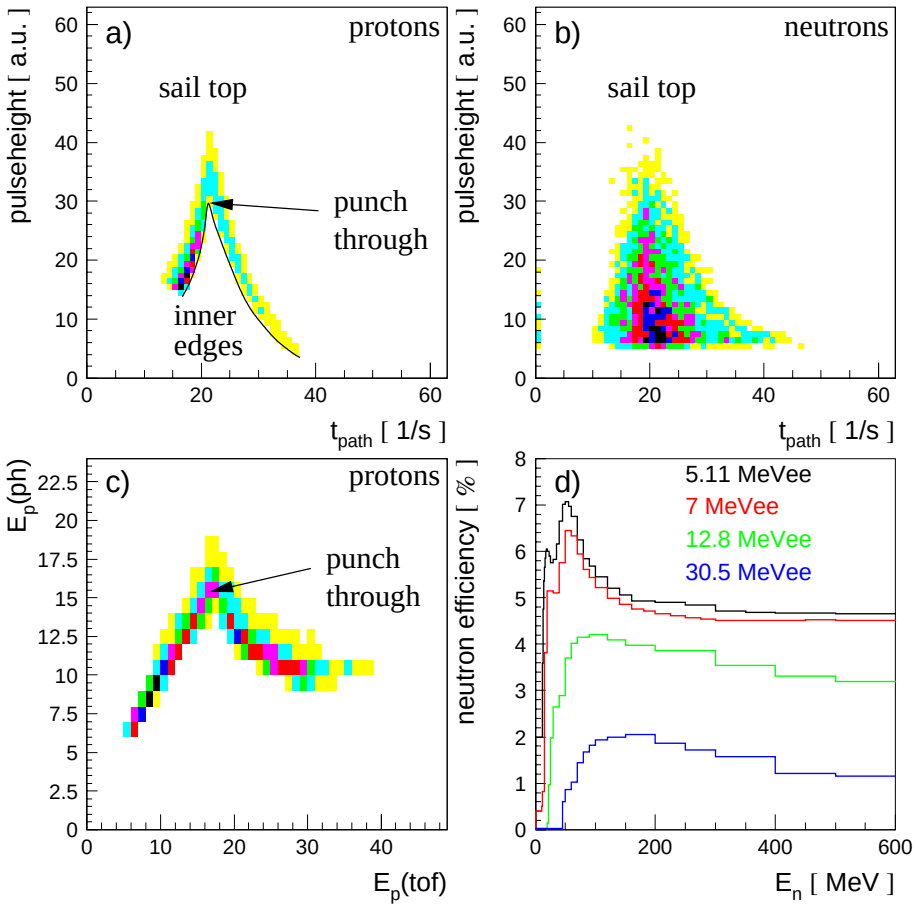

Figure 5.11: The ToF pulse height versus t_{path} is plotted in a) and b) for protons and neutrons seperately. Plot c) compares the proton energy $E_p(ph)$ obtained from the pulsheight and from the time of flight $E_p(tof)$. d) ToF pulsheight calibration and neutron detection probability (so-called neutron efficiency) ϵ_n as a function of neutron energy for different detection thresholds in electron equivalent energy (eVee).

5.5.3 Particle identification

Charged and uncharged particles in ToF can be identified by help of the SVD. The particle which is perceived in a ToF bar is identified as being charged, if the SVD element covering the respective ToF bar has fired. This discriminates protons, deuterons and pions from neutrons and photons. Fig. 5.12 below shows the flight time for particles identified as being uncharged. The sharp peak originates from photons produced in atomic scattering in the target or from pions which decay into photons along their way to ToF. The particles producing this peak travel with nearly the speed of light and therefore the position of this peak allows to determine the offsets of the flight time spectra and to perfectly align all ToF bars. After that procedure a minimum limit in this spectrum rejects all these photons and

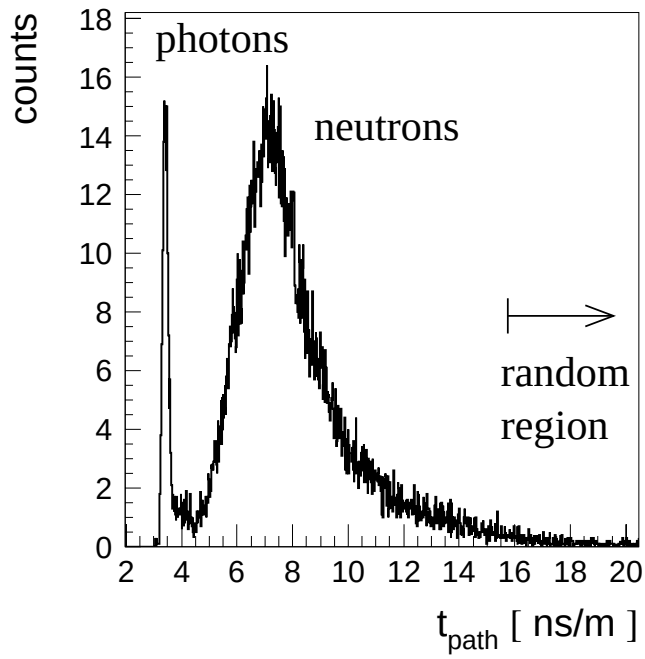

Figure 5.12: Typical time of flight spectrum for uncharged particles; here for 8 bars of stand E. t_{path} is the inverse velocity, hence flight time over flight path. The photon peak has a FWHM of ≈ 0.6 *ns.*

only neutrons are left.

ToF as proton detector

Charged particles, which are selected via the SVD, can be well distinguished in a plot of puls height versus flight time per meter. This is shown for protons, pions and deuterons in Fig. 5.13 below. The turning point typical for such spectra arises from the punch-through of the particles (for more details see Section 5.5.1). Faster particles deposit more energy in the scintillator until they have enough energy to pass through the whole scinitillater which henceforth only measures the energy loss. Heavier particles have a smaller velocity for the same energy, so the turning point occurs from short to long times in order of increasing particle mass. Below 4 ns/m pions and protons overlap and cannot be distinguished any more, therefore only protons with energies below 250 MeV are selected for the (γ,pp) analysis by a two-dimensional cut in this spectrum.

For the measurement of the proton momentum in ToF, the long flight path implicates a reduced resolution in energy and angle [23]. The impact of the flight path on the proton energy loss is the strongest effect and therefore considered subsequently. The energy of protons is measured by their flight times, just as for neutrons, which provides a better resolution than the pulse height in ToF. Due to the continuous energy loss along the flight path of a proton, its velocity is not constant as for neutrons but decreases monotonically. The measured flight time thus reflects a mean velocity v_m and energy E_m, but not the ones at the target v_T, E_T. The correction ΔE_A is deduced from the so-called time of path

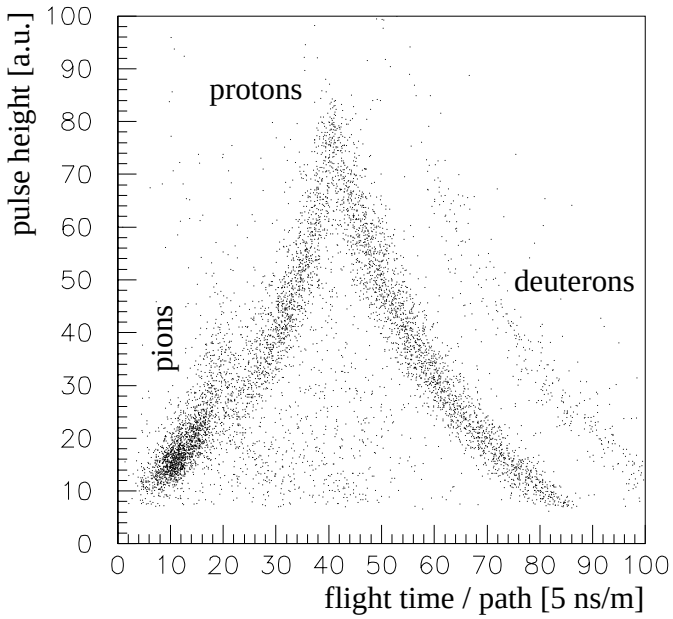

Figure 5.13: Charged particle identification via cuts in pulse height versus timeter (time of flight over flight path). The particles can be clearly discriminated; but fast protons overlap with pions.

integral

$$v_m T = \int_0^T dt\, v(t) \tag{5.15}$$

which makes use of the Bethe-Bloch equation to calculate $-dv/dx$ and with it $v(t)$. For this analysis, the energy loss and energy correction was not determined eventwise for the particular flight paths. A mean flight path of $\bar{s}_{\text{path}} = 7.6$ m was taken instead. This is justified by the small range of possible flight paths from 6 up to 8 m, and consequently by a small variation in energy loss of less then 0.5 MeV. From (5.15) a parametrization of the form $\Delta E_A = a/E_m + b$ can be deduced, with $a = 190.62$ and $b = 1.71$ for the mean flight path $\bar{s}_{\text{path}}$ given in this setup. All energy losses which are experienced by the proton along its path to ToF, are calculated [128] and corrected for each individual proton. Their

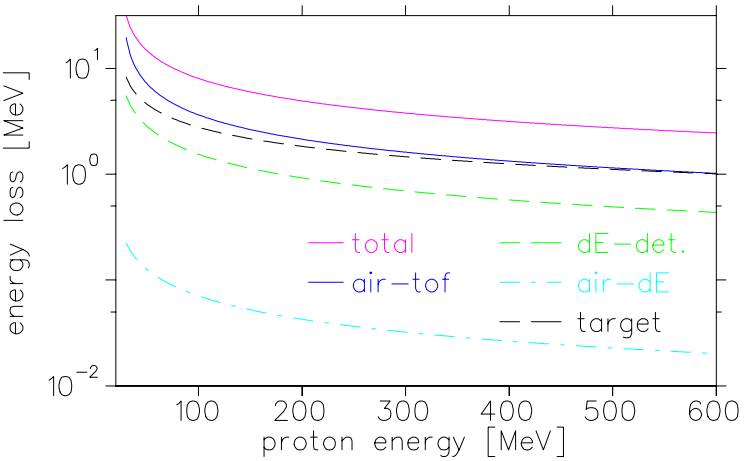

Figure 5.14: Energy losses of protons in the ToF-arm from the Bethe-Bloch equation [123]. The losses in the target and in the air to ToF are average values.

impact is shown in Fig. 5.14 above in dependence of its energy. The total proton energy loss between the target and ToF results in a relatively high energy threshold of about 30 MeV up to 40 MeV depending on the flight path. Therefore, only protons in ToF between 40 and 250 MeV were used further on for the (γ,pp) analysis.

5.5.4 Neutron efficiency and double layers

Neutron scattering reactions in ToF produce mainly free protons in the final state, which generate light in the scintillator. The STANTON [133] Monte Carlo code simulates the resulting light produced and predicts the neutron efficiency ϵ_n as a function of the pulse height threshold and the incident neutron energy. The pulse height threshold was set to 5.11 MeVee (10 MeV) as a compromise between a high detection efficiency and minimal background contribution resulting in an average detection probability of about 5% per ToF bar, see Fig. 5.11 on page 92. For detectors covering the same solid angle, the detection probability, thus the efficiencies, add to an effective efficiency for that total detector volume. In case of a multilayer ToF detector with the same efficiency ϵ_0 for each layer, the effective efficiency ϵ_{ToF} for m layers is given recursively:

$$\epsilon_{\mathsf{ToF}} = \begin{cases} \epsilon_m & \text{neutrons} \\ 1 & \text{protons} \end{cases} \tag{5.16a}$$

$$\epsilon_m = \epsilon_{m-1} + (1 - \epsilon_{m-1})\,\epsilon_{m-1} \tag{5.16b}$$

$$\epsilon_1 = \epsilon_0 / \sin\phi_n \tag{5.16c}$$

Each neutron hit in an arbitrary layer has to be accounted for by a weight of $1/\epsilon_{\mathsf{ToF}}$, which depends in addition on the neutron angle ϕ_n with respect to the scintillator normal vector.

If two hits (i, j) in neighbouring bars which are defined as follows fall within a time Δt and a position Δy window then the later hit is omitted (see Fig. 5.15 below).

$$\left(\vec{r}_i^{\,\mathrm{bar}} - \vec{r}_j^{\,\mathrm{bar}}\right)^2 < d_{\mathrm{bar}}^2 + d_{\mathrm{lay}}^2 \tag{5.17}$$

It is assumed that this succeeding hit originates from the proton of the first bar, which is knocked-out by a neutron. This is supported by that figure, because plot *d)* resembles the pulse height versus t^{path} spectrum of a proton (compare with Fig. 5.11 on page 92).

5.6 Thresholds and acceptance

For the comparison of theoretical predictions with the measured cross sections, the angle and energy acceptances of the detectors are needed. The cross sections given in this thesis are marked as visible cross sections σ^{vis}, which resembles the integral over the detector acceptance of the cross section differential in the proton and neutron variables and photon

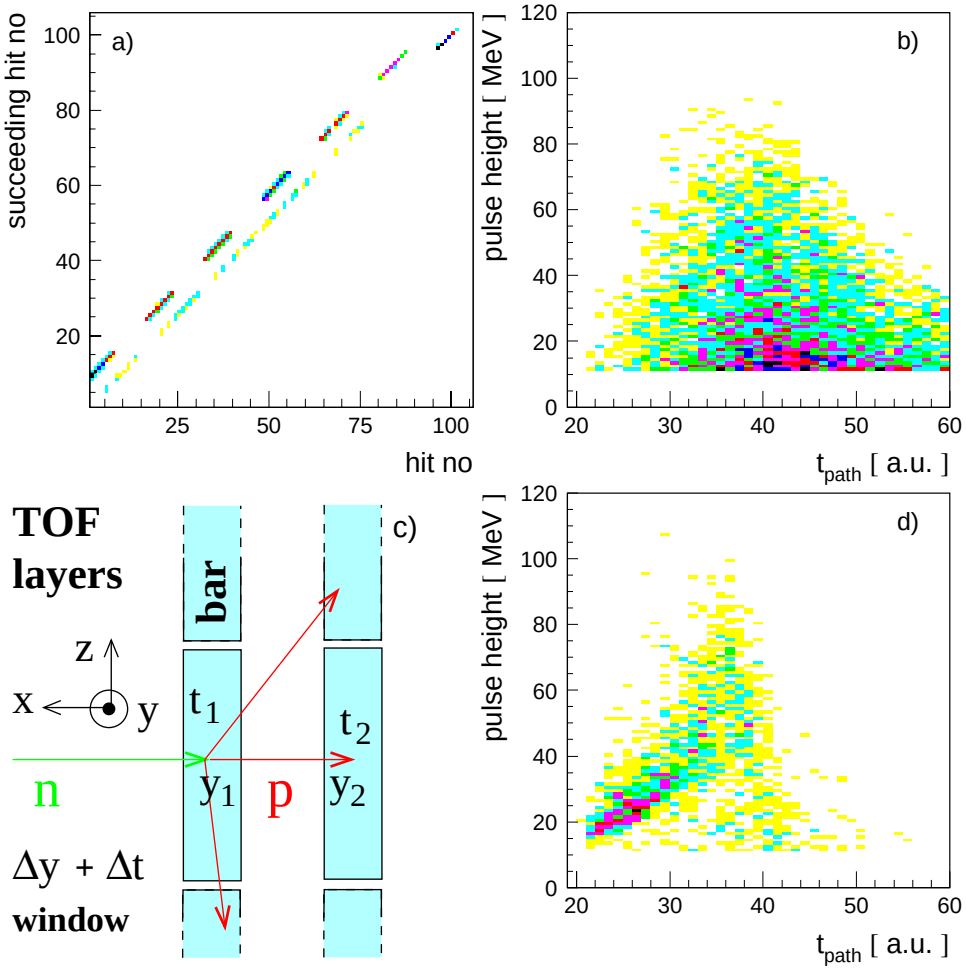

Figure 5.15: Plot a) shows succeeding hits versus the original one. Note that the hit number of the second layer is shifted by 8. In b) the pulsheight versus t_{path} is plotted for all hits and in d) for succeeding hits only. c) The sketch exemplifies possible succeeding hits in a ToF double layer array and its resulting effective efficiency ϵ_{ToF}.

energy. The angular acceptances are gathered in Tab. 5.3 and Tab. 5.4 and are illustrated in Fig. 5.16 below, whereas the energy acceptance is specified subsequently. The proton threshold for PiP due to energy losses (see Fig. 5.14 on page 94) and the detector threshold was set to 40 MeV. The proton threshold in the ToF arm was a little lower and amounted to 36 MeV, but was set in the offline analysis to 40 MeV, like for PiP. Due to the uncharged nature of the neutrons, they do not lose energy on their way to ToF, but there is still the detector threshold amounting to 10 MeV. For ease of comparison between (γ,pn) and (γ,pp) cross sections two thresholds were analysed: 10 MeV and 40 MeV like the protons in ToF or PiP. For both cases different neutron efficiencies (Fig. 5.11 on page 92) had to be used. In principle PiP can stop protons with an energy close to 350 MeV, but to restrict hadronic losses of protons in the detector and due to its construction an upper limit of

Table 5.3: Angular acceptance of PiP and the ToF stands. The angles are given in degrees. b/t denote the bottom/top edges and l/r the left/right ones, respectively.

	ϑ				φ			
Det.	bl	tl	br	tr	bl	tl	br	tr
A,B	12.36	15.52	22.02	23.88	233.67	117.87	207.45	144.16
C,D	26.31	27.82	37.90	38.88	202.63	149.90	196.26	157.93
E,F	44.61	45.38	56.63	57.16	194.10	160.76	192.09	163.42
G,H	63.30	64.00	79.85	80.11	195.13	159.40	194.01	160.87
I,J	89.26	89.29	107.12	106.62	194.61	160.08	195.44	158.99
K,L	128.89	127.10	148.46	144.88	202.57	149.98	215.43	135.31
M,N	21.16	23.66	14.90	18.34	326.71	42.40	309.59	59.25
PiP	126.34	126.34	53.53	53.53	337.32	22.68	337.32	22.68

Table 5.4: Solid angle acceptance of PiP and ToF.

Detector	PiP	ToF	A	C	E	G	I	K	M
Ω [sr]	1.03	1.06	.093	.092	.094	.178	.208	.301	.092
$\bar{\vartheta}$ [deg]	90	-	14.5	31.5	50.6	72	99.6	143.5	13.9

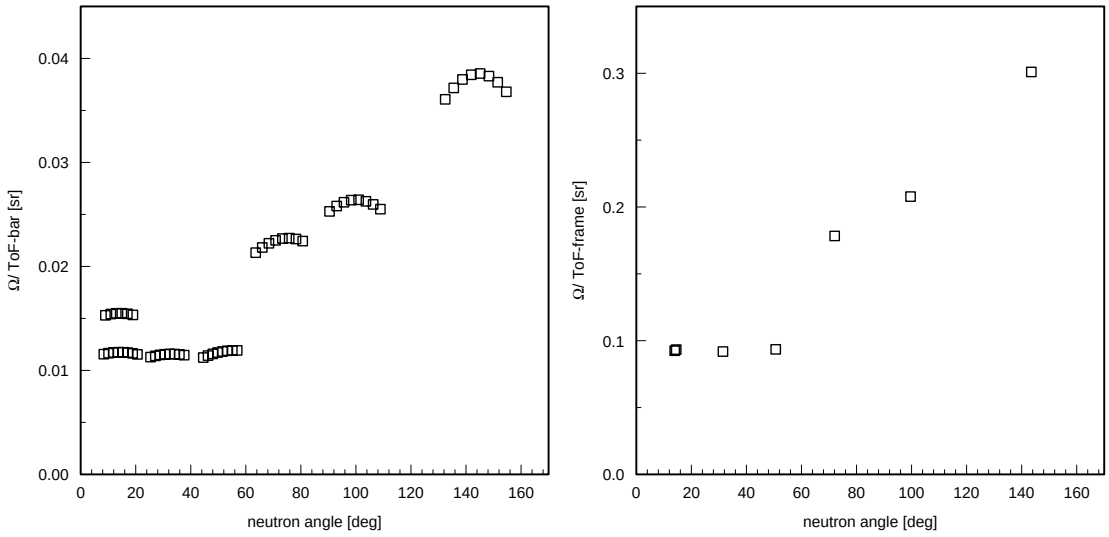

Figure 5.16: ToF solid angle acceptance for each bar (left) and per frame (right) versus the respective mean polar angle.

250 MeV had to be applied. In ToF the upper energy acceptance of protons was set to 250 MeV as well, because protons with higher energies cannot be distinguished from pions, see Section 5.5.3.

5.7 Background correction

If a proton in PiP causes a trigger, the events recorded during the readout gate originate not only from the ^{4}He(γ,NN) reaction, but there are also interfering background events. They have their source from cosmic rays, unwanted hadronic reactions and random hits which are not associated with the event which caused the trigger. These events form a flat continuous contribution in the TDC spectra because they are assumed to be uncorrelated in time with the reaction in consideration, as are the prompt events. The latter are analysed on an eventwise method, which is also applicable for the background events. By use of an appropriate negative weight for the randoms, they pass through the analysis in the same way as the prompts.

In case of the tagger randoms, the suitable weights solely have to account for the widths of the prompt and random regions, i.e.:

$$w_{\mathrm{reg}}^{\mathrm{tag}} = \begin{cases} +1 & \text{prompt} \\ -\frac{\Delta T_P}{\Delta T_1 + \Delta T_2 + \Delta T_3} & \text{random} \end{cases} \tag{5.18}$$

Here, ΔT_p is the width of the prompt region and ΔT_i are the respective widths of each of the three random regions, see also Fig. 5.12 on page 93. As the Tagger time has no influence on the reaction kinematics, these randoms are treated like the prompts to subtract the random contribution in the prompt region, as described above.

In case of neutron randoms in ToF, there are also regions in the time of flight spectrum which are solely due to randoms. These are the unphysical region left of the photon peak (with $\beta > 1$) and the region of very large flight times starting at a point where the number of counts does not exceed that of the random background. This time is well-defined and is given from the pulse height threshold of ToF via (5.14). Here indeed the method used for the Tagger randoms has to be altered such that the randoms are reproduced in the prompt time region. The time of flight corresponds directly to the neutron energy and consequently to the reaction kinematics. Therefore this observable cannot be used for both, the determination of the energy of neutrons being correlated with the hadronic reaction and the neutron random subtraction. This alternative method proceeds as follows: The time of flight t_R of a random event which is defined by $t_R \in [l_R, h_R]$ is mapped n times onto the prompt region $[l_P, h_P]$. Thereby for each random event about $n = \mathrm{integer}(\Delta T_p / \Delta T_R) + 1$ pseudo subevents are created, which are then analysed as a real event utilizing a negative

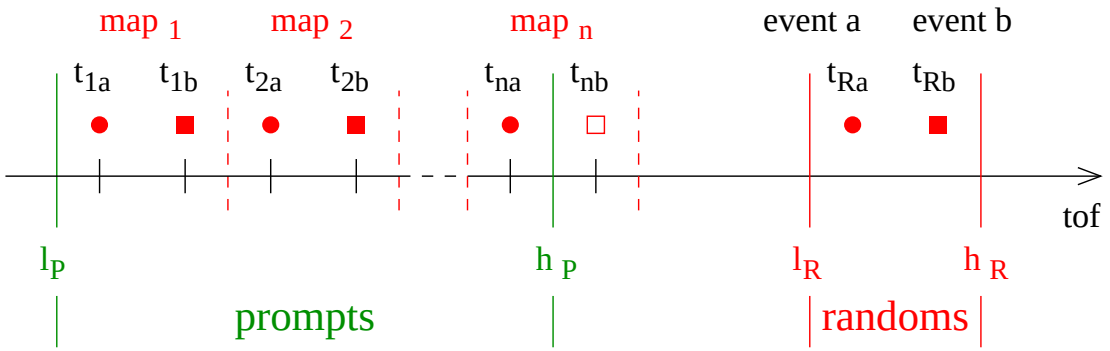

Figure 5.17: ToF background subtractin scheme: The random region is mapped n times onto the prompt one, thereby creating m subevents. In this example $m_a = n$ and $m_b = n-1$ subevents are created for event a and b respectively.

weight $w_{\text{reg}}^{\text{ToF}}$. Hence, the weights and flight times t_i of these subevents are given by:

$$t_i = (t_R - l_R)\cdot i + l_P \qquad i = 1 \ldots m \tag{5.19}$$

$$w_{\text{reg}}^{\text{ToF}} = \begin{cases} -\frac{1}{m} & \text{random} \\ +1 & \text{prompt} \end{cases} \tag{5.20}$$

Here, m denotes the actual number of subevents which is sometimes smaller then n, depending on whether or not the last mapping of the flight time t_n exceeds the prompt region and is thus determined by t_R as: $m = \text{integer}(\Delta T_p + l_R - t_R)/\Delta T_R$ (Fig. 5.17). For charged particles, in particular protons, the random subtraction was performed in the same way, although the random contribution in this case was only about 1-2%. That is due to the following reasons: a much higher proton detection efficiency compared to that for neutrons, the requirement of a hit in the SVD and intrinsic lower rates.

Chapter 6

Results

6.1 Evaluation of the cross sections and asymmetries

The data acquired in this ^{4}He experiment are presented simply as the cross section seen by PiP and ToF which is referred to as visible cross section (σ^{vis}) defined in (6.1). An extrapolation into regions of phase space not covered by the detectors would be desirable in order to obtain the total cross section and to facilitate comparisons with data from other experiments or theoretical predictions. This, however, introduces extra uncertainties due to the dependence on the model employed. On the other hand, a direct comparison of theoretical calculations and data can be made by including the detector thresholds and acceptances of this setup in the calculation (if the model is able to do so).

The unpolarized measured cross section is differential in photon energy and the two nucleon momenta $\vec{X} = (E_\gamma, \vec{p}_1, \vec{p}_2)$. The cross sections shown in this chapter are reduced to single differential and depend in general on one observable X_i or on a function $f(\vec{X})$ like missing energy E_m; both are further denoted as X. They are defined by an integration over the other observables $\vec{X}_{\bar{\imath}} = (X_1 \dots X_{i-1}, X_{i+1} \dots X_7)$, and hence are empirically obtained by a summation over all events or a subset which is subject to appropriate cuts. This single differential cross section is denoted as σ^{vis}:

$$\sigma^{\text{vis}}(X_i) = \frac{d\sigma^{\mathcal{DA}}}{dX_i} = \int_{\mathcal{DA}} d^6 X_{\bar{\imath}} \, \frac{d^7\sigma}{dE_\gamma d^3p_1 d^3p_2}(\vec{X}) \tag{6.1}$$

The boundaries are defined by the detector acceptances and thresholds ($\mathcal{DA}$) and are listed in Tab. 5.3 on page 97 and Tab. 5.4. All observables in this chapter are plotted in units of MeV corresponding to $c = 1$.

The photon can be described by two independent polarization states $\epsilon_\perp$ and $\epsilon_\parallel$ with respect to an arbitrary reference plane, as explained in detail in Chapter 3. Therefore, the (γ,X) cross section divides into two contributions, $\sigma_\perp$ and $\sigma_\parallel$, according to the two

polarization states. The total cross section σ and the asymmetry Σ for a totally polarized photon beam are thus given from these contributions as:

$$\sigma = \sigma_\perp + \sigma_\parallel \qquad\qquad \Sigma = \frac{\sigma_\perp - \sigma_\parallel}{\sigma_\perp + \sigma_\parallel} \tag{6.2}$$

In general the response of a nucleus to a (virtual) photon is expressed in longitudinal and transverse[1] structure functions W. In case of polarized real photons only the transverse W_T and transverse-transverse W_{TT} structure functions contribute. Apart from kinematical factors, the former is proportional to the total cross section, whereas the latter is related to the asymmetry: $\Sigma = -W_{TT}/W_T$. The strength of photo-induced 2N emission depends, as mentioned above, on the azimuthal angles of the two outgoing nucleons ϕ_1 and ϕ_2 respectively. If this dependence is rewritten in terms of ϕ_m and ϕ_d, the mean and difference azimuthal angles, which read in the laboratory frame as follows, the common factor $\cos 2\phi_m$ can be pulled out of the asymmetry [42, 98].

$$\phi_d = \phi_1 - \phi_2 \tag{6.3a}$$

$$\phi_m = \frac{\phi_1 + \phi_2}{2} - \begin{cases} \text{para.} & \pi/2 \\ \text{perp.} & 0 \end{cases} \tag{6.3b}$$

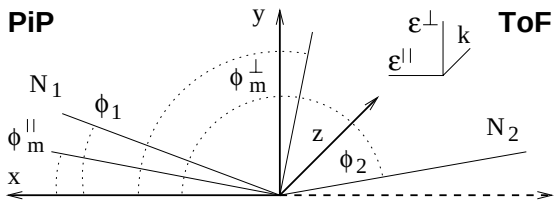

The experimental setup was such that the azimuthal angle covered by PiP and ToF only amounts to $\sim \pm 20°$. Yet, the two crystal settings produce photons polarized mainly in the detector plane respectively perpendicular to it, which thus are the two reference planes for the definition of the photon polarizations. These two orientations are accounted for by the two azimuthal mean angles $\phi_m^{\parallel}$ and $\phi_m^{\perp}$. Regarding the photon polarization, the cross section may be casted into the following form, where ϕ_m defines the reaction plane and suits as a reference for the photon polarization:

$$d^7\sigma_{\phi_m}(\vec{X}) = d^7\sigma_0(\vec{X})\big(1 + P(E_\gamma)\Sigma_7(\vec{X})\cos 2\phi_m\big) \tag{6.4}$$

Due to reasons of symmetry, Σ is now a function of $p_1, \theta_1, p_2, \theta_2$ and ϕ_d only, and does not depend on ϕ_m. Based on (6.4) the (visible) single-differential asymmetry is defined in analogy to (6.1) as follows:

$$\Sigma(X_i) = \int_{\mathcal{DA}} d^6X_{\bar{\imath}}\, \frac{d^7\sigma_{\phi_m}\,(P(E_\gamma)\cos 2\phi_m)^{-1}}{dE_\gamma d^3p_1 d^3p_2} \Bigg/ \int_{\mathcal{DA}} d^6X_{\bar{\imath}}\, \frac{d^7\sigma_0}{dE_\gamma d^3p_1 d^3p_2} \tag{6.5}$$

Starting from this expression, the eventwise evaluation of the cross sections and asymmetries was performed via summation — in place of the above integrals — of appropriate weights per event. The resulting expressions are derived from (6.4) and (6.5). They take

[1] with respect to the photon momentum (and polarization for W_{TT})

into account the two diamond settings described by (6.3b), hence $\sigma^{\parallel}_{\phi_m}$ and $\sigma^{\perp}_{\phi_m}$:

$$\sigma^{\mathrm{vis}}_{\alpha}(X) = \frac{1}{n_t} \sum_{\mathrm{events}} \frac{w_{\mathrm{BG}} w_{\alpha}}{\epsilon_p \epsilon_{\mathrm{ToF}} \epsilon_{\gamma}}(\vec{X}) \cdot 10^{30} \mu\mathrm{b/MeV} \tag{6.6a}$$

$$\Sigma^{\mathrm{vis}}_{\alpha}(X) = \sigma^{\mathrm{vis}}_{\alpha}(X) \big/ \sigma^{\mathrm{vis}}_{0}(X) \qquad \alpha \in [\phi_m, +, -] \tag{6.6b}$$

The label α (see Tab. 6.1) marks the utilized weight for obtaining the unpolarized cross section σ^{vis}_0 and the asymmetry Σ^{vis}. The detector efficiencies ϵ, photon flux N_γ and background subtraction w_{BG} are defined and discussed in detail in Chapter 5. The target density n_t denotes the number of target atoms per area in [cm^2] and explains thus the factor 10^{30} in (6.6b).

Table 6.1: Definitions of weights to obtain the unpolarized and polarized cross sections and therewith the asymmetry for an eventwise analysis. The period labels refer to the condition restricting the photon energy region which are given in Tab. 6.2 on page 105.

weight $w^{-1}_{\alpha}(E)$	α	analysis label	condition	period label
$N_\gamma(E)$		unpol	none, all events	D220...D350
$\pm N_\gamma(E)$	$\pm$	para,perp	para/perp polarization	"
$N_\gamma(E)P(E)\cos 2\phi_m$	ϕ_m	pol	for $P_\gamma > P_{\mathrm{min}}$	P220...P350
$N_\gamma(E)$	0	unpol	for $P_\gamma > P_{\mathrm{min}}$	"

The polarized cross sections $\sigma_{\pm}$ were used for reasons of consistency checks: Instead of an eventwise calculation of ϕ_m, the asymmetry can also be analysed in terms of $\sigma_{\pm}$ averaged over the azimuthal angle. In that case the ratio of both asymmetries should reflect the azimuthal detector acceptance ($\mathcal{DA}$) via:

$$r_\phi = \int_{\mathcal{DA}} \frac{d\phi}{\cos(2\phi)} \Big/ \int_{\mathcal{DA}} d\phi \approx 1.06 \tag{6.7}$$

This ratio is plotted in Fig. 6.1 below from the data using both methods and yields $r_\phi = 1.06$ and 1.07 for the low respectively high energy range which complies with the theoretical value. Nevertheless, the exact method stated in (6.6b) was used further on, because r_ϕ depends on the polar ToF angle. The number of r_ϕ stated in (6.7) is the average value.

To reduce the statistical uncertainty, thereby enhancing the quality of the data and enabling more explicit interpretations, the measured yield has to be binned appropriately. Depending on the statistical error three methods were applied: They are further referred to as arithmetical mean (mean-a), error-weighted mean (mean-e, mean-0) and mean asymmetry (mean-A). Taking the average of N data-points x_i with errors δx_i into one bin is

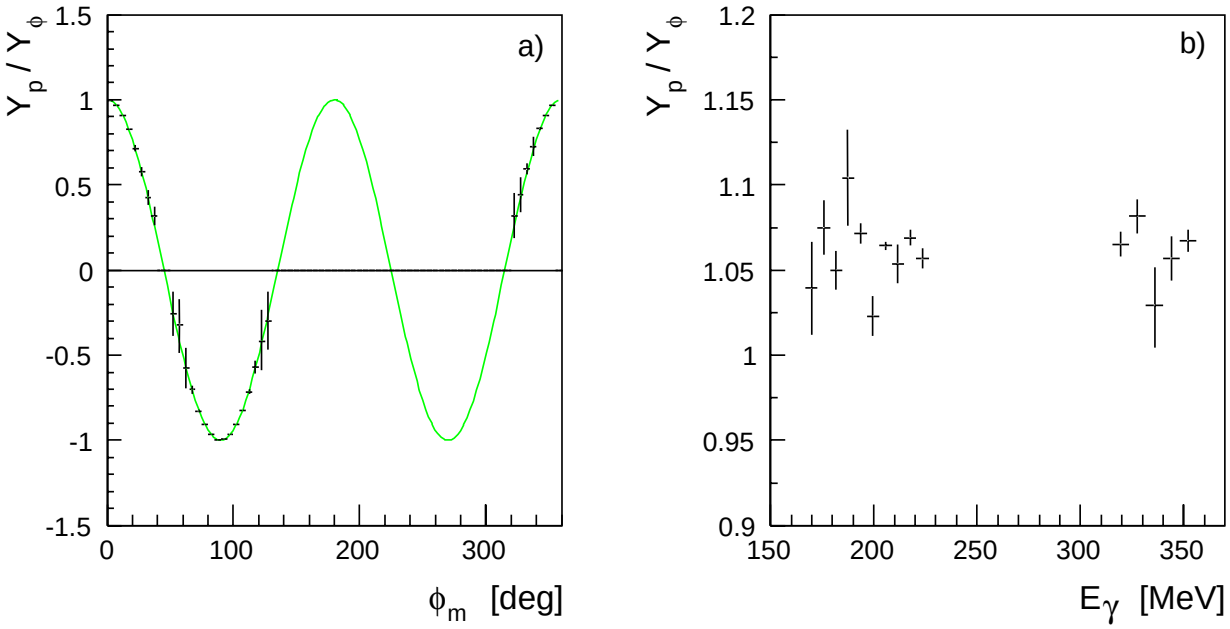

Figure 6.1: Ratios of two distinct methods of evaluating the asymmetry (see text). (left) The dependence of the cross section on $\cos 2\phi_m$ *is revealed by this ratio according to* (6.5) *or* (6.4)*. (right) The ratio is plotted versus the photon energy and exhibits, as expected, no significant energy dependence.*

defined as follows:

$$\text{mean-a:} \qquad \langle x\rangle_a = N^{-1}\sum x_i \qquad \delta x_a = N^{-1}\sqrt{\sum \delta x_i^2} \tag{6.8a}$$

$$\text{mean-e:} \qquad \langle x\rangle_e = \left.\frac{\sum x_i/\delta x_i}{\sum 1/\delta x_i}\right|_{x_i\neq 0} \qquad \delta x_e = \sqrt{N}\left(\sum 1/\delta x_i\right)^{-1}\Big|_{x_i\neq 0} \tag{6.8b}$$

$$\text{mean-0:} \qquad \langle x\rangle_0 = \frac{\sum x_i(\bar\delta + \delta x_i)^{-1}}{\sum(\bar\delta + \delta x_i)^{-1}} \qquad \bar\delta = N^{-1}\sum \delta x_i\Big|_{x_i\neq 0} \tag{6.8c}$$

$$\text{mean-A:} \qquad \langle \Sigma\rangle_A = N^{-1}\sum \frac{\sigma_\perp^i - \sigma_\parallel^i}{\sigma_\perp^i + \sigma_\parallel^i} \qquad \langle \Sigma\rangle_a = \frac{\sum \sigma_\perp^i - \sigma_\parallel^i}{\sum \sigma_\perp^i + \sigma_\parallel^i} \tag{6.8d}$$

Generally the arithmetical mean (6.8a) should be employed, but for poor statistics, the error-weighted mean (6.8b) is preferred. In general the latter yields a different result which is closer to the arithmetical mean the less the values x_i vary. However, it has the advantage that the resulting error δx_e is significantly smaller, still providing reliable values even in case of poor statistics. This method relies on the definition of χ^2 which also weights the data with the inverse error. Zero values, which may occur if an observable tends to zero and the statistics are insufficient, cannot be considered in this procedure. In contrast to the arithmetical mean, these values would not enter the average $\langle x\rangle_e$ owing to their vanishing weight $1/\delta x \to 0$, which leads to an overestimation of the average value $\langle x\rangle_e$. Therefore a slightly altered technique, labeled by mean-0, was employed in this instance.

Therewith both is ensured by this procedure: the use of the error-weighted method and the consideration of zero values. In some rare cases, especially for spectra of pion production and $3B^2$ emission, the asymmetry shows a very poor statistic necessitating the application of an alternative average. If so, the asymmetry values were binned via the mean asymmetry method (mean-A in (6.8d)) instead of the arithmetical one $\langle\Sigma\rangle_a$. Compared to the latter this method results in principle in an incorrect asymmetry value. However, $\langle\Sigma\rangle_A$ is still a measure of the asymmetry $\langle\Sigma\rangle_a$, but has a strongly reduced error and facilitates therewith the interpretation of the data.

In the following spectra, the plots of single periods show the data for all recorded photon energies and are denoted by D220, D280 and D350 respectively (for the meaning of these labels see also Chapter 3). When these periods were averaged to obtain a combined spectrum, only data with photon energy above 200 MeV were taken, because for the D280 and D350 periods a lower limit of 200 MeV was set in the experiment. If the data shown in a spectrum were restricted to the energy range with significant photon polarization, i.e. where $P_\gamma > P_{\min}$, then it was labeled by P220, P280 and P350 as defined in Tab. 6.2. In some of the following spectra it occurred that data points were very close or on top of each other. In these cases they were shifted along the abscissa by a tiny amount to avoid overlapping of the error bars.

Table 6.2: Energy regions of the three periods with significant photon polarization determined by a minimal polarization P_{min}.

label	E_γ range	label	E_γ range for $P > P_{\min}$	$P_{\min}$
D220	110...600	P220	139.6...237.3 and 311.8...357.3	0.2
D280	199...600	P280	199...290.2 and 376.4...419	0.15
D350	199...600	P350	235...364.5 and 460.8...504	0.1

6.1.1 Missing energy and energy resolution

The so-called missing energy E_{2m}, which is defined by the energy of the two outgoing nucleons and the recoiling system T_{rec}, is a measure of the excitation energy E_x of the residual system (4.5a). In Section B.1 the missing energy is derived from a relativistical ansatz leading to the following expression defined in the laboratory system:

$$E_{2m} = E_\gamma - T_n - T_p - T_{\text{rec}} = E_x + Q$$

In the spectator model, the missing momentum $\vec{p}_{2m} = \vec{q} - \vec{p}_p - \vec{p}_n$ can be identified with the momentum of the recoiling system which allows the calculation of T_{rec}. The two nucleon

[2] three body or three nucleons (3N)

separation energy is denoted by Q and amounts in ^{4}He to

$$Q_{pn} = M_{\mathrm{He}} - M_D - M_p - M_n = 26.1\ \mathrm{MeV} \tag{6.9a}$$
$$Q_{pp} = M_{\mathrm{He}} - 2M_n - 2M_p = 28.3\ \mathrm{MeV} \tag{6.9b}$$

In case of pp emission, there is no bound residual system, therefore the Q values for these two channels differ sligthly, i.e. about the amount of the deuteron binding energy. For helium, in contrast to heavy nuclei, the excitation energy reflects the relative kinetic energy of the two residual nucleons; higher E_x, i.e. above 140 MeV (see Fig. 6.2), mostly indicate the production of a pion. The strength of the two-nucleon-emission process with a residual

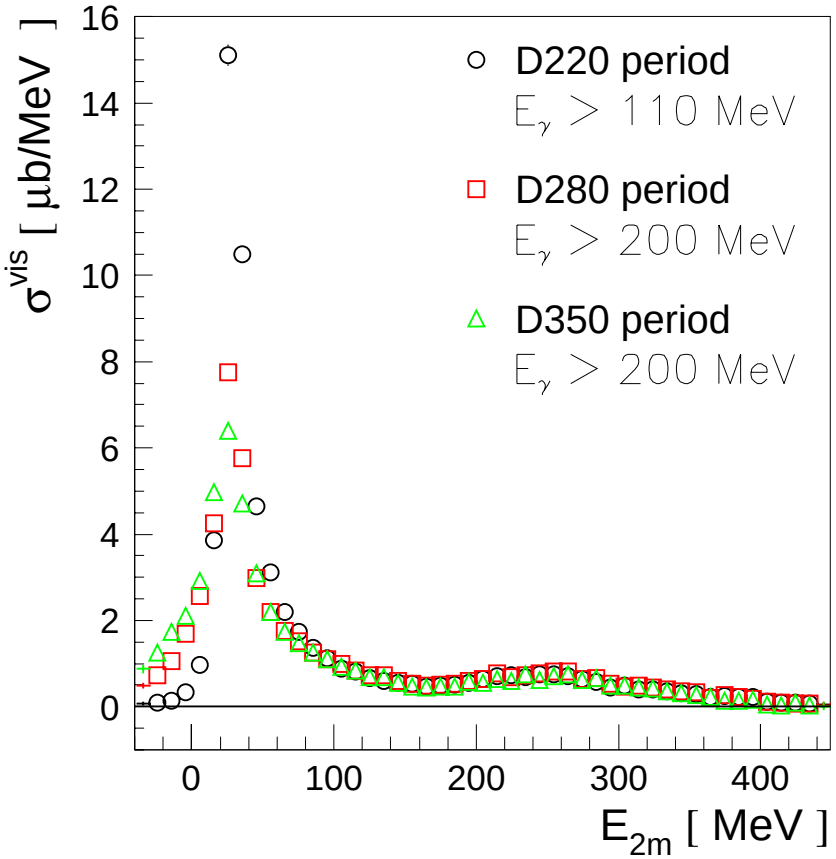

Figure 6.2: Missing energy (pn))for the three settings of the crystal angles, which are denoted by D220, D280, D350. The peak at low E_{2m} stems from G2N emission (see text) and exhibits the lower energy resolution at higher photon energies. Pion production is located around $E_{2m} = 200 \ldots 300$ MeV because extra energy of at least $m_\pi \sim 140$ MeV is needed.

deuteron, hence ^{4}He(γ,pn)D, resides at $E_{2m} = Q_{pn}$ with vanishing natural width. Assuming there are only events with a deuteron in the final state, the measured width would be due to the limited detector resolution only and would have a Gaussian-like distribution around Q. Yet, most of the events result in a four-body final state [134], which yield strength above the Q value due to the relative kinetic energy of the two unobserved nucleons and thus they lead to an asymmetrical E_{2m} distribution (this kinetic energy implies $E_{2m} \gtrsim Q$ based on (4.5c)). Therefore the measured width reflects the folding of this distribution with the detector-resolution function. Additionally, at intermediate missing energy, i.e. $Q \lesssim E_{2m} \lesssim Q + m_\pi$, photon energy is transferred to the residual two nucleons via FSI

or 3B absorption. Hence only the left slope of the two-nucleon-emission peak was used to determine the peak width employing a Gauss fit, which is shown in Fig. 6.3 for the pn final state. The E_{2m} peak widths of six different photon energy regions allow the derivation of

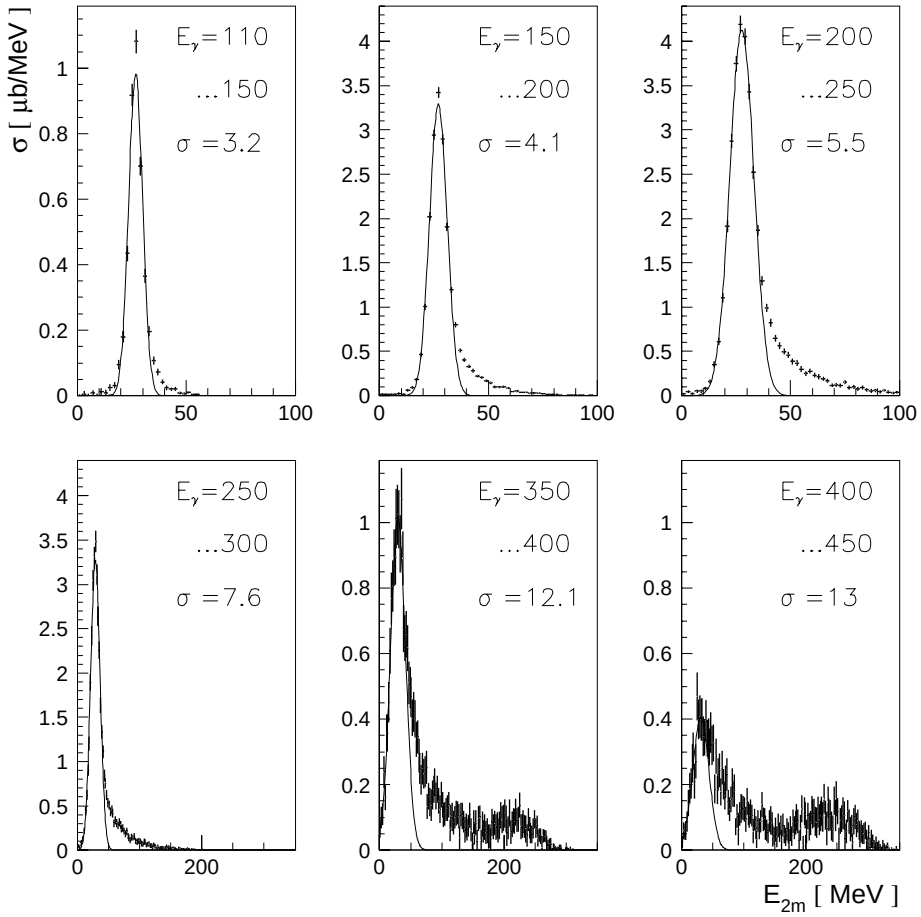

Figure 6.3: Missing energy of the D220 data for six photon energy windows. The Gauss fits to the left slope of the break-up peak indicate the decrease in energy resolution with increasing photon energy. At low photon energies the cross section is just due to G2N absorption, whereas at intermediate energies additional contributions from FSI and 3B arise. At high photon energies pion production starts to contribute. Alle units are MeV.

an energy-dependent overall detector resolution[4]. The evaluation of the peak widths gave an experimental detector resolution of $\sigma_{E_m} = E_\gamma/28 - 2$ MeV. This resolution is not as good as the one in the PiP-ToF experiments on carbon. That is due to the larger energy straggling in the liquid He target, air and scintillators and the shorter neutron flight time with higher photon and thus neutron and proton energies.

The comparison of the carbon and helium missing energy spectra reveals one common and one distinct feature: The dominant peak at $E_{2m} = Q$ arises from G2N absorption (see Feynman graphs of these processes in Fig. 1.2 on page 6) which is supported by the model from R. Carrasco and E. Oset [32–34] and indicated by the hatched areas in Fig. 6.4 below. At higher missing energy, namely around 150-350 MeV, the major contribution stems from the production of real pions leaving the nucleus. The strength located in between

[4]More details about the angular and energy resolution of the PiP and ToF detectors can be found in Chapter 5 and [23, 57].

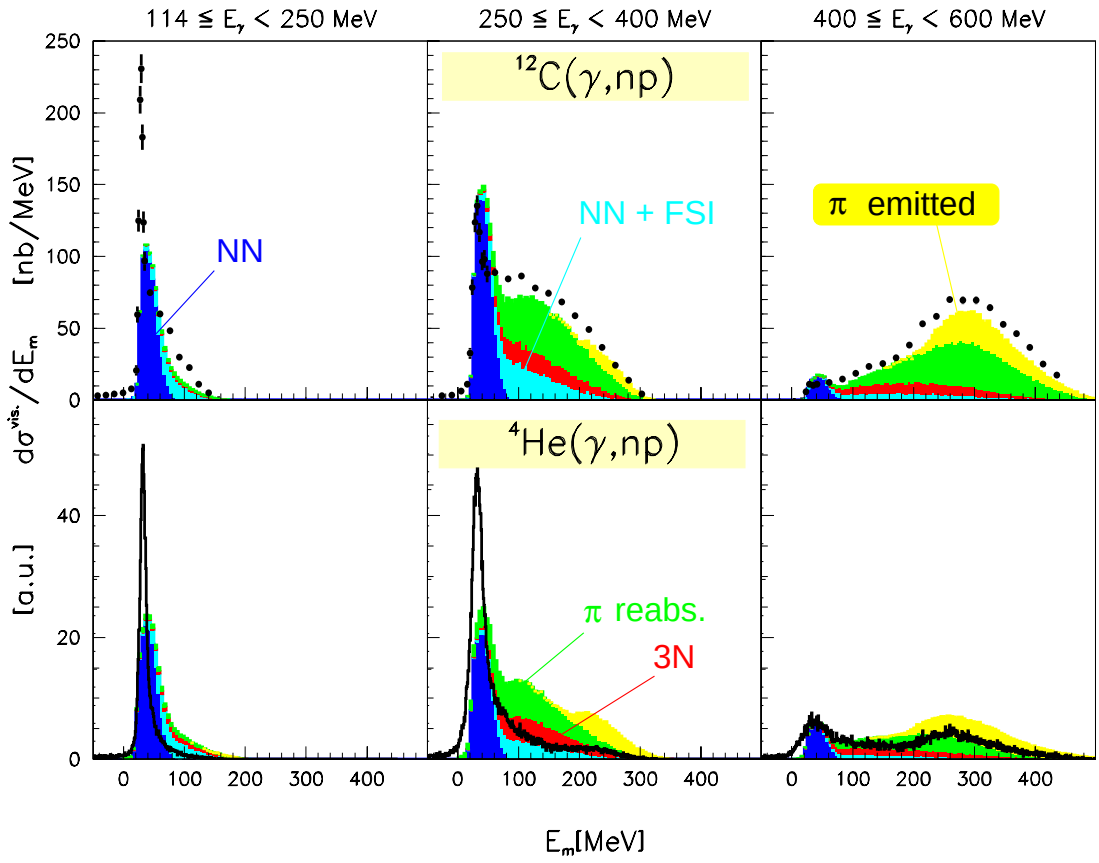

Figure 6.4: Comparison of missing energy spectra for carbon and helium at three successive energy bins. The Monte Carlo model from Carrasco and Oset predicts the various contributions to E_{2m} [134] which are marked in the figure by shaded areas and the legends.

originates from FSI, 3B absorption and pions produced in the photo-absorption process and then reabsorbed while travelling through the nucleus. While the Oset model describes the carbon data fairly well (see discussion in [23, 57]), it fails for ^{4}He but is still providing a qualitative picture. The reason may emanate from the treatment of nuclear structure as a Fermi gas, which is a good approximation for heavy nuclei only, and from the semi-classical, incoherent Monte-Carlo description of pion propagation through the nucleus. The difference between the measurements of both targets is found in the ratio of G2N absorption to pion production strength. The latter overtops for $E_\gamma > 400$ MeV in the case of carbon, while for ^{4}He the G2N absorption remains always the dominant feature.

6.1.2 Genuine two nucleon absorption

From all 2N emission processes only the G2N absorption has the potential to get clear signals from SRC. Former investigations [23, 57] demonstrated that yield from this process can

be significantly enhanced by a cut in missing energy around the Q value. Other processes like successive FSI or pion production lead to higher E_{2m} values. Respecting the energy resolution of the detectors, the cut C_{G2N} : $E_{2m} \in [11, 45]$ MeV should be appropriate. To support this notion, the excitation functions for seven small E_{2m} regions, indicated in Fig. 6.5 by $l_1 \ldots l_3, r, u_1 \ldots u_3$, were compared to the reference spectrum subject to the cut C_r. The region r of this cut tightly encloses the break-up energy Q. The other cut regions

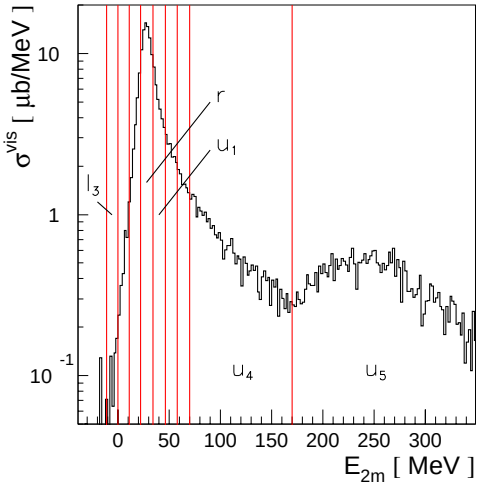

Figure 6.5: Missing energy spectrum plotted on logarithmic scale with E_{2m} regions used as cuts for the excitation function. r denotes the cut tightly enclosing the break-up peak which defines the reference spectrum.

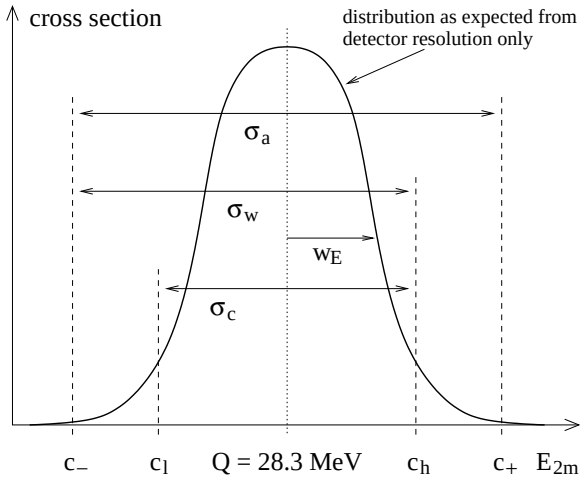

Figure 6.6: Illustration of the determination of the E_{2m} cut correction factor f_{ECC}. All events originating from the break-up peak are denoted by a where $c_\pm$ is set to $3w_E$. However, only the counts in region c are taken and corrected by the counts in w.

$l_3 \ldots l_1$ have the same width than r (12 MeV) and they are situated below Q whereas $u_1 \ldots u_3$ are symmetrically placed above Q. The excitation functions $\sigma_{E_\gamma}(l_3) \ldots \sigma_{E_\gamma}(u_1)$, hence for $E_\gamma < 45$ MeV, agree qualitatively in their shapes, whereas above 45 MeV corresponding to $\sigma_{E_\gamma}(u_2)$ and $\sigma_{E_\gamma}(u_3)$ significant different features could be observed. Therefore the cut C_{G2N} is considered as being appropriate and applied further on to enhance the genuine two nucleon absorption process and eliminate FSI and 3B absorption as much as possible.

The three different periods D220, D280, D350 have photons with significant polarization at different energy regions, see Fig. 3.12 on page 43 and Tab. A.5 on page A13. In order to obtain asymmetries of functions $f(\vec{X})$ of measured observables $\vec{X}$, like E_{2m} or the missing momentum p_{2m}, it is necessary to combine these data sets to cover as much as possible of the photon energy ranges with significantly polarized photons enhancing the overall polarization. The regions of dominant photon flux of these periods reside at diverse energies implying a different overall energy resolution. This induces varying G2N peak widths, which is demonstrated in Fig. 6.2 on page 106. Using the same cut C_{G2N} for all three periods would

yield various consequences; for example the G2N absorption cross sections would not agree with each other. One solution would be the application of cuts according to the respective energy resolution. However, an alternative method was employed: The assumption that the missing energy strength originating from G2N absorption has a Gaussian distribution (around $E_{2m} = Q$ with standard deviation w_E) caused by the limited detector resolution enables the estimation of lost strength due to the cut. The application of the same E_{2m} cut and an appropriate cut correction factor f_{ECC} per period facilitates the comparison of the three periods. Compared to the use of adapted cuts, this procedure improves the qualitiy of the data, because for all periods consistently, only events with the same maximal deviation from the break-up peak are taken. The correction factor is determined by the yield below the C_{G2N} cut, hence at $E_{2m} < c_l = 11$ MeV (see Fig. 6.6 above), and not at higher misssing energies. The reason for doing so is that at higher E_{2m} the data exceed the shape of a Gaussian due to extra strength originating from FSI and 3B absorption (see discussion in Section 6.3). Therefore the fit of the Gaussian was limited to the left slope (compare with Fig. 6.3 on page 107) and thus the correction factor f_{ECC} is given by:

$$\sigma_Q = \sigma_c \cdot (2\sigma_w/\sigma_c - 1) = \sigma_c \cdot f_{\mathrm{ECC}} \sim \sigma_a \tag{6.10}$$

The cross section subject to the cut C_{G2N} is marked with σ_c and results in σ_Q, which has the same integral as the yield of the whole break-up peak σ_a (see Fig. 6.5 above). σ_Q is the cross section with cut on G2N and successive cut correction ECC. This cross section is denoted in the plots by '$E_{2m} < 45$ MeV'. The cut correction factors f_{ECC} determined by this method are applied for all following spectra with G2N cut and read: 1.074, 1.407, 1.515 for the periods D220, D280 and D350 respectively.

6.2 Results for the pn channel

This section presents the results of the measurement concerning the pn final state. Up to now the 2N knock-out reaction off helium was not investigated in full detail. Also, reliable theoretical calculations are not available. Therefore the results obtained are merely listed and commented in the following sections, but they (esp. the asymmetries) cannot be interpreted and explained to full extend without comparison to a model.

The excitation function for the photo-induced inclusive pn emission is presented in Fig. 6.7 below. For all three periods the upper panel displays the visible excitation function with the requirement of a proton in PiP and a neutron in ToF. These data sets were analysed with different calibration parameters (see Chapter 5), e.g. tagging efficiency or scaling factors for the PMT gains. Their mutual agreement indicates the reliability of the calibration and their discrepancy supplies a measure for the systematic uncertainty. The lower panel shows the mean of the excitation function over the periods for low E_{2m} (G2N absorption) and for high missing energy (pion production). The G2N absorption shows a characteristic peak at 250 MeV originating from Delta excitation which is dominant at that energy. Above 400 MeV

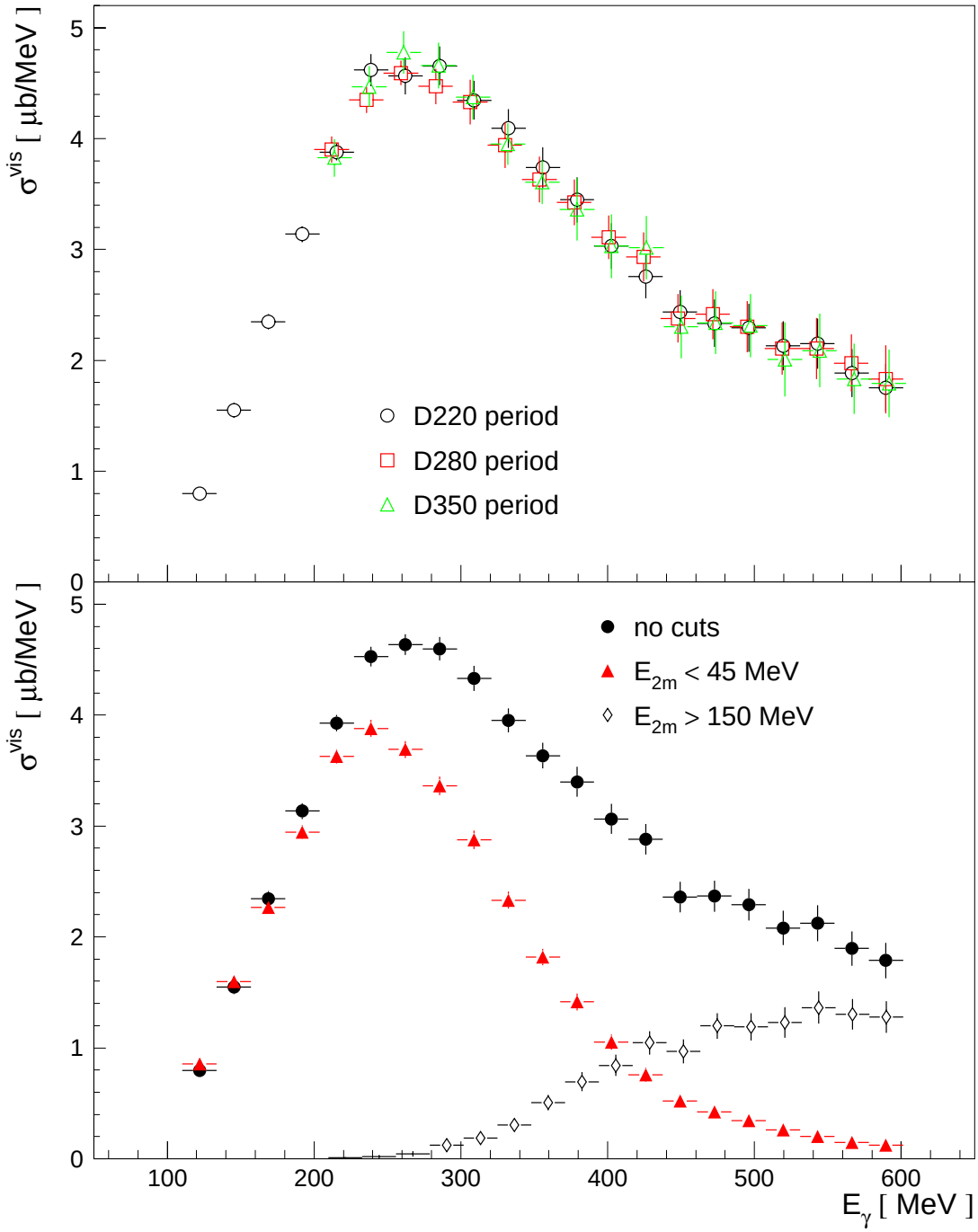

Figure 6.7: (upper) Excitation function of pn emission without any cuts for three data sets. (lower) Combined (averaged with mean-a method) excitation function together with cuts in missing energy on G2N absorption and pion production.

pion production strength together with contributions from FSI and 3B absorption exceed the G2N process. Compared to carbon (see [23], Fig. 8.3 and [135]) the ^{4}He excitation function decreases above the Delta peak much more rapidly. This observation complies with the missing energy spectra for helium and carbon at high energy, which demonstrates that the pion production channel is weaker for the helium target. From the comparison of the carbon excitation function [135, 136] and the one for helium a ratio of roughly 3.5 can be deduced. This ratio can be explained in the cluster model where carbon is composed of three α clusters (helium nuclei). However, a trivial scaling behaviour with the mass number of the excitation function for inclusive 2N emission is not expected. That is partially due to the dependence of the 2N-emission strength on the 2N wave function and the nuclear density and size. Additionally nuclear resonances are smeared out stronger the larger the nucleus [137] and their resonance mass depend on the nuclear density as well. Furthermore the probability of FSI increases with the nuclear mass number on account of the mean free path of pions of roughly 2 fm which implies that successive hadronic reactions and thus one- and two-pion production processes are more likely for heavier nuclei. The combined result of these effects causes the faster fall-off of the excitation function above the Δ resonance compared to heavier nuclei, e.g. carbon.

In the spectator model, which assumes no energy and momentum transfer to the uninvolved nucleons, the missing momentum can be identified with the initial pair momentum (see Chapter 4):

$$\vec{p}_{2m} = \vec{q} - \vec{p}_p - \vec{p}_n = -\vec{K}$$

The total pair momentum is shown in Fig. 6.8 on page 114, together with the cuts on G2N absorption and pion production. For the latter case the distribution extends to much higher pair momenta than the one of the G2N process and its maximum is located just above 200 MeV, hence about 70 MeV higher. The pion increases the final-state phase-space and thus picks up additional momentum. For comparison with the pp channel a polynomial fit to the pnπ distribution was performed and reads apart from an overall scaling factor: $p^2 \exp(-p^2/a_1^2) + a_2 p^2 \exp(-p^3/a_3^3)$ with $a_1 = 322.93$, $a_2 = 3.4$ and $a_3 = 211.04$ (all constants are in MeV). At 280 MeV pair momentum both processes are comparable in cross section. A cut of 250 MeV in missing momentum was used as a cut for the missing energy spectra in Fig. 6.9 on page 114 to support this picture. Indeed, low pair momentum implies the dominance of the G2N absorption and high momenta enhance the pion production process. Unfortunately this cut is not sufficient to separate both processes.

As already mentioned in Chapter 1 on page 5, K. Gottfried has derived that the G2N absorption cross section is approximatively proportional to the initial pair momentum distribution $F(K)$, the absolute square of the pair-momentum wave function. Likewise, M. Vanderhaeghen and J. Ryckebusch have shown in [92], Fig. 12 that for $E_\gamma \gtrsim 250$ MeV the factorization is a fairly good approximation for some observables, getting worse at lower energies. The data are plotted for $E_\gamma > 200$ MeV so that the factorization approximation holds to a great extend, which is investigated in more detail in Section 6.6 and its validity is demonstrated in Fig. 6.43 on page 150. Thus, the measured cross section integrated over photon energy and plotted versus the missing momentum can be compared directly (with

some restrictions) with the pair-momentum wave function. In Fig. 6.9 below (right) an HO pair momentum distribution $F(K)$ is fitted to the data and plotted with the same norm (integral) as the measured cross section. The Glöckle group [37] has rigorously calculated the ^{4}He wave function employing the realistic Bonn-C nucleon-nucleon potential. Apart from the NN potential and the applied model of the 3N force, this result is considered to be very precise. Indeed, compared to the data, this calculation yields a much better description than the HO pair momentum distribution. However, due to the limited detector acceptance and the factorization being only partially fulfilled, the data reflect the pair-momentum wave function only approximative[5]. Already the high momentum components of $F(K)$ indicate deviations from mean field behaviour. Thus the data of the pair momentum distribution provide a rough measure of SRC effects, or, to be cautious, at least an indication of its presence.

Next, the asymmetries are investigated, starting with the dependence on photon energy. The asymmetry is subjected to the C_{G2N} cut and is then plotted in the upper panel of Fig. 6.10 on page 115 for the three periods individually. It exhibits a decreasing behaviour from about -0.3 at $E_\gamma = 150$ MeV to zero around $E_\gamma = 450$ MeV. The respective data points of the periods were analysed at energy ranges with significant photon polarization only (Tab. 6.2 on page 105); the data agree in the overlapping regions within their statistical errors. In order to provide a consistent data set, the asymmetry of all periods combined and rebinned (averaged) with and without respecting zero values (mean-e/0) is plotted in the lower panel. The asymmetry reveals a small bump around 250 MeV which might be due to the interference of the MEC with the IC current being strongest at that energy. The interferences between the resonant, non-resonant IC and MEC change their contributions from about 200 MeV, by reason of an increasing imaginary part of the resonant Δ propagator (see (B.31)). The influence of tensor correlations could be another possible explanation, because they have their maximal contribution at the Delta resonance energy and are supposed to yield a less negative asymmetry than the central correlations solely [139]. The hypothesis arises that not all possible descriptions of SRC would reproduce that bump implying that these data could help to discriminate SRC models. Sophisticated detailed theoretical calculations are needed to clarify that observation; especially the explanation of the fact that this bump is not found in the carbon data [135,136] will be rather intricating.

The asymmetry Σ was also analysed according to (6.6) for other observables, for example missing momentum or missing energy. In Fig. 6.11 on page 116, Σ is presented for the latter for all periods seperately and combined. At high missing energy, namely for E_{2m} in the range of pion production, the statistic demanded a larger binning via an error-weighted average (mean-0). The D220 period has a larger asymmetry as already demonstrated in Fig. 6.10 on page 115. Its largest value is located around the break-up peak $E_{2m} = Q_{pn}$. This is a common feature for the three energy regions and indicates that the contributions of FSI and 3B absorption at medium missing energies lead to a smaller asymmetry than

[5] See also the comparison of the model calculation with the data in Fig. 6.46 on page 153 and the impact of the detector acceptances shown in Fig. 4.10 on page 68

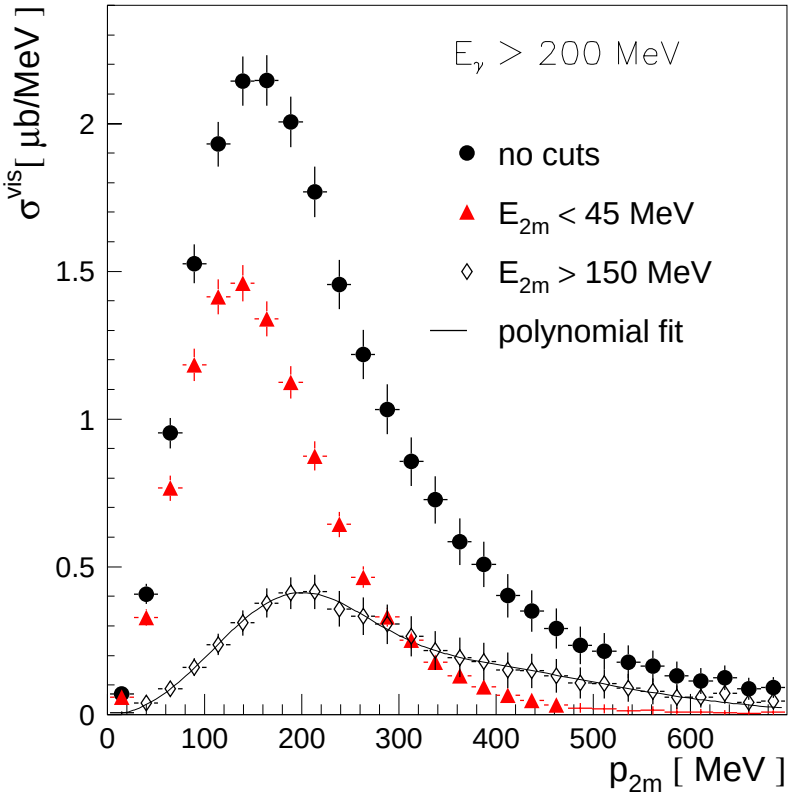

Figure 6.8: Missing momentum, as defined in (4.5b). Total cross section and cuts on low (G2N) and high (pion production) missing energy. The data is averaged over all periods for $E_\gamma > 200$ MeV. For comparison with the pp channel a polynomial fit to the pnπ distribution is plotted as well.

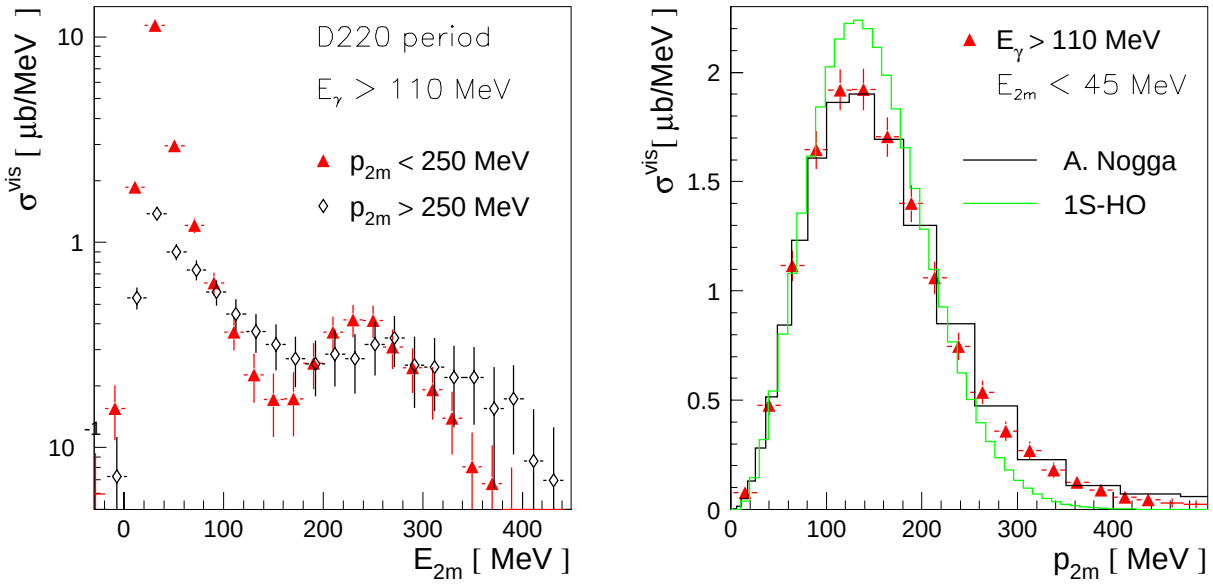

Figure 6.9: (left) Missing energy plotted on logarithmic scale with cuts on low (high) missing momentum enhancing G2N absorption (pion production). (right) Measured missing momentum with cut C_{G2N} is compared with an HO and a realistic pair momentum distribution [138]. The models are normalized to the data by demanding the same radial integral.

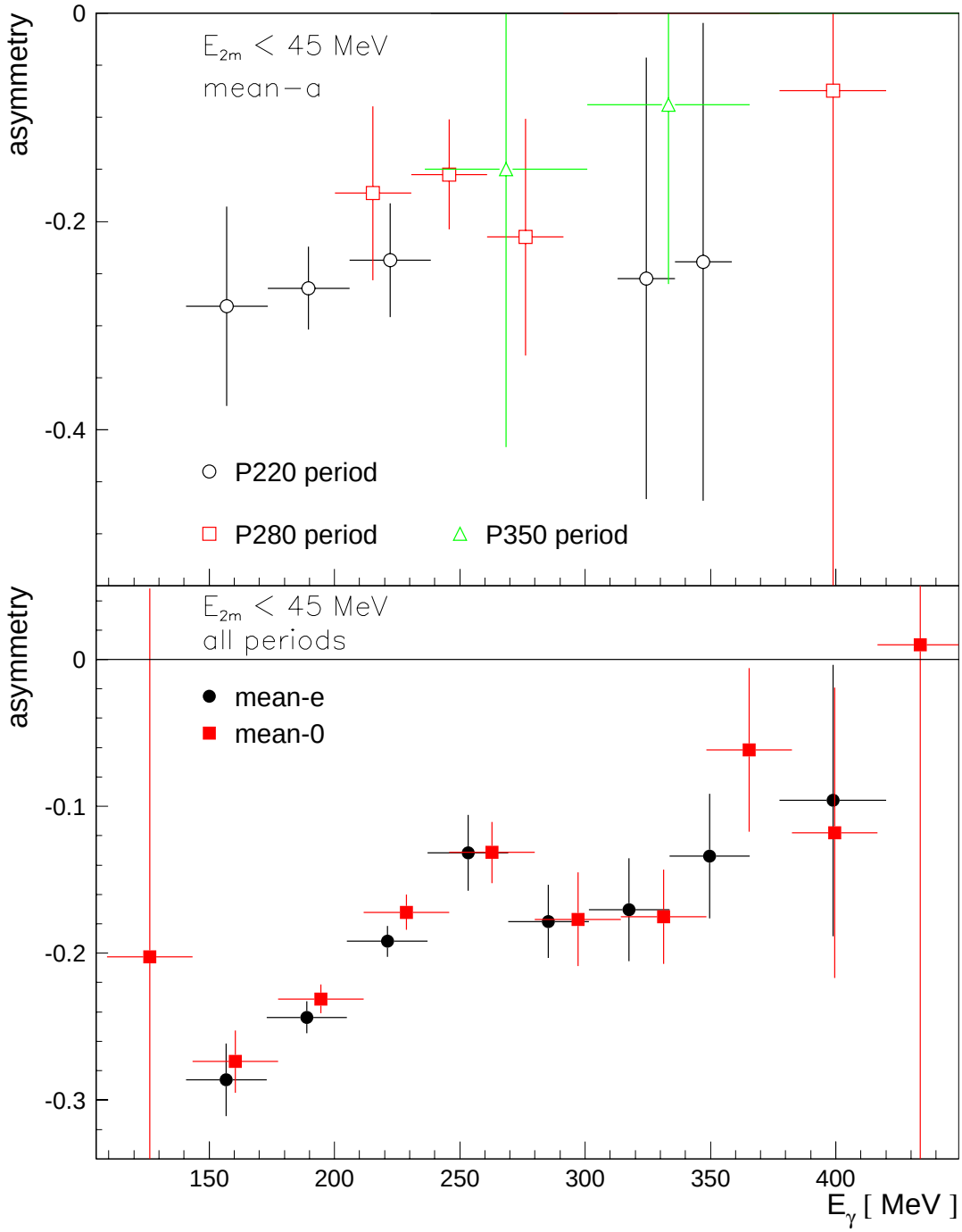

Figure 6.10: (upper) Asymmetry of excitation function of G2N absorption for three periods individually and rebinned with the mean-a method. (lower) Combined asymmetry averaged over all periods via the error-weighted mean. Discrepancies between the mean-e and mean-0 method are only expected in regions with low statistics, which are located around 130, 300, 370 and 430 MeV, hence in the border and overlapping regions of the three data sets.

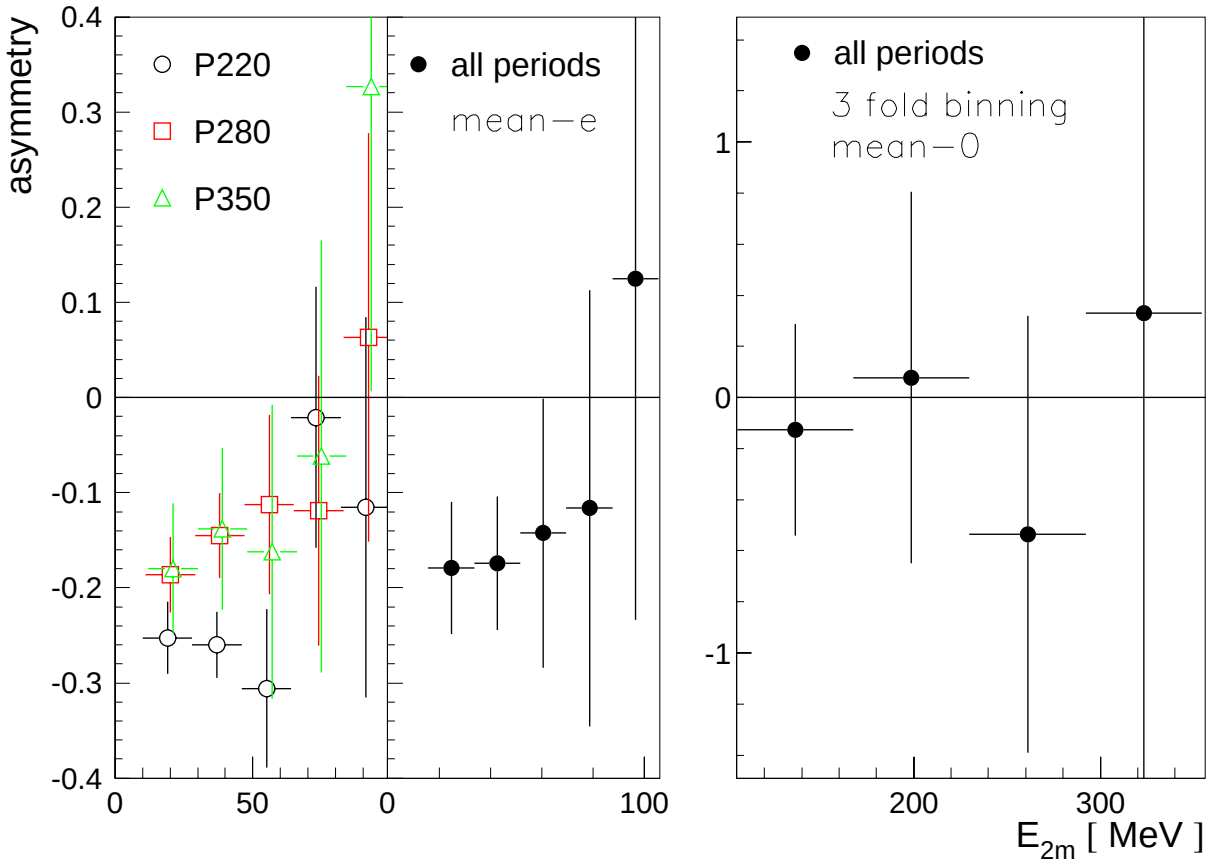

Figure 6.11: Asymmetry in dependence of the missing energy plotted for all periods seperately (left) and combined (middle) via the mean-e method. (right) Asymmetry in the missing energy range of pion production. Only photons with significant polarization enter the data of these asymmetries, see Tab. 6.1 on page 103 and Tab. 6.2 on page 105.

the G2N knock-out. Although the periods show a rather different behaviour, the average (of the periods) was performed for reasons of comparison and for a complete presentation of the data. At high missing energy the asymmetry vanishes caused by the participation of a third particle, the pion. With the enlarged final phase space, the correlation between the photon polarization and the reaction plane ceases. The 2N knock-out with accompanying pion production is a two-stage process, where the orientation of the photon polarization is thus in average equally distributed to the three particles yielding a quasi-isotropic final state.

The asymmetry of the missing momentum (Fig. 6.12 below) supports the findings from the missing energy spectra: In the domain of pion production, Σ is compatible with zero over the whole momentum range (right panel), while the G2N absorption yields a negative asymmetry, which for all periods is largest around the maximum of the pair momentum distribution, i.e. $p_{2m} \sim 120 \ldots 160$ MeV (compare with Fig. 6.8 on page 114). At low and

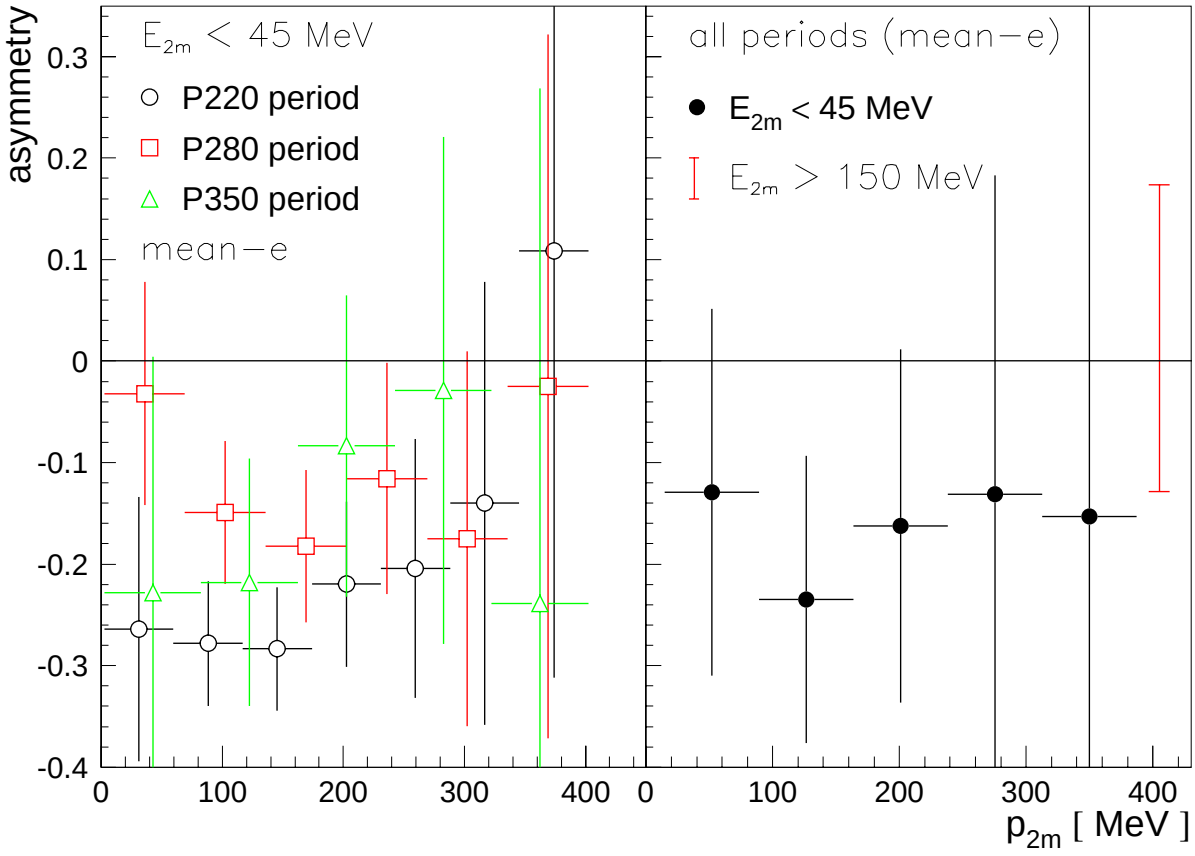

Figure 6.12: (left) Missing momentum asymmetry with cut on low missing energy for all periods individually. (right) Error-weighted average of the periods. The large errors stem from the large variations and strong dependence of the asymmetry on photon energy. The vertical bar in the right panel represents the margin of the asymmetry values in the p_{2m} spectrum of pion production events.

high momenta an energy dependence of the asymmetry can be observed: The asymmetry at high photon energy (P350) tends rather steeply to zero with increasing momentum, whereas at low momentum it stays significantly high comparable to the P220 data. That behaviour is in contrast to the mid-energy period having a vanishing asymmetry in the low momentum regime. This energy dependence is presumably based on the diverse contributions of the G2N absorption currents which preferably sample different momentum regimes due to the involved propagators (Chapter 4). Especially the run of the asymmetry curve in the momentum region 250 . . . 400 MeV is of high interest and possibly holds information about SRC, because extra strength compared to the SM was found at these momenta. Unfortunately the errors in that region are rather large.

6.3 3N absorption

In (γ,NN) experiments only direct 2N absorption allows quantitative measurements of SRC effects to be performed and clear and reliable conclusions to be drawn. Besides the G2N absorption, as it is presented in Chapter 4, and processes leading to real pion production, there are other photo-absorption mechanisms. These comprise, as is indicated in Fig. 6.4 on page 108, 2N absorption followed by FSI of one or both of the outgoing nucleons, production of a virtual pion or a real one which is reabsorbed by the nucleus, as well as 3N absorption. The latter might include the photon coupling to the 3N nuclear interaction exemplified in Fig. 6.13. A model to describe 3N photo-absorption would involve three body currents.

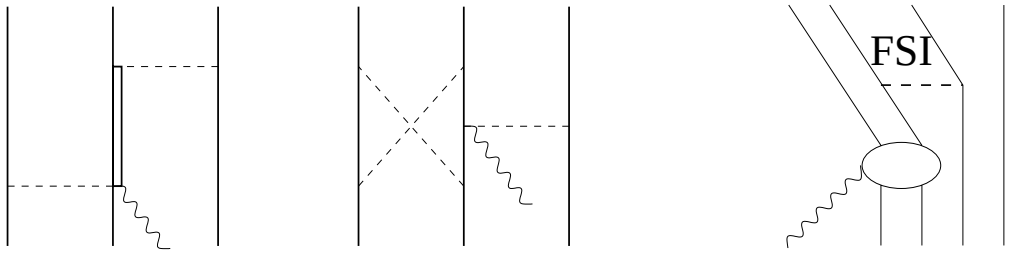

(a) Possible 3N interaction diagramms not included by the standard NN-forces

(b) 2N absorption followed by FSI

Figure 6.13: 3N interaction diagramms and FSI in the context of 3B absorption. Both lead to three (fast) nucleons in the final state. Note, the time axis is directed upward.

Just as the ground state correlations, these three (or even multi-) body currents are a natural manifestation of the many-body dynamics of the nuclear system. The 3N force is still under discussion, but new support of its existence is given from calculations of ^{4}He properties [37]. Although there are qualitative differences between these processes which lead to three (fast) nucleons in the final state, both processes are adressed in the following by 3B absorption. 3B absorption was investigated in more detail to ensure for further investigations, that only genuine two nucleon absorption processes are selected or at least their contributions are relatively enhanced as much as possible. From the ^{4}He(γ,pX) data only a subset subject to the condition of a proton in PiP and a neutron-proton pair in ToF was used in the following discussion.

For 3B emission without pion production, the calculation of the non-relativistic (owing to the expression of the recoil term) 3 body missing energy E_{3m} and missing momentum p_{3m} is well-defined due to the completely determined kinematic:

$$\vec{p}_{3m} = \vec{q} - \vec{p}_{\mathrm{p}}^{\,\mathsf{PiP}} - \vec{p}_{\mathrm{n}} - \vec{p}_{\mathrm{p}}^{\,\mathsf{ToF}} \stackrel{!}{=} \vec{p}_{\mathrm{n}}^{\,\mathrm{mis}} \tag{6.11a}$$

$$E_{3m} = E_\gamma - T_{\mathrm{p}}^{\mathsf{PiP}} - T_{\mathrm{n}} - T_{\mathrm{p}}^{\mathsf{ToF}} - \frac{p_{3m}^2}{2M} \tag{6.11b}$$

Therefore a clear peak arises in the three body missing energy spectrum in Fig. 6.14 at the ^{4}He binding energy $Q = 28.3$ MeV. The energy resolution now reflects the three-

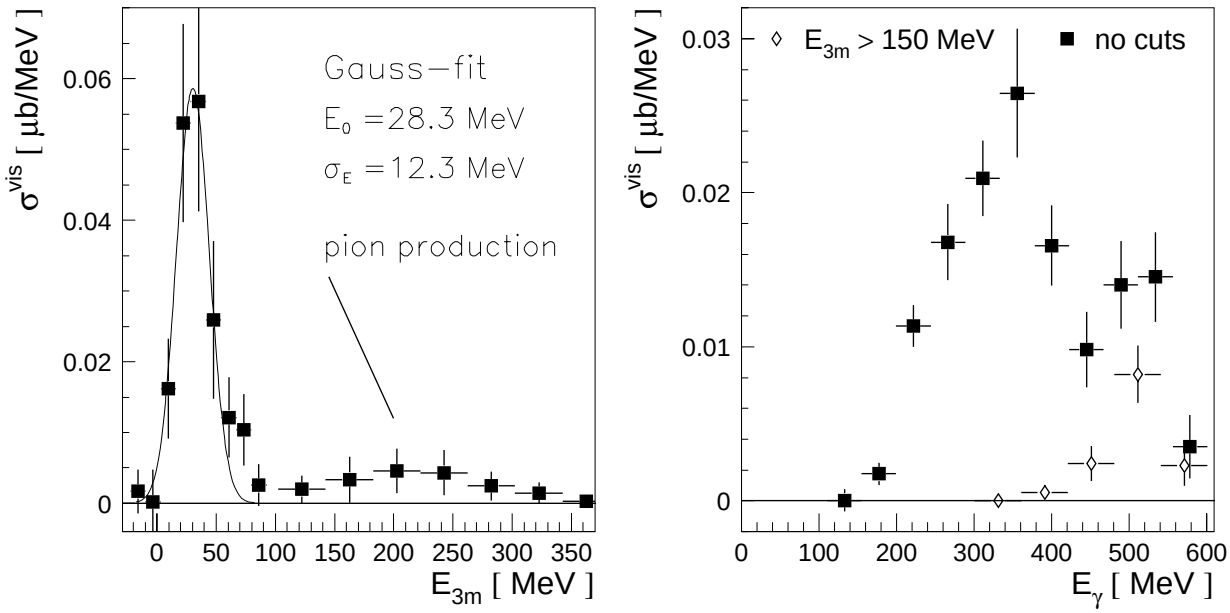

Figure 6.14: (left) 3B missing mass of ppn emission according to (6.11) *together with a Gaussian fit to the break-up peak. (right) Total excitation function of ppn events along with an additional cut on pion production, hence the (γ,ppn)nπ reaction.*

fold detector resolutions for one particle. In addition the energy resolution is somewhat deteriorated because fairly large energy bins had to be used due to the poor statistics. It can be deduced from this spectrum that the calibration is consistent and reliable. Furtheron the energy resolution per particle may be appraised to $\sigma_N = 7.4$ MeV. The excess at about 70–140 MeV is probably due to imperfect calibration. One source, for example, is the incomplete separation of protons which suffered hadronic losses in PiP due to the neccessary finite width of the windows used by the range method, see Section 5.4.3. Above 140 MeV there is some minor but statistically significant strength which is obviously due to pion production: ^{4}He(γ,ppn)nπ.

The conclusion can be drawn from the excitation function, see Fig. 6.14, that the phase space for 3B emission opens at a rather high photon energy, which is about 200 MeV. The threshold for accompanying pion production is even higher (at about 350 MeV). Furthermore the comparison to the exclusive 2N emission (Fig. 6.7 on page 111), taking a reliable correction for solid angle for granted, reveals that the strength of 2N emission with pion production is comparable to 3B emission between 200 and 400 MeV, but clearly dominant above this energy range. In other words 2N photo-absorption accompanied by subsequent π production (exclusive 2Nπ emission) has a larger probability than 3B absorption. That complies with the fact that 3N forces are much weaker, if they exist at all. Consequential it can be concluded that the photon coupling to the 3N interaction has a smaller probability

than to the 2N one. Hence above π threshold more strength is found in 2N absorption where part of the energy is used for π production than in the emission of a third nucleon.

From the 3B data, a two body missing energy E_{2m}(3N) and missing momentum p_{2m}(3N) can be calculated using all permutations of the nucleons involved. This allows to estimate the contribution of the 3B absorption in the 2N spectra, where a possible third nucleon is not detected, as was the intention of this section. With the assumption of an isotropic distribution of the undetected neutron, the ppn portion in 2N spectra can be approximated by scaling the ppn yield with the appropriate solid angle ratio, that is $4\pi/\Omega_{\mathrm{ToF}} \approx 12.5$. All further comparisons of 2N with 3B spectra employ this scaling factor for the latter and these figures are marked accordingly.

Fig. 6.15 shows the 2 body missing energy along with the E_{2m} distribution calculated from the ppn yield. In the peak of the ^{4}He break-up the ppn yield is already about 2 orders of

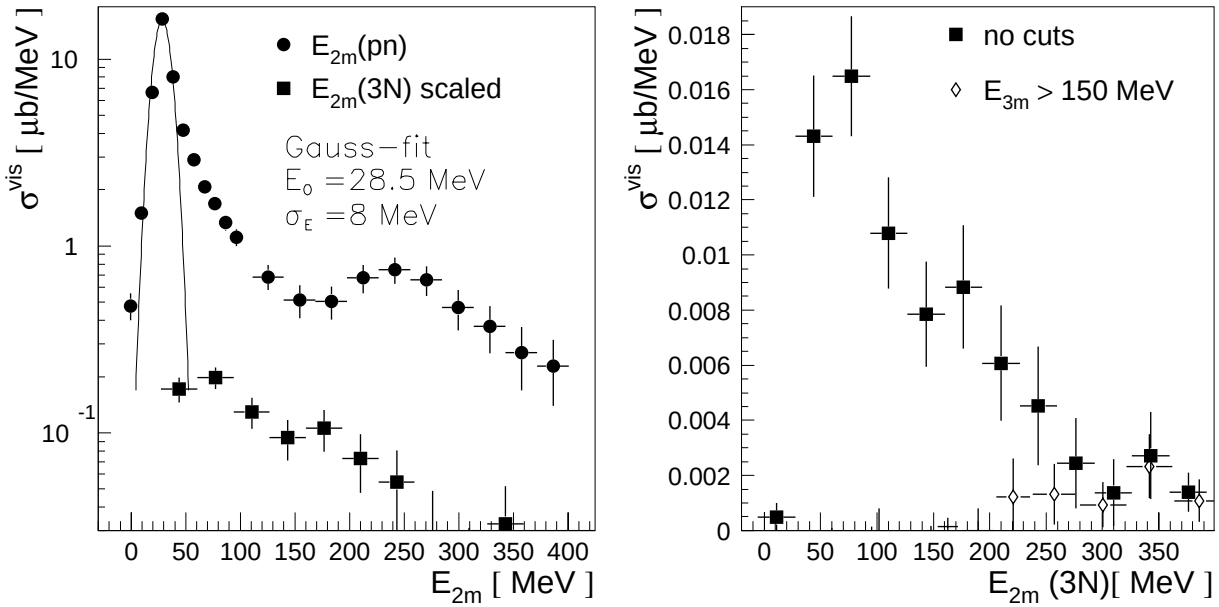

Figure 6.15: Missing energy of two nucleon emission (pn-channel) is compared with the two body missing energy calculated from three nucleon emission data. (right) E_{2m}(3B) plotted as total on a linear scale and with a cut on (γ,ppn)nπ.

magnitude smaller. Furthermore, the structure of the curves suggests a suppression of 3B absorption with and without accompanying pion production by a cut on missing energy (E_{2m}) below 45 MeV. The cross section for $E_{2m} > 150$ MeV does not rest upon 2N knock-out accompanied by pion production solely, but originates from 3B absorption as well. Not until 200–250 MeV, pion production accounts for the total cross section, but between 150–250 MeV there is still significant strength from 3B absorption. This means that in a E_{2m} spectrum one cannot distinguish completely between those two processes, although the maximum of the 3B data is considerably higher, namely $\sim$ 70 MeV. That interpretation

is also supported by the Oset calculation (Fig. 6.4 on page 108). The same holds true for p_{2m}(3N) plotted in Fig. 6.16: Here the 3B portion is located much higher in photon energy, with its main contribution around 200–400 MeV. It can be deduced from Fig. 6.15 above that the strength at medium missing energies, i.e. between the break-up peak and pion production, is about 1/5 due to 3B absorption, so that the rest must originate from FSI leading to a residual pn pair with high relative kinetic energy of about 50–100 MeV. But, from the discussion above it became clear that the 3B share to the total cross section of pn emission is negligible and that its contribution is nearly completely eliminated by the C_{G2N} cut.

If no pion was produced, the momentum of the unobserved neutron is well defined from the definition of the 3B missing momentum in (6.11). Assuming FSI effects are small, which is supported by Fig. 6.4 on page 108, the missing momentum can be identified within the scope of the spectator model from the neutron momentum prior the photon absorption. The p_{3m} distribution is plotted in Fig. 6.16 showing a peak at about 170 MeV followed by a sharp fall-off with an extra shoulder above 350 MeV. Additionally p_{3m} is shown for two

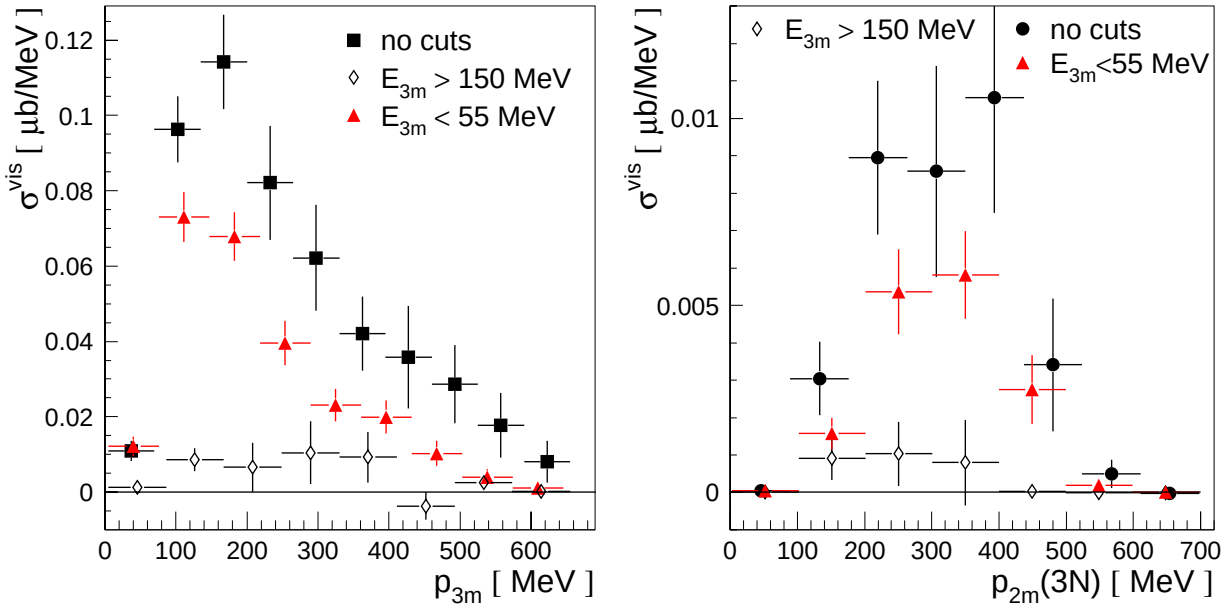

Figure 6.16: (left) Missing momentum according (6.11) *plotted as total and with cuts on low and high 3B missing energy selecting exclusive 3B emission and* (γ,ppn)$n\pi$ *events. (right) 3B contribution in a 2N missing momentum spectrum for the same cuts.*

cuts: above 150 MeV in 3B missing energy selecting pion production events and below 55 MeV ensuring exclusive 3B absorption reactions. The maximum of the p_{3m} distribution in case of a real pion in the final state is located at $\sim$ 300 MeV about 100 MeV higher than in the 2N knock-out process (see Fig. 6.8 on page 114). For exclusive 3B absorption, the maximum of the momentum distribution is around 120 MeV, which is in the range of the maximum in the $p_{2m}(pn)$ spectrum, with an astonishingly long tail. An uncorrelated mean

field wave function is expected to fall off faster with much less high momentum components. Phase space and detector acceptance corrections might alter the shape of this distribution slightly, but cannot account solely for the excess at high momenta.

As mentioned above, apart from restrictions due to the limited detector acceptance and the assumptions of the spectator model, the 3B missing momentum can be identified with the neutron momentum distribution prior the photon absorption. The study of this observable can thus be viewed as an additional approach offering a rather direct access to SRC; although, at least at low excitation energies, $(e, e'n)$ reactions are better suited to measure neutron momentum distributions. Therefore single particle momentum distributions (see Chapter 4, (4.22a)), based on an HO and correlated, Jastrow-type pair wave functions, are compared to the measured p_{3m} distribution. In Fig. 6.17 below the standard HO and a correlated momentum distribution with fitted parameters b and c are plotted along with the 3B missing momentum distribution. The HO description badly fails to describe the enhancement at high momenta which is present in the data. In contrast the correlated distribution is able to account for these high momenta components and reveals, like the data, a shoulder around 400 MeV due to the short range repulsion. These comparisons provide a clear indication of SRC beeing present. The fit to the p_{3m} distribution yields the best parameters (see Tab. 6.3) for the SRC model used here. It has to be noted that the fit respects the constraint (4.23) of the ^{4}He charge radius and d stems from (4.21b) in order to achieve consistency with this model.

In order to qualitatively reach sensible ranges of the correlation parameters four rather distinct correlated wave functions are compared in Fig. 6.18 below to the measured distribution. Thereby one of the correlation parameters b, c is kept fixed and the other is fitted to the data. The parameter c governs the strength of the repulsive potential and therewith the repulsive part of the wave function and consequently is a measure of the impact of the SRC on the wave function (see Chapter 4,esp. (4.22a)).

Two correlated wave functions ($b, c = 3, .15$ and $2, .21$) comply with the measurement whereas the other ($4, .11$ and $1.14, .3$) just manage to meet the data and thus mark the extremes of these parameters. With the caveats mentioned above, the range of these

param.	HO	1.14,.3	2,.21	3,.147	4,.11	b,c fit
a	.534	.526	.534	.534	.534	.534
b	0	1.14	2	3	4	1.55
c	0	.3	.21	.147	.11	.25
d	.534	.8	.62	.57	.553	.672
s_c	-	15.2	16.2	16	15.5	16
r_c	-	1.7	1.4	1.2	1.1	1.5
r_f	-	1.6	1.2	1	.83	1.3

Table 6.3: Parameters of the correlation function used in the comparison with the measured 3B missing momentum distributions. The definitions of d and s_c, r_c, r_f are given in (4.21b) *and* (4.29).

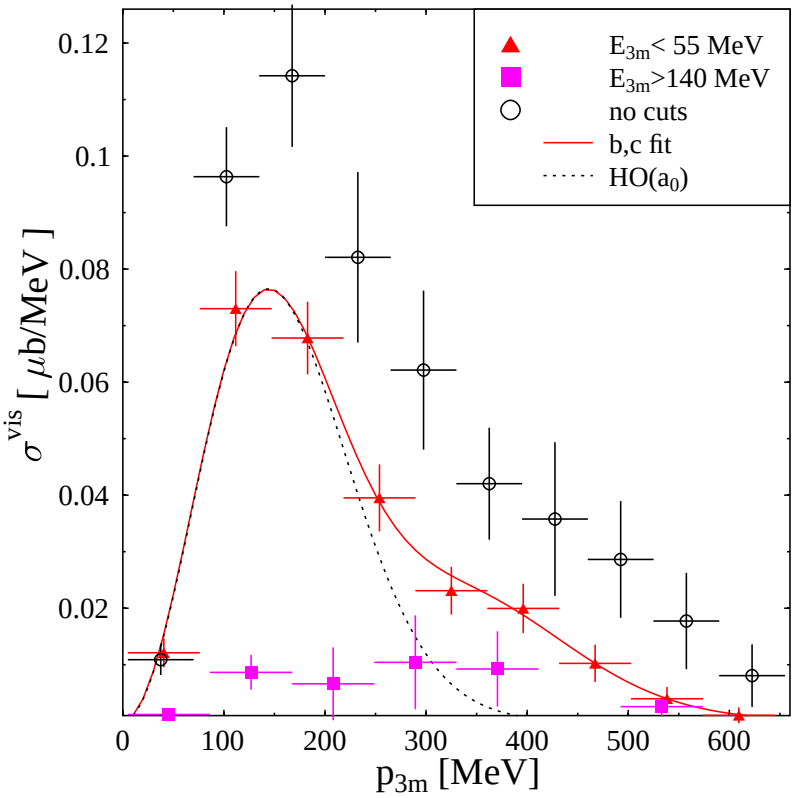

Figure 6.17: Total missing momentum of ppn emission along with cuts on 3B absorption and pion production. Single particle momentum distributions $w_a(k_N)$ based on an HO wave function with standard parameter a_0 and a correlated wave function with fitted parameters b and c are plotted for comparison. Note, the data with(out) cuts is binned via the mean-e (-a) method, which explains the sizes of the error bars.

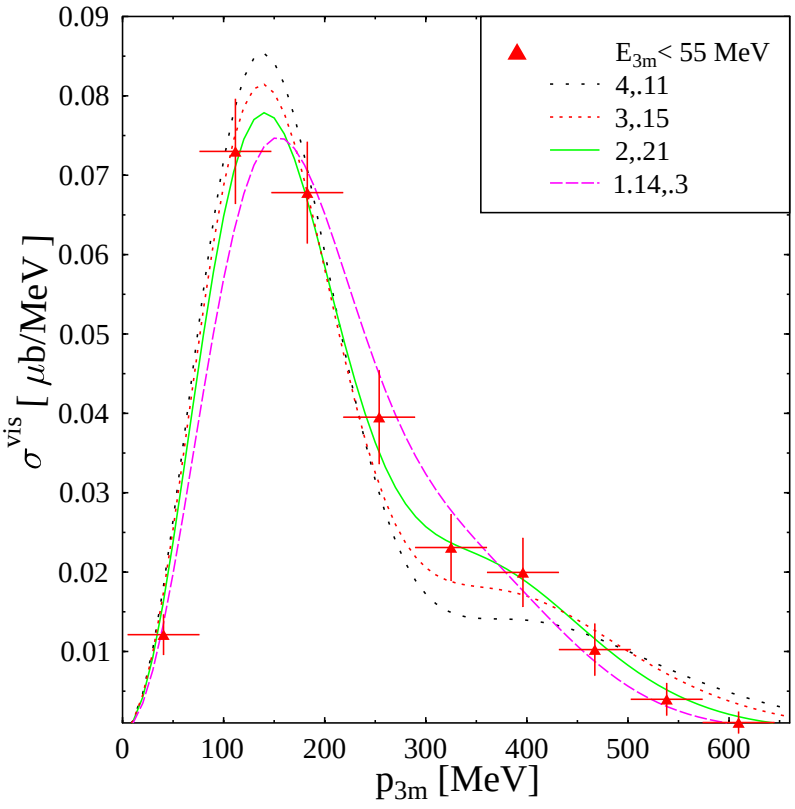

Figure 6.18: Missing momentum of 3B absorption compared with various fitted single-particle momentum distributions. Four correlated wave functions (see Tab. 6.3 above) are plotted whereby one of the correlation parameters b, c is kept fixed and the other is fitted to the data (see text).

parameters derived from a larger survey than presented here, is stated:

$$c \in [0.15, 0.3] \qquad b \in [1.5, 2.5] \tag{6.12}$$

It has to be emphasized that these numbers are not meant to provide a quantitative description of SRC in helium. The reason is found in restrictions such as validity of spectator model, limited detector acceptance, influence of FSI and a rather simple model of a correlated wave function. Moreover, the p_{3m} distribution is integrated over a wide photon energy range, also threshold and acceptance corrections have to be applied. Therefore it would be premature in the present stage to draw serious conclusions about the correct correlation function. However, this paragraph demonstrates the principle feasibility of this approach.

For the ($\vec{\gamma}$,3N) reaction an asymmetry can also be defined and is studied with the ppn data as well. The asymmetry is analysed utilizing the weight $w_{\pm}$ instead of w_p (see Section 6.1) thereby avoiding ambiguous and complicated rules to define the reaction plane for ϕ_m. The reason for doing so is based on the necessity of selecting one of the two nucleons in ToF in order to define the reaction plane, i.e. the angle ϕ_m in (6.3b). Actually the 3B asymmetry must therefore be scaled by the ϕ acceptance factor $r_\phi \approx 1.06$ according to (6.7), which was *not* done for Fig. 6.19. The photon energy dependence of the asymmetry is plotted only

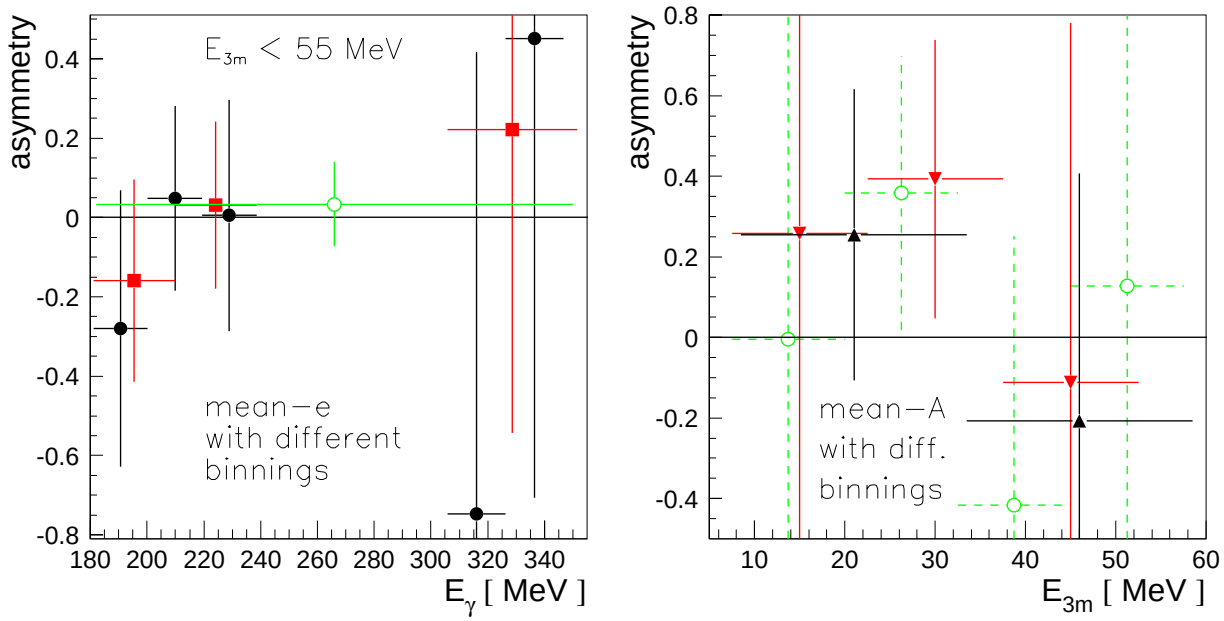

Figure 6.19: (left) Photon energy dependent asymmetry of the ($\vec{\gamma}$,ppn) reaction. Only the P220 data were analysed, explaining why Σ is just given in two small energy regions. (right) Asymmetry versus 3B missing energy. In both figures the same data set is plotted for different binnings to provide different resolutions and statistical quality.

for the P220 data with a cut on $E_{3m} < 55$ MeV to discriminate pion production events. The data are presented with three different binnings wherefore the averaging was done via

the mean-A method due to the low statistics. In general the asymmetry is very small and comparable with zero. Yet at low photon energy it meets the asymmetry value of the 2N knock-out reaction whereas at high energy the asymmetry is positive, such that the overall value is slightly positive. In Fig. 6.19 above the asymmetry is plotted versus the 3B missing energy for three different binnings revealing a positive and rather large asymmetry around the break-up peak. Over the missing energy range up to 55 MeV the averaged asymmetry is quite small; however, it is still positive. The significance of the 3B absorption was shown in a ^{3}He($\vec{\gamma}$,NN) experiment reported in [140]. In this experiment the photodisintegration of ^{3}He for the pn and pp channel was measured and it was found that (i) the pp final state is dominated by 3B absorption and that (ii) the pp(X) asymmetry is essential zero. The vanishing or possibly even slightly positive asymmetry of the 3B absorption is indicated by this result and supports therewith the findings here. The 2N absorption mechanism with or without FSI leads in general to a negative asymmetry through the dominant influence of the negative asymmetry of the Δ resonance. If pion production is involved, the asymmetry ceases. Therefore, the positive asymmetry around the break-up energy indicates that the process does not involve the conventional G2N absorption mechanism, but possibly takes place via a coupling of the photon to the conjectural 3N nuclear interaction.

The results in this section agree with an analysis of ^{4}He photo-absorption data with Daphne [141,142]. In this work it was shown that around the Delta resonance the total cross section of three- and four body photo-absorption is comparable with the 2N absorption. Yet, these results cannot be compared directly due to the rather different solid angle acceptance: Daphne covers nearly the whole solid angle and the PiP-ToF setup is limited to in-plane final states. The latter is a rather severe limitation for multi-nucleon emission, which in particular renders the extrapolation into the full solid angle unreliable.

6.4 Results for the pp channel

The photo-induced pp knock-out is based on the same basic reaction mechanisms as the pn knock-out apart from the MEC. A pp pair can only exchange neutral pions[6] to which the photon cannot couple and thus both MEC, the pion in flight and seagull, do not contribute. Additionally, the IC strength is altered as well in comparison to the pn channel, due to a different isospin structure of the Δ current involving only π^0. This results in a much smaller cross section, different angular distributions and asymmetries. The missing energy spectra (Fig. 6.20 below) show that the G2N knock-out is much weaker compared to competing processes, FSI, 3B absorption and pion production, especially for high photon energies. However, as already mentioned above, in ^{4}He real and virtual pion production is not as dominant as in carbon. The data suggest that the model overestimates the probability of virtual pion production and pion reabsorption. Still, the comparison with the model supports that a cut on low E_{2m} enhances the G2N absorption reaction significantly.

[6] Most of the realistic NN potentials include, of course, other types of exchange fields, like the ρ and ω, but only pions are considered in this discussion.

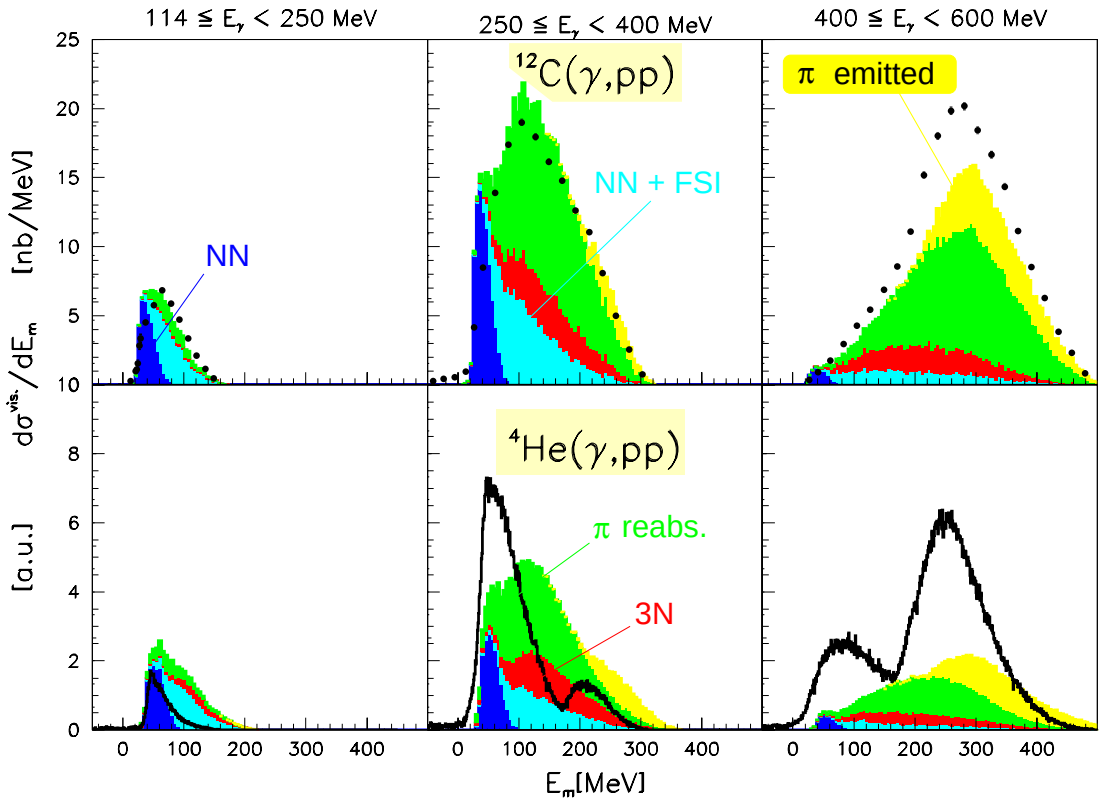

Figure 6.20: Missing energy for inclusive pp knock-out for three successive photon energy bins is compared with the Monte Carlo model from Carrasco and Oset. The various contributions to E_{2m} [134] are marked in the figure by shaded areas and denoted in the legends.

Compared to the pn channel the pp strength is much weaker and thus the total 3B contribution is about half of the total and hence comparable with the genuine pp emission cross section. Additionally, the break-up peak in the missing energy spectrum in Fig. 6.21(a) below is shifted to higher energies, namely to 35–40 MeV. In order to disentangle both contributions at least to a great extend, the excitation function was analysed for successive cuts in the missing energy spectra, see Fig. 6.21(b) below. The boundaries of the cuts read: $22<r<34<u_1<46<u_2<58<u_3<70<u_4<90<u_5<110$ MeV. The ratios of these excitation functions with respect to the reference spectrum subject to the cut $C_r : E_{2m} \in [22, 34]$ are plotted in the lower panel. The ratio with region u_1 shows an approximative constant dependence with structures due to the shifted missing energy regions. However, already ratio u_2 indicates a rising slope for high photon energy which becomes more pronounced for higher E_{2m} cuts (regions $u_3 \ldots u_5$) respectively. From the slopes of these ratios it can be concluded that pp emission in the E_{2m} ranges r and u_1 dominates and in $u_4, u_5, \ldots$ 3B emission prevails. In between there is a continuous transition which implicates that those two reactions cannot be distinguished via the observable E_{2m} alone. Therefore in Fig. 6.22 on page 128 the cross section is plotted versus missing momentum and missing energy tak-

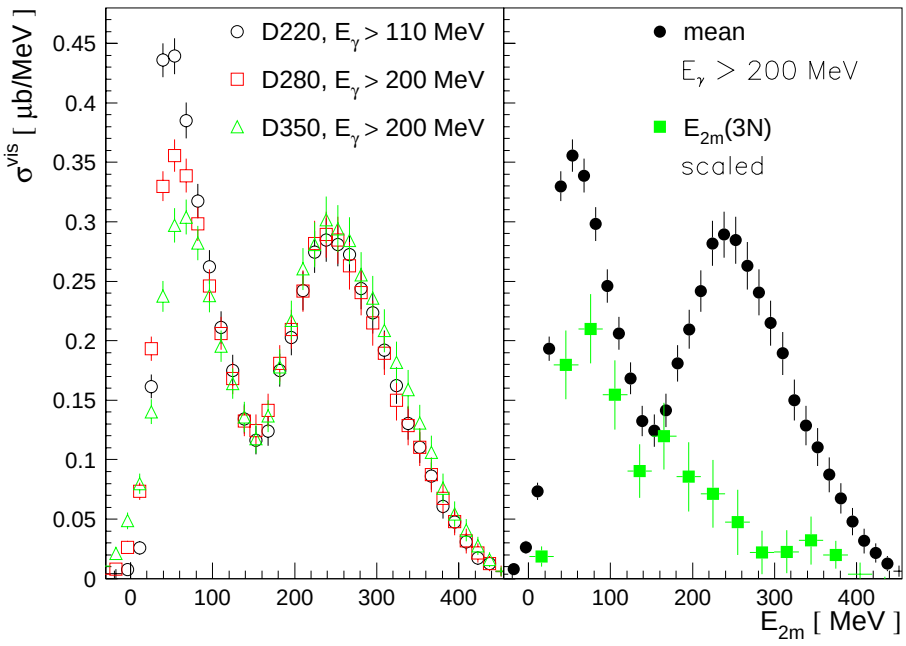

(a) *(left)* E_{2m} per period and *(right)* combined (mean-a) along with the scaled 2N missing energy calculated from the ppn data (see text)

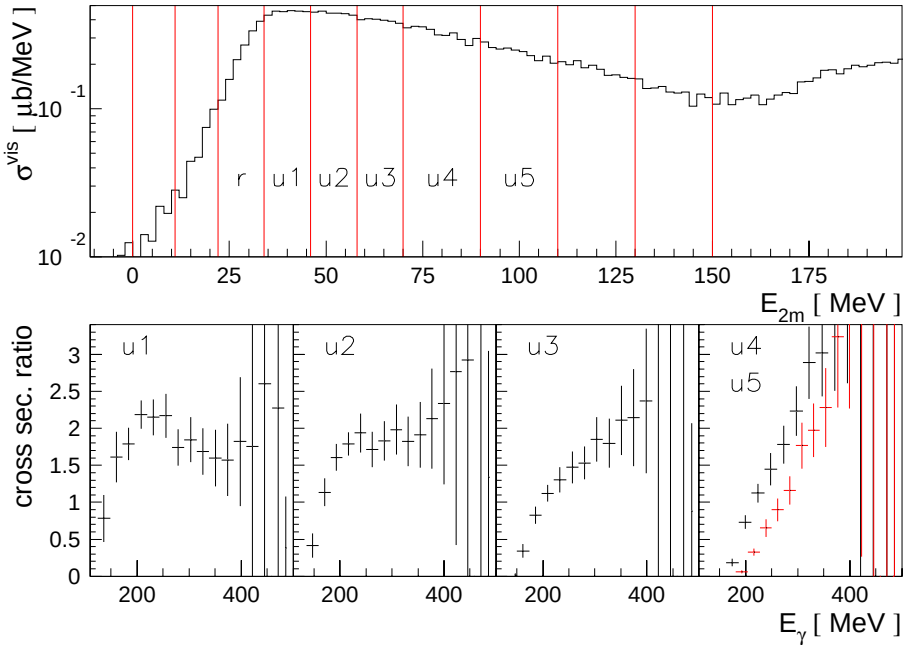

(b) *(upper)* E_{2m} on logarithmic scale with the limits of the cuts used for the excitation-function ratios (see text). *(lower)* The ratio was calculated with respect to C_r, the region where only pp emission is expected

Figure 6.21: E_{2m} plots of inclusive pp emission exemplifying the strong 3B contribution.

ing advantage of their kinematical correlation. The pn channel is displayed in panel *a)* and

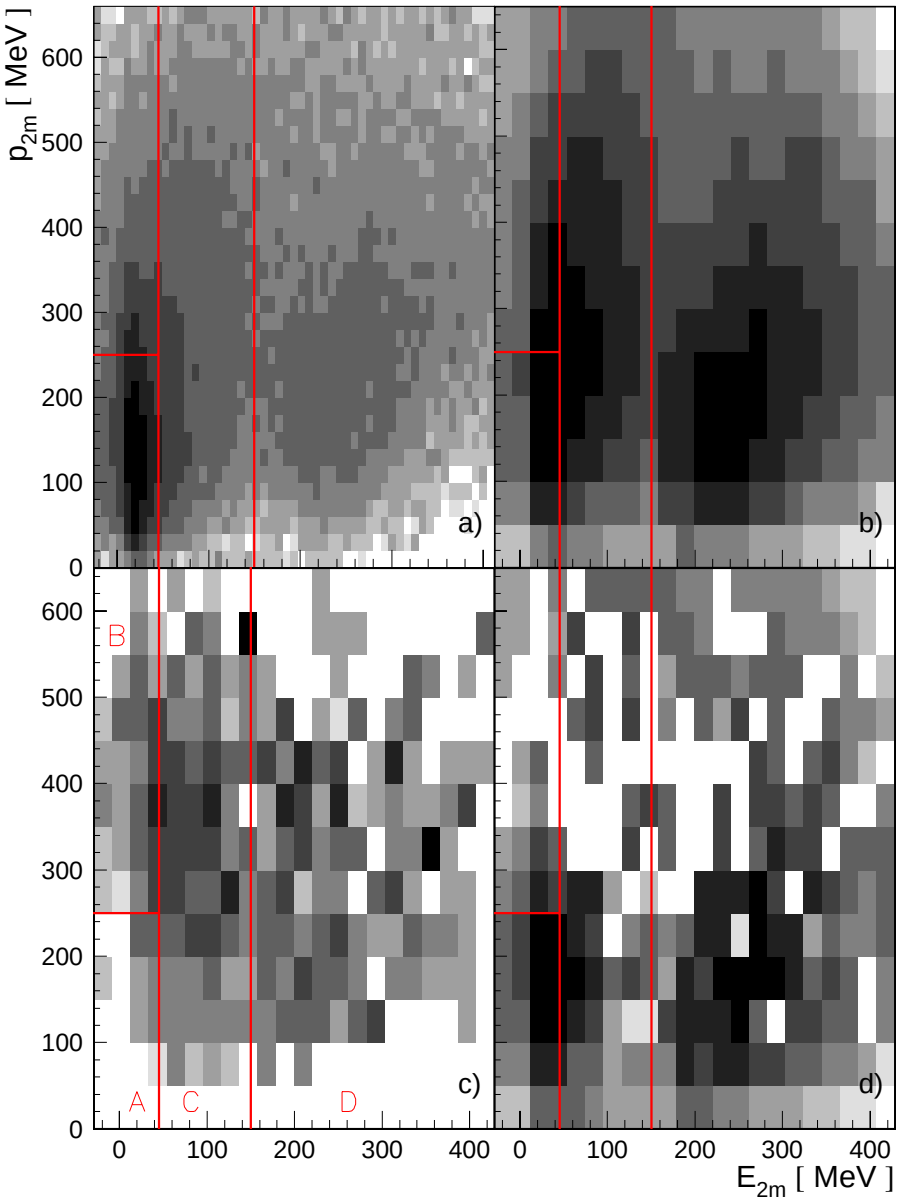

Figure 6.22: Inclusive 2N emission cross section versus missing energy and missing momentum on logarithmic scale. a) pn, b) pp and c) 3B absorption processes obtained by demanding a neutron, proton and neutron + proton in ToF respectively. d) pp emission subtracted by the scaled 3B contribution. The lines mark the cuts A...D used in the analysis.

clearly exhibits the G2N peak and the region of pion production. Events from 3B absorption reside around $E_{2m} \sim 80$ MeV and $p_{2m} \sim 300 \ldots 400$ MeV (see Section 6.3), which is in region C. The boundaries of the four regions A...D are the same in all plots; the labels are given in panel *c)* only. The G2N cut (region A and B) provides no full separation but the discrimination of the 3B absorption is sufficient. Panel *b)* demonstrates that compared to (γ, pn) the two protons from the G2N reaction are shifted in the spectrum towards the 3B regime which renders the separation via the cut in missing energy impossible. However, the main contribution of the 3B strength is located between 200 and 400 MeV in p_{2m}, so that the cut in missing momentum $p_{2m} < 250$ MeV (region A solely) discriminates most of

the 3B events. This is demonstrated in panel *d)* . There, the pp strength after subtraction of the scaled 3B contribution resides almost completely in region A. Therefore the cuts A and A+B, denoted by C^{A}_{G2N} and C_{G2N} respectively are used further on to enhance the G2N absorption. Unfortunately, this additional cut in missing momentum implicates the risk of loosing good G2N events with high p_{2m}. For most of the spectra C_{G2N} was applied, but further studies employing both cuts are performed in Section 6.6. The cut $C_{\pi} : E_{2m} > 150$ MeV defines region D and dominantly selects pion production (2Nπ) events.

Although, there is no clear separation possible, all events with $E_{2m} < 45$ MeV are considered as genuine pp photo-absorption, above this value as 3B absorption and above 150 MeV as pion production[7]. The excitation function is plotted in Fig. 6.23 below for these three missing energy cuts. The total cross section for the data periods comply nicely with each other ensuring the reliability of averaged spectra which are considered further on. The upper panel demonstrates that the strength of the direct pp-absorption reaction is rather small. From about 350 MeV pion production dominates and accounts almost for the total cross section at higher photon energy. The lower panel displays the total cross section averaged over the periods. Additionally, the pp data subject to the cut on 3B absorption is plotted, which meets the scaled ppn strength. The bump in the ppn data is due to supplementary pion production (see Section 6.3). It is therewith demonstrated that up to 400 MeV 3B absorption dominates and genuine pp absorption accounts only for a small portion of the measured pp strength which is located at low photon energies, i.e. $\lesssim 300$ MeV only. The reason, which is unique for the ^{4}He nucleus, is found in the fact that the residual two neutrons do not have a bound state, in contrast to the pn channel. As discussed above it is more likely that energy and momentum are transferred to the nn pair, respectively to their relative kinetic energy, than to a pn pair. That results presumably from the repulsion of two neutrons whereas a pn pair is loosely bound. Furthermore this observation indicates that different reaction mechanisms, in particular distinct FSI processes, are involved.

This observation is supported by the findings from the missing momentum spectrum, see Fig. 6.24 on page 131. Both the momentum distribution of the events with pion production involved and of G2N have their maxima around 200 MeV, which is considerably higher than the expected[8] pair momentum of a nn pair inside ^{4}He. The HO pair momentum distribution which was fitted to the pn data (see Fig. 6.8 on page 114) is plotted for reasons of reference and indicates that a significant amount of photon momentum is transferred to the relative momentum of the residual nn pair. Possibly the photon was not absorbed on the observed pp pair rendering the SPA invalid. That is corroborated by the similarity (with respect to the peak and the tail) of the missing momentum for $E_{2m} < 45$ MeV and $E_{2m} > 150$ MeV. At these high missing energies part of the photon momentum is taken by the pion produced and leads therefore as in case of pp emission to a p_{2m} distribution with a long tail.

[7] In Section 6.6 an extra constraint to enhance G2N absorption is investigated.

[8] One would anticipate that the pn relative momentum distribution differs from the nn pair one, but there seems to be no reason why this distribution could be much wider.

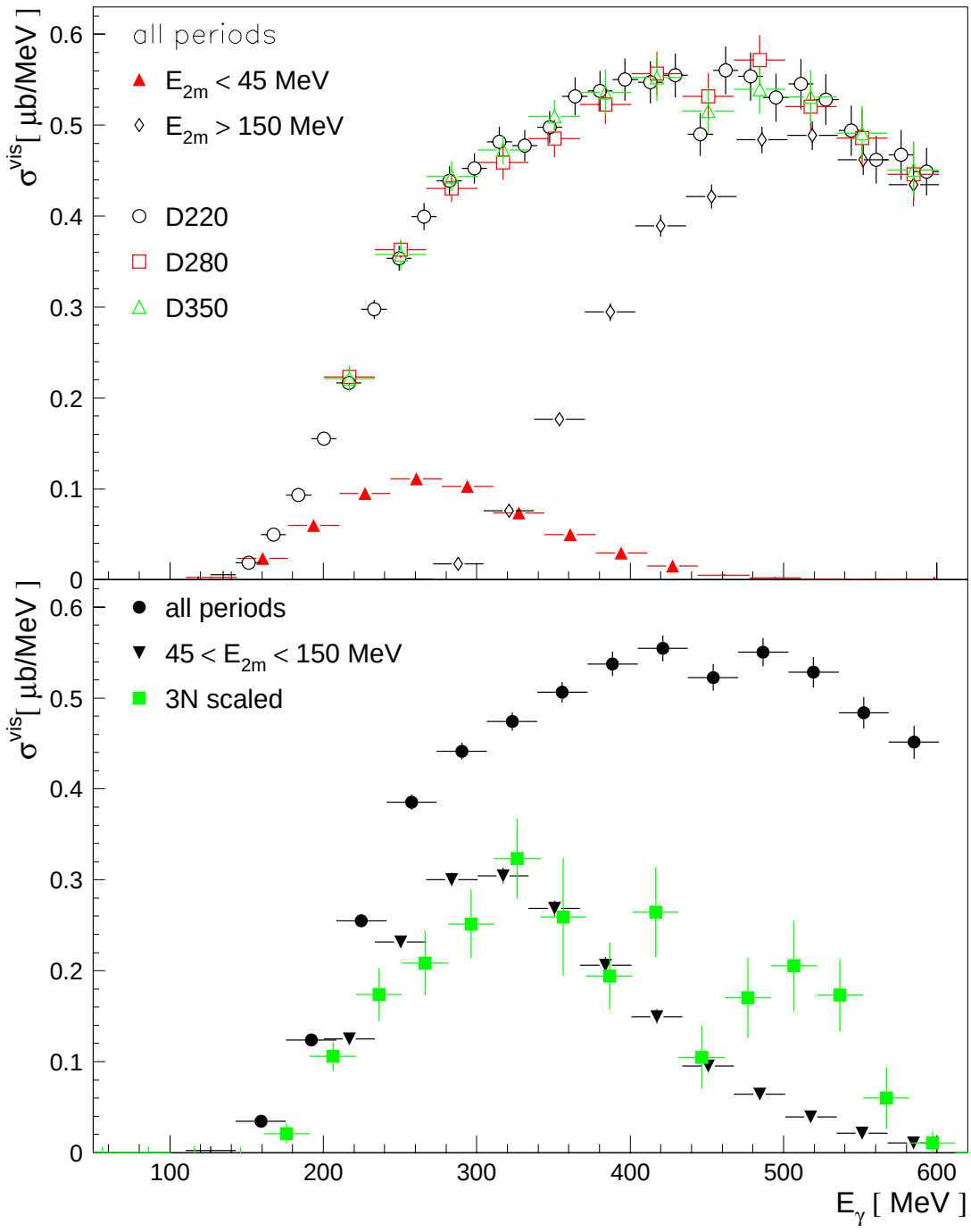

Figure 6.23: (upper) Total pp excitation function for all periods individually along with cuts on G2N and pion production. (lower) Plot of combined (mean-a) excitation function. Additionally, the strength of the (γ,ppn) reaction scaled by $4\pi/\Omega_{ToF}$ is compared with the 2N excitation function for medium missing energy, the region between G2N emission and pion production (compare Fig. 6.21 on page 127).

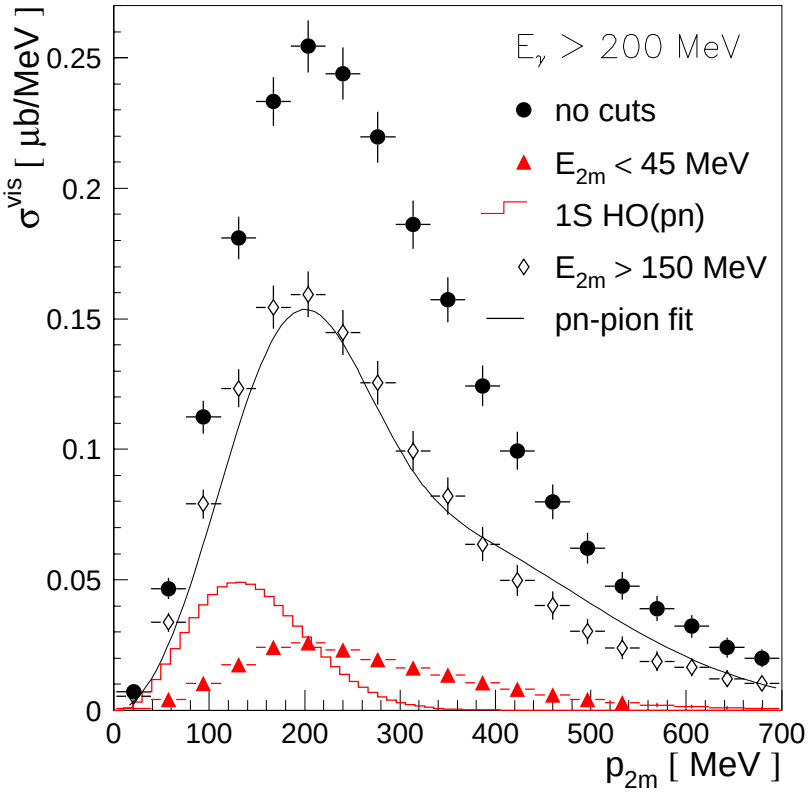

Figure 6.24: Plot of inclusive pp emission cross section in dependence of the missing momentum. The results of cuts on G2N and pion production are displayed. An HO pair momentum distribution fitted to the pn data and the pnπ missing momentum distribution (Fig. 6.8 on page 114) are shown for comparison as well.

The photon energy dependent asymmetry is shown in Fig. 6.25 below for each period individually in the upper panel and averaged subject to the cuts on G2N, 3B absorption and pion production. The asymmetry values of the three periods meet each other within the statistical errors revealing a rather different photon energy dependence compared to the pn case. At low and high energies the pp asymmetry agrees with the pn channel but instead of having a small bump the asymmetry nearly vanishes at about 240 MeV. Also, at 350 MeV, the pp asymmetry has regained the large negative value displayed at low missing energy, in contrast to the pn case which tends rather monotonically to zero with increasing photon energy. Yet, apart from the rather different behaviour at medium photon energies, both isospin channels have the same features at low ($\sim$ 150 MeV) and high photon energy ($\sim$ 400 MeV).

It can be concluded from the excitation function that the portion of the 3B absorption increases with higher photon energy whereas the genuine pp strength decreases. This is also found in the E_{2m} spectra, plotted in Fig. 6.26 on page 134 for three different energy regions. Around the break-up energy ($E_{2m} \leq 45$ MeV) the low and high photon energy data sets yield an asymmetry comparable with the pn channel. The asymmetry tends towards zero in the missing energy domain of the 3B absorption having a slightly positive (negative) value for high (low) photon energies. Their behaviour at high missing momentum results from different contributions of 3B and G2N absorption in dependence of photon energy, compare Fig. 6.23 above.

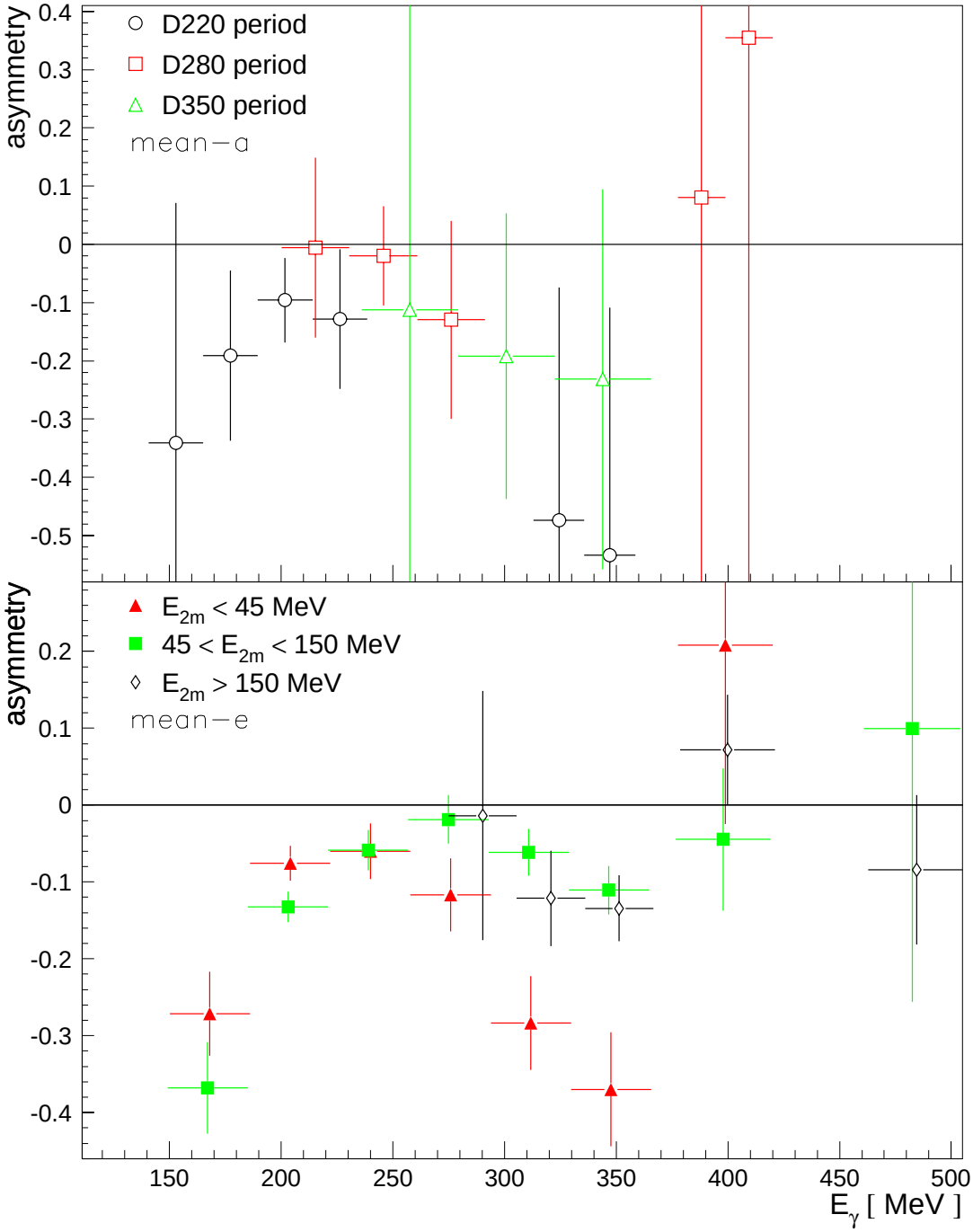

Figure 6.25: Photon energy dependent asymmetry for all periods binned via the mean-a average (upper). Below the combined asymmetry is plotted for G2N absorption, pion production and a cut on medium missing energies.

The asymmetry of the missing momentum distribution plotted in Fig. 6.27 below for low E_{2m} shows a contrary behaviour compared to the pn channel. The latter has its maximal value around the peak of the p_{2m} distribution ($\sim$ 130 MeV), but in the pp case the asymmetry is minimal at its pair momentum peak, that is around 200 MeV (compare Fig. 6.24 on page 131). All three periods show the same momentum dependence but have a considerably lower asymmetry. Therefore only the P220 data and the average over the three energy regions are plotted. Obviously, this different behaviour is due to the presence of the MEC and altered IC contribution along with their interference terms. As observed in the pn channel already, pion production exhibits no significant asymmetry.

6.5 Angular dependences

In the previous sections the cross sections are presented integrated over proton and neutron angles. These dependences are investigated in the following. It is anticipated that the angular distribution of the cross section exhibits additional information regarding the physics of the photo-absorption and SRC. The various contributions leading to G2N emission have different angular distributions. Considering the photon energy dependence, the MEC strength has a slightly decreasing contribution, whereas the IC shows a resonance-like structure and dominates around the Δ mass, hence around 250 ... 300 MeV. Consequently, due to the differently varying strength of these contributions and their interference, the total proton or neutron angular distributions depend on photon energy. In the top panel of Fig. 6.28 on page 135 the pn cross section versus neutron angle, which is averaged (mean-a) over all periods, is plotted for G2N knock-out and pion production. While the former reveals its maximum at about 80°, which is expected for back to back emission in the (^{4}He,γ)-CM system, the neutrons from the pion production process are distributed towards smaller polar angles. That is caused by the three-body phase space weakening the kinematical correlation between the two nucleons. It allows a more isotropic distribution, which is concentrated along the Lorentz boost in the laboratory system. The middle panel displays the angular distribution of the G2N process for $E_\gamma > 110$ MeV and the limited energy regions of the three periods (Tab. 6.2 on page 105). Note that, as for all the other spectra, the ToF solid angle acceptance (see Fig. 5.16 on page 97) has to be taken into account if these are compared with theoretical calculations. As has been expected, they show different features: While for low energies the distribution is smooth showing only the back to back correlation peak, at higher energies a second structure arises at about 50° which is more pronounced at higher energies. Whether this bump stems from 3B-absorption processes, MEC-ρ contributions or from SRC effects can only be clarified by comparison to theoretical calculations.

As mentioned above, the dependence of the transverse structure function W_{TT} and thus of the asymmetry on ϕ_m, the angle of the photon polarization with respect to the reaction plane, is trivial: a common factor of $\cos 2\phi_m$ can be pulled out of all terms of the structure function. However, the difference of the proton and neutron azimuthal angle ϕ_d, which

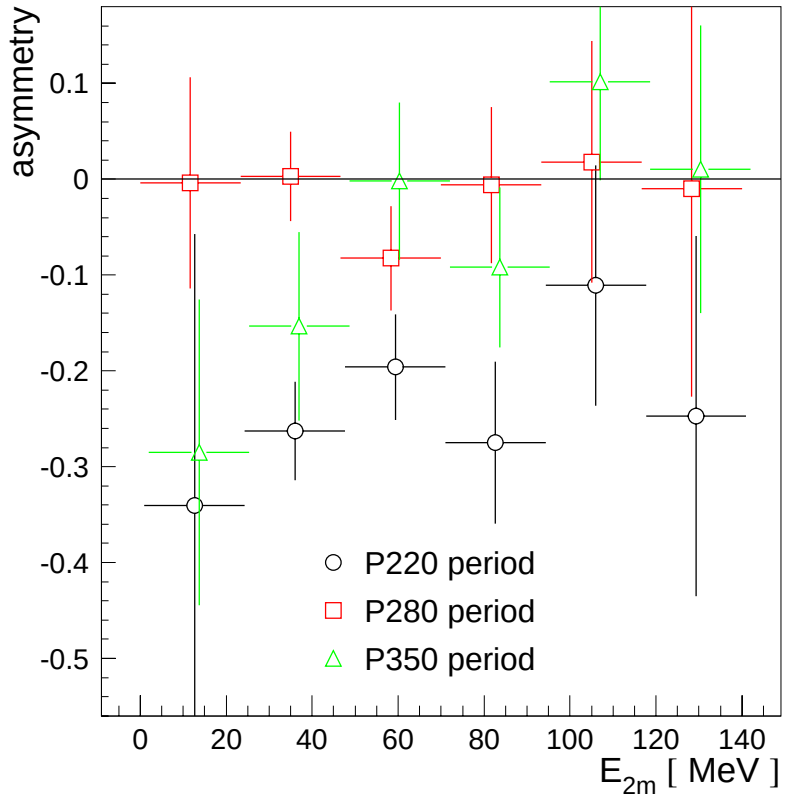

Figure 6.26: Plot of inclusive pp emission asymmetry versus missing energy in the range below pion production. For higher E_{2m} the asymmetry vanishes. The asymmetries for the photon energy regions are shown separately.

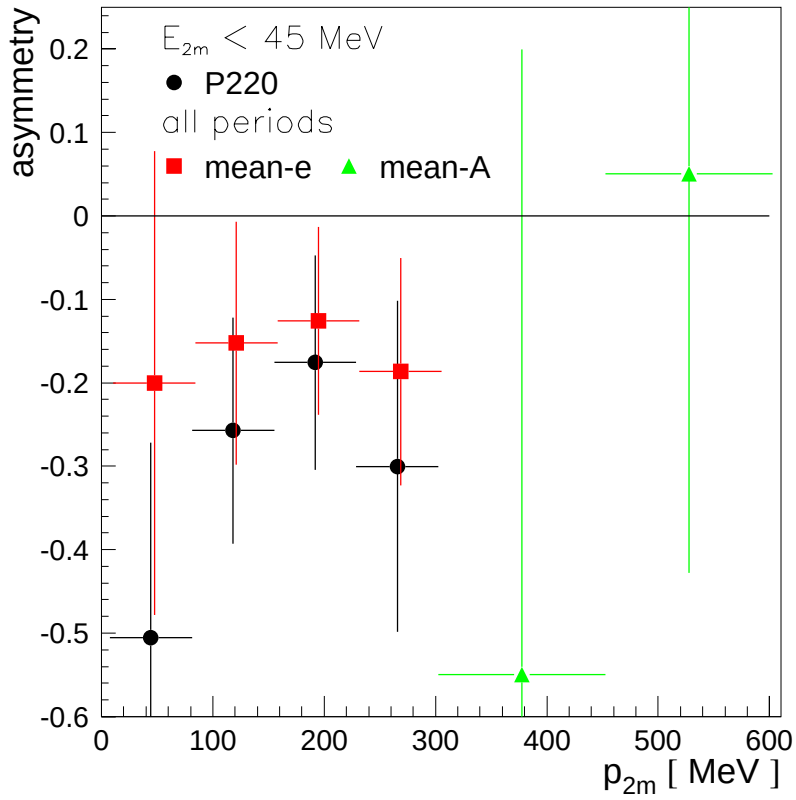

Figure 6.27: Asymmetry of G2N absorption in dependence of the pair momentum for the P220 period and combined. The average of the periods was performed via the mean-e (mean-A) method for low (high) p_{2m} with respect to the statistics.

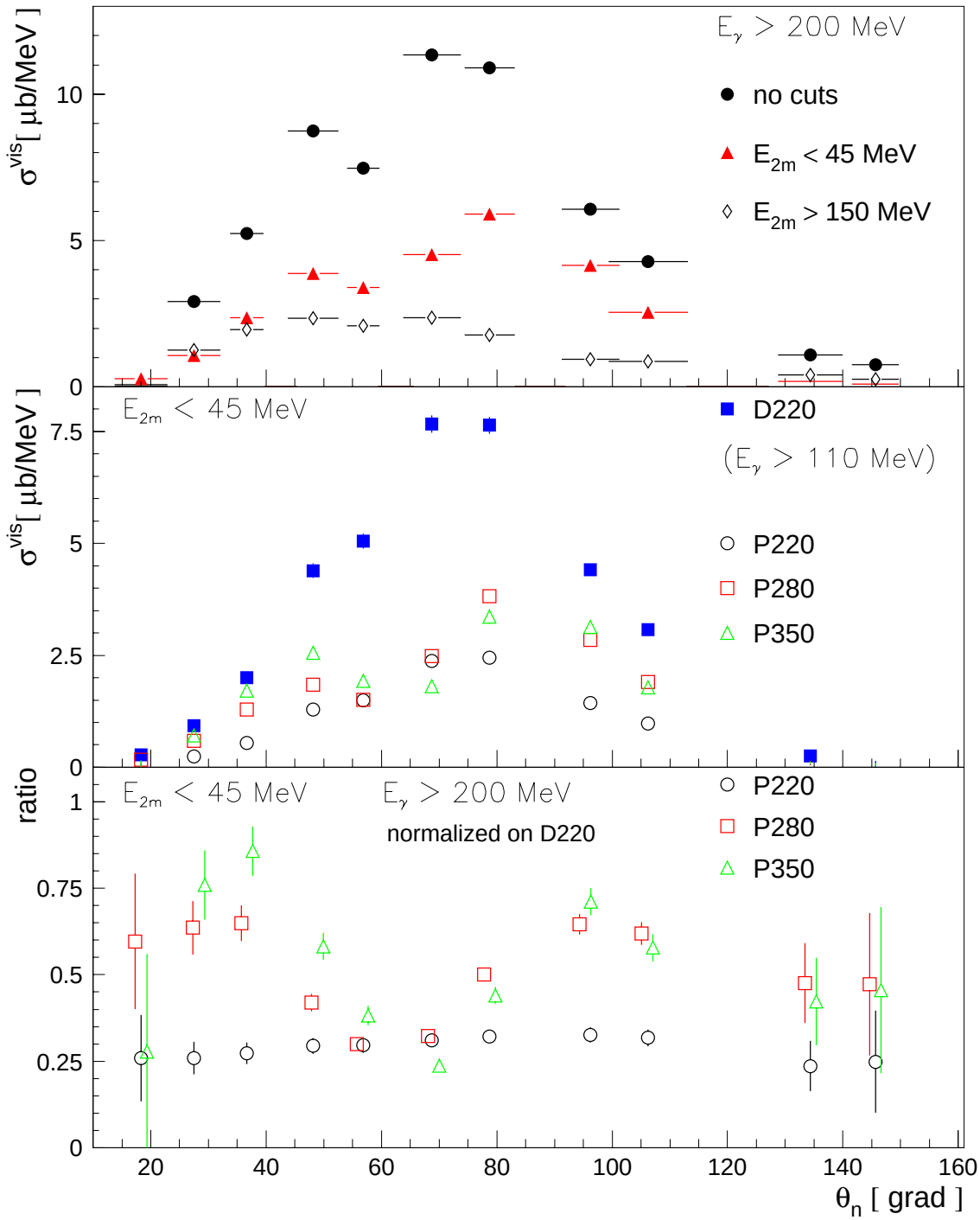

Figure 6.28: (upper) Total pn cross section versus neutron polar angle together with cuts on C_{G2N} and C_π. (middle) Neutron angular distribution with C_{G2N} cut for the whole energy range D220 and three energy regions (P220...P350). The latter are plotted (lower) as ratios with respect to the angular distribution for all photon energies (D220). The error bars along the neutron angle are omitted in the lower panels for the sake of clarity.

is a measure for the non-coplanarity, enters the asymmetry. Fig. 6.29 shows that the ϕ_d dependence of the asymmetry differs for the three energy regions illustrating its complicated dependence on photon energy and ϕ_d. Parabolas were fitted to the data to guide the eye

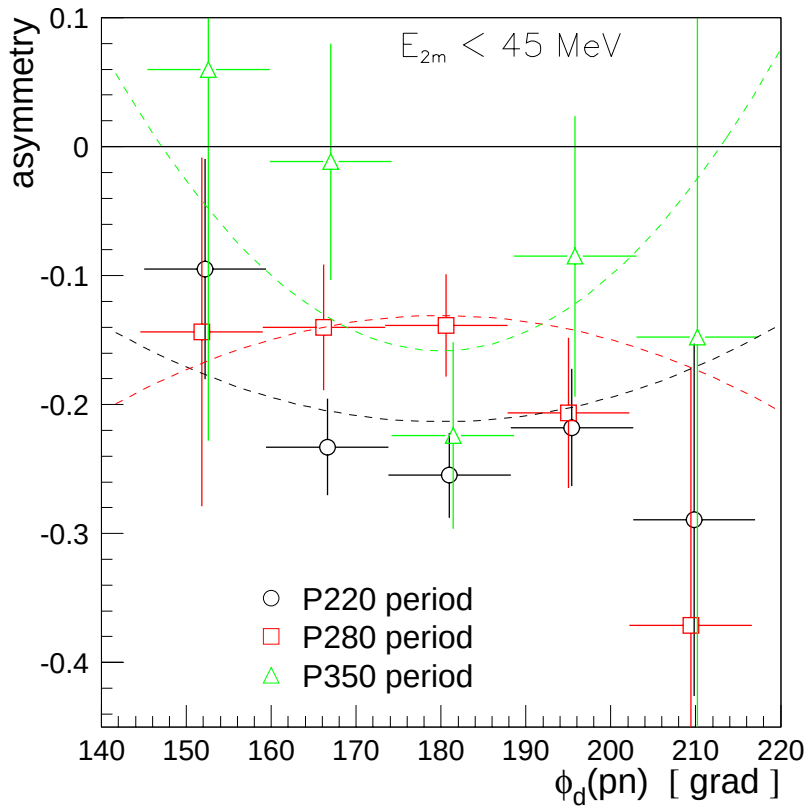

Figure 6.29: Asymmetry versus the proton-neutron difference azimuthal angle ϕ_d for three periods. The parabolas fitted to the data are meant to guide the eye. Due to symmetry reasons, they are restricted to the quadratic term only: $\Sigma = a + b(\phi - 180°)$ All three fits result in $\chi^2 \lesssim 1$.

(Σ is symmetric with respect to ϕ_d constraining the fit to the quadratic term). Again, these data demonstrate the interference of the 1BC, MEC and IC currents and thus impose constraints on the choice of the SRC-model entering the calculation of these contributions.

The same complicated behaviour of the asymmetry for pn knock-out is found in the observable θ_p, the proton polar angle, see Fig. 6.30 on page 138. While at intermediate energy the asymmetry stays rather constant over PiP's angular range, with larger proton angle it raises at low energy and tends to zero at high energy. In the same manner as for the neutron angular dependence (see Fig. 6.31 on page 138), this is the result of diverse magnitudes of the three contributing currents at different photon energy. Because the IC current dominates in the P280 period, one can conclude that it has only a weak proton angular dependence in the respective range. At low energy (D220) the MEC dominates and at high energy it is comparable with the IC strength. Obviously the interference of the MEC with the 1BC and the IC is such that it yields the same asymmetry value at forward but a totally different value at backward angles. From this observation, it can be assumed that especially the angular dependence at low energies — where the 1BC contributes most — should be a sensitive measure of the 1BC strength and thus of the SRC model utilized in calculations.

The asymmetries as a function of the neutron angle spectrum (Fig. 6.31 below) exhibit the same shape for all periods. The maximum value of the asymmetry is not located at the maximum cross section, which is reached around 80°, but at more forward angles, namely about 50°. The large increase of the asymmetry in between 30° and 50° coincides with the extra strength at low neutron angles (compare with the bump in Fig. 6.28 on page 135, lower panel). In that angular range, the steps in the asymmetry increase with photon energy and thus reveal the same energy dependence as the respective bumps in the cross section.

The distribution of the proton-neutron opening angle θ_{pn} shown in Fig. 6.32 on page 139 is closely related to the proton and neutron polar angle spectra. While for the proton angular spectrum θ_p all neutron angles were summed over (and vice versa for θ_n), the θ_{pn} spectrum comprises a summation over arbitrary final pair- and relative momenta leading to the same opening angle. This observable is plotted per period and low missing momentum in addition to linear fits indicating the run of the curves. At low and medium energies the asymmetry rises with larger opening angles, whereas at high energy (above the Δ resonance) the asymmetry decreases. As for the proton angle asymmetry (see Fig. 6.30 below), the high energy data exhibit a diametrical behaviour. The question arises, whether the basic contributions to G2N emission — the 1BC, MEC and IC — and their interference are sufficient to account for this energy dependence, or whether a new type of reaction takes place. A possible explanation could be a 2N absorption involving a virtual pion in the final state, hence some sort of FSI (compare Fig. 6.13(b) on page 118) which does not alter the energy of the knocked-out nucleons.

Another interesting observable emerges from the comparison of the 2N knock-out with the so-called quasi-deuteron (QD) model. This model describes the pn pair inside a nucleus as a deuteron moving with the pair momentum of this pn pair. The cross section of the 2N knock-out in the CM frame of the pn pair is thus taken to be the one of a free deuteron. Hence, in that model the neutron angle in the CM frame is defined by the proton kinematics alone. θ_{diff}, which is plotted in Fig. 6.33 on page 139, is the difference of the actual measured neutron angle and the one given by the QD model in the laboratory frame. The smaller θ_{diff} the more the pn pair behaved like a deuteron inside the nucleus. Large values indicate different relative momenta with respect to the momentum distribution inside a deuteron. Due to the higher density in helium compared to deuteron, the mean nucleonic distance is smaller and therefore SRC effects should be enhanced. Hence, especially the short range part of the correlated relative wave function of a pn pair inside a nucleus differs from the deuteron one which leads to a distinct final state. Therefore it can be supposed that large θ_{diff} events originate from photo-absorption processes where the involved nucleons have been in close proximity and thus carry information about SRC. These observations might be explained by the dominance of the IC current at medium energies which has a different strength in the deuteron[9]. Astonishingly the asymmetry is rather constant for the low

[9] Due to conservation of angular quantum numbers, the non-resonant IC current (see Fig. 4.7 on page 62) does not contribute

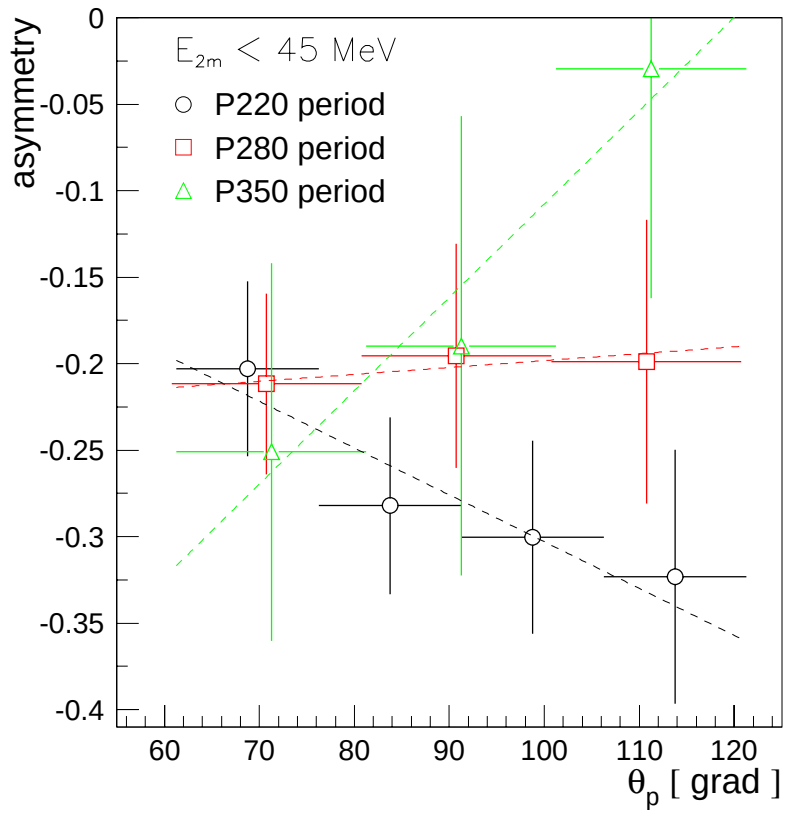

Figure 6.30: Asymmetry for pn knock-out plotted versus the proton polar angle covered by PiP. The angle is plotted for three photon energy regions along with linear fits to emphasize the runs of the data points. All fits yield $\chi^2 \lesssim 1$.

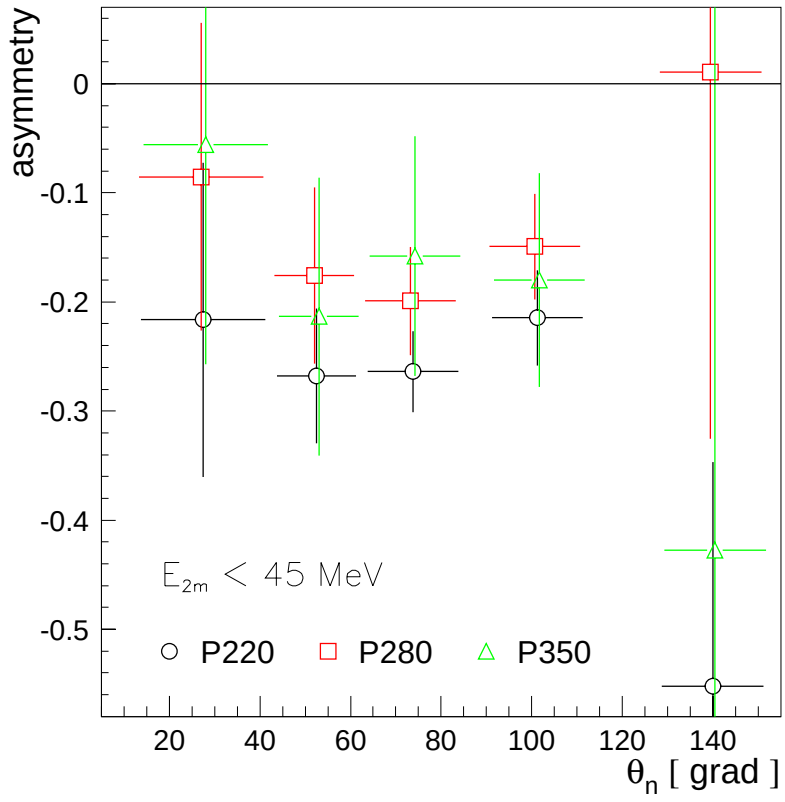

Figure 6.31: Neutron angular asymmetry over the range covered by ToF. The distribution is plotted for each period separately. The events are subject to the cut on low missing energy, i.e. the C_{G2N}.

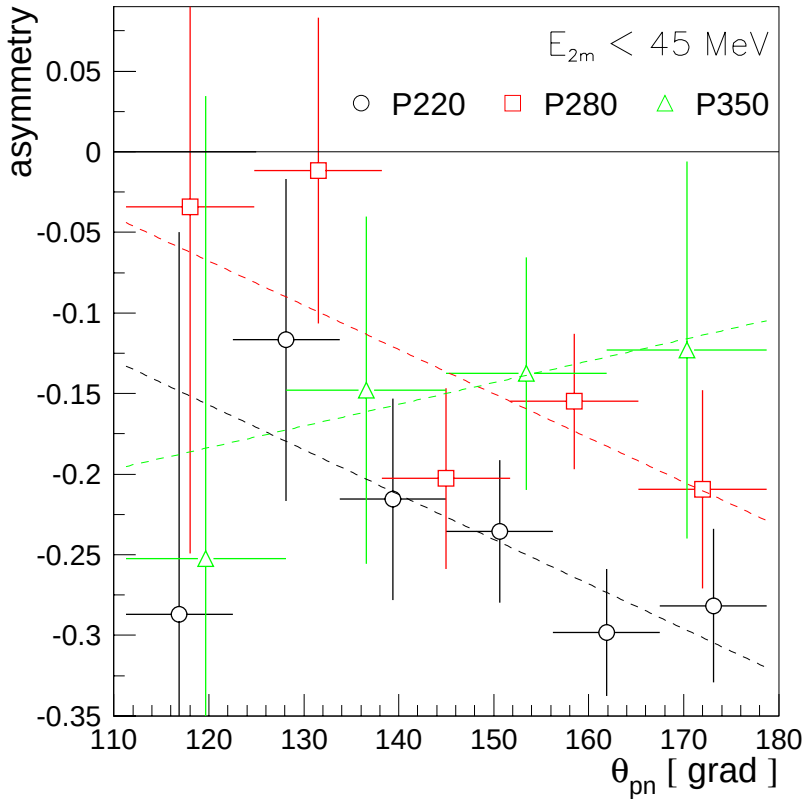

Figure 6.32: Asymmetry per period for low missing energy (C_{G2N}) versus the proton-neutron opening angle. There is no underlying physical model of the linear fit. They are just meant to guide the eye.

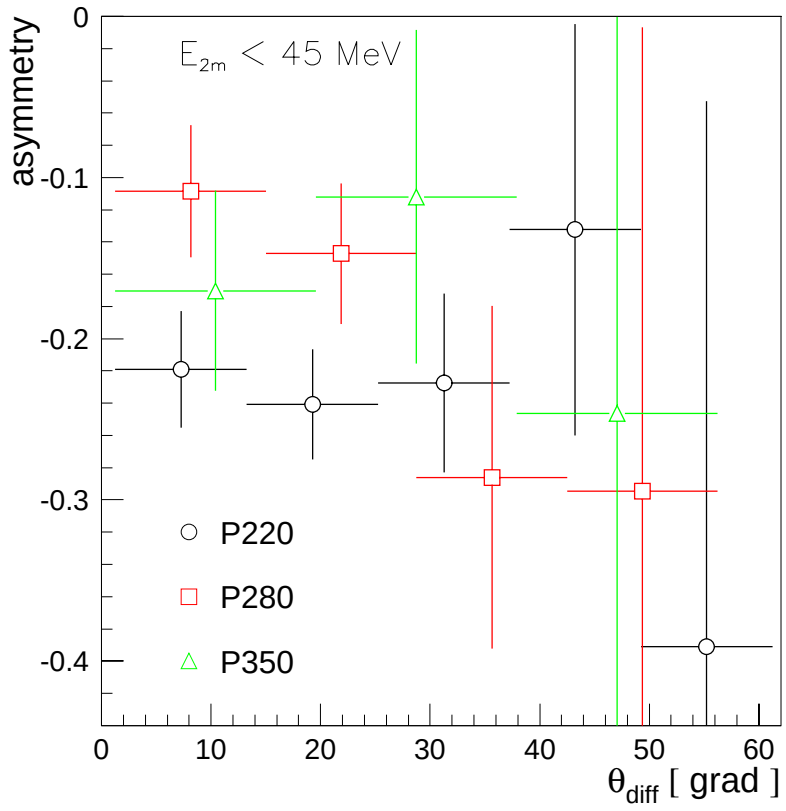

Figure 6.33: The polar difference angle θ_{diff} is defined by the measured neutron direction and the one given from the QD model (see text). The asymmetry of this observable is displayed for each period separately with a cut in missing energy on the break-up peak.

and high energy regions. However, at medium energy it increases the larger the deviation from the QD model. For a more detailed interpretation of this spectrum (Fig. 6.32 above), theoretical calculations are essential.

Differences between the pn and pp emission strength, which were found in Section 6.2 and Section 6.4 are also seen in the angular distributions. The cross section of pp emission versus the proton polar angle in ToF is shown in the upper panel of Fig. 6.34 below and demonstrates the different neutron angular dependence of the G2N emission and pion production. The latter is strongly forward peaked (even more pronounced than in the pn channel), whereas the pure pp emission strength has its maximum at 80°, as has been expected from the favoured back-to-back kinematics. Compared to the neutron angular distribution of the pn channel (Fig. 6.28 on page 135), several discrepancies can be observed: the bump around 35° occuring for medium and high photon energies (P280,P350) is only present in the pp case for the lower energies, but is not seen in the P350 data (compare middle and lower panel). There is a dip at about 95° in all three photon energy regions. Due to the fact, that MEC do not contribute, the angular distribution observed in the pp channel is based on the IC and its interference with the 1BC solely. It is astonishing, but emphasizes the different angular dependence of the pp and the pn channel, that the ϕ_d asymmetry of pp emission (Fig. 6.35 on page 142) shows no significant structure. For all periods the asymmetries are fairly flat, reflecting just the average asymmetry values in the respective photon energy ranges. From this observation it can be deduced that the IC is obviously rather independent from ϕ_d. Only at high photon energies (P350) the asymmetry seems to decrease with larger ϕ_d. It is thus conceivable that the richer structure of the ϕ_d asymmetry in the pn channel results from the interference with the MEC. Yet, both statements can only be veryfied and explained with the help of theoretical calculations. It would be interesting to see whether different descriptions of SRC would lead to different ϕ_d behaviour thus providing an extra contraint to discriminate certain SRC models.

A similar situation is observed in the proton polar angle asymmetry of PiP, which is plotted in Fig. 6.36 on page 143 for the three periods. In contrast to the pn case, the dependence on the proton angle, namely a decrease of the asymmetry with larger backward angles, shows no or only a marginal photon energy dependence. While for pn knock-out the asymmetry of the low photon energy data (P220) increases and for P350 decreases with larger proton angles, the pp data set show a common decreasing asymmetry for backward angles.

The reason for the vanishing asymmetry at medium photon energies, i.e. the P280 period, is found in the proton polar angular spectrum of ToF (see Fig. 6.37 on page 143). In both observables (proton polar angle in PiP and ToF) the asymmetry has positive and negative values, but with a contrary behaviour: for small ToF-proton angles the asymmetry is positive and negative for large angles and vice versa for the PiP-proton angular distribution. In the asymmetry of the excitation function, these findings result in a very small asymmetry in the respective energy region due to the summation over both angles. At high and low photon energy a very similar behaviour of the asymmetry is observed; yet, they have a larger negative bias than the medium photon energy data.

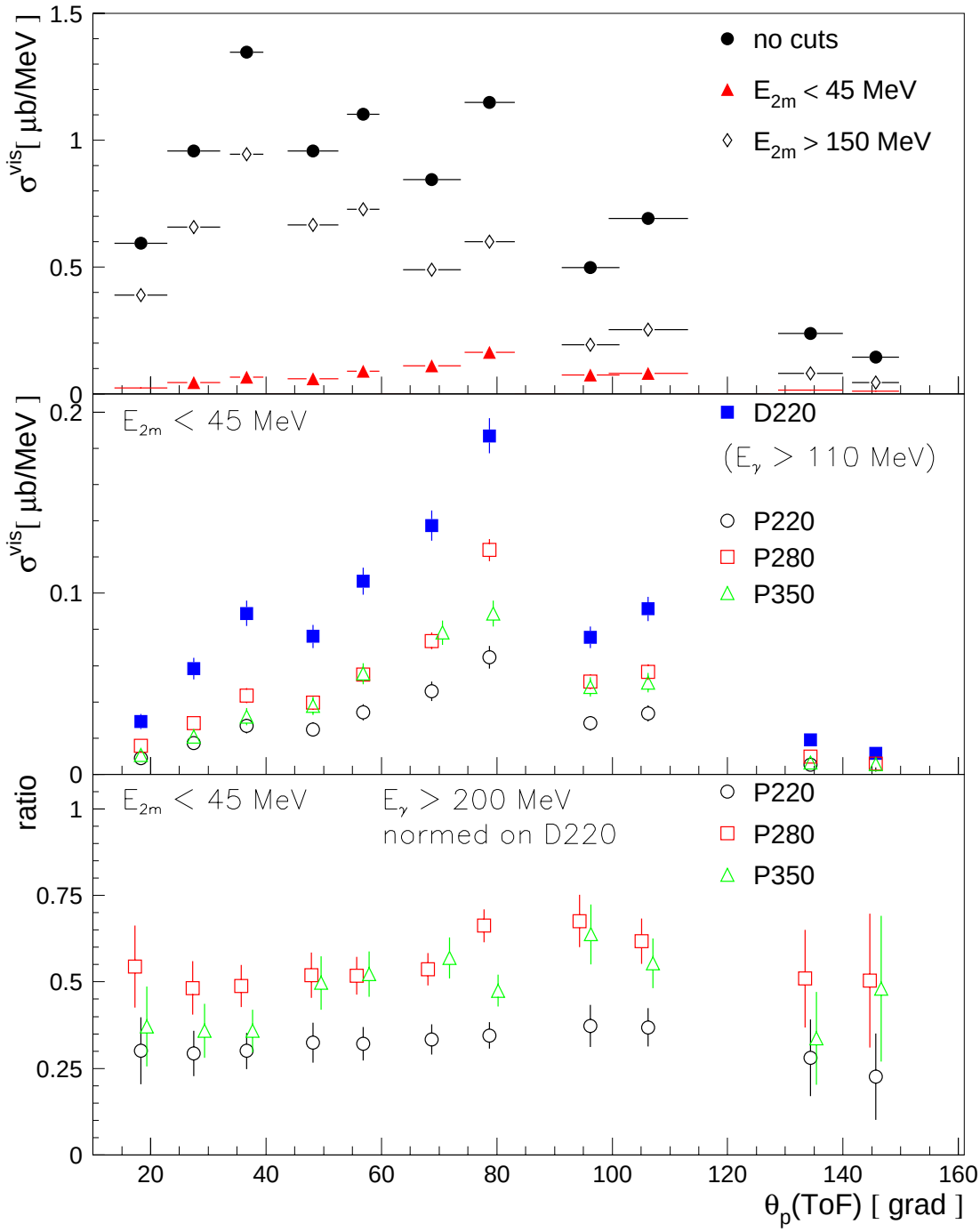

Figure 6.34: Cross section for pp emission versus proton angle in ToF combined (upper) and for all periods individually in the lower panels. The middle panel displays the angular distribution for the whole photon energy range and three energy regions (P220...P350). (lower) The ratios of these three distributions with respect to the D220 period are shown.

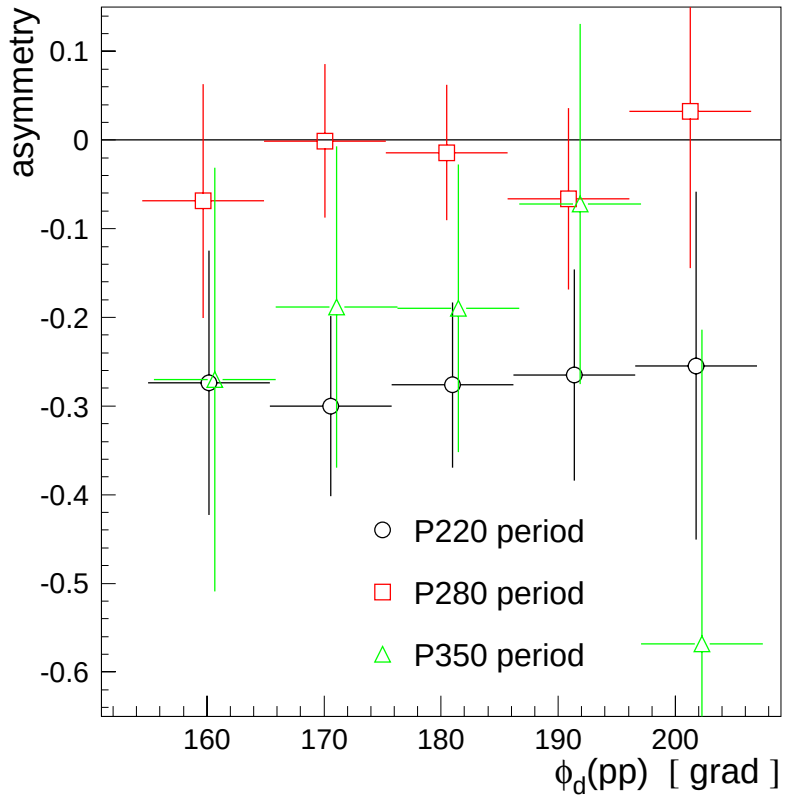

Figure 6.35: Asymmetry of pp emission versus ϕ_d for all periods separately and low missing energy, hence G2N absorption. ϕ_d is the difference of the azimuthal angles of both protons, see Section 6.1.

The proton asymmetry of both the PiP and ToF polar angles depend only marginally on photon energy and thus show the same angular behaviour which indeed is quite different with respect to the isospin channel. Therefore the asymmetry of the proton-proton opening-angle reveals a richer structure than the individual spectra of the proton and neutron angles. This observable is plotted in Fig. 6.38 on page 144 together with a fitted linear dependence to guide the eye. While the low and high photon energy data agree among each other having the largest values at small opening angles, the mid-energy data-set (P280) shows again a very small asymmetry which is even slightly positive at low angles. The latter thereby reproduces the asymmetry values of the PiP and ToF proton angular spectrum at $\theta_p(\mathsf{PiP}) \gtrsim 90°$ and $\theta_p(\mathsf{ToF}) \lesssim 40°$ respectively.

As stated in Section 6.2, the observable θ_{diff} (see Fig. 6.39 on page 144) is a measure of the different behaviour of a pn pair inside a nucleus compared to the deuteron. It is supposed that SRC effects induce large values of θ_{diff}. Despite the strong energy dependence of the asymmetry, all three periods exhibit a similar behaviour on θ_{diff}: for small and large angles the asymmetry is small but at around $20° \ldots 25°$ it is maximal. The pp asymmetry thereby reveals again its different nature with respect to the pn channel. One should expect that it is especially the θ_{diff} asymmetries of both isospin channels which impose severe constraints on SRC descriptions provided the 2N knock-out process is described correctly by the model.

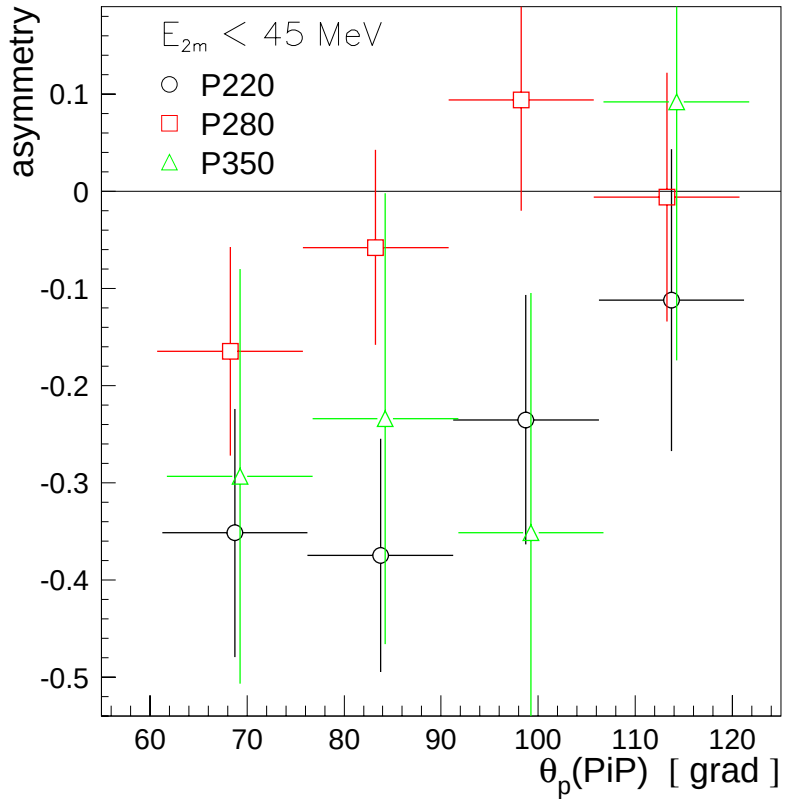

Figure 6.36: Proton polar angle dependence of the G2N-absorption asymmetry. The asymmetry is plotted per period over the range covered by PiP.

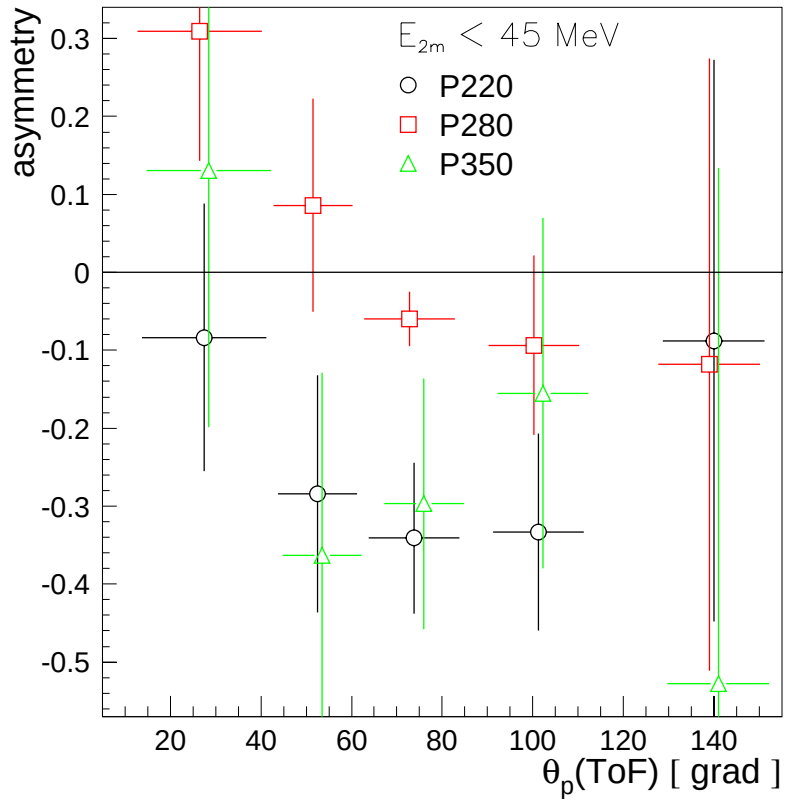

Figure 6.37: Asymmetry versus the proton polar angle covered by ToF for all photon energy ranges defined by the three periods P220...P350. The data is constrained on low missing energies.

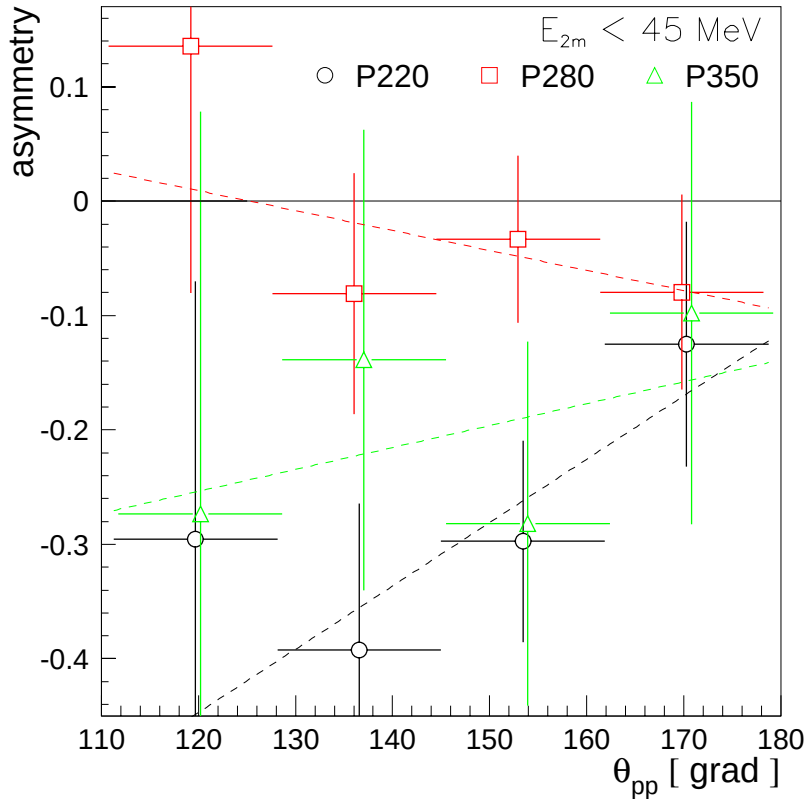

Figure 6.38: Plot of the asymmetry depending on the proton-proton opening angle. The periods are shown individually for G2N absorption process.

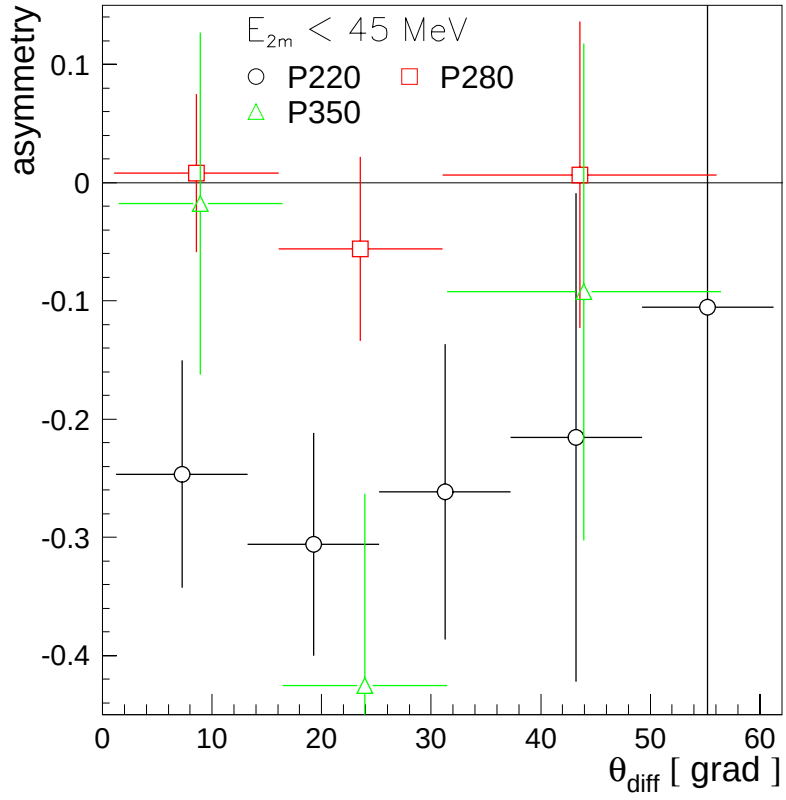

Figure 6.39: Asymmetry of θ_{diff}, the difference angle between the measured proton angle in ToF and the one given by the QD model (see text), for low missing energy and all periods separately.

6.6 Further studies

The problem of separating the 3B contribution, which is particularly severe for the pp channel (see discussion on page 126), is resumed here. The excitation function and photon energy dependent asymmetry is investigated for the standard C_{G2N} cut and the additional cut in missing momentum: $C^{A}_{\mathsf{G2N}} : C_{\mathsf{G2N}} \text{and} p_{2m} < 250$ MeV. In Fig. 6.22 on page 128 these cuts are denoted as A+B and B. With the additional constraint on missing momentum, the 3B contribution is further reduced. The excitation functions of the pn and pp channels are plotted in Fig. 6.40 below for both cuts along with the cross section ratios for cut C^{A}_{G2N} versus cut C_{G2N}. In case of pn knock-out there is no big effect: the ratio drops from 1 to 0.8 with increasing energy indicating that higher pair momenta are sampled with higher E_γ. Regarding pp emission the effect is more severe; the ratio decreases rather strongly reaching 0.5 around 300 MeV and demonstrates thereby that the 3B strength dominates for higher photon energies. The impact of this cut on the asymmetry is shown in the lower panel of this figure. In general the asymmetry is more negative for the extra constraint on missing momentum: $p_{2m} < 250$ MeV. This finding proves the further enhancement of G2N and therewith the stronger suppression of the competing 3B absorption and FSI processes. However, it is possible that this additional cut might be too severe and that thereby good G2N events with high pair momenta (compare Fig. 6.9 on page 114), possibly driven by SRC effects, are omitted.

It was observed that the angular distribution of the 2N-emission cross section depends on photon energy. For further clarification of this mutual dependence, the excitation function, missing momentum and its asymmetries are plotted for 4 neutron angular regions in Fig. 6.41 on page 147. These regions were chosen such that the extreme kinematics (far forward and backward angles) and the high strength regions (QD domain and around perpendicular angles) were sampled, see Tab. 6.4. In the first three regions a consistent

region	no.	θ^{n}_{low}	θ^{n}_{high}
far forward	1	15	57.5
forward	2	62.5	82.5
perpendicular	3	90	110
backward	4	130	155

Table 6.4: Regions of neutron polar angle used as cuts for the excitation functions and asymmetries.

behaviour is found: From far forward to perpendicular neutron angles (region 1...3), the excitation function increases at lower photon energies and the missing momentum distribution shifts to lower p_{2m} values. Yet, at backward angles a totaly different behaviour is noticed: the p_{2m} distribution is concentrated at high momenta which are necessary to compensate for the antiparallel (with respect to the incident photon) directed neutron momentum. The resonance like structure of the excitation function around 250 MeV, which is most pronounced at forward angles (regions 1 and 2) and caused by the IC contribution, is not seen at backward angles. There the excitation function drops nearly monotonically,

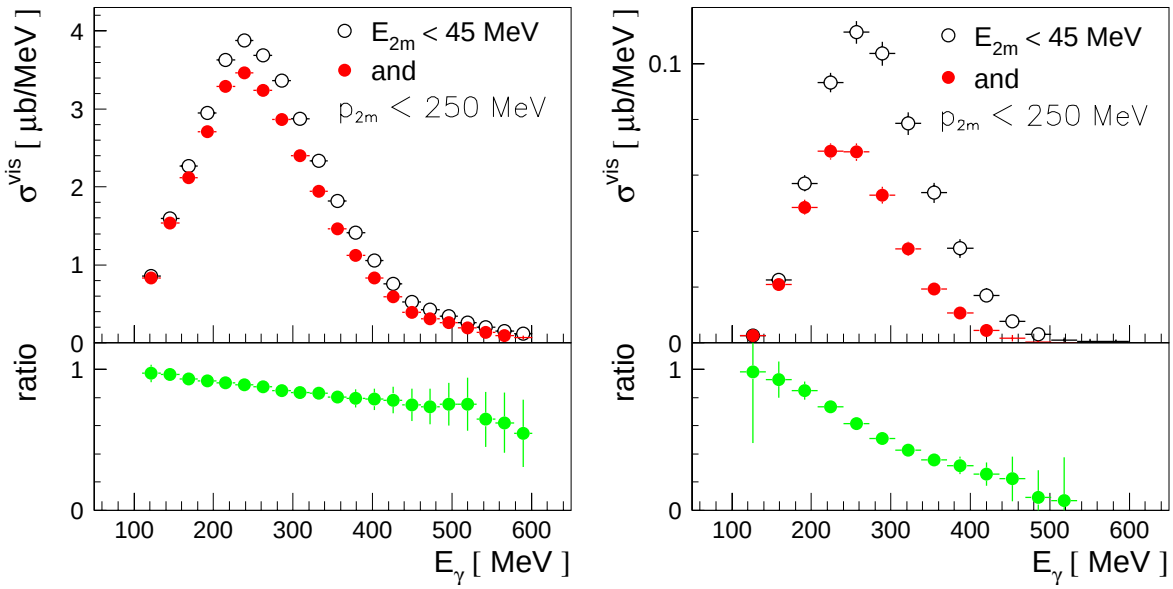

(a) Excitation functions for two cuts along with their ratio on cut C^A_{G2N}

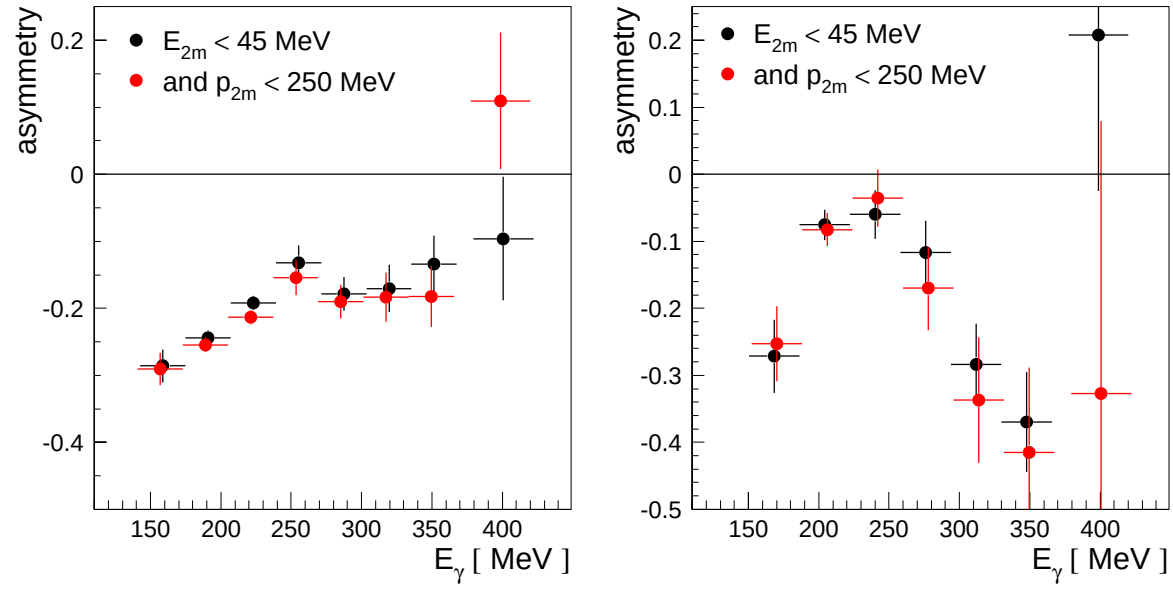

(b) Asymmetries for both cuts binned with the mean-e average

Figure 6.40: Excitation functions and asymmetries of the pn (left) and pp (right) channels for the cuts C_{G2N} and C^A_{G2N} which rejects high missing momenta in addition.

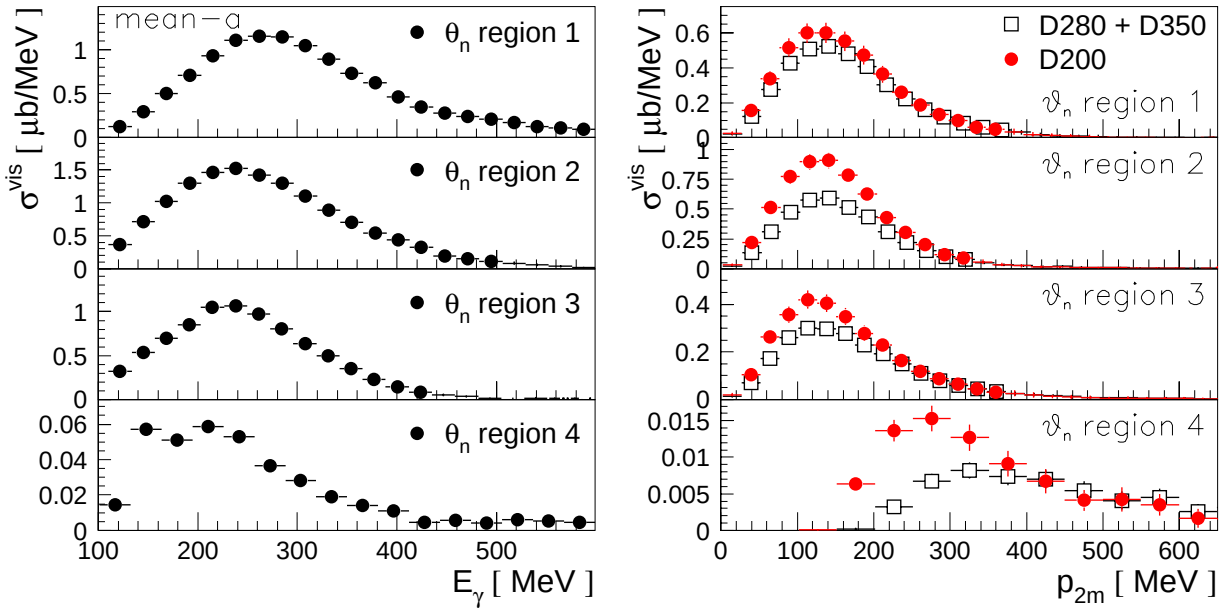

(a) Excitation function *(left)* and p_{2m} spectrum *(right)* for low and combined medium and high photon energies

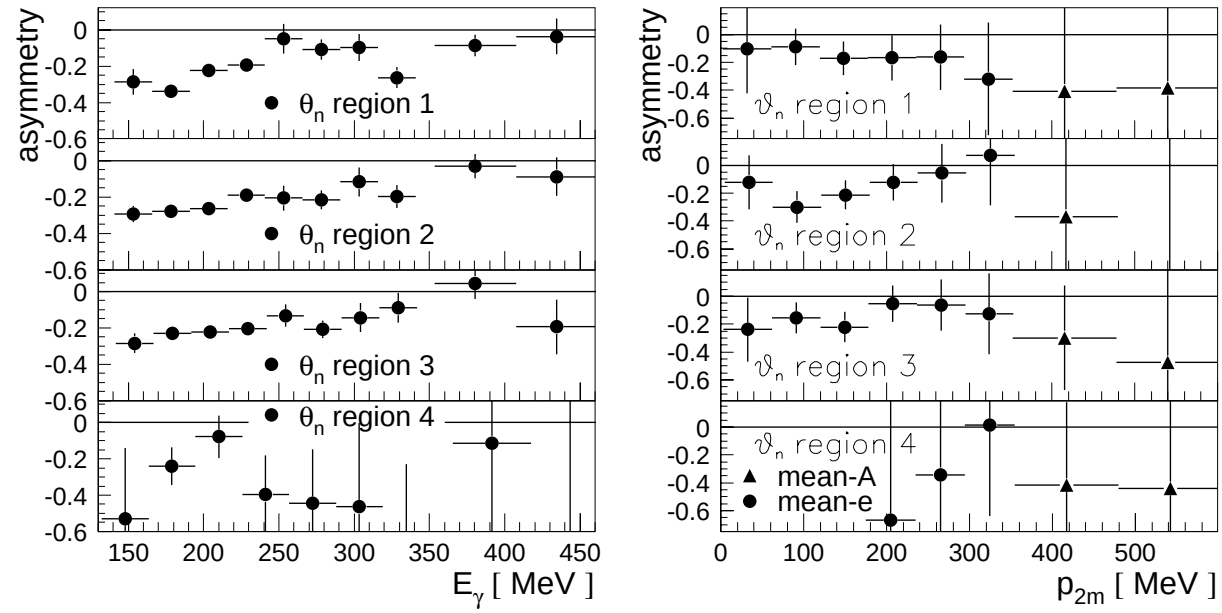

(b) Asymmetry versus photon energy *(left)* and missing momentum *(right)*

Figure 6.41: Cross sections and asymmetries plotted versus photon energy and missing momentum for four neutron angle regions defined in Tab. 6.4 on page 145.

which is a typical feature of the photon energy dependence of the MEC [92]. From these observations it could be presumed that the IC dominates at small neutron angles and the MEC at large ones. However, for clear statements this circumstance has to be studied in more detail with the help of theoretical calculations.

While the asymmetries of the excitation function reveal more or less the same photon energy dependence in regions 2 and 3, the extreme regions (far forward and backward angles) have a contrary behaviour around 250...300 MeV, hence the domain of the Δ resonance. According to [41] the IC has in principle a negative asymmetry. That implies that this contribution is maximal at far forward angles, which however would contradict the statement made above and thus urgently calls for a theoretical description to clear the situation. Similar, the behaviour of the asymmetry versus p_{2m} shows a dependence on neutron angle.

Asymmetry of observables which are functions of photon energy and thus comprise events at different energies depend indirectly on the minimal polarization $P_{\min}$. The regions of photon energy entering these observables, like E_{2m} or θ_{pn} for instance, are defined by $P_{\min}$. The question arises whether the choice of the minimal polarization is a possible source of a systematic error thereby introducing additional uncertainty. To study the impact of $P_{\min}$, the missing energy and momentum were analysed for three different values of the minimal polarization. Their asymmetries are plotted in Fig. 6.42 below as well as ratios with respect to $P_{\min} = 0.2$. Different values of the minimal polarization implicate distinct contributing photon energy regions and thus different asymmetry values which account for the discrepancies observed. For the D220 period, for example, the cuts based on the $P_{\min}$ values $0.1, 0.2$ and 0.3 result in the widths $109, 70$ and 43 MeV of the respecting photon energy ranges. Note that for $P_{\min}$ the second lattice vector, i.e. around $E_\gamma \sim 300 \ldots 350$ MeV, does not contribute. The differences of the asymmetries in both observables, missing energy and momentum, are relatively constant among the applied minimal polarization, which is clearer demonstrated by the plot of the ratios. No significant dependence on missing energy or momentum is seen in all four plots. The overlap of errors proves that the choice of $P_{\min}$ introduces no additional source of error in the asymmetries presented in this chapter.

For some derivations and resulting statements in the discussions above, occasionally use was made of the approximative validity of the factorized ansatz. Of course, unfactorized and thus more realistic treatments are available [92,143,144], but have very high computer power and time expenses [145]. For ^{4}He the theoretical calculations are not finished yet, however they are underway. The higher the photon energy, the better the factorized ansatz meets the unfactorized model. In order to test the extend to which this ansatz holds, its applicability was investigated here: The missing momentum was analysed subject to successive cuts in E_γ (see Fig. 6.43 on page 150) and plotted as ratio to a reference distribution, the missing momentum of the full photon energy range. The ratio drops significantly with increasing missing momentum for $E_\gamma < 200$ MeV, which indicates that at low energies more strength resides at low missing respectively pair momentum. However for photon

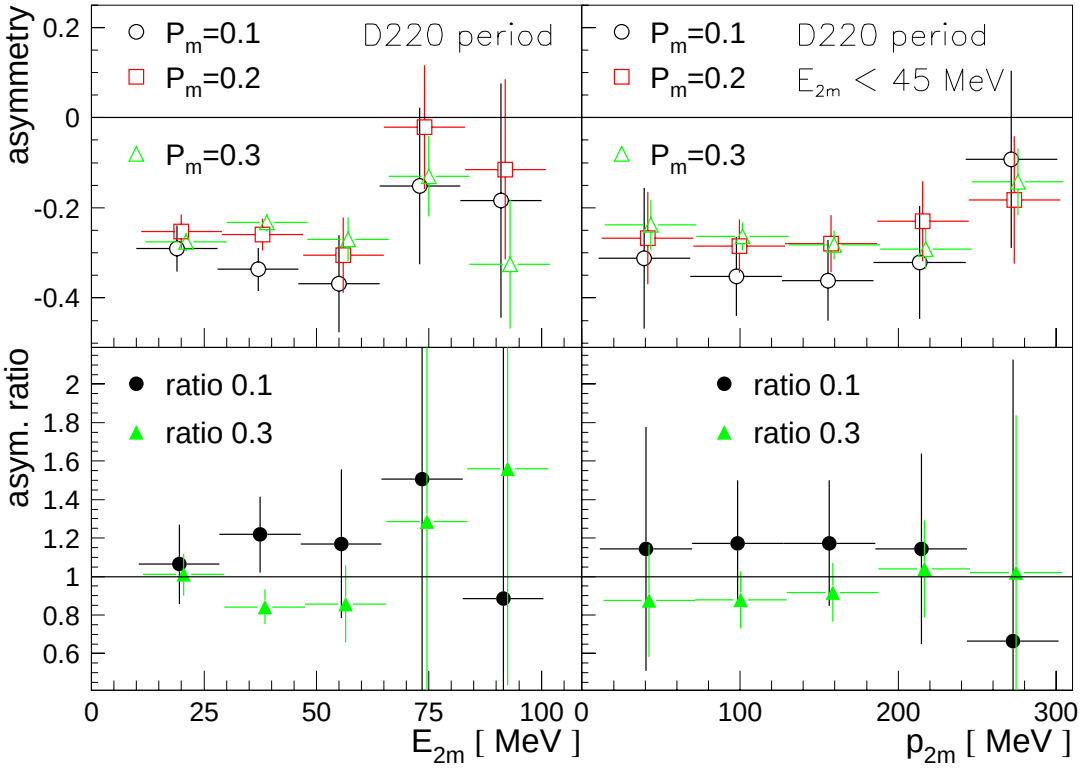

Figure 6.42: (upper) Cross section plotted versus missing momentum for three different minimal polarization P_{min}. The lower P_{min} the larger are the respective photon energy regions contributing to these spectra. (lower) Ratios of the cross sections for $P_{min} = 0.1$ and 0.3 with respect to the mean one.

energies above 200 MeV, the ratios are rather constant and show only a small momentum dependence in the range of the HO momentum regime. The latter is defined by the margin of the HO pair momentum, which reaches up to $\sim$ 250 MeV (see Fig. 6.8 on page 114). Without the extra strength at low missing momentum for $E_\gamma \lesssim 200$ MeV, the ratios would be even flatter. From these studies, which are supported by the model calculation shown in Fig. 4.13 on page 72, it can be concluded that the measured pair momentum distribution $F(K)$ is not independent from photon energy, but that for $E_\gamma \gtrsim 200$ MeV the dependence is small. Therefore, for the high energy regime the factorized cross section is a fairly good approximation, but of course it is not adequate for quantitative statements.

Theoretical considerations indicate, that the asymmetry should be less affected by FSI but should be rather sensitive to SRC effects. Indeed, the asymmetries of deuteron [146], helium, lithium and carbon, which are compared in Fig. 6.44 on page 151 show rather different features. However, the general trend of the asymmetries are similar: At low energies, just above pn emission threshold ($E_\gamma \ll 100$ MeV), the cross section is determined by an E1 transition implying a positive asymmetry. In a simple pn knock-out model (suitable only for low energies!), the pn pair is described by a quasi-particle with a dipole momentum because

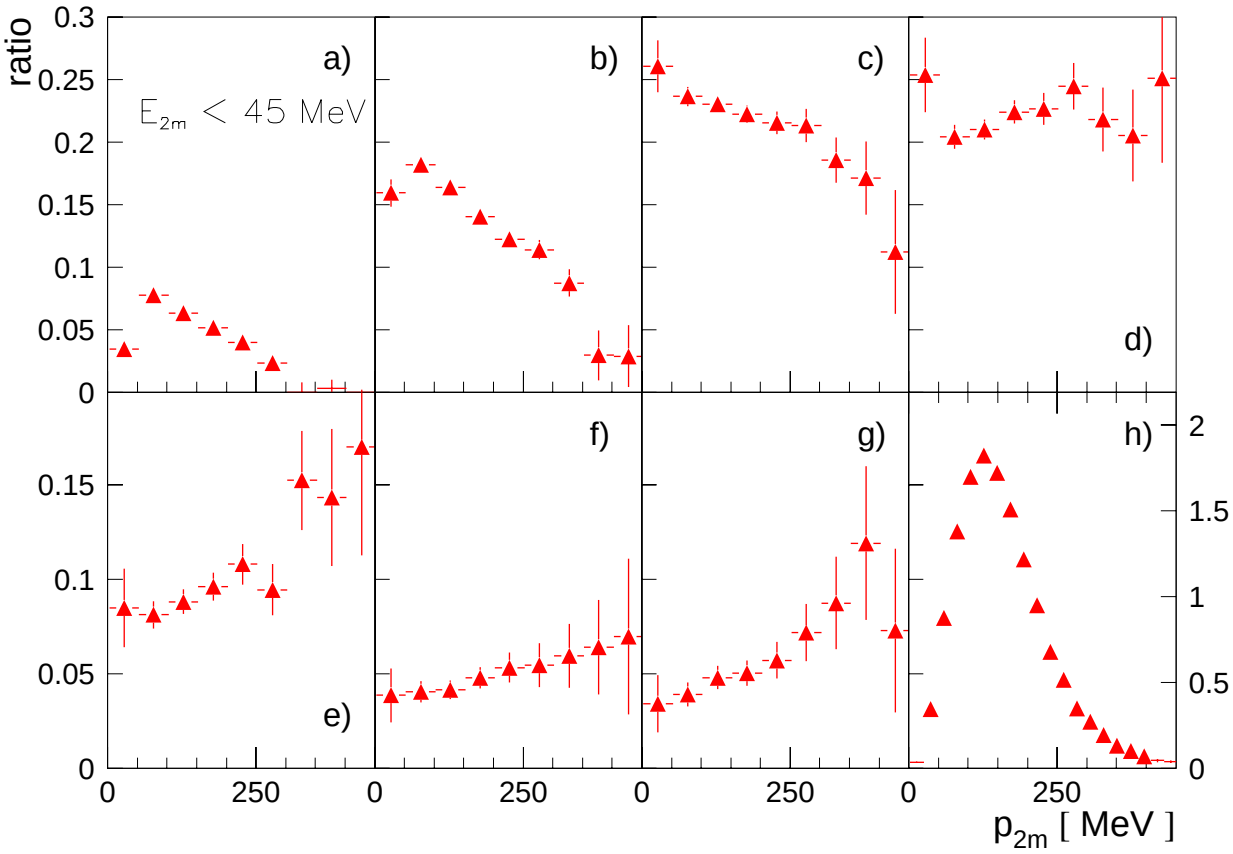

Figure 6.43: The missing momentum subject to the cut $E_{2m} < 45$ MeV is plotted for 7 small photon energy regions as ratio with respect to the missing momentum distribution for the whole $E_\gamma > 200$ range, which is shown in h). The E_γ regions are: a)=110-150, b)=150-200, c)=200-250, d)=250-300, e)=350-400, f)=400-450, g)=450-600 MeV.

the centre of mass and charge do not coincide. The photon couples with its polarization to it, which is an E1 process yielding a positive asymmetry. For photon energies around the Δ resonance, the IC dominates. The Δ excitation of the proton involves a spin flip necessitating a M1 transition. Hence, the photon couples to the spin current of a quark which results in a negative asymmetry around 200 . . . 400 MeV. At higher photon energies higher multipoles get important being the reason for the asymmetry to tend again to positive values ($E_\gamma > 600$ MeV). This qualitative behaviour is confirmed by Fig. 6.44 below. The most negative asymmetry with about -0.4 around the Delta resonance is found in deuteron target. Lithium is slightly more positive and ^{4}He even more, where the asymmetry reaches only -0.2 in this energy region. The experiments involving a carbon target [135] show that the asymmetry is a little less negative than from ^{4}He. The question whether these different asymmetries are a result of a possible medium dependence of SRC or whether these are due to nuclear many body effects (like FSI) is rather intricating and can only be solved by dedicated theoretical calculations.

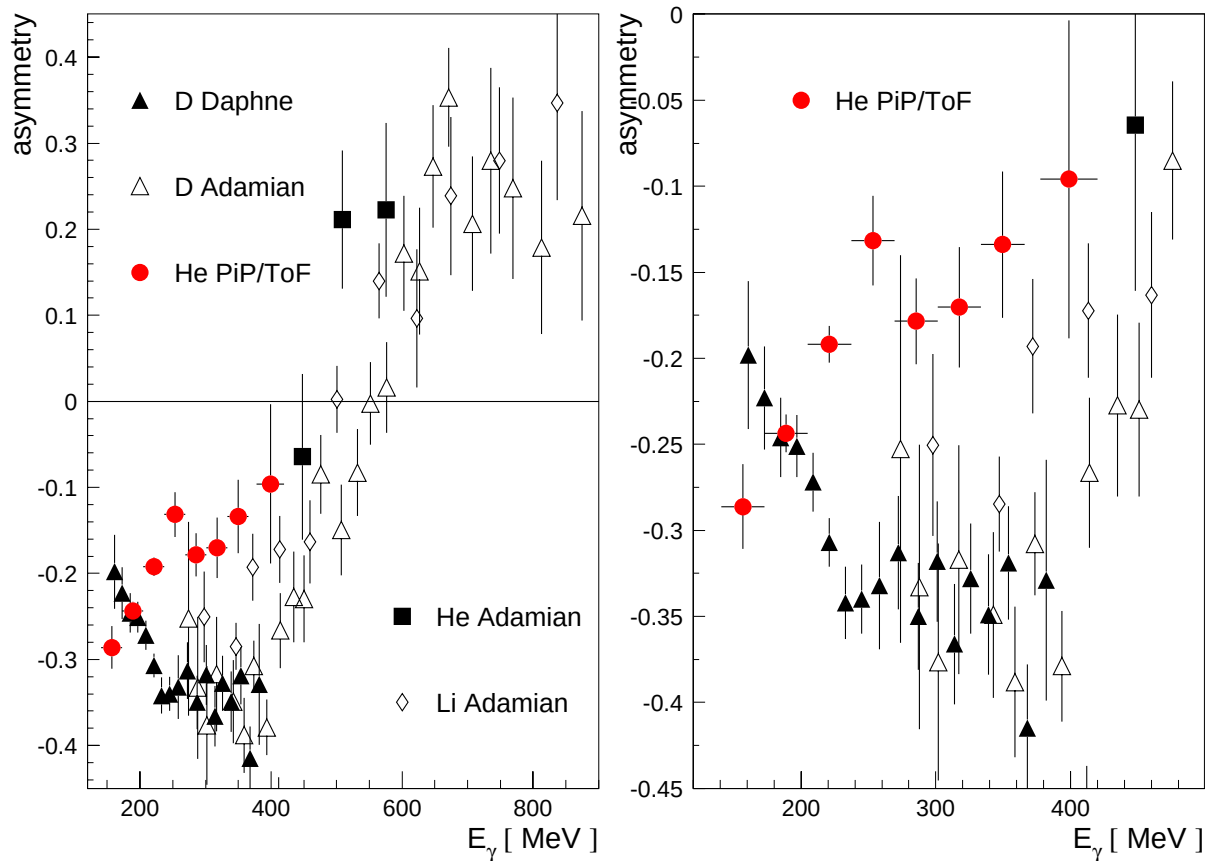

Figure 6.44: Asymmetry of pn excitation function of this experiment compared to the result of a measurement of the Adamian group [46] and of an experiment involving the Daphne detector [141, 147].

6.7 Comparisons to model

On account of the drawbacks, the model presented in Chapter 4 does not have the potential to produce quantitative and reliable predictions. However, this model is quite useful for quick surveys and for studying the expected influence of correlations on several observables. Due to the low computation-power needs — a spectrum takes typically 10 minutes on an average workstation — it can efficiently be searched for phase space or observables which show pronounced effects of SRC. Although this model it is not suitable for quantitative comparisons owing to its deficiencies, some calculations are presented together with the respective measured spectra. The calculations shown here are scaled by use of f_σ and f_Σ (see definition (4.43) and values in Tab. 6.5 below) in order to meet the measured data and render comparisons feasible. In Fig. 6.45 on page 153 calculations of the cross section and asymmetry of the pn-excitation function are shown for three different correlation functions and the HO case. Keeping in mind the simplicity of the model the calculation follows the cross section data astonishingly well. A large deviation is found above 450 MeV and is

corr. param.	HO	1,0.28	1.5,0.2	2,0.15
factor f_σ(pn)	0.69	0.87	0.77	0.67
f_σ(pp)	0.028	0.041	0.036	0.032

Table 6.5: Factors, according (4.43)*, applied to the model for comparison. All asymmetries are plotted with* $f_\Sigma = 0.6$

probably due to the limitation of this model on pion exchange. Heavier mesons, like the ρ, get important at high photon energy (past the Delta resonance), where the photon samples small nucleon-nucleon distances. The asymmetry seems to be even more sensitive to the shortcomings of the model: The disregard of heavier meson exchange leads to a wrong slope above 350 MeV, where the asymmetry should cross zero. The structure around 150 ... 250 MeV, i.e. the dip and the bump at these values, is not reproduced by the model. This originates probably from the limitation on central correlations only, because it is conceivable that the interference of currents including central and tensor correlations might produce such a structure. It is expected that the effect of tensor correlations is maximal around the Delta resonance. From the measured excitation function, it can be deduced that the description of the data improves by the use of correlated wave functions. Harder correlation (larger b and c) result in a more pronounced Delta peak due to the suppression of the MEC. A correlated wave function leads to a generally larger asymmetry above 170 MeV and causes a steeper slope at low energies which is due to the 1BC contribution. These statements emerging from the comparison of the model predictions and the data indicate the high sensitivity of the asymmetry on the reaction mechanism and the wave function.

In Fig. 6.46 below the missing momentum spectrum is compared to the strength of the initial pair momentum distribution, according (4.42b), based on an HO and four different correlated wave function. Although the data is qualitatively described by the model, there are some significant deviations. The calculations systematically overestimate the cross section at low missing momenta ($\lesssim$ 70 MeV) and underestimates the data at the peak and just slightly above on the right flank, i.e. around 160 MeV. Part of the cause might be found in the strict SPA ansatz leading to $E_{2m} = Q$. In the 2N knock-out reaction it happens, as is demonstrated by the measured E_{2m} strength, that photon energy and momentum are transferred to the $A-2$ system leading to its excitation. That alters the shape of the p_{2m} distribution with respect to the calculation, which does not account for these FSI effects. Other sources might originate from the lack of ρ-exchange or the factorized approach employed here. Still the effect of SRC on the missing momentum distribution can be investigated. Two momenta regions are mainly affected: These are around the peak and at high momenta ($\gtrsim$ 300MeV). The peak position exhibits only a very small sensitivity on the choice of the correlation function. Compared to an HO calculation, correlations are able to enchance high momenta and to influence the width and therewith the centroid of the pair momentum distribution.

Model calculations of the cross sections and asymmetries in dependence of the proton polar angle were performed as well and are shown in Fig. 6.47 on page 154. The distribution was determined at two photon energies, which are $E_\gamma = 150$ and 350 MeV. The data of the P220

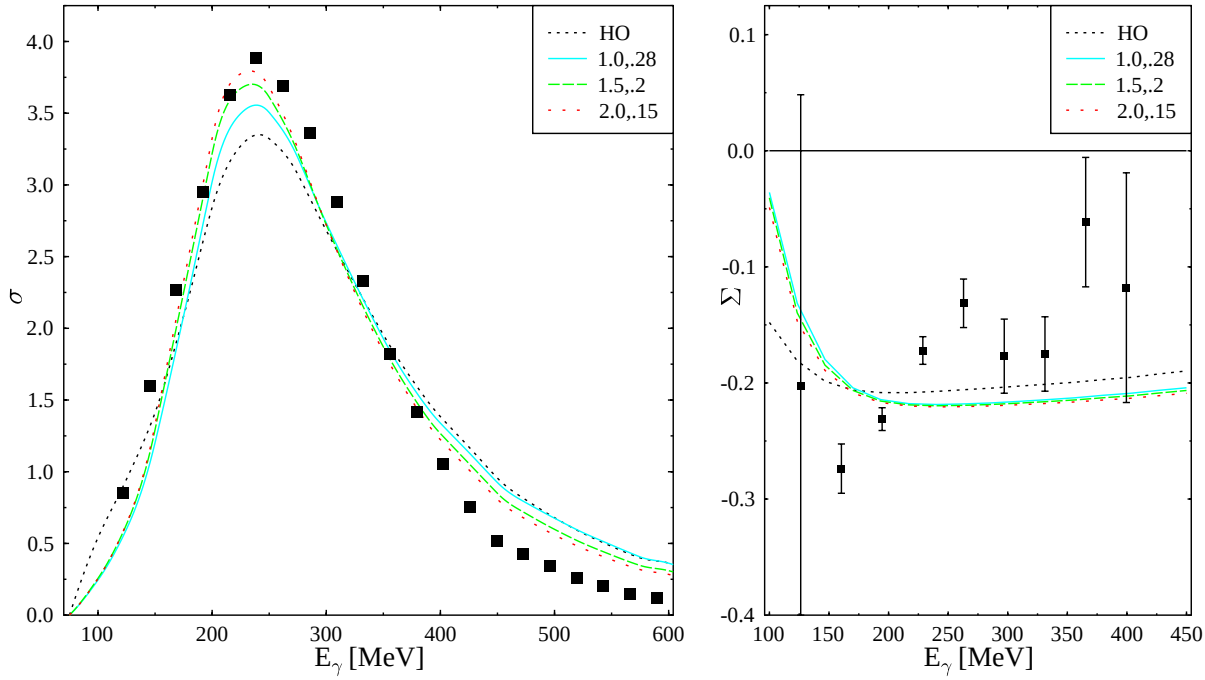

Figure 6.45: Cross section and asymmetry of excitation function for 3 different correlation functions and a pure HO wave function compared to the data.

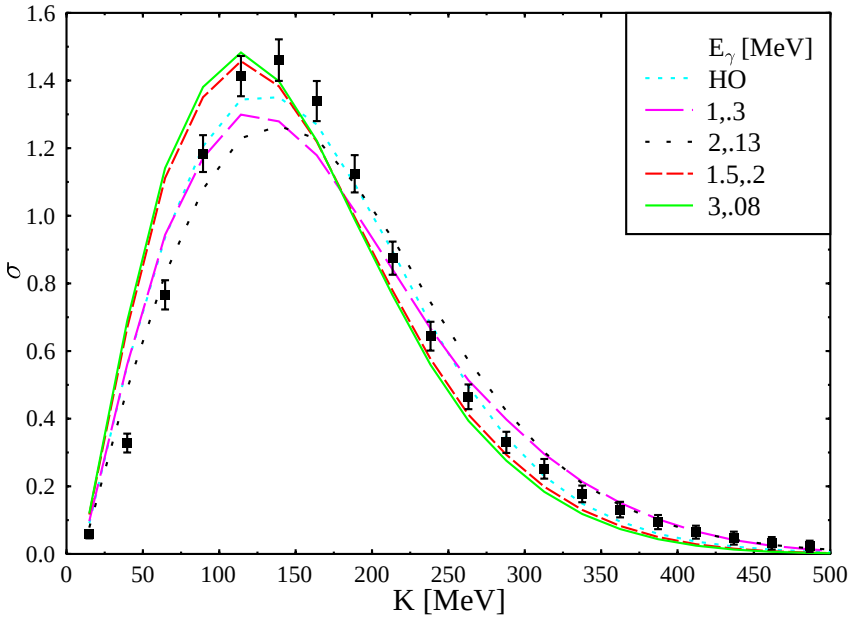

Figure 6.46: Distribution of the pair momentum $\sigma(K)$ for the HO and correlated case. The measured strength of the pair momentum is plotted along the calculations.

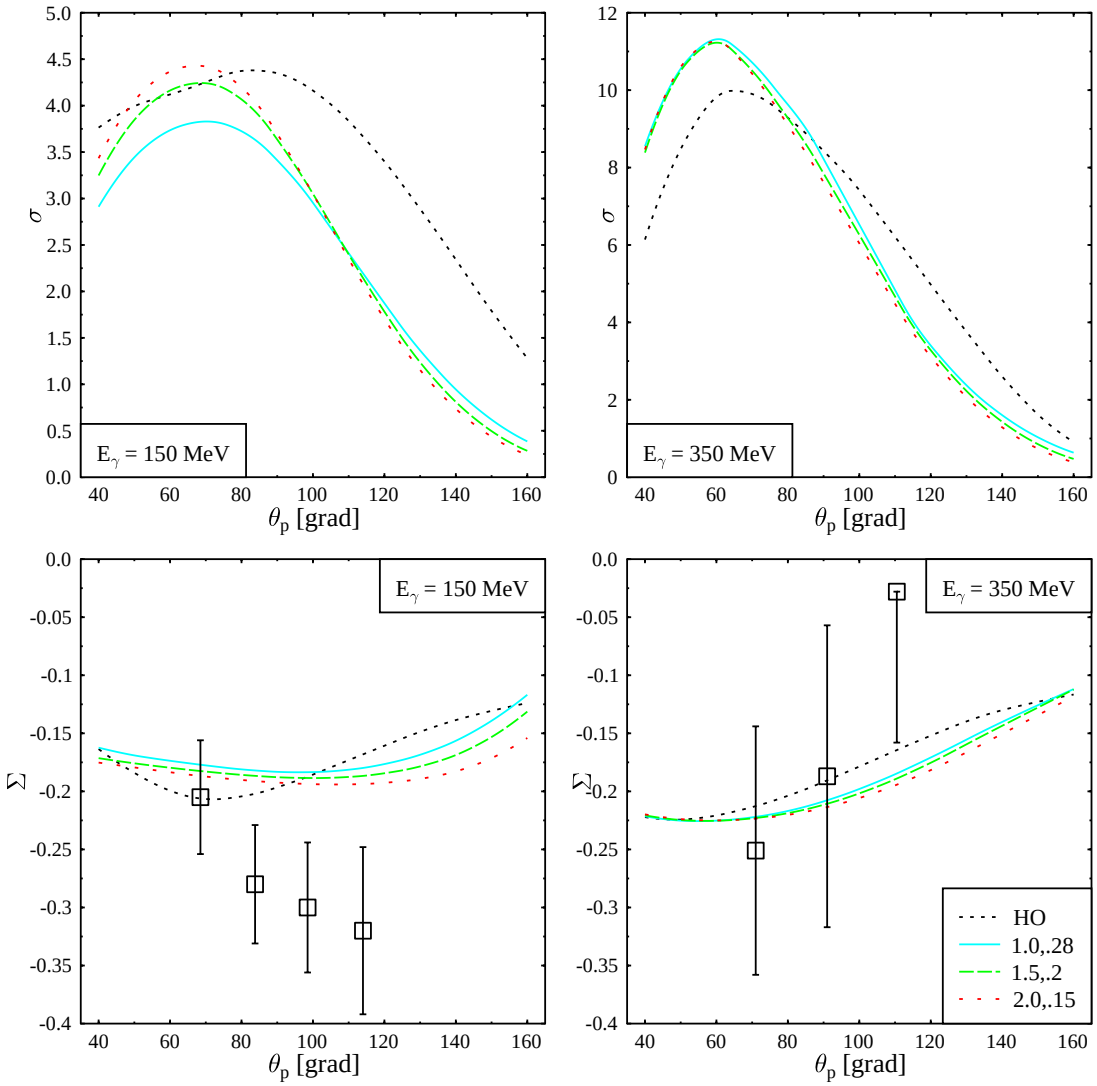

Figure 6.47: Cross section and asymmetry of proton polar angle distribution at two photon energies compared to the data of the P220 and P350 period.

and P350 period from Fig. 6.9 on page 114 are plotted aditionally for comparison. The peak of the cross section at high energies is more pronounced, compared to $E_\gamma = 150$ MeV, and it is shifted to forward angles, namely ~ 60 degrees. At low energies the peak is located at about 70°. The major effect of a correlated wave function compared to the HO case is a suppression of large proton angles which causes the distribution to become narrower and to shift to lower angles. This effect is stronger at low photon energies. For high photon energies the calculated curves describing the asymmetries for various correlated wave functions match the data and their trend, that is a decreasing asymmetry with larger proton angles. At $E_\gamma = 150$ MeV, the calculation fails to describe the data. That complies with the plot of the asymmetry of the excitation function. There, the calculation does not show the sine-like

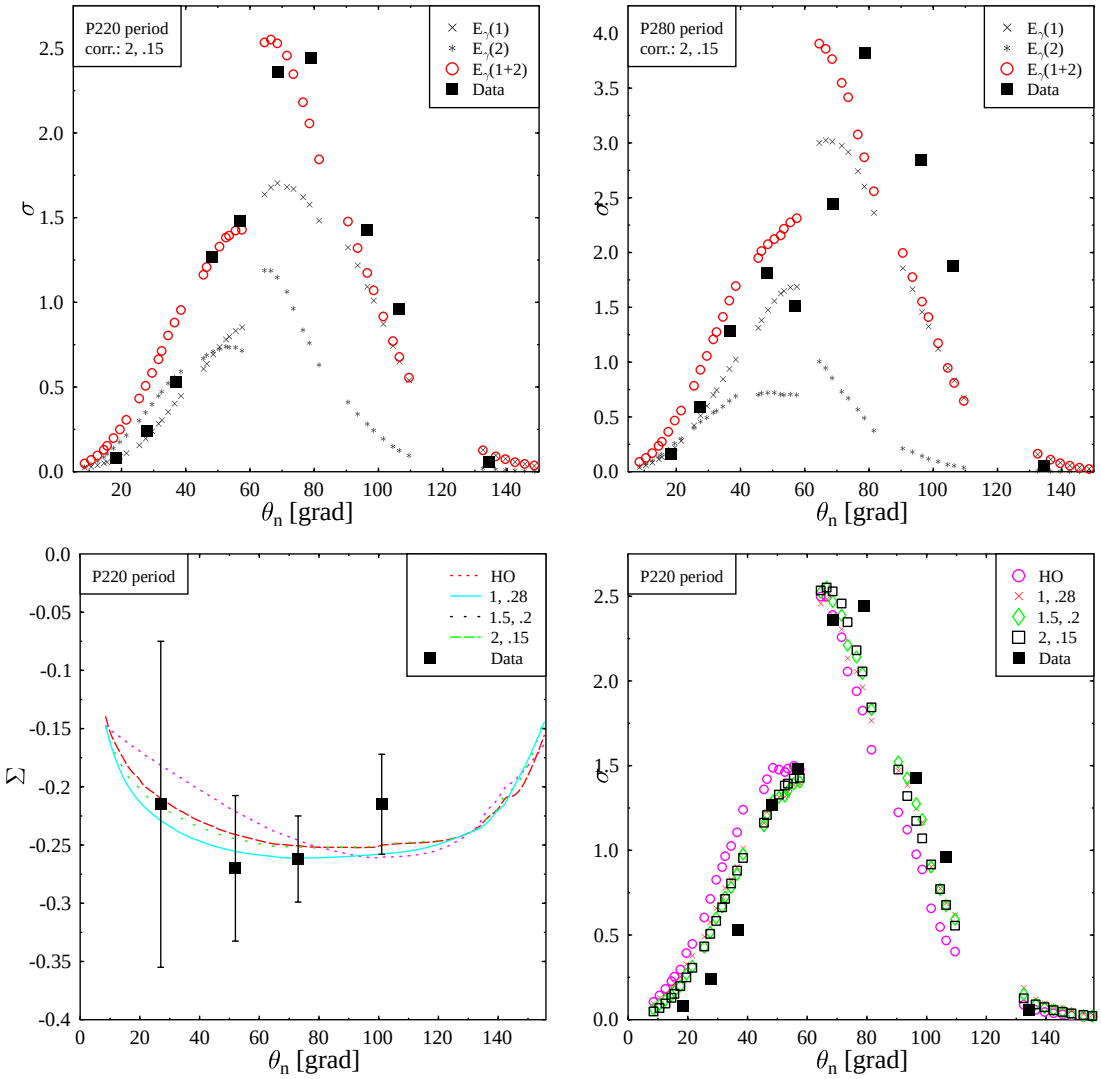

Figure 6.48: (upper) The strength of the of the neutron polar-angle distribution from the P220 and P280 data sets is compared with the model predictions. (lower) Effect of correlations on strength and asymmetry of the ϑ_n distribution.

structure of the data around $E_\gamma = 150$ MeV. Obviously these two discrepancies have the same cause. Compared to the rising slope of the calculated asymmetry at 350 MeV, the model predicts a fairly flat asymmetry at low photon energy. It thereby shows somehow the same tendency than the data. According to this model, the strongest effects of SRC are to be expected at forward (around 60°) and at backward angles ($\sim 140°$)

The measured neutron angle spectrum is supposed to yield a richer source of information due to its large angular range and is thus compared with the model in Fig. 6.48. Two measurement periods, which are P220 and P280, are plotted together with the respective

calculations. Due to the restriction on sufficient polarization ($P > P_{\min}$) each period contains contributions (see Chapter 3) from two photon energy ranges shown in Tab. 6.2 on page 105. The individual contributions are denoted by $E_\gamma(1)$ and $E_\gamma(2)$ and the combined one by $E_\gamma(1+2)$. For the P220 period, the strengths from both photon energy regions at forward angles are about the same, whereas at $> 70°$ the lower region $E_\gamma(1)$ is dominant. This behaviour indicate the shift to forward angles at higher photon energies, as already found in Fig. 4.9 on page 67. The calculations including both photon energy regions $E_\gamma(1+2)$ describe the data fairly well, but there are systematic discrepancies: The predictions overestimate forward and underestimate backward angles. Additionally, the data and the model exhibit a different behaviour at the peak region. For the P280 period, these discrepancies become larger: The model badly underestimates the strength at backward angles and fails to describe the dip at 55°. Obviously this is due to the lack of the ρ-MEC, which is rather important at higher photon energies as was shown in [24, 96]. Whether the discrepancy at $\vartheta_n \sim 55°$ originates from tensor correlations or the interference with ρ exchange currents is to be decided by a sophisticated and realistic model. Note, the step around 60° originates from the different distances and therewith acceptances of the ToF frames as already presented on page 70.

The consequences of correlated wave functions on the angular distribution and its asymmetry are shown in the lower panel. The calculations including SRC seems to follow the data better than the HO curve, but the errors are much too large for quantitative conclusions. The same result is found in the cross section (right panel). Also, the correlated cases describe the data better than the HO one. However, the differences between the distributions from these correlated wave functions are too small to discriminate certain SRC descriptions. The sensitivity of the neutron angular cross section on different choices of SRCs is small, but there is an significant effect in the asymmetry at forward angles around 30°. Unfortunately the errors of the data are too large due to the small cross section at these angles.

Apart from the neutron and proton angular distribution, their opening angle is an extra observable which might reveal additional information regarding SRC effects. The data plotted along with model predictions in Fig. 6.49 below shows a negative slope at low photon energies (P220 period) and has a rather flat behaviour (possibly a slight positive slope) at high energies demonstrated by the P350 data set. Correlated wave functions improve the description of the P220 data because they result in a slope of the asymmetry which complies with the data whereas the slope of the HO calculation is significant smaller. The correlation with the parameters $(b, c) = (1, .28)$ even succeeds to meet the data. That situation is not reproduced at high photon energies; here the HO description seems to be the appropriate choice. However, it has to be noted that the inclusion of heavier meson exchange might alter this notion.

In Fig. 6.50 below model calculations of the excitation function and its asymmetry for the pp channel are compared to the data from Fig. 6.23 on page 130. While the cross section is rather well described by the theoretical predictions, the asymmetries totally miss the

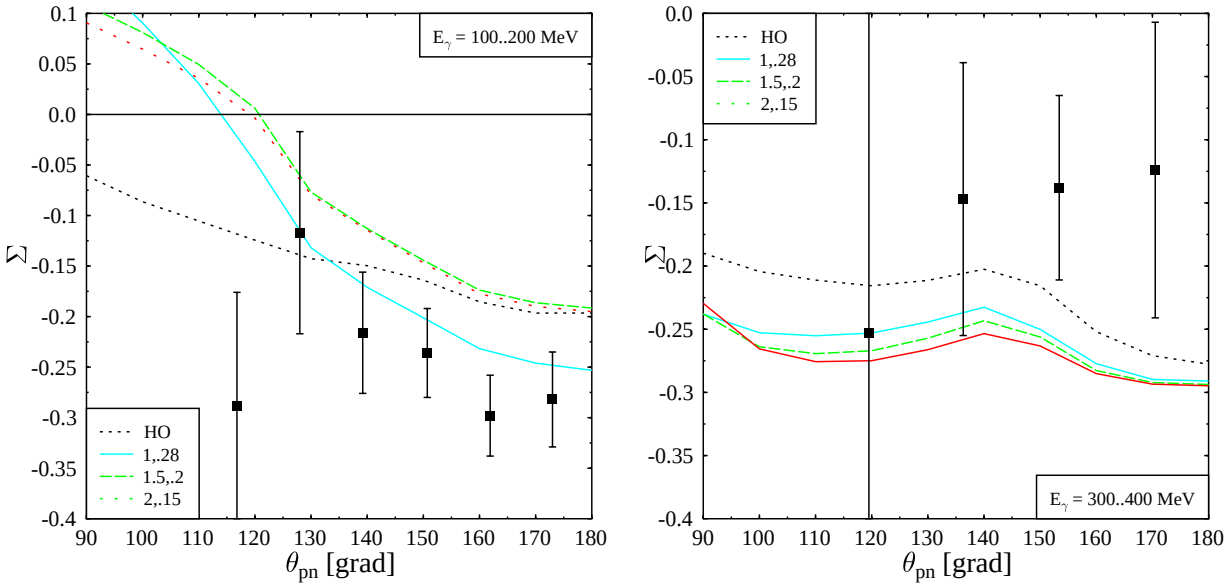

Figure 6.49: Cross section and asymmetry of the proton-neutron opening-angle distribution compared to calculations involving an HO and three correlated wave functions.

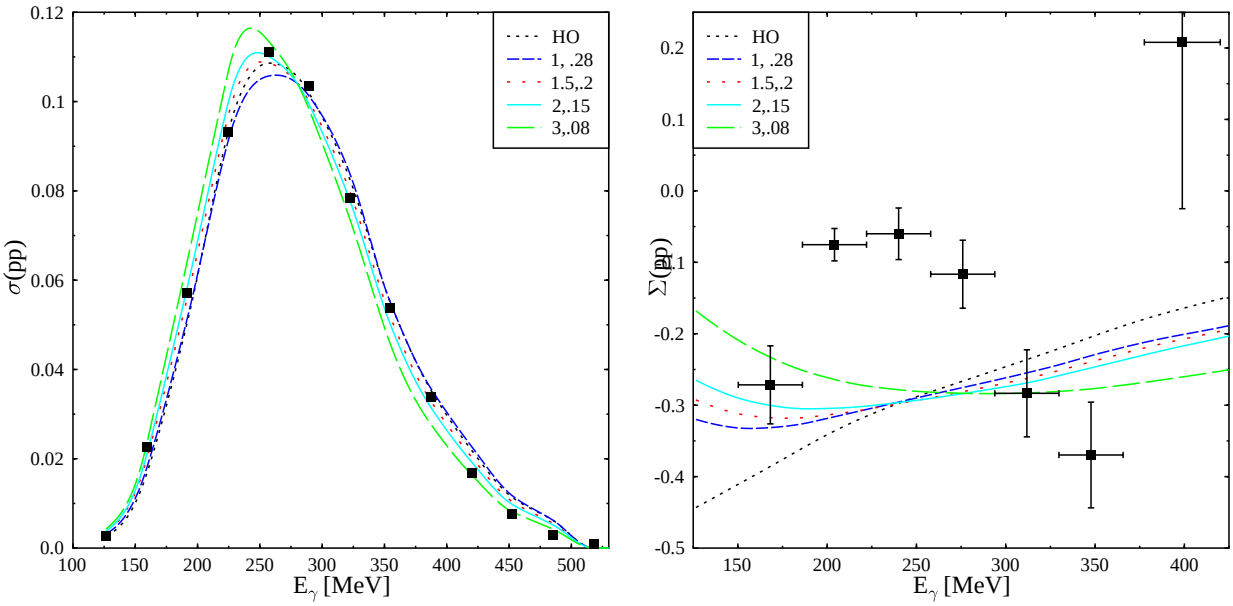

Figure 6.50: Comparison of measured excitation function and asymmetry for pp knock-out with the toy model predictions employing four sets of correlation parameters.

data. Moreover, the toy model overestimates the pp cross section by about a factor of 10 compared to the pn case, which is conspicuously pointed out by the scaling factors f_σ stated in Tab. 6.5 on page 152. An unique reasion for this behaviour cannot be found and it is possible due to the shortcommings of the toy model, in particular the absence of ρ meson exchange and tensor correlations. It has to be emphasized, however, that the Oset model overestimated the pp data, as well, by about a factor of 3.5 [23]. The comparison with the excitation function exhibits little sensitivity of the cross section on the influence of SRC. That is mainly due to the fact that the 1BC current contributes predominantly at low photon energies, which are around 100 ... 150 MeV. According to this model the asymmetry at low photon energies seems to have a high potential to search for SRC effects. Furthermore, the discrepancy at around 250 MeV, which was also found in the comparison of the pn asymmetry with the model predictions, could hint towards the impact of tensor correlations. The latter are expected to be stronger in the pp channel than in the pn final state. These figures indicate the urgency of predictions from realistic models to be compared with these data, because one would obviuosly gain new insights of the effect of SRC.

Another observable which might reveal some interesting physics is the difference azimuthal angle ϕ_d, which enters the matrix element, respectively the structure functions W_T and W_{TT}. Different trends of the measured asymmetries for the pp and pn channel are observed: The ϕ_d asymmetries of the pn case show a parabola-like behaviour and are generally larger at 180° than 'out of plane' (see Fig. 6.29 on page 136), whereas the one of the pp final state has a rather flat ϕ_d dependence. In Fig. 6.51 the data are plotted along with the

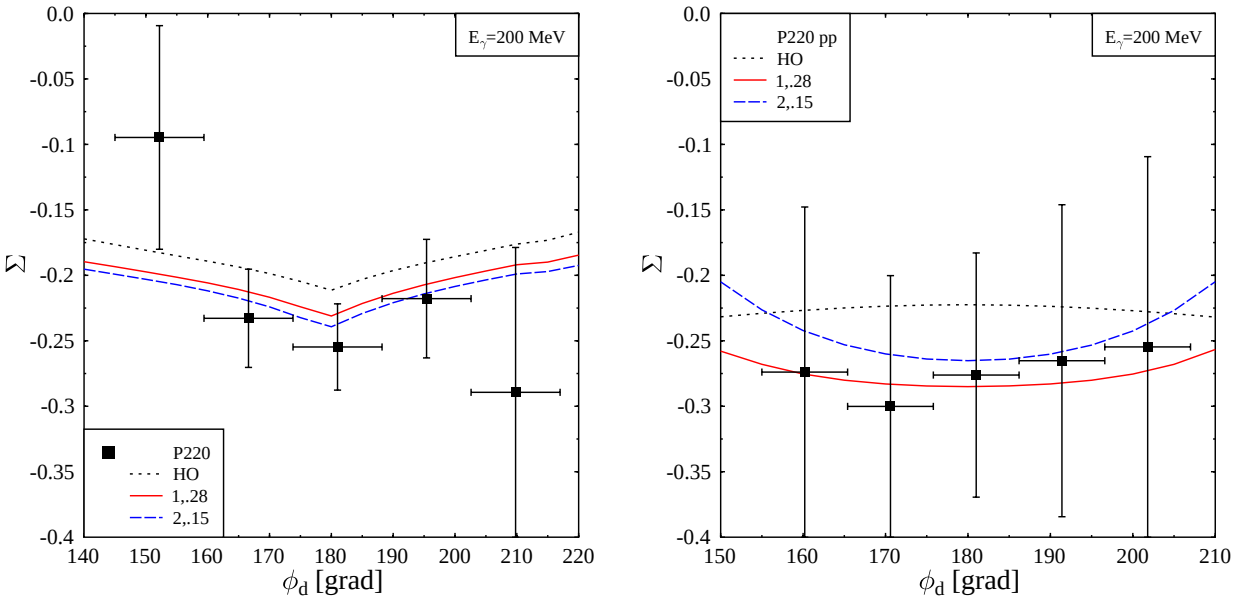

Figure 6.51: Comparative model predictions of the asymmetry in dependence of the azimuthal difference angle ϕ_d for both isospin channels.

model predictions for the HO description and two correlated wave functions. Indeed, the calculations for the pn channel indicate a rising slope for 'out of plane' angles, whereas the pp predictions are essentially flat. The quite different ϕ_d behaviour of both final isospin-states is probably due to the MEC contribution. The pp-calculations based on correlated wave functions exhibit a slight decreasing asymmetry for angles off 180° and thus follows the data better than the HO prediction. Generally the asymmetries of the toy model describe the data rather well, however, it is left to studies with realistic models to what extend the inclusion of tensor correlations and ρ exchange alter this result.

From the comparisons shown in this chapter it can be concluded that the model calculations based on correlated wave functions are favoured by the data in contrast to the HO description. The parameter ranges for b and c, which overall meet the data best, are $b \sim 1.5 \ldots 2$ and $c \sim 0.2$ and comply with the findings from the p_{3m} distribution (see on page 122). Although the presence of SRC is clearly indicated by these comparisons, the determination of the SRC parameter are by no means quantitative and reliable. Yet the importance to include SRC in the description of the nuclear dynamics is therewith demonstrated. Moreover, preliminary findings of a rather sophisticated and realistic model [148] indicate that the predictions from both models show qualitatively similar results. However these calculations are not yet completed and are still preliminary and furthermore, there are presently no alternatives on the market which adress ^{4}He and allow to implement the experimental setup, respectively the detector acceptances and thresholds. This was one of the main reasons to develop this toy model.

6.8 Summary and Outlook

The study of the ^{4}He($\vec{\gamma}$,NN) reaction with a large opening-angle detector-setup in the photon energy range $E_\gamma = 110 \ldots 600$ MeV performed at MAMI is presented in this thesis. This work integrates the experiments of photo-induced 2N emission off oxygen, carbon and lithium and therewith enlarges the data basis and it extends previous measurements by the polarization degree of freedom for both isospin final states. It is hoped that the additional degree of freedom will create optimum circumstances and an extra handle to reveal signatures of ground state correlations when a realistic microscopic model is available.

During the measurement large amount of data was produced, which could successfully be analysed by a powerful data acquisition system [62, 149]. Particular important are routines for calibration of the detectors, particle separation in PiP and ToF and background subtraction. There were three diamond settings and thus three measurement periods with different polarization which meant separate calibrations; still a consistent result could be achieved. Asides these obstacles on the way to absolute cross sections, there is another point linked to them: Extrapolation into full solid angle acceptance necessitates model assumptions. Therefore the data is presented with acceptance dependence as so-called visible cross sections and a respective model calculation has to consider the experimental thresholds and acceptances.

The separation of the various reaction mechanisms contributing to 2N knock-out is an important prerequisite to reach new knowledge of SRC. The asymmetry measurement was performed at three photon energy regions implying different missing energy resolutions and degrees of polarization. Nevertheless an equivalent cut method consistently succeeded to sufficiently separate the G2N (genuine two nucleon absorption) process in each of these data sets and even the combined one. The improved description of bremsstrahlung production including experimental limitations resulted in a rather small systematic uncertainty of the polarization degree and thus renders the asymmetries to be very reliable.

In this work three final states were investigated, these are the pn, pp and ppn (3B) channels. Cross sections similar in shape compared to carbon [23, 57] were observed for pn; yet important differences arise for example in the missing energy distribution. The ratio of G2N strength to pion production is significant larger then in the carbon case, which therewith demonstrates the smaller influence of FSI. That complies with the observation that for ^{4}He the inclusive NN excitation function drops faster past the Delta resonance than in carbon. Both observations are corroborated by earlier work, e.g. [142]. Possible hints of SRC effects in the pn channel might for example be given by the long tail of the missing momentum distribution and the bump in the asymmetry of the excitation function around 250 MeV. Dedicated calculations which are in preparation[10] should clarify the situation. Additionally the 3N-emission channel was analysed to achieve an estimate of its contribution to 2N knock-out, in particular to pp. Astonishingly, a slightly positive asymmetry was found for

[10] calculations of photo-induced 2N knock-out with a correlated ^{4}He wave function are underway by W. Van Nespen and J. Ryckebusch [148]

the ppn final state. An enhancement at high momenta of the 3B missing momentum, which can be viewed (with some approximations) as a single nucleon momentum distribution, may give rise to another evidence of SRC effects.

The pp channel proved to be rather weak compared to pn-emission strength; A similar ratio was also observed in the ^{4}He-Daphne [142] and ^{12}C-PiP-ToF [23–30] experiments. Moreover, the investigations of the 3B final state adduced that a large fraction of pp emission stems from 3B absorption. These two processes can be separated better, as it is done in this work, by a higher energy resolution, say $\Delta E_{2m} < 5$ MeV. However, it seems as if there is a continuous transition between the two processes: pp absorption with two spectator neutrons with vanishing relative energy and 3B absorption where the two unobserved neutrons have significant relative energy. Again the asymmetry yields new reasons for further investigation: The question is raised, for example, whether the significant difference between the pp and pn asymmetry of the excitation function is only due to the missing MEC contribution or whether it reflects isospin dependent SRC effects.

The same question arises from the study of the angular dependences. In the ToF-neutron angle spectrum an energy dependence is found which leads to a significant bump at higher energies at forward angles. The ToF-proton distribution urges upon an energy independent behaviour. The situation is analogous in the observable ϕ_d, the difference of the azimuthal angle of both nucleons. The cross section of pn emission exhibits a clear energy dependence whereas the one of pp knock-out is very small, if there is any at all. Also, the photon energy region has a different impact on the angular distribution of protons in PiP or the nucleon in ToF for both final isospin states. This influence continues on the respective asymmetry. It is rather important to clarify whether this is solely on account of the MEC contribution or other mechanisms like FSI, or whether SRC influences show up.

The comparisons of the calculations of the toy model with the measured data illustrate the usefulness of having a simplified model for predicting the major trends and sensitivities on SRC effects in the different observables. For reliable theoretical calculations it is mandatory to use realistic models which include heavier meson exchange and which take special care about the construction of the Delta propagator. Furthermore, the simple model used in this thesis showes that only an unfactorized approach is able to produce quantitative results, which unfortunately increases computer power needs enormously. Also, state-dependent correlation functions and and FSI have to be taken into account. Work along that line is in progress at Gent by W. Van Nespen, which then hopefully will shed additional light on correlations together with the result of this and previous measurements [23, 24, 26, 57]. Still the presence and the necessity to include SRC is proven by the comparisons performed with this model and even possible hints towards tensor correlations were found. Moreover, it can be concluded that helium as target and the extra polarization degree of freedom were both good choices to gain more information about SRC.

Another outcome of the studies done with this model are the regions of phase space with high sensitivity on SRC effects: These are at low photon energies, around 70 MeV, and at far forward and backward neutron angles (outside the QD region). Also, PiP at forward

angles between $40° \ldots 100°$ for example, with the intention to measure off QD kinematics, should enhance SRC effects. Measurements along that line [150] are underway at MAMI with the PiP-ToF detectors set up such that ToF encloses the beam down- and upstream which corresponds to the so-called superparallel kinematic.

A realistic microscopic description of the photo-induced 2N emission is very demanding due to the complexity of the reaction. That is one of the reasons for the relatively slow progress of theoretical work on that field since Gottfrieds publication. However, the quality of the present data, as for example the result of this work, necessitates for more profound theoretical studies of the reaction mechanism and accurate predictions in dependence of the correlation functions.

Appendix A

Bremsstrahlung

A.1 Coherent and incoherent intensity

All cross sections concerning bremsstrahlung, respectively their intensities, may be cast in the characteristic energy dependent form: $I = \big(1+(1-x)^2\big)\psi_1 + \frac{2}{3}(1-x)\psi_2$. Two functions $\psi_{1,2}$, which in general have a moderate energy dependence, enter the intensity and are the basis for the derivations and results presented in Chapter 3. For an ideal electron beam, the coherent intensity (3.4), expressed by means of these functions, was first derived by May [63] and reads:

$$\Psi_1^{\mathrm{coh}} = \quad 4\sum\nolimits_{\vec{g}} G\delta_x g_t^2 g_l^{-2} \tag{A.1a}$$

$$\Psi_2^{\mathrm{coh}} = 24\sum\nolimits_{\vec{g}} G\delta_x^2 (g_l - \delta_x) g_t^2 g_l^{-4} \tag{A.1b}$$

$$\Psi_3^{\mathrm{coh}} = -4\sum\nolimits_{\vec{g}} G\delta_x^3 g_l^{-4}\big[(g_2^2 - g_3^2)\cos 2\phi + 2g_2 g_3 \sin 2\phi\big] \tag{A.1c}$$

$$\text{and} \quad G(\vec{g}) = \frac{(2\pi)^2}{a^3 N_{\mathrm{cell}}} |S(\vec{g})|^2 e^{-Ag^2} F^2(g^2) g^{-4}$$

They depend substantially on the longitudinal g_l and transversal g_t momentum transfer. Through the characteristic minimal longitudinal momentum transfer δ_x, both in turn are functions of the relative photon energy x and the electron orientation relative to the lattice. The involved variables are defined in more detail in Chapter 3, see on page 25ff.

The following equation, the Schiff cross section [78] (eq. 2BS), was obtained by integration of the Bethe-Heitler differential cross section (in Born-approximation) over the angles of the outgoing electron, using an approximate screening potential. It serves as starting point

for the calculation of the incoherent collimated intensity (3.11):

$$\frac{dI^s}{du} = \left(1+(1-x)^2\right)\Psi_1^s - \frac{2}{3}(1-x)\Psi_2^s \tag{A.2a}$$

$$\Psi_1^s = 2v^2(M(v)-1) \tag{A.2b}$$

$$\Psi_2^s = 6v^2\left(1+(2M(v)-8)(1-v)v\right)$$

$$\text{with} \quad M(v) = -\ln\left[\frac{Z^{2/3}}{C^2}\left(\delta_z^2+v^2\right)\right] \text{ and } \quad \delta_z = \frac{C\delta_x}{Z^{1/3}} \tag{A.2c}$$

All orientations, like electron and photon momentum and the lattice orientation, i.e. the lattice vectors, are described in ANB and MCB by three-dimensional vectors. For some calculations however, a representation of the crystal angles Ω_0 in the electron coordinate system Ω_e is of auxiliary convenience. In the laboratory system the electron has the polar and azimuthal angle ϑ_b and ϕ_b and thus the transformation of the crystal angles (see Fig. 3.4 on page 33), which follows from (3.22b), reads:

$$\Omega_e(\underline{b}_e): \quad \theta_e = \sqrt{\theta_0^2+\vartheta_b^2-2\vartheta_b\theta_0\cos\phi_b} \tag{A.3}$$

$$\alpha_e = \alpha_0 - \arcsin(\vartheta_b/\theta_0 \cdot \sin\phi_b)$$

A.2 Form factor and Debye-Waller factor

The coherent intensity depends strongly on the form factor itself, i.e. at some descrete q values only: $F(\vec{g}_i^2)$. In contrast, the incoherent ψ_i functions depend on the integrated form factor and weakly on the energy x. The latter is due to the lower limit of the integral being the minimal momentum transfer δ_x, see [78] eq. 3BSb. The form factor comprises the nucleonic one, which is savely approximated by Z, and the electronic shell form factor F_s, hence $F/Z = 1 - F_s$.

LR apply the Cromer form factor [151] in both cases, whereby for the integral Cromers parametrization is used in the whole q range, although it is valid only up to $q = 0.1$. For higher q values the form factor remains constant instead of approaching zero, which leads to an underestimation of the incoherent cross section. Meanwhile a more accurate one is available from a relativistic Hartree-Fock calculation [152], being more precise than the Hartree-Slater calculation [151]. The latter is the basis for the Cromer form factor and takes exchange currents approximatively into account, as suggested by Slater. Wilsons [152] form factor, which is used here, is stated in the following equation and shown in Fig. A.2 on page A4 together with the influence of the Debye-Waller factor. Wilsons [152] form factor, which is applied in both codes (ANB and MCB), is stated in the following equation and

shown in Fig. A.2 on page A4 together with the influence of the Debye-Waller factor.

$$F_r^e(q^2)\cdot Z_{^{12}\mathrm{C}} = \begin{cases} a_0 + \sum_{i=1} a_i \exp(-b_i q^2) & q < 0.1 \\ \exp\left(\sum_{i=0} c_i q^i\right) & 0.1 < q < 0.3 \\ d_1/(1+d_2 q^2) & q > 0.3 \end{cases} \tag{A.4}$$

$$\begin{aligned} a_i &= 0.2156, 2.31, 1.02, 1.5886, 0.865 \\ b_i &= 8851.729, 4334.795, -241.5085, -21934.59 \\ c_i &= 1.7056, -32.30426, 50.50572, -37.38128 \\ d_i &= 0.6886649, 3731.4571 \quad (\rightsquigarrow C = 137) \end{aligned}$$

In order to study the values of the momentum transfer, which contribute to the incoherent cross section a weighting function is defined using the Schiff cross section ([78] eq. 3BSb) as:

$$w_q(q) = \frac{d}{dq}\left(\frac{d\sigma(3BSb)}{dx}\right) \sim (1-F_s)^2\mathcal{O}(q^{-1}) \tag{A.5}$$

The influence of the form factor and the Debye-Waller factor on the distribution of the momentum transfer and therewith on the intensity, is of particular interest for the comparison of the realistic and dipole form factor:

$$F_d(C,q^2) = \left[1+\left(qCZ^{-1/3}\right)^2\right]^{-1} \tag{A.6}$$

In case of the incoherent cross section off a crystal radiator, the form factor has to account for the Debye Waller factor f_{Deb}, which leads to an effective form factor $\sqrt{1-f_{\mathrm{Deb}}}\big(1-F_s(q^2)\big)$. For the Hubbell intensity the dipole form factor has to be retained, therefore the impact of f_{Deb}, silicet the suppression of lower q values, has to be modelled by an alternative method.

Two approximative approaches, the effective screening and the reduction factor method, were investigated The weighting of the momentum transfer by w_q together with the mean values of q for the different form factors respecting the influence of the Debye-Waller factor is shown in Fig. A.3 on page A5. It indicates that the realistic form factor in the incoherent case is sufficiently approximated by the dipole form factor based on the effective screening method. For comparison, the total intensity, as defined by Heitler [78]: $\Phi = E_0^{-1}\int_0^{T_0} dk\bar{\sigma}I(k)$, with those form factors and the mean momentum transfer is recorded in Tab. A.1 on page A5. The latter is exemplary given at $x = 0.25$ although the energy dependence is mild. (see Section A.3).

A.3 Effective screening and reduction factor

The implementation of a reduction factor $I^{\mathrm{inc}} = r_D I^{\mathrm{amo}}$ is one method to deal with the impact of the Debye-Waller factor, if r_D can be successfully modelled by an analytical

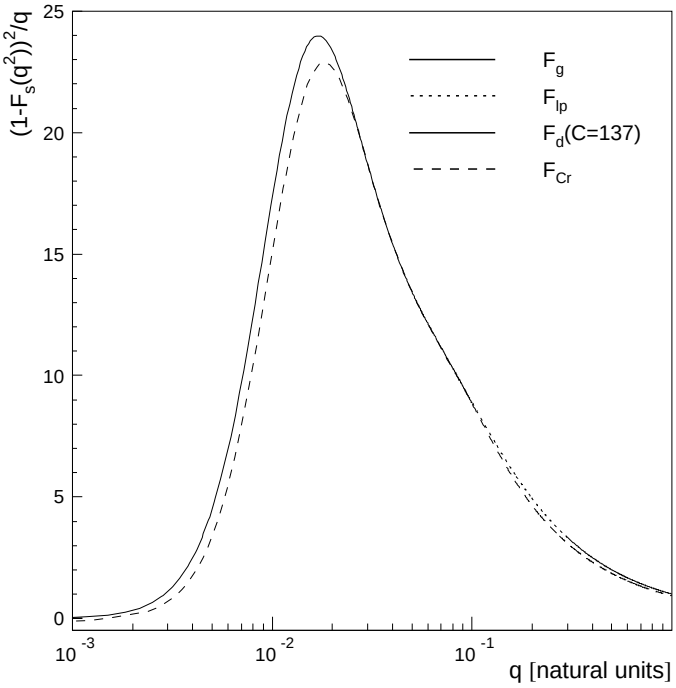

Figure A.1: Comparison of carbon form factors from Cromer [151] labeled with F_{Cr} and Wilson [152] in a double logarithmic plot. Note the separation into three momentum regions, according to (A.4). The Gaussian, logarithmic polynomial and the dipole extension are marked by F_g, F_{lp} and F_d respectively. At low q values the relativistic Hartree-Fock calculation yields a larger form factor then the Hartree-Slater one.

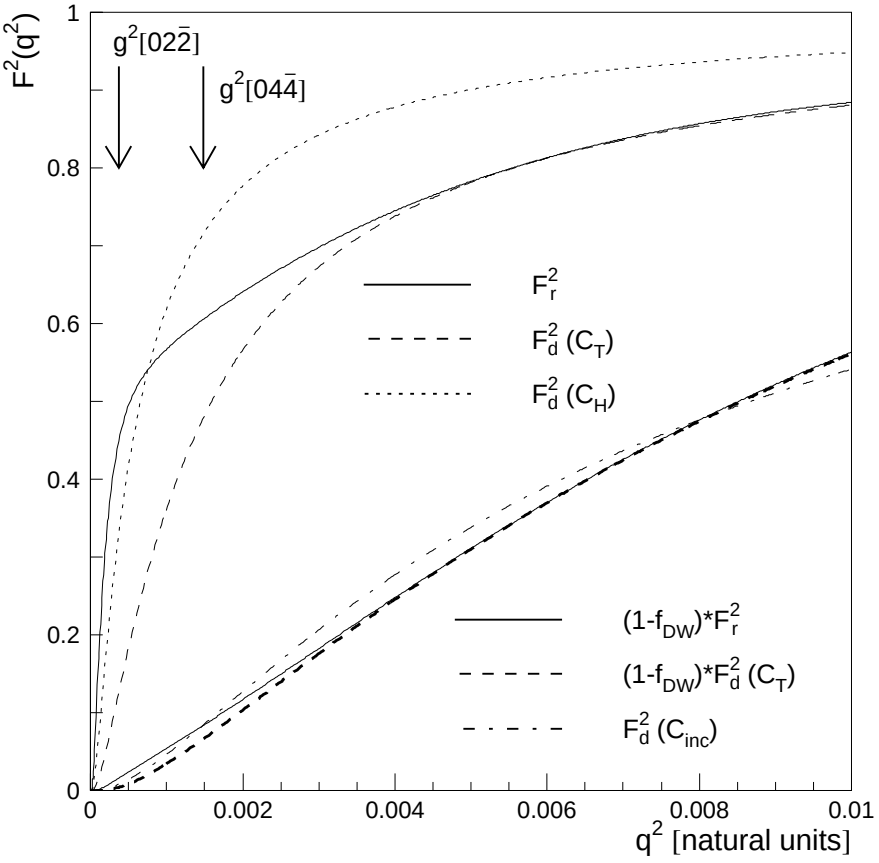

Figure A.2: The form factor from Wilson with and without the Debye Waller factor is compared to the dipole form factors with screening constants $C_H = 111$ [72] and $C_T = 71$ [67]. The product $(1 - f_{DW})F_r^2$ is modelled by an effective dipole form factor.

Figure A.3: Distribution of the momentum transfer for relative photon energy $x = 0.5$ of incoherent bremsstrahlung in dependence of the dipole and realistic form factor and the Debye-Waller factor. The mean values of the momentum transfer are also given for these cases exemplifying the suppression of small values of momentum transfer due to the Debye-Waller factor.

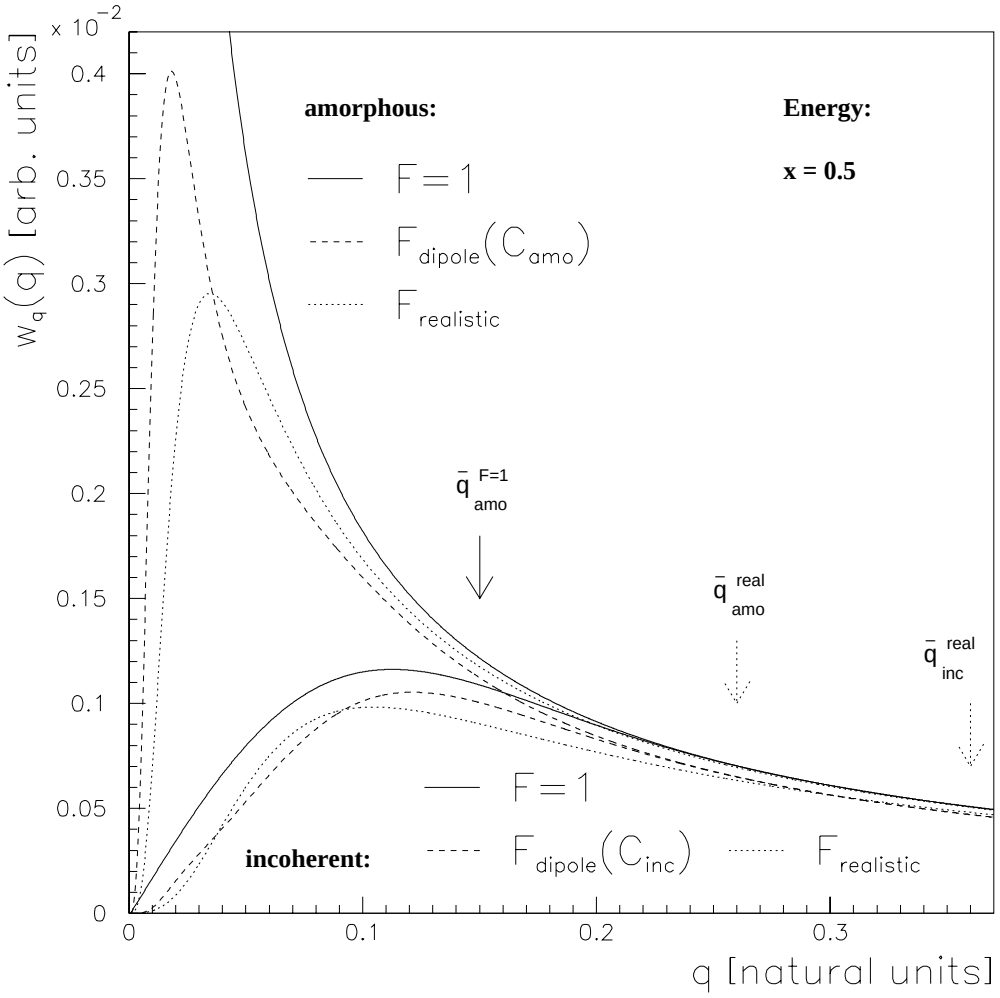

Table A.1: Total intensity and mean momentum transfer $\bar{q}$ of incoherent bremsstrahlung calculated with the realistic form factor at $x = 0.25$: $\bar{q} = q_0 + q_1\delta_x$

		Φ	$\bar{q}$	q_0	q_1
amo	$F = 1$	649	.152		
	F_r	366	.261	.2591	3.14
inc	$F = 1$	300	.353		
	F_r	278	.364	.3631	0.992

function. The other approach still uses the original Hubbell intensity, except that an appropriate screening constant is applied. Both, the reduction factor and the effective screening constant are defined such that the absolute intensities are in agreement with the original Bethe-Heitler expression in [153] or [78] eq. (1BS). With the definition of the integral measure $d^n\Gamma$, the total uncollimated intensities for the amorphous and incoherent case read:

$$I_n^{\text{amo}} = \int d^n\Gamma \; I_{\text{BH}}(1 - F_r)^2 \tag{A.7a}$$

$$I_n^{\text{inc}} = \int d^n\Gamma \; I_{\text{BH}}(1 - f_{\text{Deb}})(1 - F_r)^2 \tag{A.7b}$$

$$\text{with} \quad d^2\Gamma = d\vartheta_e d\phi, \quad d^3\Gamma = d\vartheta_\gamma d^2\Gamma, \quad \text{and} \quad d^4\Gamma = dx d^3\Gamma$$

These (up to 4-fold) integrations are even numerically non-trivial due to the dynamical behaviour of the kernel, but turned out to be feasible when employing the Monte Carlo integration code VEGAS [114]. A statistical accuracy of less than 10^{-3} was required for the integration. Consequently the reduction factor and effective screening constant were obtained as follows:

$$r_D(x,\vartheta) = \frac{I_2^{\text{inc}}}{I_2^{\text{amo}}} \qquad r_D(x) = \frac{I_3^{\text{inc}}}{I_3^{\text{amo}}} \tag{A.8a}$$

$$\int dx \; I_{\text{Hub}}(C_{\text{inc,amo}}) \stackrel{!}{=} I_4^{\text{inc,amo}} \tag{A.8b}$$

Both methods agree in the range of the statistical errors, which therewith prove their validity, see also [75]. f_D depends weakly via a function $A(T_{\text{Debye}}, T)$ on room and Debye temperature, with a value of $A = 101.6$ at 21 C°. To account for this, the temperature dependence of the incoherent intensity was determined for the effective screening method to $C_{\text{inc}}(T) = 31.29 + 0.01251 \cdot T/K$. For the amorphous radiator, in [72] and [78] a screening constant of $C = 111$ is stated, derived from a numerical comparison to a Thomas Fermi model with complete screening. In contrast, Timm [67] suggests an approximation of the realistic form factor F_r by a dipole form factor with a screening constant of $C = 71$, compare Fig. A.2 on page A4. The effective screening method (A.8b) yields $C_{\text{amo}} = 109.8$ in good agreement to the standard screening value and $C_{\text{inc}}(T_{\text{room}}) = 35$ in case of the incoherent contribution. To adopt the reduction factor method (see Fig. A.4 on page A7) for ANB and MCB, two fit functions for room temperature were destilled (A.9). The residual deviations of the numerical calculation compared to the fit are in the order of 1% and this figure reveals their pure statistical nature.

$$r_D(x) = a_1 + a_2/(1 - a_3 x) \tag{A.9a}$$

$$r_D(x,\vartheta) = \left(b_1 + b_2 e^{b_3 x}\right)\left(b_4 + b_5\vartheta + b_6\vartheta^2\right) \tag{A.9b}$$

$$a_i = 0.7435, .0043, 0.9863$$

$$b_i = 0.6642, 4.0924 \cdot 10^{-6}, 11.107, 0.93219, 0.2371, -0.056487$$

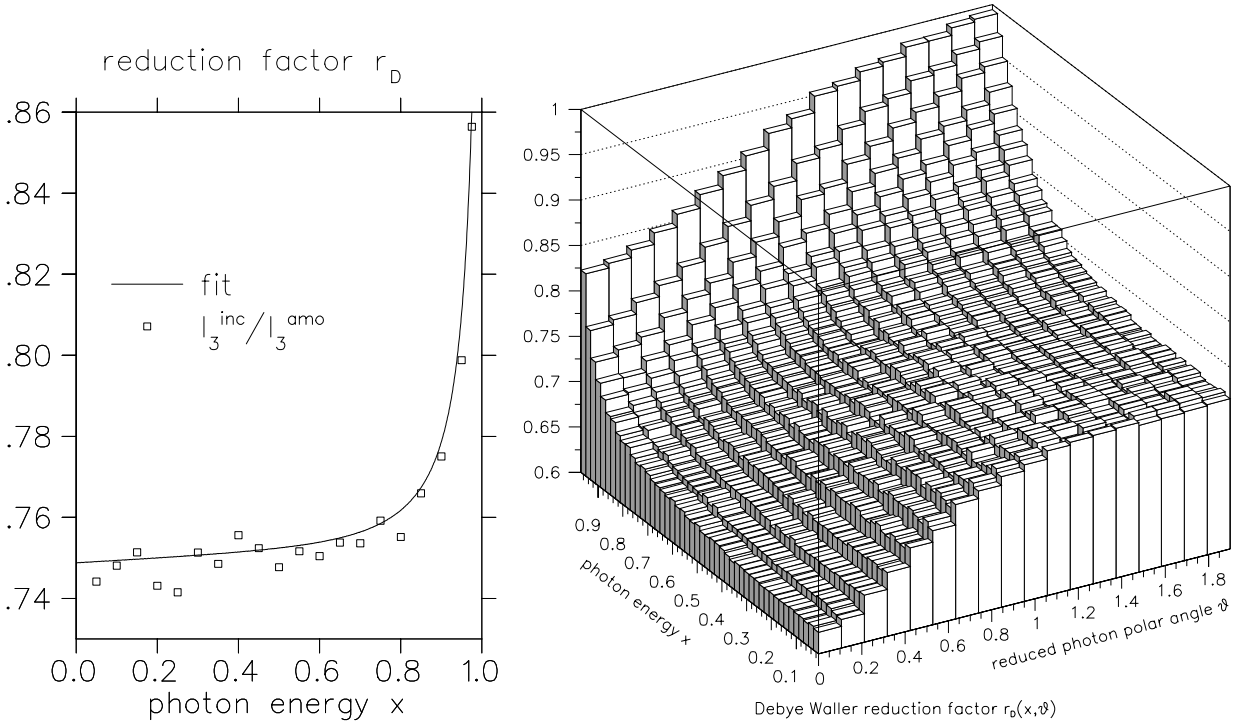

(a) Fit to $r_D(x)$ and its numerical integrations

(b) Two-dimensional reduction factor $r_D(x, \vartheta)$ from numerical integrations

Figure A.4: Reduction factor from (A.8a) *and a fit of* (A.9a) *to* $r_D(x)$*. The two-dimensional fit to* $r_D(x, \vartheta)$ *is of the same quality. Note that the data points show fluctuations, which are of statistical nature only, as a result of the integration method.*

A.4 Systematic error

For a complete survey of the errors originating from each experimental parameter X_i, the influence of their uncertainty on the degree of polarisation was investigated. The parameters $\vec{X} = (\vartheta, \alpha, \sigma_s^r, \sigma_p^r, z_R, z_c)$ comprise crystal angles, beam spot size, beam divergence, diamond thickness and collimator geometry. For a calculation of their error propagation, the slope $\partial\bar{P}/\partial X_i$ of the mean polarisation (A.10) was determined by computing the polarisations for 10 sampling points per parameter about its nominal value X_i^0 [75]. From that, E_X can be derived and is recorded in Tab. A.2 on page A8 for four different collimators. It can be deduced from the table that the largest effects arise from the diamond thickness, crystal

angle α and beam divergence, whereat the latter two have the larger uncertainties.

$$\frac{\Delta P}{P_0}(X_i) = \left| \frac{\partial \bar{P}}{\partial X_i} \frac{X_i^0}{P_0} \right| \frac{\Delta X_i}{X_i^0} = E_X \frac{\Delta X_i}{X_i^0} \tag{A.10a}$$

$$\bar{P} = \int_{x_{1/2}}^{x_d} dx\, \sigma^{\mathrm{coh}}(x) P(x) \Big/ \int_{x_{1/2}}^{x_d} dx\, \sigma^{\mathrm{coh}}(x) \tag{A.10b}$$

$$\text{with} \quad x_{1/2} < x_d \quad \text{from} \quad P(x_{1/2}) = \frac{1}{2} P_{\max} \tag{A.10c}$$

Exemplifying the result of the error propagation, the error of the polarization induced by the beamdivergence is considered subsequently. According to Tab. A.2 an error in beam divergence of 20% (one sigma) leads to a difference in the degree of collimated polarisation of scarcely 1% absolute (2% around the $[02\bar{2}]$ peak region and much less elsewhere). Recapitulative it can be estimated that the maximal systematical error amounts to 1.5% averaged of the the whole energy range and 3% in the peak regions; for more detail see [75].

Table A.2: Variation of polarisation E_X (A.10a) in dependence of the parameters X_i for three different collimators (radii r_c in mm) and the uncollimated situation.

X_i		X_i^0	units	$r_c = 1.5$	2.5	4	uncoll.
ϑ	crys. angle	.0607	rad	0.18	0.19	0.19	0.18
α	crys. angle	.694	rad	1.18	1.33	1.43	1.5
$\sigma_s^{x,y}$	BS	.2,.06	mm	0.003	0.002	0.001	0
$\sigma_p^{x,y}$	BD	.15,.15	mrad	0.047	0.013	0.007	0.007
z_R	radiator thickn.	.1	mm	0.071	0.02	0.004	0.005
z_c	col. distance	2.5	m	0.11	0.17	0.09	0

Another source of error stems from the calculation itself and was assessed via a comparison of ANB and MCB and the two approximate methods dealing with the Debye Waller factor (A.8). Concerning the two codes, it was found that the difference of polarisation in the peak region accounts to about 0.02 but much less elsewhere, apart from some obvious fluctuations due to statistics within MCB. The discrepancy of the polarization based on the effective screening as well as the reduction factor method was investigated in both codes. In the collimated case, the absolute differences amounts to less than 0.02 and again the largest discrepancy was found to be in the peak region. The very good overall accordance of the resulting spectra from both methods and codes indicate their reliability.

A.5 Ratio method

There are cases, when the calculated bremstrahl intensities might fail to describe the measured yield sufficiently well. For example, if the experimental parameters are not known precisely, or the beam emittance is highly non-spherical and does not comply adequately with a Gaussian. Also, an off-axis collimator would produce yields which quite differ from the calculation, e.g. Fig. 3.8 on page 39. In these circumstances the polarization prediction may be unreliable and can be improved by the method described here.

The polarization $P \propto I^{\mathrm{dif}} = I_{\parallel} - I_{\perp}$ can be corrected by accounting appropriately for the discrepancy of the calculated crystal intensity and the measured one (Fig. A.6 on page A10, middle). With the assumption that the differences arise mainly from the coherent contribution, the discrepancy ϵ may be calculated by subtracting the incoherent from the crystal intensity. For the incoherent contribution either the calculated one I^{inc} or the corrected nickel spectrum may be taken: $Y^{\mathrm{inc}} = Y_{\mathrm{ni}} \cdot I^{\mathrm{inc}}/I^{\mathrm{amo}}$. The coherent intensity I^{coh} and I^{dif} shows a related energy behaviour and, even more important, the experimental parameters X_i have an analogue impact on both. This explains that the ratio $f(x, \vec{X}) = I^{\mathrm{dif}}/I^{\mathrm{coh}}$ depends scarcely on $\vec{X}$, which is exploited by this method. Consequently the improved polarization P_i reads:

$$\epsilon = Y^{\mathrm{cry}} - Y^{\mathrm{inc}} - I^{\mathrm{coh}} \qquad \text{or} \quad \epsilon = Y^{\mathrm{cry}} - I^{\mathrm{cry}} \tag{A.11a}$$

$$P_i = \frac{I^{\mathrm{dif}} + f\epsilon}{I^{\mathrm{cry}} + \epsilon} \qquad f = \frac{I_{\mathrm{dif}}}{I_{\mathrm{coh}}} \tag{A.11b}$$

The realistic polarization P_r is still not resembled by P_i because the ratio f is not the realistic one but usually comes from a calculation which does not describe the measurement precisely. The error induced thereby amounts to $(P_r - P_i)/P_r = \delta f/2 = (f_r - f_i)/2f_r$, yet from ANB studies it turned out that δf is very small ($\lesssim \delta X_i/10$). However, P_i is much closer to the realistic polarization than the original prediction. The disadvantage of this procedure is either the statistical fluctuation of ϵ or the error introduced by a smoothing method, if applied.

To clarify this method, measured spectra simulated by a reference calculation I_r are compared in Fig. A.5 on page A10 with a second one I, which results from a distinct parameter set and plays the role of the prediction. The larger electron divergence and thicker target result in a smaller yield and lower degree of polarization. However, applying the ratio method on the prediction I yields the improved polarization P_i and intensity I_i, which meet the reference calculation rather well and indicates therewith the validity of this procedure. This improvement of the predicted polarization is demonstrated also in Fig. A.6 on page A10 with a measured spectrum. Both Y^{cry} and I^{cry}, which on purpose stems from a calculation with slightly wrong parameters, are plotted together with the intensity difference ϵ and their smoothed versions. In the lower panel the result of the model calculation is compared with the improved polarisation P_i. As expected, at regions where the crystal intensity is overestimated, the polarization prediction is too high and vice versa. So

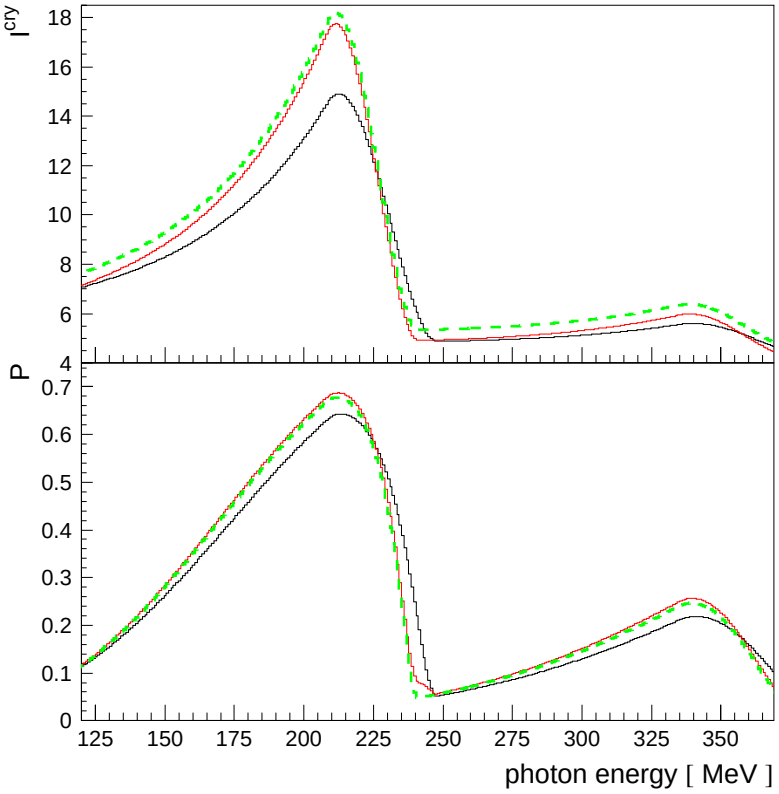

Figure A.5: The dashed green lines mark the reference intensity I_r and polarisation ($\alpha = 0.694$, $z_R = 0.1$, $r_c = 1.5$, $\sigma_s = 0.12$, $\sigma_p = 0.15$). The calculation I with a slightly different parameter set is indicated by a thick black line ($\alpha = 0.692$, $z_R = 0.12$, $r_c = 1.57$, $\sigma_s = 0.25$, $\sigma_p = 0.25$). I_i^{coh} and P_i from the ratio method (thin red line) are based on calculation I.

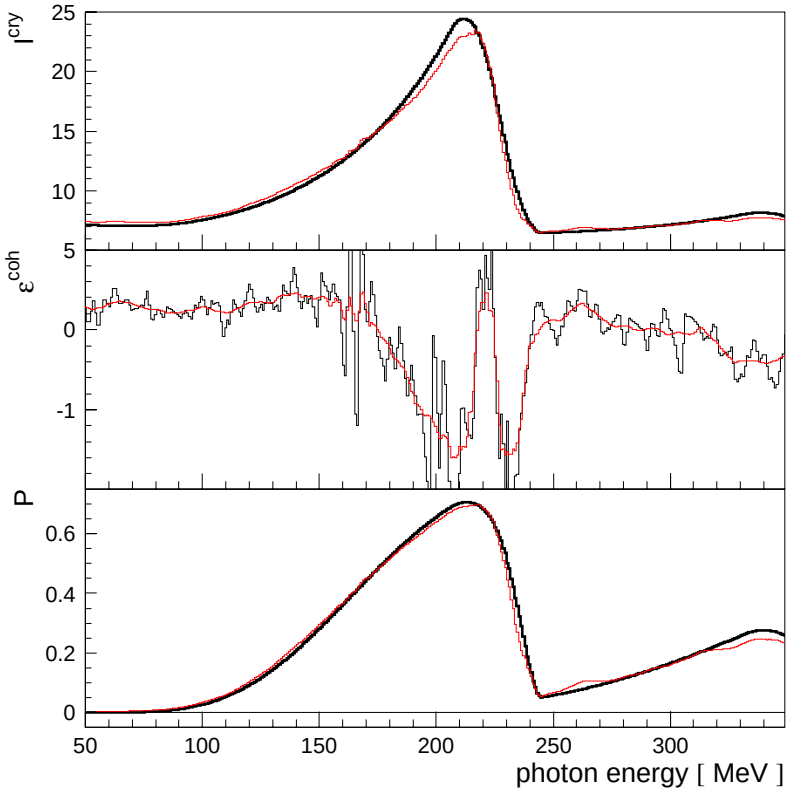

Figure A.6: In the upper and lower panels the crystal intensity and polarization prediction (thick black line) are plotted together with the smoothed measured yield and improved polarization P_i (thin red). Note that the calculation is intentionally a bit off. (middle) Raw and smoothed difference ϵ of intensities.

the improved polarization (thin red line) is closer to the realistic one than the orginial prediction.

Another consequence of this technique is the extraction of the error of the predicted polarisation P:

$$\left|\frac{P_i - P}{P}\right| \lesssim \left|\frac{\epsilon}{I^{\mathrm{coh}}}\right| + \left|\frac{\delta f}{2}\right| \tag{A.12}$$

From the comparison between calculations and the measured spectra from the ^{4}He experiment the maximal error, which is predominantly located around the discontinuity, is determined to $\lesssim 2.5\%$ and much less elsewhere.

A.6 Photon-flux

In Chapter 3 the calculated intensities or cross sections are compared with measured yields scaled onto the calculation. Subsequently a formula is presented to calculate the photon-flux from the intensity. Furtheron, the absolute photon yield derived from the electron beam current is compared with the model calculation.

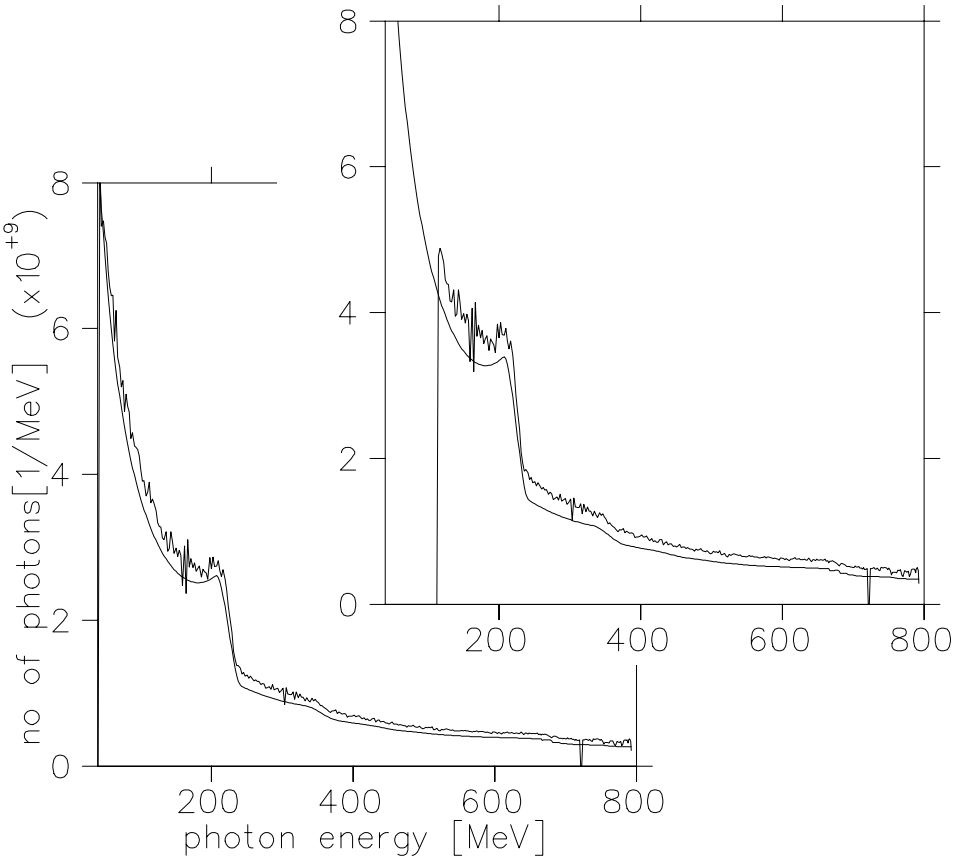

Figure A.7: Total number of photons per MeV from a beam charge of 25.2 nAh (left) and 32.8 nAh (right). In average the beam current was about 3.9 nA and 5.9 nA, respectively. Switching off the lower Tagger section allowed to increase the current.

The photon-flux $d\dot{N}/dk$ is related to the intensity $I(k)$ via the electron current and target properties:

$$\frac{d\dot{N}}{dk} = \frac{J_e}{e}\frac{\rho d N_A}{m} \cdot \frac{d\sigma}{dk} = \frac{J_e \rho d N_A \bar{\sigma}}{emk} \cdot I(k) \tag{A.13}$$

Here J_e/e is the electron flux and ρ and d the target density and depth, respectively. m denotes the target mass and the cross section unit is given by $\bar{\sigma} = 0.5795 Z^2$ mbarn with $Z_{\mathrm{di}} = 6$.

The calculation presented in Fig. A.7 on page A11 predicts the number of photons based on the values of Tab. A.3 on page A13 and the parameters labeled M220 in Tab. A.4 on page A13). It is compared with the measured yield from a diamond radiator during the D220 measurement period of the ^{4}He experiment. The discrepancy, which is around $10 - 15\%$, is due to the uncertainty of the measurement of the electron beam current at MAMI. The current was not monitored continuously but average values were recorded hourly. It is expected that a more precise measurement of the current would yield a better agreement. Nevertheless this comparison of absolute cross sections indicates the reliability of the model calculation.

constant	ρ^{di}	d	m^{di}	$\bar{\sigma}$
unit	[g/cm^3]	[cm]	[g/mol]	[cm^2]
value	3.513	0.01	12.01	$2.086 \cdot 10^{-26}$

Table A.3: Constants used in (A.13) *for calulating the photon-flux*

Table A.4: All parameters which entered the calculation of the bremsstrahl spectra for the respective figures. For the MAMI setup a collimator length of 16 cm was used and the crystal angle ϕ was set to 0.738352. *The definition of these parameters can be found in Chapter 3*

figure	label	E_0	Θ	α	σ_r^s	σ_r^p	z_R	θ_c
	MeV	rad	rad	mm	mrad	mrad	mm	mrad
3.9a	M220	855	0.0607	0.694	0.2	0.084	0.1	0.564
3.9b	M280	855	0.0607	0.662	0.2	0.084	0.1	0.564
3.9c	M350	855	0.0607	0.662	0.2	0.084	0.1	0.564
3.9d	TAGX	1160	0.15	0.818	0.1	0.39	1.1	1.13
3.11a	M225	855	0.0607	0.634	0.1	0.12	0.1	
3.11b	M227	855	0.0607	0.634	0.1	0.12	0.1	
3.13a	MAMC	1500	0.0607	0.650	0.11	0.15	0.1	0.6
3.13b	JLAB	6000	0.0471	0.738	0	0	0	0
3.13c	ELFE	25300	0.03	0.77	1	0.01	0.1	0

Table A.5: Mean polarisation and properties of the bremsstrahlung for three different diamond settings, applied in the ^{4}He experiment. For the definition of $\bar{P}$ and $k_{1/2} = E_0 x_{1/2}$ see (A.10b) *and* (A.10b).

edge (label)	observable	unit	220	280	350
discontinuity	k_d	MeV	224.7	277.6	357.9
uncollimated	$P_{\max}$	%	48	42	32
polarisation	$\bar{P}$	%	38	32	24
photon energy	$k_{\max}$	MeV	210	266	346
	$k_{1/2}$	MeV	159	207	280
collimated	$P_{\max}$	%	70	64	54
polarisation	$\bar{P}$	%	58	52	42
photon energy	$k_{\max}$	MeV	212	266	346
	$k_{1/2}$	MeV	159	205	280

Appendix B

Theory

B.1 Kinematics and (iso)spin

Missing energy

Starting from the relativistic energy- and momentum conservation in the lab-system

$$q^\mu + p_A^\mu = p_1^\mu + p_2^\mu + p_x^\mu \tag{B.1}$$

the momentum of the recoiling system is given by: $\vec{p}_x = \vec{q} - \vec{p}_1 - \vec{p}_2$. $p_{1,2}$ denotes the momenta of the outgoing two nucleons, p_x the residual system and the photon and the target nucleon at rest is given by $q^\mu = E_\gamma(1,0,0,1)$ and $p_A^\mu = (M_A, \vec{0})$, respectively. The energy of the recoiling system with rest mass $M_x = M_{A-2} + E_x$ and intrinsic excitation E_x is defined by $p_x^0 = T_x + M_x$. Plugging this relation together with the kinetic recoil energy $T_x = (p_x^2 + M_x^2)^{\frac{1}{2}} - M_x$ into the energy component of (B.1) yields the correct relativistic relation of the excitation or missing energy $E_{2m} = E_x + Q$ with

$$E_x = \left[(M_{A-2} + E_\gamma - T_1 - T_2 - Q)^2 - p_x^2\right]^{\frac{1}{2}} - M_{A-2} \tag{B.2}$$

If this relation is expanded to first order in E_x, which is valid for $E_x \ll M_{A-2}$ given in this experiment, the following formula is retained:

$$E_{2m} = E_\gamma - T_1 - T_2 - T_x \tag{B.3}$$

Therewith the expression of the missing energy used in Chapter 4 and Chapter 6 is derived and presented. It is proved that these are very good approximations of the relativistic expressions: The numerical difference of the missing energy considered here is negligible.

Final relative momentum

In Section 4.2 a relation between p, E_γ and P is derived, see (4.4c), which expresses the final relative momentum as a function of the photon energy and missing- respectively pair-momentum. Substituting $\vec{P} = \vec{K} + \vec{q}$ therein explains the square-root like behaviour of the final relative momentum on photon energy, as it was observed in [23]. The experimental spectrum shown in this work demonstrates the strong (but purely kinematical) correlation between photon energy and final relative momentum. This relation is weakened by the distribution of $\vec{K}$ resulting in a band-like structure in the plot of the measured final momentum p versus photon energy E_γ. The kinematic of the deuteron case is simpler. Here, all variables are determined by the photon energy E_γ and the polar angle of one nucleon, for example particle a: ϑ_a. The pair momentum $\vec{K}$ vanishes, hence $\vec{P} = \vec{p}_a + \vec{p}_b = \vec{q}$, which leads to the energy and momentum relations:

$$E_\gamma + M_D = E_a + E_b = \frac{p_a^2 + (\vec{q} - \vec{p}_a)^2}{2M} + 2M \tag{B.4a}$$

$$\Rightarrow \quad 2p_a(E_\gamma, \vartheta_a) = E_\gamma \cos(\vartheta_a) + \sqrt{4M(E_\gamma + M_d - 2M) - E_\gamma^2(2 - \cos^2(\vartheta_a)} \tag{B.4b}$$

The small influence of $\vec{K}$ on $p(E_\gamma, \vec{K})$ in (4.4c) allows the use of the average over the recoil momentum $\vec{K}$ as an approximation. With $\bar{K} \approx 145$ MeV in the ^{4}He case, which stems from $\langle K^2 \rangle = \int d^3K\, K^2 |\phi(K)|^2 = a$, the mean dependence of the relative momentum and photon energy reads:

$$p(E_\gamma) \approx \sqrt{E_\gamma(4M - E_\gamma) - MQ - \bar{K}^2/2} \tag{B.5a}$$

$$E_\gamma(p) \approx 2M - \sqrt{M(4M - Q) - \bar{K}^2/2 - p^2} \tag{B.5b}$$

(Iso)spin operators

The evaluation of the isospin operators of the 2N knock-out current on the initial ^{4}He wave function is the first step of the calculation presented in Section 4.4. The initial isospin wave functions involved in the pn case are $i_0 = |\mathsf{pn} - \mathsf{np}\rangle / \sqrt{2}$, $i_1 = |\mathsf{pn} + \mathsf{np}\rangle / \sqrt{2}$ and the one for the pp case is given by $i_2 = |\mathsf{pp}\rangle$. The effects of the respective isospin operators (see (4.37)) on the initial wave function are collected in Tab. B.1 on page A16. Note that the isospin projection operators $\tau^{p,n}$ on proton and neutron states act on the initial wave function symetrically in particle a and b: $\tau^p_{a,b} |i_{\mathsf{pn}}\rangle = \tau^n_{b,a} |i_{\mathsf{pn}}\rangle$, respectively $\tau^n_{a,b} |i_{\mathsf{pp}}\rangle = 0$. The application of the results of the isospin operators given in Tab. B.1 on page A16 together with the isospin scalar products $(\mathsf{pn}|\, i_{0,1} = 1/\sqrt{2}$ and $(\mathsf{pp}|\, i_2 = 1$ removes the isospin dependence of the 2N knock-out current. Both, the 2N current and the initial wave function are presented in Section 4.4 in a single particle basis. Therefore the effect of each term in the current on the wave function can be calculated conveniently. However, the sum of these terms is defined only in a coupled spin and isospin basis. The transformation into

Table B.1: Result of isospin operators on initial wave function, which is composed of spin s_0, s_1 and isospin i_0, i_1 components defined in Section 4.3

	T_{ab}	τ_a^p	τ_b^p	$\tau_{a,b}^z$
$\|i_{\mathsf{pn}}\rangle$	$2i(s_1 i_0 - s_0 i_1)$	$(s_1+s_0)(i_1+i_0)/2$	$(s_1-s_0)(i_1-i_0)/2$	$\pm s_0 i_0$
$\|i_{\mathsf{pp}}\rangle$	0	i_2	i_2	$i_2/2$

that basis can be performed by use of the respective Clebsch-Gordon coefficients which yield the following projection operator $\Lambda = \Lambda^S \Lambda^T$ to be applied in spin and isospin space to each term:

$$\Lambda^{S,T} = \left(\frac{1}{\sqrt{2}} \left|00\right\rangle \left\langle \tfrac{1}{2}\tfrac{-1}{2} - \tfrac{-1}{2}\tfrac{1}{2} \right| , \left|1-1\right\rangle \left\langle \tfrac{-1}{2}\tfrac{-1}{2} \right| , \frac{1}{\sqrt{2}} \left|10\right\rangle \left\langle \tfrac{1}{2}\tfrac{-1}{2} + \tfrac{-1}{2}\tfrac{1}{2} \right| , \left|11\right\rangle \left\langle \tfrac{1}{2}\tfrac{1}{2} \right| \right) \quad \text{(B.6)}$$

In contrast to pp, for a pn pair both singlet and triplet isospin states are possible and antisymmetrization has to be fullfilled (if not ensured by the initial wavefunction) by means of the projection operator Λ^A. Hence, the necessity to project onto states with spin 1 and isospin 0 (denoted by Λ_{10}) and vice versa (Λ_{01})is given and performed by the following operator, which is presented in two representations:

$$\begin{aligned} \Lambda^A &= \Lambda_{01} + \Lambda_{10} \\ &= \frac{1}{4}(1-\sigma_a\sigma_b)\frac{1}{4}(3+\tau_a\tau_b) + \frac{1}{4}(3+\sigma_a\sigma_b)\frac{1}{4}(1-\tau_a\tau_b) \qquad \text{(B.7)} \\ \Lambda_0^S &= \left(\left|00\right\rangle \left\langle \uparrow\downarrow - \downarrow\uparrow \right| / \sqrt{2}, 0, 0, 0 \right) \qquad \text{(B.8)} \\ \Lambda_1^S &= \left(0, \left|1-1\right\rangle \left\langle \downarrow\downarrow \right| , \left|10\right\rangle \left\langle \uparrow\downarrow + \downarrow\uparrow \right| / \sqrt{2}, \left|11\right\rangle \left\langle \uparrow\uparrow \right| \right) \end{aligned}$$

Note that the first expression still calls for a projection onto the two particle coupled basis in spin and isospin space.

B.2 Relative momentum integrals

In Section 4.4 it is shown that the transition amplitude is written as an integral over the relative momentum of terms comprising kinematical variables and (iso)spin operators. This expression is reformulated in a way that the (iso)spin operators are formally pulled out of the integral and the latter runs over terms of kinematical observables only, see (4.35), (4.38) and (4.40). These are denoted by H and their calculation is presented here. This calculation is simplified by evaluating the integrals in a frame where the z axis of the relative momentum points along $\vec{p}_\pm = \frac{\vec{q}}{2} \pm \vec{p}$ implying the momenta exchanged between the pair is given by: $\vec{q}_{a,b} = \vec{p}_\pm \mp \vec{k}$. That results in a pure dependence of the seagull integral on

the scalar value of $\vec{p}_\pm$ therefore allowing to calculate the seagull integral H^S exactly. This can also be achieved for the IC integral, if the Delta propagator is taken at $k = 0$, which is necessary to facilitate the integral (see Section B.4). H^p and G^p with $p = +, -$ denote the Delta integral entering the amplitude (4.38c) and the Delta propagator, respectively. Hence, both integrals do not depend on the direction of $\vec{p}_\pm$, which thus can be pulled out of the integral:

$$\vec{H}^S_{a,b} = \hat{p}_\pm I^S(p_\pm) \qquad \text{note:} \quad I^S(p_-) = -I^S(p_+) \tag{B.9a}$$

$$\underline{H}^p_{a,b} = \pm\Big[\hat{p}^i_\mp \hat{p}^j_\mp I^D_0(p_\mp) + \underline{I}^D_2(p_\mp)\Big] G^p_{ab,k=0} \tag{B.9b}$$

Unfortunately the pion-in-flight integral is only symmetric around $\vec{p}$, i.e in the azimuthal angle ϕ_p, but depends on photon energy E_γ, the final relative momentum p and its polar angle ϑ_p. This complicated integral and its non-trivial dependence is a result of the two pion-propagators involved. The ϕ_p depencence can be taken care of by calculating the integral in a system where the azimuthal angle of $\vec{p}$ vanishes and a successive rotation into the laboratory frame. The latter is performed by means of a rotation matrix $D_z(\pm\phi_p)$, where the rotation around the z-axis about the angle $\pm\phi_p$ is marked by $D_\pm$. In this system the photon polarization and the integral tensor defined in (4.40c) are denoted by $\check{\epsilon} = D_+\vec{\epsilon}$ and $\check{I}_F$ respectively. Note that $\check{I}^{lmy}_F$ as well as $\check{\epsilon}^z$ and ϵ^z are identical zero. Furthermore, to reduce the number of dependences the photon energy entering the pion-in-flight integral is calculated by applying the approximate correlation (4.4a) between E_γ and the final relative momentum $\bar{E}_\gamma(p) = 2M - \left(4M(M-Q) - 2\bar{K}^2 - p^2\right)^{1/2}$ derived in Section B.1:

$$\vec{\epsilon}(\underline{\vec{H}}^F)_{ij}(\vec{p}, E_\gamma) \approx D^{il}_- D^{jm}_- \check{\epsilon}^x \check{I}^{lmx}_F(p, \vartheta_p) \tag{B.10}$$

The resulting integrals presented subsequently are numerically well behaved. For a given parameter set they are evaluated and tabulated. Interpolation from this table speeds up the integrals over the final phase space, which can be repeated for various observables.

$$I^S(\tilde{p}) = \int \frac{k^2\,dk\,dx}{(2\pi)^2} \frac{(\tilde{p}+kx)F^2(\tilde{p}^2)\psi(k^2)}{\tilde{p}^2 + k^2 + 2\tilde{p}kx + m^2} \tag{B.11}$$

$$I^D_0(\tilde{p}) = \int \frac{k^2\,dk\,dx}{(2\pi)^2} \frac{F^2(\tilde{p}^2)\psi(k^2)\tilde{p}^2}{\tilde{p}^2 + k^2 + 2\tilde{p}kx + m^2}$$

$$\underline{I}^D_2(\tilde{p}) = \int \frac{k^2\,dk\,\sin\vartheta\,d\vartheta}{2(2\pi)^2} \frac{F^2(\tilde{p}^2)\psi(k^2)k^2}{\tilde{p}^2 + k^2 + 2\tilde{p}kx + m^2} \begin{pmatrix} \sin\vartheta & 0 & 0 \\ 0 & \sin\vartheta & 0 \\ 0 & 0 & 2x \end{pmatrix}$$

$$\check{I}^{lmx}_F(p, \vartheta_p) = 2\int \frac{d^3k}{(2\pi)^3} \frac{q^l_a q^m_b (\vec{p}_{\phi=0} - \vec{k})^x}{(q^2_a + m^2)(q^2_a + m^2)} F(q^2_a)F(q^2_b)\psi(k^2)\Big|_{E_\gamma = \bar{E}_\gamma(p)} \tag{B.12}$$

The integration variable x is defined by $\cos\vartheta$, ϑ denotes the polar angle of the initial relative momentum $\vec{k}$ with respect to $\vec{p}_\pm$ and $\tilde{p}$ abbrevates the scalar value $|\vec{p}_\pm|$ in (B.9).

B.3 Gottfried approximation

The cross section of the pn knock-out employing the so-called Gottfried approximation shall be derived in order to study the impact of this ansatz and to provide calculations to be compared to the more sophisticated model presented in Section 4.5. According to Gottfrieds notion [21], the two nucleons are dominantly in a relative S state and have most probably a very small distance when hit by a photon implying $r_{12} \approx 0$. This assumption allows to factorize out the CM wave function and simplifies significantly the relative momentum integrals shown in Section B.2. Starting from the expressions of the 2N emission cross section (4.6) this approach leads to the following factorized form of the matrix element:

$$d\sigma = d\Gamma \mathcal{M} \qquad \text{with} \qquad \mathcal{M}_\lambda = F(K) S_{fi}^\lambda \tag{B.13a}$$

In coordinate space the relative momentum integral according to (4.32) is replaced by the integral over r, the relative spatial nucleon-nucleon distance. Hence the matrix element S_{fi}^λ, which is defined as the absolute square of the transition amplitude, reads as follows:

$$S_{fi}^\lambda = \int d^3r d^3r' \, e^{-i(r-r')k} f(r) f(r') s_\lambda \tag{B.13b}$$

$$\text{with} \quad s_\lambda = \sum_{m_1, m_2} \left\langle m_1 m_2; pn \right| J_\lambda(r) \Lambda^A J_\lambda^\dagger(r') \left| m_1 m_2; pn \right\rangle \tag{B.13c}$$

For the shell model, the spatial part of the pair function is assumed to be given by the product of two uncoupled single particle wave function belonging to the same shell. As a consequence the two nucleons are in a symmetric state. For the pn pair considered here, both singlet and triplet isospin states are possible and thus antisymmetrization of (B.13c) is fulfilled by projecting out the two allowed (iso-)spin states by means of the operator Λ^A, see on page A16.

In order to satisfy Gottfried's zero range approximation the currents entering s_λ, which are shown in Section 4.4 in momentum space, have to include Dirac's delta functions like $\delta(r - r_{1,2})$. This approach is also known as the "quasi-deuteron approximation", which adopts the view that no momentum is exchanged between the pair and thus leads to a relation between the final p and initial k relative momentum:

$$p_{1,2} = p_\pm = k \pm \frac{q}{2} \tag{B.14}$$

These two solutions correspond to the photo-absorption on nucleon a or b. Using a simplier form of the correlation function, namely $f(r) = 1 - \exp(-\beta r)$, even facilitates to perform these integrals analytically in coordinate space. The integral over r in (B.13b) corresponds to the Fourier transform of the correlation function. Therefore, the correlation functions

for the factorized cross sections enter the matrix element S_{fi}^{λ} as follows:

$$g_\pm = \int d^3r\, e^{-ip_\pm r}\, f(r) \qquad G_\pm = \int d^3r\, e^{-ip_\pm r}\, f(r) \frac{e^{-mr} - e^{-\Lambda_c m}}{4m} \tag{B.15a}$$

$$= -\frac{8\pi\beta}{(p_\pm^2 + \beta^2)^2} \qquad = \frac{1}{p_\pm^2 + m^2} - \frac{1}{p_\pm^2 + (m+\beta)^2} - (m \leftrightarrow \Lambda_c) \tag{B.15b}$$

The exponential term in G is the Yukawa factor which accounts for the finite life time of a pion and therewith for the finite range of the NN potential. The factor includes a monopole regularisation corresponding to the monopol form factor introduced in (4.36b). Due to these expressions and the delta functions mentioned above the integral over r, r' is readily performed. Hence only the calculation of s_λ is left, which is rather lengthy but straight-forward and yields for the unpolarizied matrixelement $S^T = S^x + S^y$:

$$\begin{aligned} S_{\mathsf{1BC,MEC}}^{T,pn} &= \left(\frac{e}{M}\right)^2 \left((p_{a,x}^2 + p_{a,y}^2) g_+^2 + \frac{\mu_p^2}{2} q^2 g_+^2 + \frac{\mu_n^2}{2} q^2 g_-^2 \right) \\ &+ 8 \left(\frac{f^2 e}{M}\right)^2 \left(p_a^2 G_-^2 + p_b^2 G_+^2 - (p_{a,x} p_{b,x} + p_{a,y} p_{b,y}) G_+ G_- \right) \\ S_{\mathsf{IC}}^{T,pp} &= \frac{256}{81} \left(\frac{f_{\gamma N\Delta} f_{\pi N\Delta} f_{\pi NN}}{m^3} \right)^2 |G_\Delta|^2 q^2 (p_x^2 + p_y^2) \left[G_+ - G_- \right]^2 \end{aligned} \tag{B.16}$$

The polarised matrixelement, also referred to as transversal-transversal matrixelement $S^{TT} = S^x - S^y$, reads:

$$\begin{aligned} S_{\mathsf{1BC,MEC}}^{TT,pn} &= \left(\frac{e}{M}\right)^2 \left(p_{a,x}^2 - p_{a,y}^2 \right) g_+^2 \\ &- 8 \left(\frac{f^2 e}{M}\right)^2 \left(p_{a,x} p_{b,x} - p_{a,y} p_{b,y} \right) G_+ G_- \\ S_{\mathsf{IC}}^{TT,pp} &= \frac{256}{81} \left(\frac{f_{\gamma N\Delta} f_{\pi N\Delta} f_{\pi NN}}{m^3} \right)^2 |G_\Delta|^2 q^2 (p_y^2 - p_x^2) \left[G_+ - G_- \right]^2 \end{aligned} \tag{B.17}$$

Note that these expressions are not complete and contain only 1BC and seagull currents for the pn case and Delta current for the pp channel and no interference terms between these contributions, because the number of terms exceeds the patience of the author. That means that the total matrixelement would by no means produce a realistic cross section because, for example, the IC-MEC interference is expected to be larger than the 1BC contribution.

The impact of the correlation on the seagull and 1BC employing (B.16) and (B.15) is shown in Fig. B.1 on page A20 for three values of β. The result of the individual contributions can directly be compared to the outcome of the toy model presented in Chapter 4. Therewith the findings of the toy model are supported: Most of the 1BC cross section is situated at low photon energies, namely around 100 MeV, and increases with the strength of the correlation. The effect of the SRC on the seagull contribution is opposite: The stronger the correlations the smaller the seagull cross section.

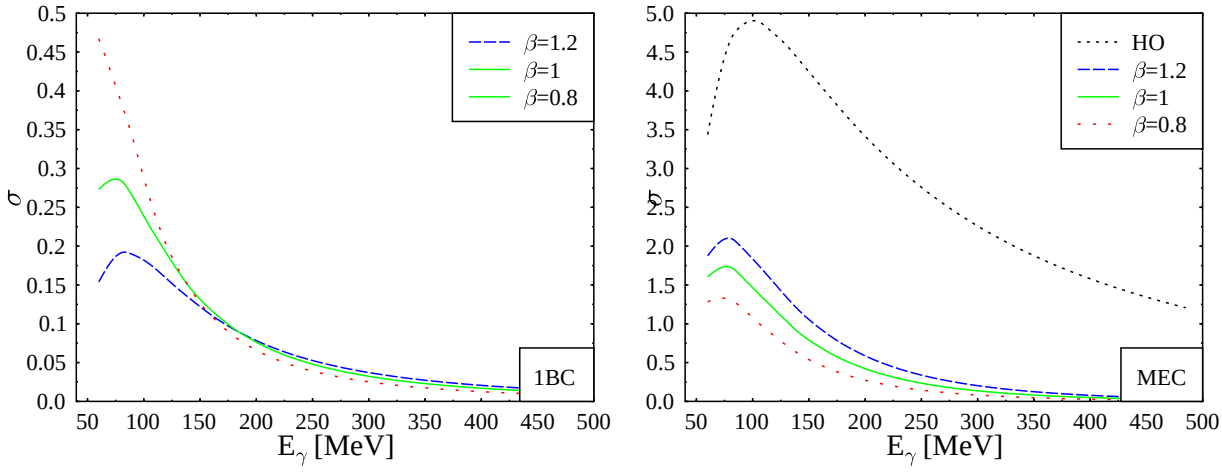

Figure B.1: Cross section (pn-channel) of the individual 1BC and MEC contributions from the expressions derived in this section for three correlation parameters.

B.4 Delta propagator

Due to the fact, that there is still no agreement in the literature on the treatment of the Delta propagator, its derivation and expressions used in this calculation are presented here in detail. Additionally a survey of the propagators stated in the literature shall be given here. In general the free Delta propagator can be cast in the following form:

$$G_\Delta^{-1} = M_\Delta - \sqrt{s_\Delta} - \frac{i}{2}\Gamma(s_\Delta) \tag{B.18}$$

The invariant energy of the Delta is denoted by $s_\Delta = p_{\Delta,\mu}^2$ and Γ is the energy-dependent decay width. The photo-absorption via a Delta can take place in two time orderings: (i) a meson exchange excites a nucleon to a Delta succeded by a photo-induced deexcitation, (ii) a photo-induced excitation of a nucleon followed by a meson-mediated deexcitation of the Delta. These processes, which are referred to as non-resonant and resonant Delta excitation, are displayed in Fig. B.2 on page A21 together with the Delta decay graph. Compared to the free Delta propagator, the non-resonant propagator used here may not decay and has therefore no imaginary part:

$$G_r^{-1} = M_\Delta - \sqrt{s_r} - \frac{i}{2}\Gamma(s_r) \qquad\qquad G_n^{-1} = M_\Delta - \sqrt{s_n} \tag{B.19}$$

Here, G_r refers to the resonant propagator and G_n to the non-resonant one. Fig. B.2 on page A21 illustrates that the invariant energy s_n of the non-resonant graph depends on the particle which absorbes the photon:

$$G_{a,b}^n : \qquad s_n^{a,b} = M_\Delta^2 - 2(qE_{a,b} - \vec{q}\vec{p}_{a,b}) \tag{B.20}$$

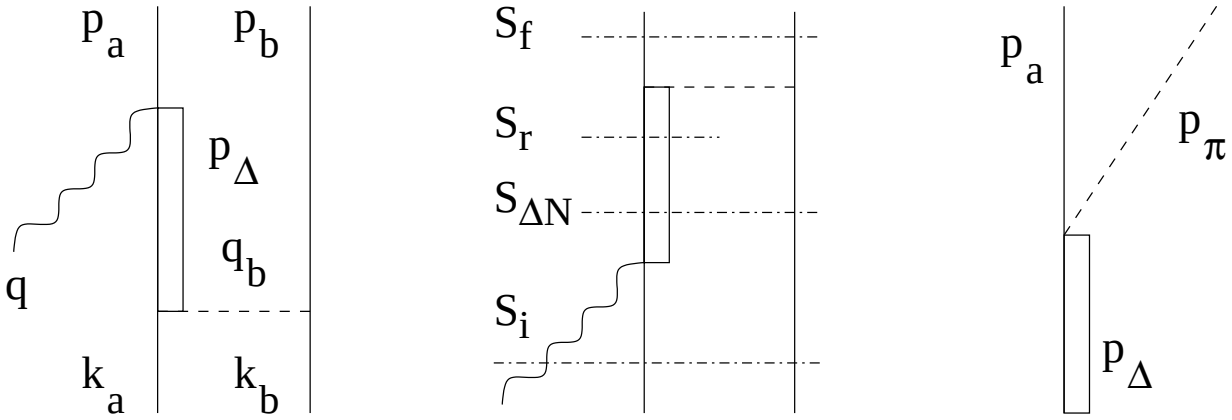

(a) non-resonant Feynman graph

(b) resonant Δ excitation

(c) Delta decay graph

Figure B.2: Relevant Feynman graphs involving the Delta. a) and b) describe the isobaric photo-absorption and c) the Delta decay. The time axis is directed upward.

At low photon energies the static propagator is retained: $G_s : s_n = M^2$. Starting with Fig. B.2(a) and neglecting the Delta momentum $\vec{p}_\Delta = 0$ allows to derive an alternative expression of the non-resonant propagator, which yields:

$$G_q^n : \qquad \sqrt{s_n} = \sqrt{q^2 + M^2} - q \tag{B.21}$$

Comparative calculations with $G_{a,b}^n$ and G_q^n show that there is only a minor numerical difference in the strength of the IC between these two propagators: G_q^n increases monotonically while $G_{a,b}^n$ reaches a fairly constant strength at about $E_\gamma \gtrsim 400$ MeV. The static propagator G_s overestimates the yield from G_q^n and $G_{a,b}^n$ by about a factor of 3 and should never be used above $E\_gamma = 100$ MeV.

In case of the resonant graph there are in principle two approaches: (i) the direct calculation of s_r from the photon and the involved nucleon momentum and (ii) the determination of s_r from the invariant Delta-nucleon energy $s_{\Delta N}$. The direct calculation considers the second (respectively the others) nucleon as spectator and thus the invariant energy is given by:

$$s_r = p_{\Delta,\mu}^2 = (q + k_N)_\mu^2 \tag{B.22}$$

$$\rightsquigarrow \quad s_r^{a,b}(\vec{k}) = \epsilon_N^2 + 2q\epsilon_N - (\vec{K}/2 \pm \vec{k})^2 - 2\vec{q}(\vec{K}/2 \pm \vec{k}) \tag{B.23}$$

Here, the energy of the bound nucleon is taken at its mean value respecting the binding energy: $\epsilon_N = M - E_B$. This expression together with (B.19) can now be used in the relative momentum integral, (see Section B.2) and should give a rather realistic description. Unfortunately the integration would be rather cumbersome and time consuming; therefore this expression is frequently approximated by $\vec{k}_N = 0$ which leads to:

$$G_{Ni}^r : \qquad s_r = \epsilon_N^2 + 2q\epsilon_N \tag{B.24}$$

However, a less severe approximation was also studied, namely neglecting the relative momentum only: $\vec{k} = 0$ which gives:

$$G^r_{NP}: \qquad s_r = \epsilon_N^2 + 2q\epsilon_N + (3q^2 - P^2 - 2\vec{q}\vec{P})/4 \tag{B.25}$$

In the other approach of determing s_Δ, the relation between the invariant Delta energy and the one of the Delta-nucleon system is exploited. Hence, we have:

$$s_{\Delta N} = (p_\Delta + k_N)^2_\mu \tag{B.26}$$

$$= s_r + E_N^2 - k_N^2 + 2E_\Delta\epsilon_N - 2\vec{p}_\Delta\vec{k}_N \tag{B.27}$$

Neglecting the smallest term corresponding to $\vec{k}_N = 0$ and using $E_\Delta = \epsilon_N + q$ one gets:

$$s_r = s_{\Delta N} - \epsilon_N(3\epsilon_N + 2q) \tag{B.28}$$

It can be shown that the expression $\sqrt{s_r} = \sqrt{s_{\Delta N}} - M$ together with the propagator $G^r_M : s_{\Delta N} = 4M^2 + 4qM$ which are frequently applied [94, 107, 154], is an approximation of (B.28) and (B.27) for small values of q. Although this propagator is used in serious models and in many theoretical publications, less severe approximations are investigated in the following paragraph.

The invariant energy of the Delta-nucleon system $s_{\Delta N}$ can be calculated via the final s_f or the initial state s_i (compare Fig. B.2(b) on page A21). For the latter the CM energy reads with $s_{\Delta N} = s_i$:

$$G^r_i: \qquad s_i = (q + k_a + k_b)^2_\mu = (q + 2\epsilon_N)^2 - P^2$$
$$= 4\epsilon_N^2 + 4q\epsilon_N - K^2 - 2\vec{q}\vec{K} \tag{B.29}$$

The final CM energy is given in the following formula, whereby the binding energy of the two nucleons involved is not taken into account. This leads to a shift of the Delta peak in the excitation function. It can be taken care of, however, by substituting M in the final state by $M + E_B$ or by an altered relation between s_f and $s_{\Delta N}$. Calculations proved that these two methods yield numerically the same result and are thus both denoted by G^r_{fB}.

$$G^r_f: \qquad s_f = (p_a + p_b)^2_\mu = (E_a + E_b)^2 - P^2 \tag{B.30a}$$

$$G^r_{fB}: \qquad s_{\Delta N} = s_f + 4(E_a + E_b)E_B \tag{B.30b}$$

The propagators derived above are plotted in Fig. B.3 on page A23 for comparison. Employing G_M, which is defined above, results in a too low resonance energy and should therefore never be used for reliable quantitative calculations. The resonance peak is overestimated by G_{Ni} and reveals therewith that the approximation of a nucleon at rest $k_N = 0$ is too crude. The better approximation of a vanishing relative momentum (G_{NP}) improves the situation. G^r_f and G^r_i yield numerically almost the same Delta contribution and thus only G^r_f is plotted. That propagator was considered by the author as the one best suited for the model presented in Chapter 4 and thus used for the 2N knock out calculations.

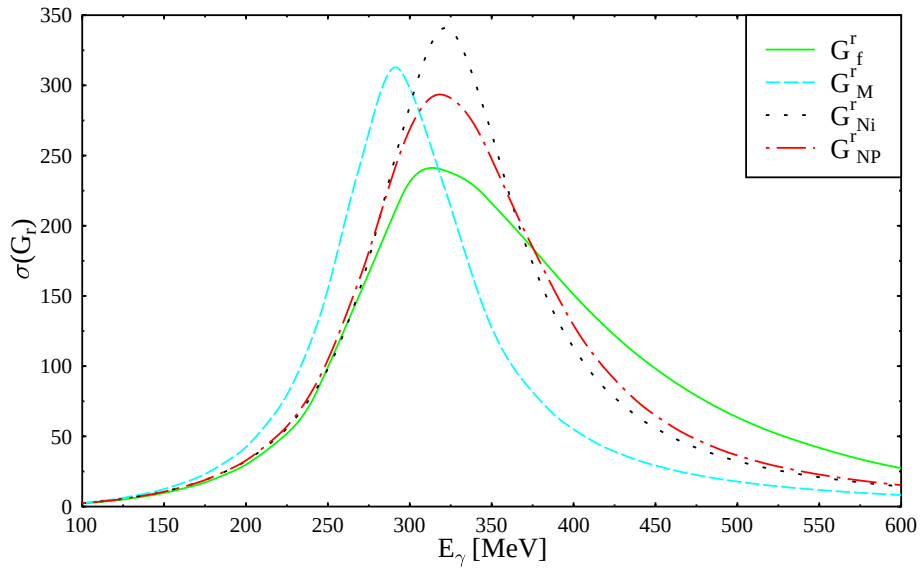

Figure B.3: Sole contribution of the IC for diverse Delta propagators. The labels in the figure correspond to the ones of the equations presented in this section.

The decay width was taken from [113], which is a standard parametrization and frequently used. As there is energy transfer into the resonance, the decay width depends on it:

$$\Gamma(s) = \frac{f^2_{\pi N\Delta}}{6\pi} \frac{|\vec{p}_\pi|^3}{\sqrt{s}} \frac{M}{m^2} \tag{B.31}$$

Here, $\vec{p}_\pi$ denotes the decay momentum and $\sqrt{s}$ the total energy in the nucleon-pion CM frame, which is defined by $\vec{p}_N = -\vec{p}_\pi$. From the expression of the invariant mass: $s_\Delta = (E_N + E_\pi)^2$, see Fig. B.2(c) on page A21, a relation between the pion momentum and the CM energy can be derived in order to calculate these two quantities entering the decay width (B.31):

$$\begin{aligned} \left(s_\Delta - (M^2 + m^2) - 2p^2_\pi\right)^2 &= 4(M^2 + p^2_\pi)(m^2 + p^2_\pi) \\ \rightsquigarrow p^2_\pi(s_\Delta) &= \left(s_\Delta - (M+m)^2\right)\left(s_\Delta - (M-m)^2\right)/4s_\Delta \end{aligned} \tag{B.32}$$

Lists

Acronyms

3B three body or three nucleons (3N)

1BC correlated one body current

ADC analog to digital converter. Either time- or charge-to-digital converter, which are refered to by TDC or QDC.

ANB analytical bremsstrahlung-calculation. Code for calculating bremsstrahlung using an approximative analytical formulation.

BD beam divergence of the electron beam at the radiator

BS beam spot size of the electron beam on the radiator

CD collimator displacement. Transversal position distribution of the collimator viewed in the electron system.

CM center of momentum system. Often incorrectly referred to as center of mass system. The condition of this coordinate system, however, is a vanishing total momentum.

CFD constant fraction discriminator

ΔE_{pip} start and ΔE detector of PiP

DWIA distorted wave impulse approximation. If used for the final state, FSI is approximately taken into account.

DALINAC Darmstadt linear accelerator, 120 MeV beam energy

ELFE Electron Laboratory for Europe. Proposed high energy electron accelerator to explore the confinement domain of QCD.

E_{pip} energy layer of PiP

ED total electron divergence

ES beam energy spreading. Energy distribution of electron beam from accelerator.

FPD focal plane detector. A ladder of 352 partially overlapping scintillators in the focal plane of the Tagger dipol magnet to determine the energy of the electrons.

FSI final state interaction: Interaction of one or both emitted hadrons with each other or primarily with the rest of the nucleus, hence with the $A-2$ system.

FWHM full width at half maximum

G2N genuine two nucleon absorption. Photoinduced two nucleon emission based on the Feynman graphs shown in Fig. 1.2 on page 6 excluding 3N absorption or FSI.

GSI Gesellschaft für Schwerionenforschung mbH. GSI is a heavy ion research center located in Darmstadt, Germany

HO harmonic oscillator

IC Δ isobar current

ISI inital state interaction. Interaction of the incident projectile with the nucleus prior the appropriate nuclear reaction.

JLAB Jefferson Laboratory

IPM independent particle model. Nuclear shell model of independent moving particles in a central potential.

LDA local density approximation. Folding of the cross section with the nuclear density distribution.

LED leading edge discriminator

LeD light emitting diode

MAMI Mainz Microtron. Three race track microtrons with maximal beam energy of 855 MeV (MAMI-B).

MCB Monte-Carlo bremsstrahlung-calculation. Code for calculating bremsstrahlung on a Monte Carlo based method.

MEC meson exchange current

MS multiple scattering. Scattering of an electron in the radiator before producing a bremsstrahl photon.

PWIA plane wave impulse approximation

QCD Quantum Chromo Dynamics. Non abelian gauge theory of strongly interacting particles (quarks and gluons).

QDC charge to digital converter

PiP pion-proton hodoscope. Large solid angle detector for pions and protons consisting out of 23 scintillator bars.

PMT photo multiplier tube

PLU programmable lookup unit. A fast memory, hence also called memory lookup unit (MLU), which allows to map arbitrary logical combinations of the input signals onto the output.

RTM race track microtron

rms root mean square

SM nuclear shell model

SPA spectator approximation. In 2N knock-out reactions, this approximation assumes no energy and momenta transfer to the residual nucleous.

SRC short range correlations. NN correlations as a result of the short range (mostly repulsive) potential.

SVD start and veto detector of the PiP-ToF setup

Tagger photon-tagging magnetic spectrometer

TAPS originally 'two arm', then 'three arm' and now 'travel around photon spectrometer'. The spectrometer consists of 6 blocks of 8×8 BaF_2 scintillator arrays.

TDC time to digital converter

ToF time-of-flight detector

TRIUMF Canada's National Laboratory for Particle and Nuclear Physics. A meson factory based on a large cyclotron for negatively charged hydrogen ions.

OGEP one gluon exchange potential

PIN positive intrinsic negative doted diode

QD quasi-deutron (model)

List of Figures

List of Tables

Bibliography

[1] B. Pudline and V. R. Pandharipande, Phys. Rev. **C56** (1997) 1720

[2] R. Schiavilla, V. R. Pandharipande, and R. B. Wiringa, Nucl. Phys. **A449** (1986) 219

[3] V. R. Pandharipande, Nucl. Phys. **A577** (1994) 131

[4] A. Fabrocini, F. A. de Saavedra, G. Co', and P. Folgarait, Phys. Rev. **C57** (1998) 1668

[5] (R. Neuhausen and L. Tiator, eds.), *Jahresbericht*, Institut für Kernphysik, Mainz, 1999

[6] W. Bertozzi and G. Rosner, Studying the internal small-distance structure of nuclei via the triple coincidence (e,e'p+n) measurement, Technical Report Proposal 97-106 (update), Jefferson Laboratory, 2000

[7] (S. D. Bass and P. A. M. Guichon, eds.), *Confinement Physics*, Editions Frontieres, 1995

[8] (W. F. Henning and G. Siegert, eds.), *Annual Report 2000*, Gesellschaft für Schwerionenforschung mbH, Darmstadt, 2000

[9] Experiments E719/E725/E785, Annual reports, http://www.triumf.ca/annrep, 2001

[10] J. J. O. Haxel and H. Suess, Phys. Rev. **75** (1949) 1766

[11] M. Goeppert-Mayer, Phys. Rev. **75** (1949) 1969

[12] P. Grabmayr, G. Mairle, and U. Schmidt-Rohr, Physikalische Blätter **55** (1999) 35

[13] D. A. Liberman, Phys. Rev. **D16** (1977) 1542

[14] C. E. D. Tar, Phys. Rev. **D17** (1978) 323

[15] B. Povh, *Teilchen und Kerne*, Springer-Verlag Berlin Heidelberg, 1993

[16] A. Faessler, F. Fernandez, G. Lübeck, and K. Shimizu, Prog. Part. and Nucl. Phys. **29** (1992) 251

[17] U. Straub *et al.*, Nucl. Phys. **A483** (1988) 686

[18] H. Müther, In Proc. *Workshop on Electromagnetically Induced Two-Hadron Emission* (A. Lallena, C. Garcia-Recio, P. Grabmayr, and R. Owens, eds.), 1999

[19] P. Grabmayr, Prog. Part. and Nucl. Phys. **29** (1992) 251

[20] H. Müther, A. Polls, and W. H. Dickhoff, Phys. Rev. **C51** (1995) 3040

[21] K. Gottfried, Nucl. Phys. **5** (1958) 557

[22] P. Grabmayr, J. Ahrens, J. R. M. Annand, I. Anthony, D. Branford, G. E. Cross, T. Davinson, S. J. Hall, P. D. Harty, T. Hehl, J. D. Kellie, T. Lamparter, I. J. D. MacGregor, J. A. MacKenzie, J. C. McGeorge, G. J. Miller, R. O. Owens, M. Sauer, R. Schneider, K. Spaeth, and G. J. Wagner, Phys. Lett. **B370** (1996) 17

[23] T. Lamparter, PhD thesis, Physikalisches Institut, Tübingen, 1997

[24] T. T. H. Yau, I. J. D. MacGregor, J. Ahrens, J. R. M. Annand, R. Beck, D. Branford, P. Grabmayr, S. J. Hall, P. D. Harty, T. Hehl, D. G. Ireland, J. D. Kellie, T. Lamparter, K. Livingston, M. Liang, J. A. MacKenzie, S. McAllister, J. C. McGeorge, R. O. Owens, M. Sauer, R. Schneider, and D. P. Watts, Eur. Phys. J. **A1** (1998) 241

[25] S. J. McAllister, J. C. McGeorge, I. J. D. MacGregor, J. R. M. Annand, S. J. Hall, P. D. Harty, J. D. Kellie, G. J. Miller, R. O. Owens, D. P. Watts, T. T.-H. Yau, D. Branford, J. A. MacKenzie, M. Liang, P. Grabmayr, T. Hehl, T. Lamparter, M. Sauer, R. Schneider, J. Ahrens, and R. Beck, Phys. Rev. **C60** (1999) 044610

[26] I. J. D. MacGregor, T. T.-H. Yau, J. Ahrens, J. R. M. Annand, R. Beck, D. Branford, P. Grabmayr, S. J. Hall, P. D. Harty, T. Hehl, J. D. Kellie, T. Lamparter, M. Liang, J. A. MacKenzie, S. McAllister, J. C. McGeorge, R. O. Owens, J. Ryckebusch, M. Sauer, R. Schneider, and D. P. Watts, Phys. Rev. Lett. **80** (1998) 245

[27] P. D. Harty, J. C. McGeorge, I. J. D. MacGregor, R. O. Owens, J. R. M. Annand, I. Anthony, G. I. Crawford, S. J. D. Dancer, G. J. Miller, B. Schoch, R. Beck, H. Schmieden, J. M. Vogt, and J. Ryckebusch, Phys. Rev. **C51** (1995) 1982

[28] P. D. Harty, I. J. D. MacGregor, P. Grabmayr, J. Ahrens, J. R. M. Annand, I. Anthony, R. Beck, D. Branford, G. E. Cross, T. Davinson, S. J. Hall, T. Hehl, J. D. Kellie, T. Lamparter, J. A. MacKenzie, J. C. McGeorge, G. J. Miller, R. O. Owens, M. Sauer, R. Schneider, and K. Spaeth, Phys. Lett. **B380** (1996) 247

[29] P. D. Harty, I. J. D. MacGregor, J. Ahrens, J. R. M. Annand, I. Anthony, R. Beck, D. Branford, G. E. Cross, T. Davinson, P. Grabmayr, S. J. Hall, T. Hehl, J. D. Kellie, T. Lamparter, J. A. MacKenzie, J. C. McGeorge, G. J. Miller, R. O. Owens, M. Sauer, R. Schneider, and K. Spaeth, Phys. Rev. **C57** (1998) 123

[30] J. A. MacKenzie, D. Branford, J. Ahrens, J. R. M. Annand, R. Beck, G. E. Cross, T. Davinson, P. Grabmayr, S. J. Hall, T. Hehl, D. G. Johnstone, J. D. Kellie, T. Lamparter, M. Liang, I. J. D. MacGregor, J. C. McGeorge, R. O. Owens, M. Sauer, R. Schneider, A. C. Shotter, K. Spaeth, P. J. Woods, and T. Yau, Phys. Rev. **C54** (1996) R6

[31] V. I. Kukulin, V. T. Voronchev, T. D. Kaipov, and R. A. Eramzhyan, Nucl. Phys. **A513** (1990) 221

[32] R. C. Carrasco and E. Oset, Nucl. Phys. **A541** (1992) 585

[33] R. C. Carrasco and E. Oset, Nucl. Phys. **A536** (1992) 445

[34] R. C. Carrasco, M. J. V. Vacas, and E. Oset, Nucl. Phys. **A570** (1994) 701

[35] J. S. Levinger, Phys. Rev. **84** (1951) 43

[36] T. Hehl, private communication, 1999

[37] A. Nogga, H. Kamada, and W. Glöckle, Phys. Rev. Lett. **85** (2000) 944

[38] C. C. degli Atti and S. Simula, Phys. Rev. **C53** (1995) 1689

[39] G. Anagnostatos, A. Antonov, P. Ginis, J. Giapitzakis, M. Gaidarov, and A. Vassiliou, Phys. Rev. **C58** (1998) 2115

[40] S. Boffi, C. Giusti, F. D. Pacati, and M. Radici, Nucl. Phys. **A564** (1993) 473

[41] J. Ryckebusch, D. Debruyne, and W. Nespen, Phys. Rev. **C57** (1998) 1319

[42] J. Ryckebusch, W. Nespen, and D. Debruyne, Phys. Lett. **B441** (1999) 1

[43] S. M. Doran, I. J. D. MacGregor, J. R. M. Annand, I. Anthony, S. N. Dancer, S. J. Hall, J. D. Kellie, J. C. McGeorge, G. J. Miller, R. O. Owens, P. A. Wallace, B. Schoch, H. Schmieden, and S. Klein, Nucl. Phys. **A559** (1993) 347

[44] T. Emura, I. Endo, S. Endo, H. Itoh, S. Kato, M. Koike, K. Maeda, T. Maki, , S. Maruo, K. Maruyama, Y. Murata, K. Niki, C. Rangacharyulu, A. Sasiki, T. Suda, Y. Sumi, Y. Wada, and H. Yoshida, Phys. Lett. **B267** (1991) 460

[45] T. Emura, I. Endo, S. Endo, H. Itoh, S. Kato, M. Koike, K. Maeda, T. Maki, , S. Maruo, K. Maruyama, Y. Murata, K. Niki, C. Rangacharyulu, A. Sasiki, T. Suda, Y. Sumi, Y. Wada, and H. Yoshida, Phys. Lett. **B286** (1992) 229

[46] F. V. Adamian, A. Y. Buniatian, G. S. Frangulian, P. I. Galumian, V. H. Grabsky, A. V. Hairapetioan, H. H. Hakopian, V. K. Hoktanian, G. V. Karapetian, A. H. Vartapetian, and V. G. Volchinsky, J. Phys. G: Nucl. Part. Phys. **17** (1991) 1657

[47] P. Grabmayr, T. Hehl, A. Stahl, J. R. M. Annand, and R. O. Owens, Nucl. Instr. Methods **A402** (1998) 85

[48] T. Hehl, P. Grabmayr, M. Sauer, and G. J. Wagner, Nucl. Instr. Methods **A354** (1995) 505

[49] I. Anthony *et al.*, Nucl. Instr. Methods **A301** (1991) 230

[50] S. J. Hall *et al.*, Nucl. Instr. Methods **A368** (1996) 698

[51] S. Oberkirsch, Diploma thesis, Physikalisches Institut, Tübingen, 1996

[52] S. Oberkirsch, P. Grabmayr, T. Hehl, and V. Leon, Nucl. Instr. Methods **A418** (1999) 507

[53] A. Settele, Diploma thesis, Physikalisches Institut, Tübingen, 1996

[54] T. Lamparter, Diploma thesis, Physikalisches Institut, Tübingen, 1993

[55] D. Branford, Nuclear Physics News **4** (1964)

[56] I. J. D. MacGregor, In Proc. *Proc. Workshop on Furture Detectors for Photonuclear Experiments* (D. Branford, ed.), 1992

[57] R. Schneider, PhD thesis, Physikalisches Institut, Tübingen, 1996

[58] J. A. MacKenzie, PhD thesis, Department of Physics, University of Edinburgh, 1995

[59] M. Mayer, Diploma thesis, Physikalisches Institut, Tübingen, 1997

[60] P. Grabmayr, Timing and timing correction in the holy grail, Technical Report 2, Physikalisches Institut, Tübingen, 1997

[61] *FASTBUS: modular high speed data acquisition and control system, VME-bus specification, CAMAC: modular instrumentation system for data handling*, 1972, ANSI/IEEE Std 960-1086, ANSI/IEEE Std 1014-1987, EUR 4100e

[62] J. R. M. Annand, I. Anthony, and A. Sibbald, Acqu manual, Technical report, Kelvin Lab, Glasgow, 1995

[63] M. M. May, Phys. Rev. **84** (1951) 265

[64] H. Überall, Phys. Rev. **103** (1956) 1055

[65] H. Überall, Phys. Rev. **107** (1957) 223

[66] G. Diambrini Palazzi, Revs. Mod. Phys. **40** (1968) 661

[67] U. Timm, Fortschr. d. Physik **17** (1969) 765

[68] D. Lohmann, J. Peise, J. Ahrens, I. Anthony, H.-J. Arends, R. Beck, R. Crawford, A. Hünger, K. H. Kaiser, J. D. Kellie, C. Klümper, P. Krahn, A. Kraus, U. Ludwig, M. Schumacher, O. Selke, M. Schmitz, M. Schneider, F. Wissmann, and S. Wolf, Nucl. Instr. Methods **A343** (1994) 494

[69] D. Lohmann, Diploma thesis, Georg-August-Universität, Göttingen, 1992

[70] R. Rambo, B. Krusche, and U. Siodlaczek, Elsevier Preprint (1999)

[71] R. Rambo, Diploma thesis, II Physikalisches Institut, Georg-August-Universität Göttingen, 1995

[72] J. H. Hubbell, J. Appl. Phys.**30** (1958) 981

[73] J. L. Matthews and R. O. Owens, Nucl. Instr. Methods **111** (1987) 157

[74] W. Greiner and J. Reinhardt, *Theoretische Physik, Quantenelektrodynamik*, Harri Deutsch, Thun, Frankfurt (Main), 1984

[75] F. A. Natter, Analytical treatment of coherent bremsstrahlung, Technical report, Physikalisches Institut, Tübingen, 1998

[76] H. Bilokon *et al.*, Nucl. Instr. Methods **204** (1983) 299–310

[77] J. A. Wheeler and W. E. Lamb, Phys. Rev. **55** (1939) 858

[78] H. W. Koch and J. W. Motz, Revs. Mod. Phys. **31** (1959) 920

[79] F. A. Natter, In Proc. *Electromagnetically Induced Two-Hadron Emission* (A. M. L. C. Garcia-Recio, P. Grabmayr and R. O. Owens, eds.), p. 59, 1999

[80] G. Molière, Z. Naturforschung **3a** (1948) 78

[81] M. Voit, private communication, 1999

[82] T. Suda, private communication, 1998

[83] F. A. Natter and P. Grabmayr, Comment on the paper by F. Rambo *et al.* 'coherent π^0 photoproduction', Technical report, Physikalisches Institut, Tübingen, 1999

[84] F. A. Natter and P. Grabmayr, Prediction of linearly polarized bremsstrahlung production for ELFE at CERN, Technical report, Physikalisches Institut, Tübingen, 1999

[85] D. Marchant, F. A. Natter, and R. V. de Vyver, A high-energy, high-intensity and highly polarized photon beam for elfecern using coherent bremsstrahlung, Technical report, HaPHEEP, Report of the European Real Photon Working Group, 1999

[86] B. Seitz, F. A. Natter, and *et al.*, Using coherent bremsstrahlung for high energy photons at hera and elfe, Technical report, HaPHEEP, Report of the European Real Photon Working Group, 1999

[87] P. Grabmayr and F. A. Natter, In Proc. *Proceedings of Symposium on Nuclei and Nucleons Darmstadt, oct 11-13, Nucl. Physics A690(2001)251*, 2000

[88] R. Jastrow, Phys. Rev. **98** (1955) 1479

[89] L. Boato and M. M. Giannini, J. Phys. G: Nucl. Part. Phys. **15** (1989) 1605

[90] L. Boato and M. M. Giannini, Nucl. Phys. **A533** (1991) 441

[91] C. Giusti, F. D. Pacati, and M. Radici, Nucl. Phys. **A546** (1992) 607

[92] M. Vanderhaeghen, L. Machenil, J. Ryckebusch, and M. Waroquier, Nucl. Phys. **A580** (1995) 551

[93] J. Ryckebusch, M. Vanderhaeghen, L. Machenil, and M. Waroquier, Nucl. Phys. **A568** (1994) 828

[94] D. Knoedler, PhD thesis, Universität Tübingen, Theoretisches Institut, Tübingen, 1998

[95] L. Machenil, M. Vanderhaeghen, J. Ryckebusch, and M. Waroquier, Phys. Lett. **B316** (1993) 17

[96] T. Yau, PhD thesis, University of Glasgow, Physics Departement, Glasgow, 1996

[97] J. Ryckebusch, V. Sluys, K. Heyde, H. Holvoet, W. Nespen, M. Waroquier, and M. Vanderhaeghen, Nucl. Phys. **A624** (1998) 581

[98] J. Ryckebusch and W. Nespen, In Proc. *Workshop on Electromagnetically Induced*

Two-Hadron Emission (A. Lallena, C. Garcia-Recio, P. Grabmayr, and R. Owens, eds.), 1999

[99] H. Müther and L. D. Skouras, Phys. Lett. **B306** (1993) 201

[100] H. Müther, G. Knehr, and A. Polls, Phys. Rev. **C52** (1996) 2955

[101] O. Bohigas and S. Stringari, Phys. Lett. **B95** (1980) 9

[102] O. Benhar, C. C. degli Atti, S. Fantoni, S. Rosati, A. Kallio, L. Lantto, and P. Toropainen, Phys. Lett. **B64** (1976) 395

[103] G. Co', A. Fabrocini, S. Fantoniand, and I. Lagaris, Nucl. Phys. **A549** (1992) 439

[104] J. Dubach, J. Koch, and T. Donnelly, Nucl. Phys. **A271** (1976) 279

[105] M. Wakamatsu and K. Matsumoto, Nucl. Phys. **A392** (1983) 323

[106] T. Wilbois, P. Wilhelm, H. Arenhövel, J. Ryckebusch, L. Machenil, M. Vanderhaeghen, V. Sluys, and M. Waroquier, Phys. Rev. **C54** (1997) 3311

[107] T. Wilbois, P. Wilhelm, and H. Arenhövel, Phys. Rev. **C54** (1996) 3311

[108] C. Giusti, F. D. Pacati, K. Allart, W. J. W. Geurts, W. H. Dickhoff, and H. Müther, Phys. Rev. **C57** (1998) 1691

[109] M. Vanderhaeghen, L. Machenil, J. Ryckebusch, and M. Waroquier, Nucl. Phys. **A2071** (1994) 1

[110] D. Riska, Prog. Part. and Nucl. Phys. **11** (1984) 199

[111] D. Riska, Prog. Part. and Nucl. Phys. **181** (1989) 207

[112] N. Bianci *et al.*, Phys. Rev. **C54** (1996) 1688

[113] E. Oset, H. Toki, and W. Weise, pr**83** (1982) 281

[114] S. A. Teukolsky, W. T. Vetterling, and B. Flannery, *Numerical Recipes in C*, Cambridge University Press, 1992

[115] G. Rosner, Prog. Part. and Nucl. Phys. **44** (2000) 99

[116] G. Rosner, In Proc. *Workshop on Electron-Nucleus Scattering, Elba International Physics Center, Italy*, June 1998

[117] S. Boffi and M. M. Giannini, Nucl. Phys. **A533** (1991) 442

[118] R. Madey *et al.*, Nucl. Instr. Methods **151** (1978) 445

[119] S. Klein, PhD thesis, Physikalisches Institut, Tübingen, 1990

[120] M. Sauer, Diploma thesis, Physikalisches Institut, Tübingen, 1993

[121] J. Leypoldt, Simulation of 2d lightguides and scintillators, Technical Report 5, Physikalisches Institut, Tübingen, 1994

[122] M. Sauer, A. Fuchs, P. Grabmayr, and J. Leypoldt, Nucl. Instr. Methods **A378** (1996) 143

[123] P. D. Group, *The European Physical Journal C, Review of Particle Physics*, EDP Sciences, Springer, 1998

[124] C. Grupen, *Teilchendetektoren*, BI-Wiss.-Verl., Mannheim, 1993

[125] H. H. Andersen and J. F. Ziegler, *Hydrogen Stopping Powers and Ranges in All Elements*, Pergamon Press, New York, 1979

[126] R. Schneider, A method of calculating proton ranges for different materials and the usage for energy reconstruction in a scintillator hodoscope, Technical report, Physikalisches Institut, Tübingen, 1994

[127] W. H. Barkas and M. J. Berger, National Aeronautics and Space Administration (1964)

[128] T. Hehl and R. Schneider, Energy losses of charged particles in the helium experiment, Technical Report 4, Physikalisches Institut, Tübingen, 1996

[129] K. Spaeth, Diploma thesis, Physikalisches Institut, Tübingen, 1993

[130] B. Schorr, Computer Phys. Comm. **7** (1974) 215–224

[131] CERN, *GEANT – Detector Description and Simulation Tool*, program library w5013 edition

[132] T. Hehl, Pulse height calibration of tof in the 1996 experiment, Technical Report 6, Physikalisches Institut, Tübingen, 1996

[133] S. Cierjacks *et al.*, Nucl. Instr. Methods **192** (1982) 407

[134] T. Hehl, In Proc. *Workshop on Electromagnetically Induced Two-Hadron Emission* (A. Lallena, C. Garcia-Recio, P. Grabmayr, and R. Owens, eds.), 1999

[135] C. Powrie, I. MacGregor, P.Grabmayr, and F. Natter, Phys. Rev. **C64** (2001)

[136] S. Franczuk, I. J. D. MacGregor, J. R. M. Annand, R. Beck, D. Branford, P. Grabmayr, T. Hehl, D. G. Ireland, K. Livingston, J. C. McGeorge, F. A. Natter, R. O. Owens, C. J. Y. Powrie, J. Ryckebusch, and D. P. Watts, Phys. Lett. **B450** (1999) 332

[137] M. Giannini and E. Santopinto, Phys. Rev. **C49** (1994) 1258

[138] A. Nogga, private communication, 2000

[139] W. van Nespen and J. Ryckebusch, private communication, 1999,2000

[140] D. Tedeschi, G. Audit, J. Laget, and A. Sandorfi, Phys. Rev. Lett. **73** (1994) 408

[141] M. MacCormick, J. Habermann, J. Ahrens, G. Audit, R. Beck, A. Braghieri, G. Galler, N. d'Hose, V. Isbert, P. Pedroni, T. Pinelli, G. Tamas, S. Wartenberg, and A. Zabrodin, Phys. Rev. **C55** (1997) 1033

[142] J. Habermann, Diploma thesis, Physikalisches Institut, Tübingen, 1996

[143] S. Boffi, C. Giusti, F. D. Pacati, and M. Radici, In Proc. *6th Workshop on Perspectives in Nuclear Physics at Intermediate Energies* (S. Boffi, C. C. degli Atti, and M. Giannini, eds.), p. 299, Singapore: World Scientific, 1994

[144] J. Ryckebusch, V. Sluys, M. Waroquier, L. J. H. M. Kester, W. H. A. Hesselink, E. Jans, and A. Zondervan, Phys. Lett. **B333** (1994) 310

[145] D. G. Ireland, I. J. D. MacGregor, and J. Ryckebusch, Phys. Rev. **C59** (1999) 3297

[146] S. Wartenberg *et al.*, few body systems **26** (1999) 213

[147] G. Audit, A. Braghieri, N. d'Hose, V. Isbert, S. Kerhoas, J. M. Laget, M. MacCormick, L. Y. Murphy, A. Panzeri, P. Pedroni, T. Pinelli, G. Tamas, J. Ahrens, J. R. M. Annand, R. Crawford, P. Grabmayr, S. J. Hall, and J. D. Kellie, Nucl. Phys. **A614** (1997) 461

[148] W. V. Nespen and J. Ryckebusch, In Proc. *5th Workshop on e-m induced Two-Hadron Emission, Lund 6.2001*, 2001

[149] P. Grabmayr, Acqu manual, holy grail version of acqu, Technical report, Physikalisches Institut, Tübingen, 1999

[150] I. J. D. MacGregor (spokesperson) and P. Grabmayr *et al.*, Study of short range effects in (γ,nn) reactions, Technical Report Proposal A2/11-97, Mainz, Glasgow and Tübingen University, 2000

[151] D. T. Cromer and J. T. Waber, Acta Cryst.**18** (1965) 104

[152] A. J. C. Wilson, *Int. Tables for Crystallography*, Kluwer Academic Publishers, Dordrecht, 1992

[153] W. Heitler, *The Quantum Theory of Radiation*, Clarendon Press, Oxford, 1954

[154] P. Wilhelm, H. Arenhoevel, C. Giusti, and F. D. Pacati, Z. Phys. **A359** (1998) 467

[155] A. Fabrocini, F. A. de Saavedra, and G. Co', Phys. Rev. **C61** (2000) 44302

[156] H. Müther, S. Koonin, R. Seki, and U. van Kolck, Phys. Rev. **C61** (2000) 44320

[157] H. Müther and A. Polls, nucl-th/0001007 (2000)

[158] F. Klein, J. R. M. Annand, J. Becker, P. Grabmayr, T. Hehl, W. Heil, M. Meyerhoff, F. A. Natter, E. W. Otten, R. O. Owens, and D. Rohe, Prog. Part. and Nucl. Phys. **36** (1996) 53

[159] J. Becker, P. Grabmayr, W. Heil, F. Klein, F. A. Natter, E. W. Otten, R. O. Owens, D. Rohe, and H. Schmieden, Eur. Phys. J. **A6** (1999) 329

[160] C. Herberg, M. Ostrick, J. R. M. Annand, J. Becker, P. Grabmayr, T. Hehl, W. Heil, F. Klein, K. Livingston, F. A. Natter, E. W. Otten, R. O. Owens, D. Rohe, and H. Schmieden, Eur. Phys. J. **A5** (1999) 131

[161] M. Ostrick, C. Herberg, J. R. M. Annand, J. Becker, P. Grabmayr, T. Hehl, W. Heil, F. Klein, K. Livingston, F. A. Natter, E. W. Otten, R. O. Owens, D. Rohe, H. Schmieden, and R. Watson, Phys. Rev. Lett. **83** (1999) 276

[162] F. A. Natter, P. Grabmayr, and B. Owens, NIM, http://www.pit.physik.uni-tuebingen.de/grabmayr/software/software.html (to be submitted)

[163] F. Wissmann, J. Ahrens, R. Beck, P. Grabmayr, T. Hehl, P. Jennewein, B. Krusche, A. Natter, F. Rambo, M. Schumacher, B. Seitz, U. Siodlaczek, and H. Ströher, Nucl. Phys. **A663-664** (2000) 97–400

[164] F. A. Natter, Prog. Part. and Nucl. Phys. **44** (2000) 461

[165] K. Kossert, M. Camen, F. Wissmann, J. Ahrens, H. Arends, R. Beck, G. Caselotti, P. Grabmayr, P. Harty, O. Jahn, P. Jennewein, M. Levchuk, A. L'vov, J. McGeorge, A. Natter, V. O. de León, M. Schumacher, B. Seitz, F. Smend, A. Thomas, W. Weihofen, and F. Zapadtka, to be submitted to Phys. Lett. **B** (2001)

[166] M. Camen, K. Kossert, F. Wissmann, J. Ahrens, H. Arends, R. Beck, G. Caselotti, P. Grabmayr, P. Harty, O. Jahn, P. Jennewein, M. Levchuk, A. L'vov, J. McGeorge, A. Natter, V. O. de León, M. Schumacher, B. Seitz, F. Smend, A. Thomas, W. Weihofen, and F. Zapadtka, to be submitted to Phys. Lett. **B** (2001)

[167] D. Branford, J. Arneil, J. MacKenzie, K. Föhl, F. Lee, J. Ahrens, J. Annand, R. Beck, P. Grabmayr, S. Hall, P. Harty, T. Hehl, J. Kellie, M. Liang, I. MacGregor, J. McGeorge, F. Natter, R. Owens, S. Oberkirsch, S. Wunderlich, and D. Watts, to be submitted to Phys. Rev. **C** (2001)

Academic Training

University

88-90 Vordiplom (Bacchelor) at Univerity of Stuttgart

90-91 Studies and laboratory courses in Tübingen

91-92 Study abroad as an exchange student at Missouri University

93-94 Studies in Tübingen

1995 Diploma thesis at the Physikalisches Institut of Tübingen:
"The electric formfactor of the neutron"
Diploma Degree in experimental, theoretical and high energy physics and microscopy

96-00 Employee at the Physikalisches Institut of Tübingen and Member of the Graduierten Kolleg Hadrons and Nuclei
Teacher in laboratory courses and tutorials and lecturer at the Berufs-Akademie (technical college) in Horb
Ph.D. Thesis at the Physikalisches Institut of Tübingen
"Study of Reaction Mechanisms and Short Range Correlations in Two Nukleon Emission off ^{4}He Using Polarized Photons"

Schools and Conferences

1995 International Summer school (Correlations and Clustering Phenomena in subatomic Physics) at Dronten, Netherlands
DPG school (Struktur des Nukleons) at Bad Honnef

1996 Elfe summer school (Confinement Physics), Cambridge, Britain
Workshop of the Graduierten Kolleg of Bonn and Tübingen in Brodenbach

1997 Photoinduced 2N Emission workshop, Glasgow, Scottland

1998 Schwerpunkt meeting of the German physical society, Bad Honnef
Gordon Conference on Photonuclear Reactions, Boston, USA
Workshop on nuclear physics of the MPI Heidelberg, Schleching

1999 Photoinduced 2N Emission workshop, Granada, Spain
Nuclear physics school (electromagnetic probes and the structure of Hadrons and Nuclei) at Erice, Sizely
Mini-Conference on "Studies of Few-Body-Systems" at NIKHEF, Amsterdam

2000 HaPHEEP-Workshop at the Center for subatomic Structure of Matter, Adelaide, Australia

95-99 Spring meeting of the German physical society (DPG) at München, Stuttgart, Köln, Freiburg, Göttingen and Bochum
and Meetings of the Graduierten Kolleg Hadrons and Nuclei (each year)

Publications[1]

[158] F. Klein et al., Electromagnetic form factors of the nucleon

[159] J. Becker et al., Determination of the neutron electric form factor from the reaction ^{3}He(e,e'n) at medium momentum transfer

[136] S. Franczuk et al., ^{12}C(γ,pn) photon asymmetry for E_γ =180-340 MeV

[160] C. Herberg et al., Determination of the neutron electric form factor in the D(e,e'n)p reaction and the influence of nuclear binding

[79] F.A. Natter et al., Production of linearly polarised photons

[161] M. Ostrick, Measurement of the Neutron Electric Form Factor $G_{E,n}$ in the Quasifree ^{2}H(e,e$'$n)p Reaction

[87] P. Grabmayr, Polarization in Photon Absorption Experiments

[162] F.A. Natter, Analytical treatment of experimental influences in producing polarized coherent bremsstrahlung

[163] F. Wissmann et al., Compton scattering from the free and bound proton above pion-threshold

[164] F.A. Natter, Photonpolarisation and Asymmetry in the ^{4}He($\vec{\gamma}$,np) Reaction

[135] C.J.Y. Powrie, Polarized photon measurements of the $^{12}C(\vec{\gamma}, pp)$ and $^{12}C(\vec{\gamma}, pn)$ reactions for $E_\gamma = 160 - 350$ MeV

[165] K. Kossert, et al., Neutron polarizabilities investigated by quasi-free Compton scattering from the deuteron

[166] M. Camen, et al., On the backward spin polarizability γ_π of the proton

[167] D. Branford et al., Investigation of Δ medium effects using ^{4}He$(\gamma, \pi^+$n$)^3$H and ^{4}He$(\gamma, \pi^+$p)nnn reactions

Reports

[85] D. Marchand, A High-Energy, High-intensity and Highly Polarized Photon Beam for ELFE at CERN using Coherent Bremsstrahlung

[86] B. Seitz, Using Coherent Bremsstrahlung for high energy photons at HERA and ELFE

[75] F.A. Natter, Analytical treatment of coherent Bremsstrahlung

[84] F.A. Natter, Prediction of linearly polarized Bremsstrahlung Production for ELFE at CERN

[83] F.A. Natter, Comment on the paper by F. Rambo *et al.* 'coherent π^0 photoproduction'

My academic teachers were:
Prof. G. Großer, Prof. E. Kasper, Prof. H. Müther, Prof. G. Staudt and
Prof. H. Clement, Prof. P. Grabmayr, Prof. R. Hübener, Prof. H. Pfister,
Prof. H. Reinhardt, Prof. H. Ruder, Prof. H. Stumpf, Prof. G.J. Wagner

[1] The citation numbers refer to the bibliography

Danksagung

Mein größter Dank gilt meinem Doktorvater, Herr Prof. P. Grabmayr, für die spannende Themenstellung und seine Unterstützung die er mir wärend meiner Arbeit gewährte. Eine große Hilfe war insbesondere seine Erfahrung auf diesem Gebiet und sein breites Wissen welches er mir stets zu Teil kommen ließ. Ebenso möchte ich mich bei Prof. G.J. Wagner für wertvolle Anregungen und sein Interesse an meiner Arbeit bedanken.
Besonders hervorheben möchte ich die wichtige Zusammenarbeit mit Dr. Torsten Hehl, der mit seinem kritischen Verstand ein wertvoller Diskussionspartner war und dessen Impulse zum Fortschritt dieser Arbeit beitrugen. Desweiteren waren die Diskussionen in der Gruppe, im Besonderen mit Dr. Markus Sauer und Jürgen Krimmer, sehr anregend und führten immer wieder zu neuen Lösungsansätzen und Ideen.

Entscheidend für den Erfolg der Messung, war der konstant qualitativ hochwertige Elektronen Strahl, der am MAMI zur Verfügung gestellt wurde. Desswegen möchte ich mich an dieser Stelle bei den Betreibern und Operateuren des Mainzer Microtrons bedanken, die durch ihr Bemühen für optimale Meßbedingungen sorgten. Mein ausdrücklicher Dank gilt auch John Annand, der sich zuverlässlich um die Elektronik der Datenerfassung kümmerte und uns wertvolle Hilfe zum Ausbau des Start und Veto Detektors gab. Ebenso trug die Zuverlässlichkeit des Helium Targets, welches Steffanie Oberkirsch entwickelt wurde, entscheidend zum Gelingen des Experiments bei. Weitere wertvolle Unterstützung erhielt ich von Prof. B. Owens, durch den ich bei einem Aufenthalt in Glasgow viel über die Physik der Bremsstrahlung lernte, so daß ich in der Lage war einige Fortschritte auf diesem Gebiet zu machen. Mein Dank gebührt auch der gesamten schottischen Kollaboration, welche beim Aufbau und Durchführung des Experiments beteiligt waren und die mir — und da möchte ich besonders Cameron McGeorge, Douglas MacGregor und Dan Watts erwähnen — wertvolle Tips bezüglich der Auswertung der Daten gaben. Dan brachte mich darüber hinaus dem Schottische Nachtleben und ihrer Guiness Kultur nahe.
Die Lösung vieler theoretischer und mathematischer Probleme erhielt ich von Jan Ryckebusch und Wim van Nespen von der Gent Universität, die ich auf einigen Tagungen treffen konnte. Einen entscheidenden mathematischen Schritt in der Berechnung der Bremsstrahlung gelang mir nur durch H. Voigt aus dem mathematischen Institut Tübingen.

Weitere, sehr hilfreiche Tips theoretische Fragen betreffend verdanke ich Uli Mayer und Andreas Hauck, die immer eine Antwort auf meine "Experimentator-typischen" Fragen parat hatten. Sie trugen ebenso wie viele Freunde und meine WG, besonders Inga Binder und Katrin Kilgus, zum notwendigen Ausgleich durch willkommene Zerstreuung und erholsame Freizeit bei.
Außdrücklich betonen möchte ich die Toleranz und Nachsicht meiner Partnerin Andrea Hartmann, die mir stets mit ihrer Hilfe eine große Unterstützung war und die viele meiner "Dissertations-Launen" zu ertragen hatte.
Besonderer Dank gilt meinen Eltern, die immer viel Geduld und Verständnis zeigten und mir durch ihre großzügige Unterstützung diese Arbeit erst ermöglicht haben.